**Dissertation**

Zur Erlangung des akademischen Grades eines “Doktor rerum naturalium (Dr. rer. nat.)”

an der

**Johannes Gutenberg–Universität Mainz**

**Fachbereich Physik, Mathematik und Informatik**

# Search for new physics in final states with a high energy electron and large missing transverse energy

**Dissertation provided**
**by Natascha Schuh**
(born in Bad Kreuznach)


Mainz, June 1, 2016

Datum der mündlichen Prüfung: 13.01.2017
Dissertation an der Universität Mainz (D77)

*For my children.*

So eine Arbeit wird eigentlich nie fertig;
man muss sie für fertig erklären, wenn man nach Zeit und Umständen das Möglichste getan hat.

*(Johann Wolfgang von Goethe, Italienische Reise, 1787)*

I hereby declare that I wrote the dissertation submitted without any unauthorized external assistance and used only sources acknowledged in the work. All textual passages which are appropriated verbatim or paraphrased from published and unpublished texts as well as all information obtained from oral sources are duly indicated and listed in accordance with bibliographical rules. In carrying out this research, I complied with the rules of standard scientific practice as formulated in the statutes of Johannes Gutenberg-University Mainz to insure standard scientific practice.

# Abstract

The most successful and comprehensive theory describing the microcosm is the Standard Model of particle physics (SM). It comprises all known elementary particles and describes in high precision the basic processes of three of the four fundamental interactions. But still, not all experimental observations and theoretical challenges are covered. Many models exist that take the SM as a good approximation of natural phenomena in already discovered energy regions, but extend it in various ways.

The Large Hadron Collider (LHC) provides the opportunity to look into these high energy regions using proton-proton collisions at significantly higher center-of-mass energies than previous experiments. This dissertation searches for physics beyond the SM especially in final states with one highly energetic electron (respectively positron) and large missing transverse energy.
With the data set recorded in 2012 by the ATLAS detector, a large multi-purpose detector making use of the LHC, the spectrum of the related combined transverse mass can be measured up to the TeV scale. To find any evidence to the existence of new physics beyond the SM, it was searched for significant deviations between the observed data and the expectations due to SM processes. Unfortunately, no significant excess could be observed and exclusion limits in the context of three different new physics scenarios are provided. Besides a so-called Sequential Standard Model (SSM) predicting additional vector gauge bosons, also the possible existence of (charged) chiral bosons is analyzed. Also inferences about dark matter candidates called "weakly interacting massive particles (WIMP)" are drawn.

With the aid of a Bayesian ansatz, the observed (expected) exclusion limit on the boson pole mass is set to 3.13 TeV (3.13 TeV) for a SSM $W'$ boson and to 3.08 TeV (3.08 TeV) for charged chiral $W^*$ bosons (at 95 % C.L.).

# Zusammenfassung

Das Standardmodell der Teilchenphysik (SM) ermöglicht es, nahezu alle bisher bekannten elementaren Teilchen und die grundlegenden Prozesse von drei der vier fundamentalen Wechselwirkungen in hoher Präzision zu beschreiben. Dennoch werden längst nicht alle experimentellen Beobachtungen und theoretischen Herausforderungen abgedeckt. Es existieren viele Modelle, die das SM als gute Näherung natürlicher Phänomene in bereits bekannten Energieregionen annehmen, es aber in vielfältiger Weise erweitern.

Der Large Hadron Collider (LHC) bietet mit einer (gegenüber vorangehenden Experimenten) signifikant erhöhten integrierten Luminosität und Schwerpunktsenergie die Möglichkeit, mithilfe von Proton-Proton-Kollisionen in völlig neue und bisher unerforschte Bereiche von Massen und Kopplungskonstanten einzudringen. Diese Dissertation untersucht insbesondere leptonische Endzustände mit einem hochenergetischen Elektron (oder Positron) und hoher fehlender Transversalenergie auf Hinweise neuer Physik jenseits des SM.
Mithilfe der im Jahr 2012 am ATLAS-Experiment aufgezeichneten Daten kann dabei das Spektrum der kombinierten transversalen Masse bis hin zu mehreren TeV ermittelt werden. Um einen Hinweis auf neue Physik zu erhalten, wurde dieses hinsichtlich signifikanter Abweichungen zwischen Daten und erwarteten SM Prozessen untersucht. Leider konnten keine solchen resonanten Überhöhungen festgestellt werden, sodass Ausschlussgrenzen im Kontext dreier erweiternder Szenarien ermittelt werden. Neben einem sogenannten sequentiellen SM (SSM), das weitere schwerere Vektorbosonen vorhersagt, wird dabei ebenfalls ein Modell herangezogen, das sich mit der Existenz (geladener) chiraler Bosonen beschäftigt. Zusätzlich werden auch Rückschlüsse auf mögliche Kandidaten dunkler Materie, sogenannte WIMPs (engl. “weakly interacting massive particles”, schwach wechselwirkende massive Teilchen) gezogen.

Mithilfe eines Bayesianischen Ansatzes wird im Falle eines SSM $W'$-Bosons die beobachtete (erwartete) untere Grenze auf die Bosonpolmasse bei 3.13 TeV (3.13 TeV), für chirale $W^*$-Bosonen bei 3.08 TeV (3.08 TeV) (95 % C.L.) ermittelt.

# Contents

# 1 Introduction

Since humans wish to understand their origins for centuries, the question for the tiniest constituents of matter has never been more relevant. Many scientists have searched for relationships in microcosm and explanations of the observed natural phenomena that are still not fully explored.
Rutherford, Marsden and Geiger achieved a decisive breakthrough in 1909 [Gei09]. Counting scattered alpha particles and studying their deflections while passing through thin metal foils, they devised a new model of an atom as a very small massive nucleus surrounded by electrons which are too light to influence the alpha particles [Rut11]. Much later, experiments revealed even more (point-like) constituents, so-called quarks, inside the already explored particles, as well as further leptons.

Over the last decades, previous theoretical predictions have been confirmed and models explaining unexpected discoveries are developed permanently. Indeed, today's well-known W and Z bosons, for instance, had been postulated already in the late 1960s while first indications of their existence were found more than ten years later [UA183, UA283]. Also the so-called Higgs boson has been recently discovered [ATL12f, CMS12], even it was devised already in 1964 [Hig64].
The most successful and comprehensive theory describing the microcosm is summarized within the Standard Model of particle physics (SM). It comprises all known elementary particles and describes in high precision the basic processes of three of the four fundamental interactions ([Gla61, Sal68, Wei67]), even it does not cover all experimental observations and theoretical challenges. Hints for neutrino flavor oscillations occuring, the hierarchy problem or the huge amount of free parameters are only a few aspects indicating that the SM might be an effective model derived from a more complex one. So, many new physics scenarios extending the SM exist which predict new particles also as a consequence of involved symmetry breakings and commonly arising for scales of at least 1 TeV.

The mostly used candidates for (charged) spin-1 gauge bosons outside the SM are the so-called $W'$ bosons. Based on a common model named Sequential Standard Model (SSM), these particles are in the subsequent analysis supposed to carry the same couplings as a SM W boson but with a strongly increased pole mass.
Also charged chiral bosons, usually called $W^*$, are prominent candidates of new physics scenarios. These heavy spin-1 vector bosons are mainly motivated by the hierarchy problem and predicted by at least three theories explaining the relative lightness of the Higgs boson. Their couplings to SM fermions are completely different to those of the $W'$ and lead in the sequel to deviating kinematic contributions.

Astrophysical observations also indicate that the known matter and energy, explained within the SM, amounts to only about 4 % of the total in universe. So-called dark matter further contributes with approximately 23 % while the rest of 73 % is described as unknown dark energy. As especially the first would explain observations of luminous matter and different gravitational phenomena, many analyses also search for an evidence of so-called weakly interacting massive particles (WIMP), possible candidates of dark matter.

Using proton-proton collisions at significantly higher center-of-mass energies and corresponding integrated luminosities than previous experiments, the Large Hadron Collider (LHC) provides the opportunity to look into totally new and undiscovered regions of masses and coupling constants. It

is the world's largest circular accelerator located at CERN, the European Organization for Nuclear Research, close to Geneva in Switzerland, and is used by six experiments in total. The ATLAS [1] experiment is, thereby, the largest multi-purpose detector making use of it.

This dissertation searches for physics beyond the SM especially in final states with one highly energetic electron (respectively positron) and large missing transverse energy, following the official ATLAS strategies in the main points. As a member of the ATLAS exotics working group, I contributed as a main analyzer in the electron chain and performed various studies of the underlying SM process description and the limit setting procedures which are also described later. The thesis on hand is structured as follows:
As an introduction and motivation to the different new physics scenarios, Chapter 2 describes theoretical foundations as well as the results of previous searches. Besides general information about the SM particles and interactions, also the various extensions as mentioned before are introduced in detail, considering not only their appearance and the coupling behavior of new particles involved but also possible interference effects with SM bosons. As the theory of hadron-hadron collisions is crucial for those LHC physics, it is explained in detail, too, by adducing the parton model of deep inelastic scattering ($\rightarrow$ Drell-Yan processes) and Feynman diagrams to visualize in addition such underlying schemes.

Experimental details of the LHC and the ATLAS detector are clarified in Chapter 3. To estimate and understand the processes occurring during the detector operations, Monte Carlo (MC) simulations are commonly utilized. These follow pre-defined conditions and probabilities that are realized via different generators and explained in detail. Based on information according certain energy depositions and various arising kinematic effects, also different signatures can be distinguished and various event reconstruction methods are used.

The wide variety of ATLAS analyses as well as calibration and efficiency measurements bring along the need also for a wide variety of dedicated triggers. Underlying trigger studies of a certain single electron trigger as well as of so-called W tag&probe triggers are briefly introduced in Chapter 4.

Finally, the main analysis of this dissertation is presented focusing on processes involving charged bosons decaying leptonically. Highly energetic leptons such as electrons or positrons are produced dominantly in the sequel of s-channel SM W production and should be detected within the central region of the ATLAS detector. Basic quality criteria of the recorded data and the selection criteria used to select these particles are explained in Chapter 5. To obtain signal efficiencies as high as possible, a minimization of arising background contributions (while keeping them describable in a reasonable way) is necessary. Chapter 6 describes the single processes expected due to the SM of particle physics and compares different distributions observed in data to those expected ones. While searching for new physics scenarios, significant discrepancies should be identified especially in terms of resonant increases at high transverse masses. If no such resonance can be found, exclusion limits are derived via both, a Bayesian and a Frequentist approach as described in Chapter 8. The last part of this dissertation (Chapter 9) provides a critical view onto the used analysis procedures and summarizes the main facts. An outlook to the near future of such kind of searches with the LHC concludes this thesis.

[1] **A** **T**oroidal **L**HC **A**pparatu**S**

# 2 Theory

This chapter describes the underlying theory of the Standard Model of Particle Physics comprising the contemporary comprehension of the known elementary particles and structures. After general introductions to the fundamental fermions and their interactions, a discussion of hadron-hadron interactions detectable with the ATLAS experiment follows in detail. Thereby, not only the known Feynman formalism will be considered but also the usage and the need for parton density functions. The last part in this chapter describes the limitations of the Standard Model, possible extensions and the current experimental status of their evidence.

## 2.1 The Standard Model of Particle Physics

The Standard Model of Particle Physics (SM) is the most successful and comprehensive theory describing the microcosm. It includes all known elementary particles and describes in high precision the basic processes of three of the four fundamental interactions (that are namely the strong, weak, electromagnetic and gravitational interaction [2]) ([Gla61, Sal68, Wei67]). In the underlying theory of the SM, matter consists of twelve fundamental fermions (meaning particles with spin $\frac{1}{2}$) and their anti-particles [3] interacting via exchange of so-called bosons. Those bosons have an integer spin and can be distinguished with respect to their kind of contribution to the fundamental forces. In fact, the photon ($\gamma$) is the mediator of the electromagnetic interaction, the $W^{\pm}$ vector gauge bosons transfer the weak charged current. The neutral $Z^0$ mediates the weak neutral current while eight gluons contribute in case of strong interaction. A summary of the processes included within the SM and the thereby not considered additional gravitation are listed in Table 2.1. The given vector boson masses are related to natural orders of magnitude for quantum mechanics and relativistic kinematics. Due to the small scales in particle physics, the energy is commonly given here in electron volts (1 eV = $1.6\times10^{-19}$ Joule) and masses in MeV/c$^2$ since a given mass $m$ corresponds to a rest energy of $mc^2$ MeV ($E = mc^2$). In addition, the values of $\hbar = \frac{h}{2\pi}$ and c are chosen to be equal to unity to simplify many calculations and to reduce the paper work. Quoting numbers and results subsequently, those natural units will be used.

| Interaction | Mediator | Spin | Mass | Relative Strength |
|---|---|---|---|---|
| Strong | 8 gluons | 1 | 0 | 1 |
| Electromagnetic | photons ($\gamma$) | 1 | 0 | $\frac{1}{137} \approx 10^{-2}$ |
| Weak | $Z^0$, $W^{\pm}$ | 1 | $Z^0$: 91.2 GeV<br>$W^{\pm}$: 80.4 GeV | $10^{-5}$ |
| Gravitation | | 2 | 0 | $10^{-38}$ |

Table 2.1: Summary of the fundamental interactions. The three interactions listed firstly are, in contrast to the gravitation, considered and fully described within the Standard Model of Particle Physics (SM). The given masses are related to natural units of quantum mechanics and relativistic kinematics [Gla61].

[2] The explanation of the gravitation is not included within the SM. However, its (relative) strength is low compared to the others and thus not relevant for the validity of the SM.

[3] Anti-particles carry the reversed quantum numbers and describe states on the negative mass shell instead.

**Fundamental fermions** The twelve fundamental fermions consist of six quarks and six leptons that are ordered each within three generations or families. The first generation considers the stable visible matter whereby the other two include the heavier particles that decayed early after the big bang to today's detectable ones. Leptons carry integer charges and are subject to weak interactions. In case of electrically charged particles, they may interact also electromagnetically. Quarks, on the other hand, carry third-numbered charges and participate in electromagnetic and weak processes, as well as under strong interactions since they carry additionally a color charge. As in nature only color neutral objects appear as free particles, the quarks cannot appear as free objects and form, bound in hadrons, the smallest punctuate constituents of the known nucleons. A summary of the known elementary particles is shown in Table 2.2.

| | 1st Generation | 2nd Generation | 3rd Generation | Electric Charge |
|---|---|---|---|---|
| Quarks | u | c | t | $+\frac{2}{3}$e |
| | d | s | b | $-\frac{1}{3}$e |
| Leptons | $e^-$ | $\mu^-$ | $\tau^-$ | $-1$e |
| | $\nu_e$ | $\nu_\mu$ | $\nu_\tau$ | 0 |

Table 2.2: Summary of the fundamental particles considered within the SM. Anti-particles are usually marked by a bar above the appropriate letter ($\bar{q}$ for quarks or $\bar{l}$ for leptons), or by indicating their opposite charge (e.g. positrons ($e^+$), anti-muons ($\mu^+$)). They are not listed explicitly as they simply carry the reversed quantum numbers. The charges are given in units of the elementary charge e.

**Gauge Transformations and Fields** Generally, free fermions are described as Dirac particles following the related Dirac equation:

$$(i\gamma_\mu \partial^\mu - m)\psi(x) = 0 \tag{2.1}$$

where $\gamma_\mu$ denotes the corresponding Dirac matrices and $\partial^\mu$ is the short form of $\frac{\partial}{\partial x^\mu}$. The corresponding wave function is described by $\psi(x)$ with $x$ as space-time coordinate. Introducing a Lagrangian density $L_{Dirac}$

$$L_{Dirac} = \bar{\psi}(x)(i\gamma_\mu \partial^\mu - m)\psi(x) \tag{2.2}$$

with $\bar{\psi}(x) = \psi^\dagger \gamma_0$ as adjoint solution, the underlying dynamics can be described.

Since the invariance of the Lagrangian density is a sufficient condition for the covariance of the theory, its behavior under a symmetry operation should be regarded in particular. Here, the related physics can be observed to be invariant, especially, if $\psi(x)$ can be transformed as follows:

$$\psi(x) \to e^{ie\theta(x)}\psi(x) \;\; and \;\; \bar{\psi}(x) \to \bar{\psi}(x)e^{-ie\theta(x)}, \;\; e^{ie\theta(x)} \in U(1)\,^4 \tag{2.3}$$

whereby $\theta(x)$ denotes a phase transformation and $e$ the electric charge of the particle. Generally, $\theta$ depends on $x$ and the symmetry operation is denoted as local gauge transformation whereas a

[4] The infinite amount of phase transformations forms the unitary group U(1). As the commutativity is given among such transformations, it is also an abelian group.

constant $\theta$ (for all values of $x$) is given in case of a global gauge transformation. With this, the Lagrangian density defined as above cannot be invariant under local gauge operations:

$$L_{Dirac} \rightarrow L_{Dirac} - \bar{\psi}(x)\gamma_\mu \psi(x)\partial^\mu \theta(x) \neq L_{Dirac} \tag{2.4}$$

In fact, the phase of the wave function of a charged particle stays invariant only while introducing simultaneously force fields (gauge fields) compensating the local transformation. These gauge fields are vector fields and the mediators of the fundamental interactions can be regarded as quanta of these. The underlying dynamics of the fields can be then described by a Lagrange function defined as integral over the Lagrangian density [5]. Nevertheless, the related gauge bosons have to be massless if the local gauge invariance should be valid. This contradiction to the massive bosons introduced above is solved within the Higgs mechanism as described below (followed by a detailed description of the various interactions).

**The Higgs Mechanism** The massive gauge bosons contradict the gauge principle that predicts massless bosons only. The problem is solved by a spontaneous symmetry breaking considered within the Higgs mechanism whereby all elementary particles receive an effective mass by coupling to a so-called Higgs field [6]. This field has a ground state not including the continuous symmetry of the Lagrangian function corresponding to the field (spontaneous symmetry breaking). By introducing a complex, scalar field $\Phi$ into the Lagrangian density such that

$$L = (\partial^\nu \Phi)(\partial_\nu \Phi) - V(\Phi), \tag{2.5}$$

the spontaneous symmetry breaking can be realized. Here, $V(\Phi) = -\mu^2|\Phi|^2 + \lambda^2|\Phi|^4$ denotes the Higgs potential with $\Phi(x) = \frac{1}{\sqrt{2}}(\Phi_1(x) + i\Phi_2(x))$ and $\lambda^2 > 0$ to obtain a bound state. The important parameter is $\mu^2$: In case of zero or positive values, a symmetric solution can be found describing free particles with $m = \sqrt{\mu}$ (potential minimum at zero). For negative $\mu^2$, no unique minimum is possible. The ground states circle with $\Phi_0 = \frac{1}{\sqrt{2}}\frac{\mu}{\lambda}$. They are degenerated and thus, cause the global symmetry to be broken spontaneously. This typical form of the Higgs potential is often described as "Mexican hat".
The Higgs mechanism as described above predicts another particle, namely the Higgs boson [Hig64]. A first evidence for this massive neutral scalar boson was found by ATLAS [ATL12f] and CMS [7] [CMS12] in 2012 [8].

### 2.1.1 Fundamental Interactions

Apart from receiving their masses by couplings to the Higgs field, the elementary particles introduced as fermions and anti-fermions can also interact among themselves. Depending on their type,

[5] The Lagrange function, in general, is defined as difference of kinetic and potential energy: $L = T - V$. By its integration over the time, its action and the equations of motion follow (Euler-Lagrange equations).

[6] Explicit fermion mass terms that are also not invariant under local gauge transformations can be explained similarly by so-called Yukawa couplings meaning fermionic couplings to the Higgs field.

[7] **C**ompact **M**uon **S**olenoid, one of the four largest experiments located at CERN, Geneva.

[8] A particle has been discovered having properties compatible with those predicted for a SM Higgs boson. Since also many different models beyond the SM predict an additional Higgs boson, careful studies of the particle's properties are on-going to ensure the existence of a SM Higgs.

they may appear in bound states only (e.g. quarks bound in mesons or baryons), carry special quantum numbers (e.g. color charge) or communicate via exchange of different gauge bosons. Also self-coupling of the latter is conceivable and shall be considered in the following, too.

**Strong interactions** The strong interaction is mediated between quarks via exchange of gluons. Following the theory of quantum chromodynamics (QCD), quarks carry an additional property (degree of freedom) denoted as color charge that can be blue, red or green [9]. Assuming total color symmetry, the related anti-quarks always have the appropriate anti-color. The underlying symmetry can be described via a special unitary $SU(3)_{color}$ group of degree three referring to the three possible values of the color quantum number.
Besides that color charge, quarks carry another important property: the so-called strong isospin that is a conserved value describing the existence of analogous states having the same spin and parity [10]. So, regarding those fermions as constituents of a nucleon, the quarks may occupy up to twelve different configurations (two spin variations, two isospin states for u- and d-quarks and three different color charges).
The potential between two quarks is composed of two terms:

$$V_s = -\frac{4}{3}\frac{\alpha_s}{r} + kr \tag{2.6}$$

whereby $r$ denotes the distance in-between and $\alpha_s \lesssim 1$ the strong coupling constant. The second term refers to a confinement of the quarks at high radii causing the production of new quark–anti-quark pairs while attempting to break up a bound quark. Thus, single quarks cannot appear as free particles.

Carrying a color charge, too, the massless spin-1 gluons couple to that quantum number and may interact not only with those quarks but also among themselves. But, in contrast to quarks, gluon color states do not follow a total color symmetry so that combinations like red – anti-blue are possible. Referring in the following to processes with gluon exchanges, always superpositions of the contributions of all possible gluon states in total are meant, as single gluon contributions are not distinguishable [11].

**Electromagnetic interactions** The quantum electrodynamics (QED) describe the theory of electromagnetic interactions between charged particles and photons with respect to the most important properties of renormalizability and gauge invariance. While the latter leading to retained currents and conservation of the electric charge, has been introduced already before, the first is important for precise calculations of such processes and will be explained subsequently. Self-coupling terms such as the possibility for a single electron to emit or reabsorb virtual photons or electron-positron pairs contribute to the mass and charge of the particle. To avoid divergences with infinite

[9] These are arbitrary values that are usually chosen in literature.
[10] Within the isospin concept, a neutron and a proton can be simply regarded as two different states of the same nucleon with isospin $I = \frac{1}{2}$.
[11] Also single free gluons cannot exist.

masses and charges, these self-coupling contributions are included by a redefinition and determination to measured physical values of those particle properties. This is also known as renormalizability.

**Weak interactions** The weak interaction appears between all fundamental fermions (quarks and leptons) and is mediated via exchange of massive vector gauge bosons ($Z^0$, $W^{\pm}$) [UA183, UA283]. Thereby, decays of heavier fermions into lighter, as well as a change of the involved quark types (denoted as quark flavor) are possible. Since the transfer is mediated via massive bosons only, the weak interaction covers only a small range and is usually overlaid by strongly or electromagnetically interacting processes. In fact, observable weak processes involve neutrinos (having no strong or electromagnetic couplings) or quarks with flavor changes (not allowed within the firstly described interactions). The single processes are distinguished by the contribution of leptons, quarks or both kinds of fermions and are denoted accordingly as leptonic or hadronic processes.

The SM harmonizes successfully the weak and the electromagnetic interactions as unified electroweak theory. It postulates the identical coupling $g$ to leptons and quarks for $W^{\pm}$ and $Z^0$ bosons as for photons (that is $g = Q$ the electric charge) and is based on the gauge theory with a special $SU(2)_L \times U(1)_Y$ symmetry group [Per00]. Here, $SU(2)_L$ describes the weak and $U(1)_Y$ the electromagnetic interaction. The $L$ visualizes the fact that left-handed particles only take part in the weak interaction (due to the weak isospin). The $Y$ denotes the weak hyper charge defined as difference of the electric charge (Q) and the third component of the weak isospin ($Y = 2(Q - I_3)$). The electric charge is commonly given in units of the elementary charge e.

The Lagrangian density of the electroweak theory includes kinematic terms due to both, vector gauge bosons and single fermions with their couplings to those gauge bosons. It is:

$$L_{EW} = L_{Gauge} + L_{Fermion} \tag{2.7}$$

Here, $L_{Gauge}$ includes the kinetic energy of the gauge bosons and their self-couplings (not for the photon) whereas $L_{Fermion}$ refers to the kinetic energy of fermions and their interactions with the gauge bosons.
Four vector fields follow by the fact that the electroweak Lagrangian density is invariant under transformations of the related symmetry group $SU(2)_L \times U(1)_Y$: The vector field $B_\mu$ couples with a coupling strength $g'$ to the hyper charge while $W^i_\mu$ ($i = 1,2,3$) couples with $g$ to the weak isospin. The known gauge bosons of the electromagnetic and the weak interactions follow in the electroweak theory by four initially massless bosons $B^0$, $W^1$, $W^2$ and $W^3$ [12]:

$$|\gamma\rangle = \cos\theta_W |B^0\rangle + \sin\theta_W |W^3\rangle \tag{2.8}$$

$$|Z^0\rangle = -\sin\theta_W |B^0\rangle + \cos\theta_W |W^3\rangle \tag{2.9}$$

$$|W^{\pm}\rangle = \frac{1}{\sqrt{2}}(|W^1\rangle \mp i|W^2\rangle) \tag{2.10}$$

[12] As described before, the observed boson masses can be explained within the Higgs mechanism.

The $B^0$ and $W^3$ carry identical quantum numbers and are therefore allowed to mix. So, two states, simply rotated through the so-called Weinberg angle ($\theta_W$), can be found as observed in measurements (Eq. 2.8, 2.9) where the photon couples to the electric charge and $Z^0$ to the weak isospin. As already mentioned, those processes are known as neutral current whereas charged currents change, indeed, the charge of an involved lepton or hadron by exchange of $W^{\pm}$ bosons [13]. The latter are obtained as linear combination of the $W^1$ and $W^2$ states (Equ. 2.10). The electric charge can be given also in dependence of the gauge coupling constant $g$ (or $g'$ respectively) by:

$$e = g \sin\theta_W = g' \cos\theta_W \quad \textit{and} \quad g^2 = \frac{4\pi\alpha_{em}}{\sin^2\theta_W} \tag{2.11}$$

where $\alpha_{em}$ denotes the electromagnetic fine-structure constant.
In contrast to the uncharged photon, the gauge bosons ($Z^0$, $W^{\pm}$) are allowed to couple among each other ("self-coupling") as these belong to the weak $SU(2)$ [14] symmetry group. This group is non-abelian so that the field operators do not commutate. This results in additional kinematic terms within the Lagrangian density involving the couplings of the gauge bosons to the weak isospin.

**Symmetry group of the SM** Summarizing the various interactions and their origins as described above, the Lagrangian density corresponding to SM processes is composed of the quantum chromodynamics (QCD) referring to processes under strong interaction, the electroweak theory (EW) and the Higgs mechanism:

$$L_{SM} = L_{QCD} + L_{EW} + L_{Higgs} \tag{2.12}$$

whereby $L_{EW} = L_{Gauge} + L_{Fermion}$. The SM is based on a gauge theory with the symmetry group $SU(3)_{color} \times SU(2)_L \times U(1)_Y$ that is broken spontaneously. The symmetry group $SU(3)_{color}$ refers to the strong interaction with three types of colors while the $SU(2)_L \times U(1)_Y$ part describes the electroweak theory.

## 2.2 Hadron-Hadron Interactions

Hadrons denote (color) neutral particles composed of quarks and gluons. One distinguishes between baryons consisting of three quarks, and mesons built by a quark–anti-quark pair. The known nucleons like protons or neutrons are assembled by three quarks and belong therefore to the group of baryons. Their quantum numbers result out of so-called valence quarks that interact via exchange of gluons and produce virtual quark–anti-quark pairs or annihilate in gluons. Those neutral pairs are usually denoted as sea quarks. Their effective quantum numbers disappear on average, so that the quantum numbers of a nucleon are fully defined by those of the valence quarks. The single partons (meaning the smallest constituents of a nucleon such as sea or valence quarks and gluons) can be described by so-called parton density functions (PDF) $f_{a,A}(x_a, Q^2)$. They give the probability for a

[13] Weak processes involving charged W gauge bosons may cause a flavor change of quarks. The description of the statistical fraction of quarks changing their flavor is summarized in an unitary $3 \times 3$ matrix, denoted as CKM matrix. It was initially introduced by Nicola **C**abbibo, Makoto **K**obayashi und Toshihide **M**asukawa.
[14] The $SU(2)$ group includes fields having a doublet structure.

parton "a" having a momentum fraction of $x_a$ [15] to be found at a momentum scale $Q^2$ (the letter $A$ denotes the hadron including the specific parton "a") [Mar09]. The momentum fraction is thereby defined as fraction of the total hadron momentum, in case the hadron is boosted strongly along the beam axis and transverse parton momenta are negligible.

Colliding (accelerated) hadrons do not interact in total but under scattering of their single partons. For the production of new particles, only the center-of-mass energy of the single partons is available. To describe the appearing processes in detail, Drell and Yan developed the idea to transfer the parton model of deep inelastic scattering to hadron-hadron interactions [Dre70].

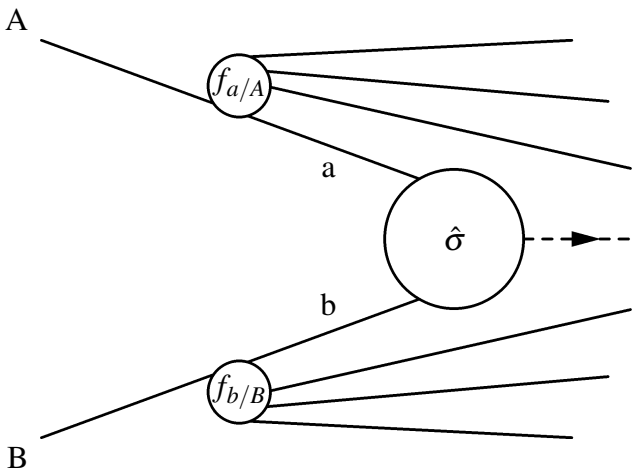


Figure 2.1: Hard scattering process. Incoming hadrons are denoted as A and B, small letters (a,b) describe the scattering partons and $f_{a/b,A/B}(x_{a/b},Q^2)$ the PDFs for momentum fractions $x_{a/b}$.

Figure 2.1 visualizes the underlying scheme of incoming colliding hadrons resulting in a scattering of partons. The probability for particles to interact during a collision can be described by a cross-section that is defined (in terms of observables) as:

$$\sigma(\Delta\Phi) = \frac{R(\Delta\Phi)}{j} \tag{2.13}$$

whereby $\Delta\Phi$ denotes the regarded region of phase space, $\sigma(\Delta\Phi)$ the cross-section for scattering into $\Delta\Phi$. The event rate in $\Delta\Phi$ is called $R(\Delta\Phi)$ and the incoming flux is $j$. In terms of a differential cross-section, the total scattering cross-section follows as its integral over the whole solid angle and provides a measure of the interaction strength between the particles:

$$\sigma(\Delta\Phi) = \int_{\Delta\Phi} \frac{d\sigma}{d\Phi}(\Phi)\,\mathrm{d}\Phi \tag{2.14}$$

with the phase space element $d\Phi$.
So, accounting for the parton composition, the final hadronic cross-section of a process $\sigma(AB \rightarrow$

[15] The momentum fraction $x$ is often denoted as "Bjørken-x" referring to Bjørken who introduced that description [Bjø69].

$l^+l^- + X$) can be derived in general by weighting the subprocess $\hat{\sigma}(q\bar{q} \to l^+l^-)$ by the appropriate PDF functions determined out of deep inelastic scattering processes. It is:

$$\sigma_{AB} = \int\int f_{a,A}(x_a, Q^2) f_{b,B}(x_b, Q^2) \hat{\sigma}_{ab \to l^+l^-} \, \mathrm{d}x_a \mathrm{d}x_b \tag{2.15}$$

where $a$ and $b$ denote the incoming quarks ($q$, $\bar{q}$) and $Q^2$ the momentum scale representing the scale up to which parton emissions may be described by the PDF. The leptons involved are called $l^+$, $l^-$.

Figure 2.2 shows the connectivity between this scale $Q^2$ and the momentum fraction $x$ of a parton for a fixed center-of-mass energy of nominal $\sqrt{s}$ =14 TeV at the LHC [Sti13]. To clarify the basic definitions influencing these observables, the simplest form of Drell-Yan processes shall be briefly discussed afterwards.

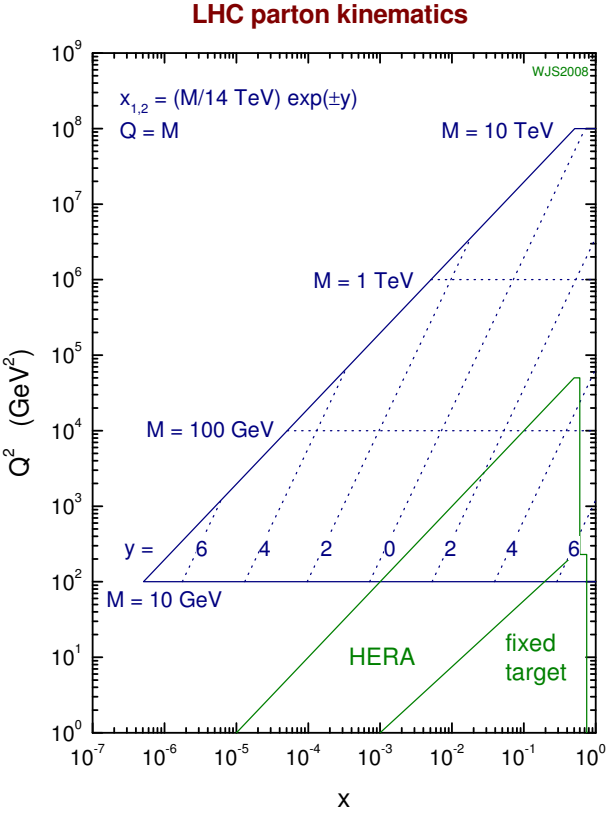


Figure 2.2: The connectivity between the momentum scale $Q^2 = M^2$ ($M$ denotes the invariant mass of the lepton pair) and the Bjørken-x is demonstrated for a fixed center-of-mass energy of $\sqrt{s}$ =14 TeV [Sti13].

In the case, a scattered parton carries a color charge, the remnant of the colliding hadron is no longer colorless. Indeed, these remaining particles may also interact further (known as so-called "underlying event" contaminating the hard process). Due to the requirement of confinement (Sect. 2.1.1), (typically low energetic) colorless hadronic states are formed subsequently. So, up to a few dozen light mesons or baryons can be usually produced by combination of high momentum partons or

in the sequel of emitted gluons annihilating into a quark–anti-quark pair which interacts in turn. These effects are summarized as hadronization and the bunches of hadrons produced are denoted commonly as jets.

**Drell-Yan processes** In the simplest Drell-Yan process, a quark–anti-quark pair annihilates to a virtual photon decaying in turn to a pair of oppositely charged leptons, meaning $q\bar{q} \to \gamma^* \to l^+l^-$. For higher center-of-mass energies, the process via a heavier Z boson becomes possible, so that $q\bar{q} \to Z^0 \to l^+l^-$ (if $M_{l^+l^-} \approx M_{Z^0}$). The cross-section for producing such a massive lepton pair out of a quark–anti-quark annihilation, $\hat{\sigma}(q\bar{q} \to l^+l^-)$, is derived by basic processes of the quantum chromodynamics. Neglecting the transverse momenta, the four-momenta describing the incoming partons follow as:

$$p_a^\mu = \frac{\sqrt{s}}{2}(x_a,0,0,x_a), \tag{2.16}$$

$$p_b^\mu = \frac{\sqrt{s}}{2}(x_b,0,0,-x_b), \tag{2.17}$$

involving the particular momentum fractions $x_i$ carried by the partons. Introducing the Mandelstam variables [Man58],

$$\hat{s} = (p_a + p_b)^2 \quad \hat{t} = (k_a - p_a)^2 \quad \hat{u} = (k_a - p_b)^2 \tag{2.18}$$

the center-of-mass energy squared $s$ is given via: $\hat{s} = x_a x_b s$. The four-momenta describing the outcoming leptons are called $k_a$ and $k_b$. Furthermore, the rapidity of a particle is given by $y = \frac{1}{2}\ln(\frac{E+p_z}{E-p_z})$ whereby $E$ denotes the particle energy and $p_z$ the longitudinal component of its momentum. In general, the rapidity behaves additively under Lorentz transformations in z direction, so that $y = \frac{1}{2}\ln(\frac{x_a}{x_b})$ in case of the process previously mentioned. The momentum fractions are derived as follows:

$$x_{a,b} = \frac{M}{\sqrt{s}} e^{\pm y}. \tag{2.19}$$

Here, the variable M denotes the invariant mass of the lepton pair.

For the charged Drell-Yan process where a charged gauge boson couples to an up-down type quark pair and a charged lepton-neutrino pair, $q\bar{q} \to W^\pm \to l^{\pm}\overset{(-)}{\nu}$, usually, the invariant mass cannot be reconstructed as the longitudinal component of the neutrino momentum is not detectable (the neutrino does not interact with material). Assuming the W boson to be produced at rest, the momenta of the subsequent decay products follow due to energy and momentum conservation as: $p_l = p_\nu = \frac{m_W}{2}$. The corresponding Mandelstam variables are exemplarily:

$$\hat{s} = (p_{\bar{u}} + p_d)^2 \quad \hat{t} = (p_l - p_{\bar{u}})^2 \quad \hat{u} = (p_l - p_d)^2 \tag{2.20}$$

and the momentum component of the lepton in the transverse plane is given by:

$$p_{T,l} = \frac{m_W}{2}\sin\theta \leq \frac{m_W}{2} \quad \textit{and} \quad p_{T,l}^2 = \frac{\hat{s}}{4}\sin^2\theta = \frac{\hat{s}}{4}(1-\cos^2\theta). \tag{2.21}$$

Here, $\theta$ denotes the angle between the lepton and the parton direction. Within the lab frame, the W system may be boosted only along the z axis and the $p_T$ distribution with its characteristic endpoint at half of the W boson mass is conserved (in other words, the transverse lepton momentum is

invariant under longitudinal boosts along the beam direction and thus, $p_{T,l}^{CMS} = p_{T,l}^{lab}$ where "CMS" denotes the center-of-mass system and "lab" the lab frame). Regarding the second equation in 2.21 (right) in particular, the angular part within the differential cross-section calculation might be extracted from the transverse momentum:

$$\frac{d\sigma}{dp_T} = \frac{d\sigma}{d\cos\theta}\frac{d\cos\theta}{dp_T} \tag{2.22}$$

The corresponding Jacobi determinant is:

$$\left|\frac{d\cos\theta}{dp_T}\right| = \frac{4p_T}{\hat{s}}\left(\sqrt{1-\frac{4p_T^2}{\hat{s}}}\right)^{-1} \tag{2.23}$$

Obviously, Equation 2.23 leads to a singularity at $p_T = \frac{\sqrt{\hat{s}}}{2} \approx \frac{m_W}{2}$ ($\cos\theta = 0$ or $\theta = \frac{\pi}{2}$) causing the characteristic maximum (commonly denoted as Jacobian peak) visible in the transverse momentum distribution of the W decay products.

Similar to the cross-section determination of the Drell-Yan process in total, also those of single subprocesses as the production of heavy gauge bosons can be regarded ($\hat{\sigma}(q\bar{q} \to Z^0)$, $\hat{\sigma}(q\bar{q} \to W^{\pm})$). Indeed, the W cross-section, for instance, decomposes into several quark subprocesses that are visualized exemplarily in Figure 2.3.

### 2.2.1 Feynman Formalism

To determine precisely the transition probability and with this also the corresponding (differential) cross-section (Equ. 2.14) for a certain process, Feynman derived various rules for a rather simple visualization of the complex interactions and provided the opportunity to calculate the scattering amplitudes (and thus the probabilities) from a field theory Lagrangian. So, specific arithmetic charts (so-called Feynman graphs) visualize the underlying schemes and help to find the related mathematical expressions.
To understand these, some basic definitions are explained firstly in the following. Describing initial and final states, the first ($|in\rangle$) means those prepared, for instance, by an accelerator, that are transformed subsequently by an interaction and resulting in a state overlapping with the latter ($|out\rangle$). Thereby, the transition probability is given by the absolute square of the transition amplitude ($A_{in\to out} = \langle out|S|in\rangle$). Depending on the regarded kinematics, these probabilities have to be added (e.g. spins, flavors) or integrated (e.g. angles, energies, momenta) afterwards to compute the differential cross-section ("Fermi's golden rule").

Within the Feynman graphs, single particles are represented as lines; a connecting point of three or more such lines demonstrates the interaction point, denoted commonly as vertex. Internal particles, meaning those not present in the initial or final state, are visualized as inner line between two vertices. Adducing a simple two-body decay (Figure 2.4), the scheme of these graphs should be demonstrated. The timelike axis follows, here, along the abscissa whereas the spacelike axis forms the ordinate. External spin-$\frac{1}{2}$ particles are realized as arrows pointing into the direction of motion

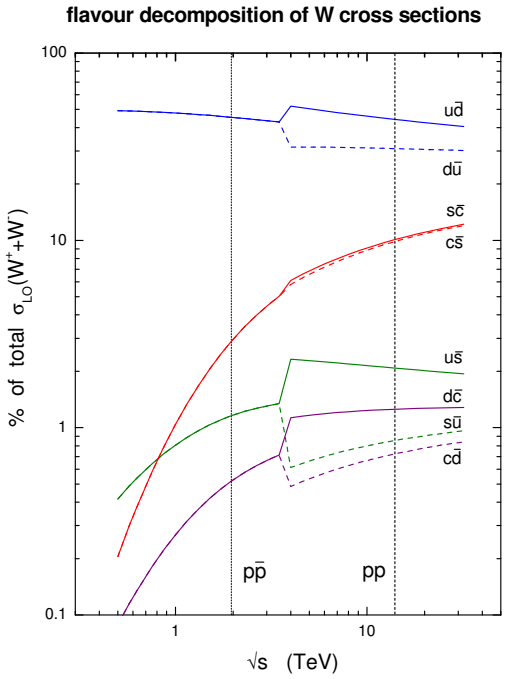


Figure 2.3: Quark subprocess decomposition of (leading order) W cross-section produced in proton-proton collisions [Sti13]. Obviously, a $W^+$ production (e.g. $u + \bar{d} \rightarrow W^+$) is slightly preferred compared to $W^-$ production (e.g. $d + \bar{u} \rightarrow W^-$) as a proton is composed of two up- and a down-type (uud) valence quark.

(charge); external spin-$\frac{1}{2}$ anti-particles vise-versa. So, the incoming and outcoming lines to a vertex carry an energy, momentum and spin whereby at each vertex, momentum conservation should be ensured to fix the momenta also of the internal lines. Incoming particles with a momentum $\vec{p}$, for instance, can be replaced always by outcoming anti-particles having a momentum of $-\vec{p}$ without changing the related matrix element. On basis of the schemes drawn for a particular process, the total scattering amplitude squared can be derived whereby each line shown is connected to a specific propagator entering the calculation. For instance, internal spin-1 particles and anti-particles with a mass not-vanishing are given (in context of the SM) by

$$P = \frac{-ig_{\mu\nu} + i\frac{k_\mu k_\nu}{M^2}}{k^2 - M^2 + i\Gamma M} \tag{2.24}$$

whereby $k$ denotes the particle momentum, $M$ is its mass and $\Gamma$ its finite width. The particular

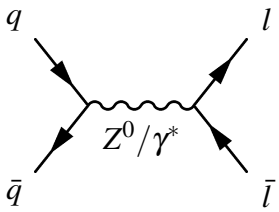


Figure 2.4: Lepton-pair production at LO visualized as Feynman graph.

particle couplings contribute to the amplitude with an additional factor proportional to the square root of the appropriate coupling constant (derived from the interaction term in the Lagrangian) such as $\sqrt{\alpha_{em}}$ in the case of electromagnetic interaction. A simple $2 \to 2$ process, for example, includes two vertices and with this, an amplitude proportional to $\sqrt{\alpha_{em}} \cdot \sqrt{\alpha_{em}} = \alpha_{em}$ follows.

The final amplitude for a certain process is obtained in total by the sum of all possible diagrams with respect to their relative signs and ensuring an anti-symmetric sum under exchange of identical initial and final state fermions (but symmetric for bosons) [16]. The cross-section can be derived subsequently and written in dependence of the appropriate coupling constants such that:

$$\sigma = \sum_{ijk} \alpha_s^i \alpha_{em}^j \alpha_{weak}^k \sigma_i^{ijk} \tag{2.25}$$

Here, the strong coupling constant is denoted as $\alpha_s$, $\alpha_{weak}$ refers to the weak interaction. The cross-section contributions of all diagrams with the same order of magnitude in $\alpha_i$ are denoted as $\sigma_i$. In general, contributions with the lowest order of magnitude according $\alpha_i$ refer to so-called leading order (LO), those of the second lowest order are called next-to-leading order (NLO) and so on.
Following these conventions, Feynman graphs for arbitrary processes can be drawn using propagators and interaction vertices connecting the initial and final states.

Starting usually with LO diagrams including the basic steps only (e.g. initial and final states, single intermediate state), various corrections may be applied to receive illustrations at higher orders. Figure 2.5 shows some possibilities exemplified for basic $2 \to 2$ processes. In general, one distinguishes real contributions meaning those of particles being really present in the initial or final state [17], and virtual contributions. The latter may originate from all possible intermediate objects contributing to the amplitude that are not visible at the end. As an example for real (QCD) corrections to lepton-pair production at LO, initial-state gluon radiation is shown in Figure 2.5 on the top left. A virtual correction to QCD processes is given in form of a fermion loop shown on the bottom right. Also particular vertex modifications are conceivable as, for example, that shown on the bottom left involving a virtual-gluon.

## 2.3 Physics beyond the Standard Model of Particle Physics

Although the SM provides the opportunity to describe all known elementary particles and basic processes of three of the four fundamental interactions in high precision with only a few assumptions, still not all observations and theoretical questions are covered. Besides unexplained aspects like the observed neutrino oscillations [18] ([MIN11],[Kam08]) or the huge matter – anti-matter asymmetry in today's universe, also the wish to unify not only two of the four fundamental forces arises. The much weaker gravitation ($\to$ "hierarchy problem"), the large range of existing fermion masses (about 511 keV - 173 GeV) and energy scales (0.2 - $10^{19}$ GeV) or the huge amount of free parameters

[16] In case of closed loops, an integration of the loop momenta is needed.

[17] If an object is emitted by an initial state particle, it is referred to so-called initial-state radiation (ISR); if a final state particle radiates off an object, the effect is known as final-state radiation (FSR).

[18] Requiring non-zero neutrino masses, these observations cannot be explained within the SM which was developed before such phenomenons have been detected.

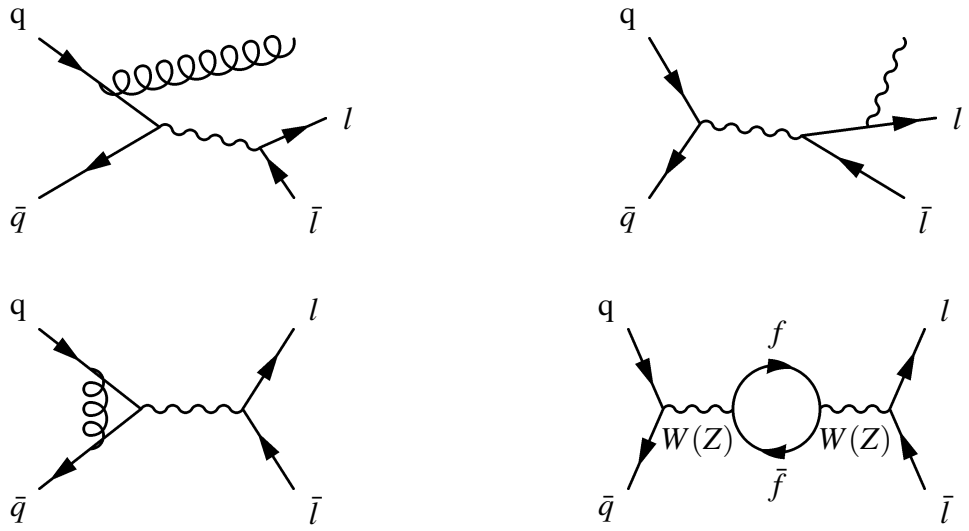


Figure 2.5: Processes contributing to NLO corrections: initial state gluon radiation (top left), final state photon radiation (top right), virtual-gluon correction (bottom left) and fermion loop (bottom right).

(27 arbitrary, fine tuned parameters) are only a few more unresolved aspects not (fully) described within the SM.
In fact, many models take the SM as a good approximation of natural phenomenons in already discovered energy regions, but extend it in various ways. Nearly all of them are based on symmetry principles and predict the existence of new (heavier) gauge bosons as a consequence of involved symmetry breakings. In the case of the electroweak theory, these were the well-known charged $W^{\pm}$ and the neutral Z boson. So, for instance, a grand unified theory (GUT [Ros84]) is conceivable comprising not only the unification of electromagnetic and weak interactions but also these electroweak effects combined with the strong force. During the cooling of the universe following the big bang, the originally combined forces decomposed into today's fundamental forces accompanied by symmetry breakings requiring additional gauge bosons. Other models ($\rightarrow$ "Kaluza-Klein" models) involve gravitational effects, too, by introducing extra-dimensions and with this also additional bosons [App87]. Further theories refer to an asymmetry between left and right-handed W bosons decaying in turn to an electron and a neutrino whereby leptonic decays of the right-handed bosons are strongly suppressed due to too heavy right-handed neutrinos [ATL15a].

To verify or at least restrict those model dependent properties and predictions, experimental measurements are needed. They may find evidences for the validity of a theory or provide at least hints for theorists how a model has to be modified.

Searching for new physics scenarios beyond the SM, two different extending theories are considered for this analysis, as well as a dark matter interpretation. The underlying models are described explicitly after the general concept of a search has been explained.

**The concept of a search** Following the theory of the SM, new physics scenarios are expected to arise above 1 TeV. As nearly all attempts to extend the current SM involve the existence of new particles with the same types, a fourth fermion generation or new gauge bosons, it is convenient to search for these in those high energy regions. The LHC provides the opportunity to look into these energy ranges using proton-proton collisions at significantly higher center-of-mass energies

than previous experiments. To have a measure for the amount of particles per beam passing a predefined area in a particular time unit, the so-called instantaneous luminosity $L$ is determined. In case of a ring collider like the LHC using beams composed of strings of particle bunches, the total instantaneous luminosity follows as sum over all bunch pairs colliding and is given especially in case of Gaussian distributed particles per beam:

$$L = \frac{nfN_1N_2}{2\pi\Sigma_x\Sigma_y} \tag{2.26}$$

where $n$ denotes the amount of colliding bunches, $f$ the orbital frequency at the collider and $N_{1/2}$ the amount of particles per bunch [19]. The dimension of the colliding area is described further by $\Sigma_x$ and $\Sigma_y$ ("convolved beam sizes") that can be determined via so-called van-der-Meer scans (see Sect. 3.2.1). The rate of events for a particular physical process follows then as $R = L\sigma$ whereby $\sigma$ denotes the appropriate cross-section. Integrating the luminosity in addition over time, $L_{int} = \int L\,dt$ (so-called integrated luminosity), the amount of events can be estimated. In fact, tuning the instantaneous luminosity, the amount of data recorded in a fixed amount of time can be optimized for a fixed center-of-mass energy such that the probability for a certain reaction to occur increases.

Having optimized these pre-conditions in an experiment, there are various ways to search for new physics scenarios arising. By colliding beams, several processes or decays respectively proceed. So, it is quite natural to look into a specific decay channel, checking the observations against the SM expectations to find any deviation. On the other hand, it is also conceivable to choose a single model and try to validate this in various decay channels. This analysis follows the first way of proceeding: Searching for new physics scenarios in final states with a highly energetic electron (respectively positron) and large missing transverse energy, two extending theories as well as a dark matter interpretation shall be considered.

Comparing data to expected SM processes, the invariant mass is usually chosen as signal discriminant as it is clearly defined and a new signature would be clearly visible. In the case of involving a neutrino in the final state, it is not possible to determine the invariant mass precisely due to the missing (not detectable) longitudinal component of the neutrino momentum. Hence, another observable is needed. The so-called transverse mass $m_T = \sqrt{2p_{T,l}p_{T,\nu}(1-\cos\phi_{l\nu})}$ coupled to the transverse momenta of the decay particles refers to known quantities only and is used in the following as signal discriminant. Thereby, the transverse momentum of the charged lepton is denoted as $p_{T,l}$, $p_{T,\nu}$ describes the transverse momentum of the neutrino and $\phi_{l\nu}$ is the angle between the charged lepton and the neutrino direction in the transverse plane. An evidence for new physics beyond the SM would be visible as (small) resonance (bump) over the steeply falling distribution resulting, for instance, from SM W boson decays. Figure 2.6 visualizes the arising excess in the case of a heavier charged spin-1 gauge boson with fermionic couplings identical to those of the SM W decaying into an electron and a neutrino. An interference between both boson decays is neglected here such that the arising signature is simply added on top of the SM contribution.

As expected, also the distribution of the heavier gauge boson forms a Jacobian peak falling sharply at the appropriate boson pole mass.

[19] For the simplification of having no relative transverse offsets and negligible crossing angles. Also beam-beam interactions are not taken into account.

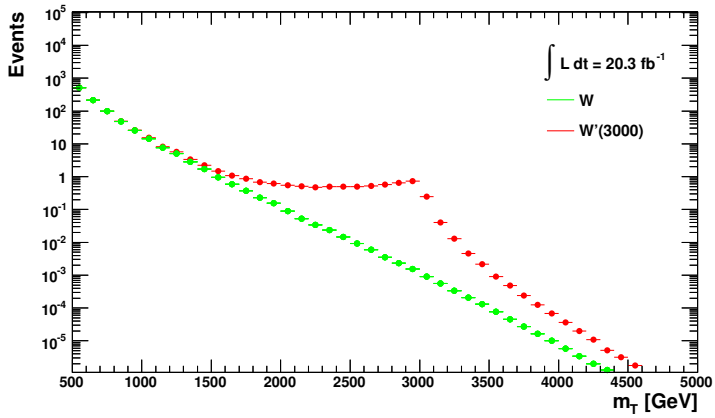


Figure 2.6: Comparison of a SM W boson to a new heavier gauge boson, denoted as W′, (having a pole mass of 3 TeV) shown in the spectrum of the transverse mass. The distributions are scaled to an integrated luminosity of about 20 fb$^{-1}$ and derived for decays into electrons (respectively positrons) and neutrinos only (on generator level, without any further selection criteria applied). The W′ is simulated as additional spin-1 vector gauge boson with fermionic couplings identical to those of the SM W. An interference between both is neglected.

In case, no such evidence for a new physics scenario appears, exclusion limits to the appropriate cross-section predictions can be derived. Also lower limitations to the new particle mass are possible. A detailed description of limit setting approaches follows in Chapter 8.

### 2.3.1 Heavy Vector Boson Models

Common extensions to the SM involve the production of additional gauge bosons mostly having much higher pole masses than the already known. In the charged case, these bosons are generally denoted as W′ whereas the neutral current involves an additional boson called Z′. The different approaches usually distinguish in the fermionic couplings of the new bosons and especially the helicity [20] of those couplings assumed. The subsequent analysis focuses on the search for new physics beyond the SM using a so-called Sequential Standard Model as benchmark model and comparing its predictions also to models involving additional (charged) chiral bosons. Because also the question for dark matter is not answered within the SM, the idea of WIMP pair production processes involving SM W radiation is considered afterwards.

**The Sequential Standard Model** A first extension considered is provided by the Sequential Standard Model (SSM) predicting additional heavier vector gauge bosons with spin-1 outside the SM, denoted as W′ (charged current) and Z′ (neutral current). Their couplings to left-handed SM

[20] The helicity describes the handedness of a particle and is dependent on the projection of its spin onto the direction of momentum. The operator form is: $\Pi^{r/l}(\vec{p}) = \frac{1}{2}(1 \pm \frac{\sigma\vec{p}}{|\vec{p}|})$.

fermions are assumed to be identical to those of the SM bosons whereas mixing or interactions with SM bosons are not considered. With this, the new gauge bosons are designed to be a simple copy of the SM bosons but with significant higher pole masses. The corresponding production process for such a SSM W′ is visualized in Figure 2.7.

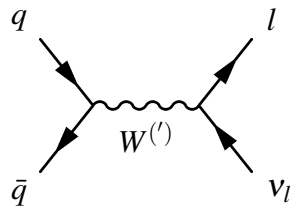


Figure 2.7: Production of a SSM W′ decaying in turn into a charged lepton (e.g. an electron or muon) and a (anti-) neutrino.

As a consequence, the typical kinematic decay distributions show the same characteristic properties as for a SM W decay such as the Jacobian peak in the spectrum of the transverse lepton momentum or the transverse mass (Eq. 2.23). The decay modes and branching fractions corresponding to a SSM W′ are very similar to those considered within the SM [21], except for an additional decay channel involving a top and a bottom-quark arising for W′ pole masses above about 180 GeV [22]. Decays of the heavier charged gauge boson via WZ are assumed to be suppressed. The intrinsic width of the new resonance increases linearly with the boson mass, and is often assumed to be small compared to the detector resolution. Due to its close relation to the known SM W bosons, the full width describing W′ boson decays can be written in dependence of the SM W boson mass and width:

$$\Gamma_{W'} = \begin{cases} \frac{m_{W'}}{m_W}\Gamma_W & \text{for } m_{W'} < 180\,\text{GeV} \\ \frac{4}{3}\frac{m_{W'}}{m_W}\Gamma_W & \text{for } m_{W'} \gg 180\,\text{GeV} \end{cases} \tag{2.27}$$

Indeed, for W′ pole masses below roughly the top-quark mass, the SM decay channels are allowed only. Above, the additional decay involving a top and a bottom quark leads to an increase of the W′ width (due to an enlarged phase space). The factor of $\frac{4}{3}$ arises with respect to the color charge of the quarks involved: Usually, decays into $du$, $sc$ or $l\nu$ are allowed only because of the small mixing between the quark generations. So, (3 colors $\times$ 2 hadronic + 3 leptonic) = 9 possible decay modes may occur in the first case. Including the additional $tb$ channel, ($3 \times 3 + 3$) = 12 possibilities arise. With this, the factor of $\frac{12}{9} = \frac{4}{3}$ becomes clear. So, especially if the leptonic decays are suppressed, the $tb$ decay channel becomes competitive. That may happen in case of considering a heavy right-handed neutrino involved, preventing the especially right-handed $W'_R \to l\nu_R$ decays (for $m_{\nu_R} > m_{W'}$) [23].

The small width approximation is only valid up to orders of magnitude of $\mathcal{O}(\Gamma_{W'}/\Gamma_W)$whereby the W′ is supposed to be produced on-shell. But for higher pole masses, the signal production goes far off-shell and the Jacobian peak at the bosons pole mass becomes less prominent. Figure 2.8 (left) shows the characteristic transverse mass spectrum for W′ decays into an electron (positron) and a

[21] The typical branching fractions for each of the leptonic decay channels are predicted to be about 8.5 %.

[22] For simplicity, both, $W'^{+} \to t\bar{b}$ and $W'^{-} \to \bar{t}b$ are referred to as $W' \to tb$ decay.

[23] Considering the existence of right-handed W′ bosons, also (light or sterile) right-handed neutrinos or further bosons coupling to right-handed quarks while still coupling to left-handed leptons have to be required.

(anti-)neutrino for such SSM bosons with various pole masses. Not only the width increasing with the W′ pole mass is visible but also the distribution shapes being significantly distorted for high masses. The effect is related to the steeply falling parton distribution functions at high Bjørken-x causing a lower probability for such processes to occur. Figure 2.8 (right) visualizes the effect in dependence of the Bjørken-x for different quark constituents [Sti13]. Another effect which is visible in Figure 2.8 (left) is the changing W′ production cross-section: it decreases as the W′ pole mass increases and causes, therefore, distributions which are scaled lower. With the Feynman formalism described already before, the matrix element going into the cross-section calculation can be derived as:

$$M = -\frac{1}{\sqrt{2}} igW'_{\mu}\bar{\psi}_i\gamma^{\mu}(1-\gamma_5)\psi_j U_{i,j} \tag{2.28}$$

including the SM couplings to fermions, $g$, and the CKM matrix $U_{i,j}$. The appropriate cross-section for W′ production follows as:

$$\frac{d\sigma}{dy}(pp \to W' + X) = \frac{4\pi^2}{3M^3_{W'}} \sum_{i,j} \int f_i(x_i, M^2_{W'}) f_j(x_j, M^2_{W'}) \Gamma_{ij}\, \mathrm{d}x_i \mathrm{d}x_j \tag{2.29}$$

where $\Gamma_{ij}$ denotes the partial width of a W′ resulting from couplings to a quark $q_i$ and an anti-quark $\bar{q}_j$ (Figure 2.7).

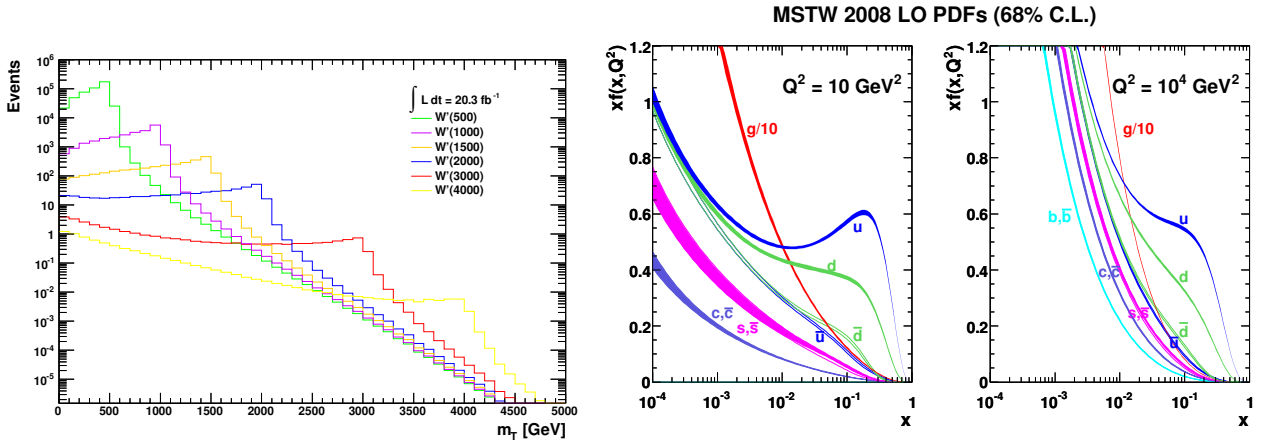


Figure 2.8: Left: The transverse mass spectra are shown for various SSM W′ bosons (the pole masses are given in GeV in parentheses) decaying into an electron (positron) and a (anti-)neutrino. The distributions are derived at LO for processes detectable at the Large Hadron Collider using a center-of-mass energy of 8 TeV. They are scaled exemplarily to an integrated luminosity of about 20 fb$^{-1}$ and no further selection criteria are applied. Right: The PDF functions in dependence of the Bjørken-x for various quark constituents, derived at LO for two different momentum scales $Q^2$. The dependence due to $Q^2$ follows because of a higher spatial resolution (for larger $Q^2$) [Sti13].

**Interference between a SM W boson and a new heavier gauge boson W′** Usually, interference effects between SM W boson decays and those of a new heavier vector gauge boson

(e.g. the SSM W′) are neglected for historical reasons within LHC analyses [24]. Also general low luminosity studies comprising low W′ pole masses and thus, on-shell W′ production with a small width approximation only, lead to difficulties while including these interferences. But such effects are well-known (on the theory side) and should be also discussed for upcoming analyses. So, the underlying calculations and principles are briefly explained subsequently.

As already described before, the probability for a process to occur depends on the absolute square of the transition amplitude. Indeed, assuming new gauge bosons behaving similar as SM bosons, the appropriate matrix element squared which is needed for a cross-section calculation, would include both, SM contributions and those belonging to the additional particles:

$$|M|^2 = |M_{SM} + M_{new}|^2 = |M_{SM}|^2 + |M_{new}|^2 + 2 \cdot Re(M^*_{SM} \cdot M_{new}) \tag{2.30}$$

Besides the expected contributions, a cross term appears in Equ. 2.30 which is usually denoted as "interference term". Obviously, close to the SM W or potential W′ pole mass, the calculation of the matrix element (and thus of the final cross-section) is dominated by the appropriate squared term and interference effects remain negligible small [25]. But for kinematic regions inbetween where the squared terms are approximately of the same order of magnitude, the cross term cannot be neglected. To clarify, the cross-section is determined such that

$$\frac{\sigma}{s} \propto (\frac{a^2_{SM}}{s - m^2_{SM}} + \frac{a^2_{new}}{s - m^2_{new}})^2 = (\frac{a^2_{SM}}{s - m^2_{SM}})^2 + (\frac{a^2_{new}}{s - m^2_{new}})^2 + 2(\frac{a^2_{SM}}{s - m^2_{SM}} \frac{a^2_{new}}{s - m^2_{new}}) \tag{2.31}$$

whereby $s$ denotes the center-of-mass energy squared, $m_i$ the pole masses and $a_i$ the appropriate fermionic coupling constants. The interference term becomes significant if $m^2_{SM} < s < m^2_{new}$ [26]. A detailed description of the impact due to interference effects can be found in [Acc12].

Figure 2.9 visualizes the interference effects at LO [27] for SM W boson decays into an electron and a neutrino with those of SSM W′ bosons having a pole mass of 2.0 TeV (left) or 2.4 TeV (right) [Acc12]. The ratios demonstrating the difference to the case of neglecting such effects, show quite impressively the decreased differential cross-section while including deconstructive interference effects, especially below transverse masses of 1 TeV. Only in a range of about 100 GeV around the Jacobian peak, the interference is negligible small. However, for historical reasons, the interference is not considered within the subsequent analysis (and especially for possible limit setting procedures) to be consistent with the current ATLAS policies.

**The W* Model** Another model considered introduces chiral bosons, denoted as W* in the charged and Z* in the neutral case. These electroweak doublet spin-1 vector bosons outside the SM are mainly motivated by the hierarchy problem and predicted by at least three theories for explaining the relative lightness of the Higgs doublets (namely the pseudo-Goldstone Higgs, the Goldstone Sister Higgs and the Higgs as Extra Dimensional Gauge Field) [Chi11]. In all approaches, the hierarchy problem should be solved by introducing a $U(3)_W = SU(3)_W \times U(1)_W$ symmetry group

[24] The generator used up to now to simulate W′ signatures (PYTHIA) has not been able to include such effects so far.
[25] Otherwise, the SM W boson had not been measured so exactly.
[26] The single terms are, especially, equal if $a_{SM} = a_{new}$ and $s = \frac{1}{2}(m^2_{SM} + m^2_{new})$.
[27] Leading order effects of electroweak and QCD interactions are considered only.

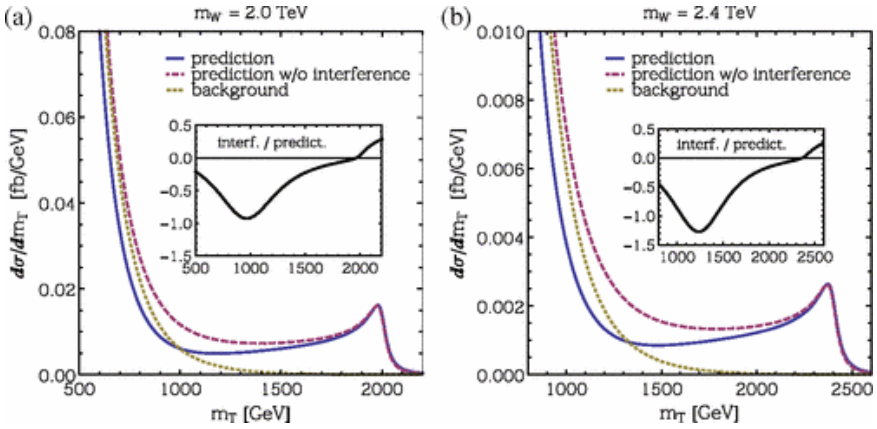


Figure 2.9: The differential cross-section drawn versus the transverse mass is shown for SM W boson decays into an electron and a neutrino ("background") compared to decays of SSM W′ bosons with pole masses of $m_{W'}$ =2.0 TeV (left) and $m_{W'}$ =2.4 TeV (right) into the same final states. The distributions are derived at LO (CTEQ PDF set) for processes detectable at the Large Hadron Collider using a center-of-mass energy of 7 TeV. The interference effects between the related decay processes are visible and shown in addition as ratio [Acc12].

as extension to the SM $SU(2)_W \times U(1)_Y$ electroweak group that breaks down spontaneously to the latter at a scale $M$ of the new physics. The internal quantum numbers of the new vector fields are predicted to be identical to those of a SM Higgs doublet whereas their anomalous (magnetic moment type [28]) couplings to SM fermions differ from SM couplings (and hence from those of the SSM W′) and result in significantly different kinematic distributions. Figure 2.10 demonstrates the deviations between such a W* and a SSM W′ boson. The transverse lepton momentum distribution (Fig. 2.10, right) corresponding to the SSM W′ shows the characteristic Jacobian peak at half of the boson mass (Equ. 2.23). In contrast to that, only a broad smooth bump having its maximum below the kinematic end-point is visible in the decay distribution of the chiral W* boson. In fact, while the underlying gauge theory preserves the fermionic helicities involved in SM W (or SSM W′) processes, a helicity flip occurs within the tensor field couplings of the chiral boson. The production of a SM W (or a SSM W′) occurs in form of left(right)-handed quark and right(left)-handed anti-quark fusion producing bosons with spin-1 and a helicity of $\lambda = \pm 1$ that may decay subsequently into light lepton pairs. In the case of chiral bosons, the production happens via interaction of a quark and an anti-quark with the same helicities (meaning either left-handed or right-handed quark–anti-quark fusion) resulting in a helicity [29] equal to zero for the (longitudinal) produced chiral boson [30]. As a further consequence of the different couplings, also the angular distributions show significant deviations. While the differential cross-section is proportional to $(1+\cos\theta)^2$ for the vector couplings in context of the

[28] Follow due to their quantum numbers.

[29] For massless particles, the helicity is equivalent to the so-called chirality. Introducing masses instead, it's slightly more complicated as the latter is related to the phase of the particle's wave function and so, to the particle's inherent quantum properties. Its operator form is: $p^{r/l} = \frac{1}{2}(1 \pm \gamma^5)$.

[30] Because the new tensor interactions do not conserve the chirality, the new bosons have to be doublets and do not mix with SM bosons (before the symmetry breaking). Hence, regarding high energy experiments, they do not interfere with the SM gauge bosons [Chi00].

SM theory, it is for the angular distribution related to the new tensor interactions:

$$\frac{d\sigma}{d\cos\theta} \propto \cos^2\theta \tag{2.32}$$

With this, the pole responsible for the Jacobian peak of the SM distribution (Equ. 2.23), is canceled out for chiral particles. Also due to Eq. 2.32, the dominant lepton production resulting out of chiral boson decays occurs preferably at small polar angles (in contrast to wide angles for SM W or SSM W$'$ decays) ([Chi06], [Chi08]). The differences in the angular distributions are shown in Figure 2.10 on the left hand side whereby $\eta$ denotes the so-called pseudo-rapidity (Sect. 3.2.2). High values of $\eta$ correspond to low values of the polar angle as it is: $\eta = -\ln(\tan(\frac{\theta}{2}))$ [31].

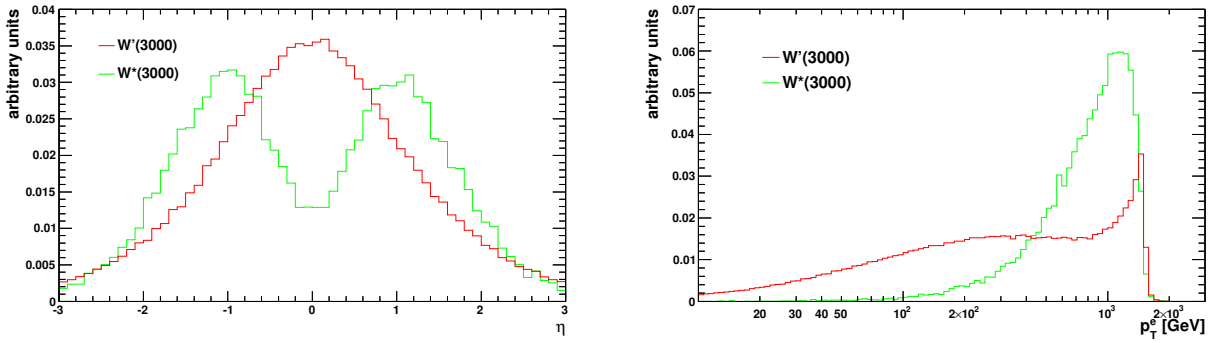


Figure 2.10: Comparison of a new heavier gauge boson W$'$ (SSM) to a charged chiral boson W$^*$ shown in the spectrum of the transverse momentum of the electron (respectively positron) (right) and the appropriate angular distribution (left) (both derived without any preselection). For the latter, the so-called pseudorapidity $\eta$ is visualized whereby high values of $\eta$ correspond to low values of the polar angle $\theta$ (Sect. 3.2.2). The single spectra are scaled to unity for both, W$'$ and W$^*$. The significantly different shapes of the kinematic distributions originate in different fermionic couplings (for the histograms shown, only decays into electrons (positrons) and (anti-)neutrinos have been considered).

### 2.3.2 Dark Matter Interpretation

The third and last new physics scenario considered concerns the question for dark matter (DM) particles appearing in various cosmological phenomena, so-called "weakly interacting massive particles" (WIMP) [Bai13]. Many analyses search for these new particles or their interactions with SM particles via an unknown mediator. Direct pair production of these DM particles via a new intermediate state leads to a missing transverse momentum signature only due to missing interaction

[31] In the parton rest frame, an emission of the final-state lepton-pair is forbidden in the plain perpendicular to the beam axis. In the lab frame, the emission probability is not exactly equal to zero due to longitudinal boosts of the colliding partons. As a consequence, the chiral bosons are produced already with negligible longitudinal momenta and thus, the lepton pseudo-rapidity distribution has a minimum around $\eta$ =0.

with detector material. However, they can be detected at colliders like the LHC via corresponding initial-state-radiation of a SM particle only. Figure 2.11 demonstrates the WIMP production under SM W radiation.

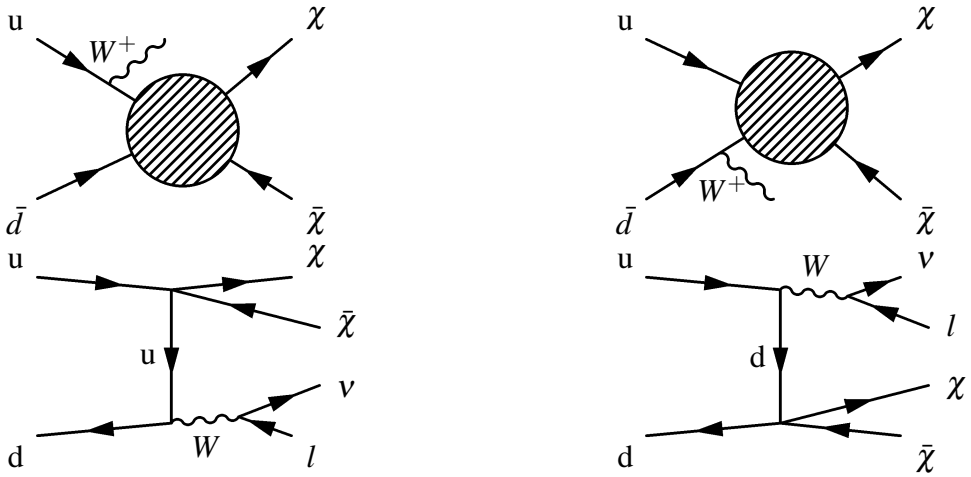


Figure 2.11: W$\chi\bar{\chi}$ production.

In general, the interaction between a DM particle and SM quarks, for instance, is characterized by the mass of that object and the corresponding elastic scattering cross-section off nuclei. The latter can be separated in particular into a spin-dependent and a spin-independent part which originate from different terms in the Lagrangian describing the interaction. While the first refers to axial-vector couplings and is dependent only on the total nuclear angular momentum and the DM spin, the spin-independent part arises due to scalar or vector couplings so that its contribution is proportional to the nucleon number squared [32]. To describe the DM interaction more generally, the reduced mass $\mu_\chi$ is usually used which is defined as:

$$\mu_\chi = \frac{m_N m_\chi}{m_\chi + m_N} \tag{2.33}$$

with $m_i$ describing the mass of the DM particle, respectively that of the nucleon. With this, the WIMP-nucleon scattering cross-section becomes:

$$\sigma_{\chi-N} = \sigma_0 (\frac{\mu_\chi}{1\,GeV})^2 (\frac{M_0}{M_*})^n \tag{2.34}$$

whereby $\sigma_0$, $M_0$ and $n$ are constants with respect to the various possible effective interactions [Goo10]. The suppression scale of the new physics is denoted as $M_* \propto \frac{M}{\sqrt{g_{SM} g_{DM}}}$ where $M$ is the mass of the unknown mediator and $g_i$ are the coupling constants for SM particles and dark matter candidates [33].

[32] In fact, the spin-independent part is dominant for heavy nuclei.

[33] In general, these approximations in context of the effective field theory are valid only if the mediator mass $M$ is larger than the energy transfer of the quarks involved. For this, also $M > 2m_\chi$ has to be required and, to ensure that the new physics are as strongly coupled as possible, $\sqrt{g_{SM} g_{DM}} < 4\pi$ (to be still perturbative) [Goo10].

The best previously derived limits to the mass scale $M_*$ of the unknown interaction and the corresponding WIMP-nucleon scattering cross-section were determined by mono-jet analyses making use of the high gluon radiation rate. But still scenarios exist where the search with respect to SM W boson radiation, for instance, can be more sensitive [Bai13]. Usually, couplings to up-type or down-type quarks are assumed to be equivalent. But if those differ - if they are in the same order of magnitude but including different signs - processes with W boson radiation could be preferred [34]. Then, two modes can be distinguished: constructive (C(u) = - C(d)) and destructive interference (C(u) = C(d)) where $C(i)$ stands for the different couplings [35]. So, as the mono-jet analyses do not distinguish between the signs of couplings to the quarks involved, a mono-lepton analysis provides a better sensitivity while regarding the case of constructive interference. Within common effective field theory approaches, WIMPs are produced pair-wise and the interaction is mediated via new particles being too heavy to be produced directly. This interaction can be parametrized with aid of effective contact operators that are usually denoted from D1 to D14, C1 to C6 or R1 to R4. The capital letter in front of the numeration indicates the treatment of the WIMPs as Dirac fermions ("D"), complex scalars ("C") or real scalars ("R") respectively whereby some account for the spin-dependent while the others do for the spin-independent part of the elastic WIMP-nucleon scattering cross-section [Goo10]. The various operators and the appropriate coefficients are listed in Table 2.3 [36]. However, since only a few characteristic kinematic distributions exist (Figure 2.12, Sect. A.8), four single operators are concerned for the subsequent analysis that treat WIMPs as Dirac fermions, namely the D1, D5(c) and the D9 operator. Regarding events with initial-state radiation of SM W bosons involved, the detectable signature would include besides boosted SM W bosons also large missing transverse energies corresponding to particles not interacting with the detector material [37].

### 2.3.3 Previous Searches

Until today, no evidence for the existence of any new physics scenario as described above has been found. But several exclusion limits to the new boson masses as well as to the mass scale $M_*$ of an unknown interaction and the corresponding WIMP-nucleon scattering cross-section have been set. For the latter, usually, four operators parametrizing the interaction have been concerned exemplarily that treat WIMPs as Dirac fermions, namely D1, D5, D5c and D9. Figures 2.13 and 2.14 summarize the various exclusion contours comparing experiments between 2010 and 2014.
Figure 2.13 shows especially the observed cross-section limits to a heavier version of the SM W normalized to the prediction for a SSM W$'$ boson in dependence of the invariant W$'$ pole mass [ATL14d]. In particular, the increase of such exclusions becomes visible, comparing previous exclusions from CDF [38] [CDF11] and ATLAS. For the latter, not only measurements at a center-of-mass energy of $\sqrt{s}$ =7 TeV and a corresponding integrated luminosity of $L_{int}$ =1 fb$^{-1}$ respectively $L_{int}$ =4.7 fb$^{-1}$ ( [ATL11d], [ATL12g]) have been included, but also the most recent results at $\sqrt{s}$ =8 TeV and about

[34] The process $u + \bar{d} \rightarrow W + \chi\bar{\chi}$ is known as "mono-W" process whereby a boosted SM W boson is involved, coupling either to an up or down quark.
[35] Contributions involving b-quarks are CKM suppressed in the mono-W case.
[36] The $SU(3)_C$ field strength tensor is denoted as $G_{\mu\nu}$.
[37] The WIMP cannot be detected directly and neutrinos are an irreducible background here.
[38] The **C**ollider **D**etector **F**acility and the so-called D0 detector are both located at the Fermi National Accelerator Laboratory (Fermilab) in Batavia, Illinois (USA).

| Name | Operator | Coefficient |
|---|---|---|
| D1 | $\bar{\chi}\chi\bar{q}q$ | $m_q/M_*^3$ |
| D2 | $\bar{\chi}\gamma^5\chi\bar{q}q$ | $im_q/M_*^3$ |
| D3 | $\bar{\chi}\chi\bar{q}\gamma^5 q$ | $im_q/M_*^3$ |
| D4 | $\bar{\chi}\gamma^5\chi\bar{q}\gamma^5 q$ | $m_q/M_*^3$ |
| D5 | $\bar{\chi}\gamma^\mu\chi\bar{q}\gamma_\mu q$ | $1/M_*^2$ |
| D6 | $\bar{\chi}\gamma^\mu\gamma^5\chi\bar{q}\gamma_\mu q$ | $1/M_*^2$ |
| D7 | $\bar{\chi}\gamma^\mu\chi\bar{q}\gamma_\mu\gamma^5 q$ | $1/M_*^2$ |
| D8 | $\bar{\chi}\gamma^\mu\gamma^5\chi\bar{q}\gamma_\mu\gamma^5 q$ | $1/M_*^2$ |
| D9 | $\bar{\chi}\sigma^{\mu\nu}\chi\bar{q}\sigma_{\mu\nu}q$ | $1/M_*^2$ |
| D10 | $\bar{\chi}\sigma^{\mu\nu}\gamma^5\chi\bar{q}\sigma_{\mu\nu}q$ | $i/M_*^2$ |
| D11 | $\bar{\chi}\chi G_{\mu\nu}G^{\mu\nu}$ | $\alpha_s/4M_*^3$ |
| D12 | $\bar{\chi}\gamma^5\chi G_{\mu\nu}G^{\mu\nu}$ | $i\alpha_s/4M_*^3$ |
| D13 | $\bar{\chi}\chi G_{\mu\nu}\tilde{G}^{\mu\nu}$ | $i\alpha_s/4M_*^3$ |
| D14 | $\bar{\chi}\gamma^5\chi G_{\mu\nu}\tilde{G}^{\mu\nu}$ | $\alpha_s/4M_*^3$ |
| C1 | $\chi^\dagger\chi\bar{q}q$ | $m_q/M_*^2$ |
| C2 | $\chi^\dagger\chi\bar{q}\gamma^5 q$ | $im_q/M_*^2$ |
| C3 | $\chi^\dagger\partial_\mu\chi\bar{q}\gamma^\mu q$ | $1/M_*^2$ |
| C4 | $\chi^\dagger\partial_\mu\chi\bar{q}\gamma^\mu\gamma^5 q$ | $1/M_*^2$ |
| C5 | $\chi^\dagger\chi G_{\mu\nu}G^{\mu\nu}$ | $\alpha_s/4M_*^2$ |
| C6 | $\chi^\dagger\chi G_{\mu\nu}\tilde{G}^{\mu\nu}$ | $i\alpha_s/4M_*^2$ |
| R1 | $\chi^2\bar{q}q$ | $m_q/2M_*^2$ |
| R2 | $\chi^2\bar{q}\gamma^5 q$ | $im_q/2M_*^2$ |
| R3 | $\chi^2 G_{\mu\nu}G^{\mu\nu}$ | $\alpha_s/8M_*^2$ |
| R4 | $\chi^2 G_{\mu\nu}\tilde{G}^{\mu\nu}$ | $i\alpha_s/8M_*^2$ |

Table 2.3: Operators coupling dark matter to SM particles while generating DM pairs with various production rates. The operators from D1 to D14 treat the WIMP as Dirac fermions (electroweak singlets) whereby those from 1-4 arise due to scalar or pseudo-scalar interactions, those from 5-8 due to vector- or axial-vector types of interaction and D9 and D10 account for tensor interactions. The spin-independent cross-section parts are described by D1 and D5 only. The treatment of the DM particles as complex scalar is realized with the operators C1 to C6 whereby couplings to gluons are especially possible through the operators C5 and C6. Operators R1 to R4 describe the WIMP as real scalars. [Goo10]

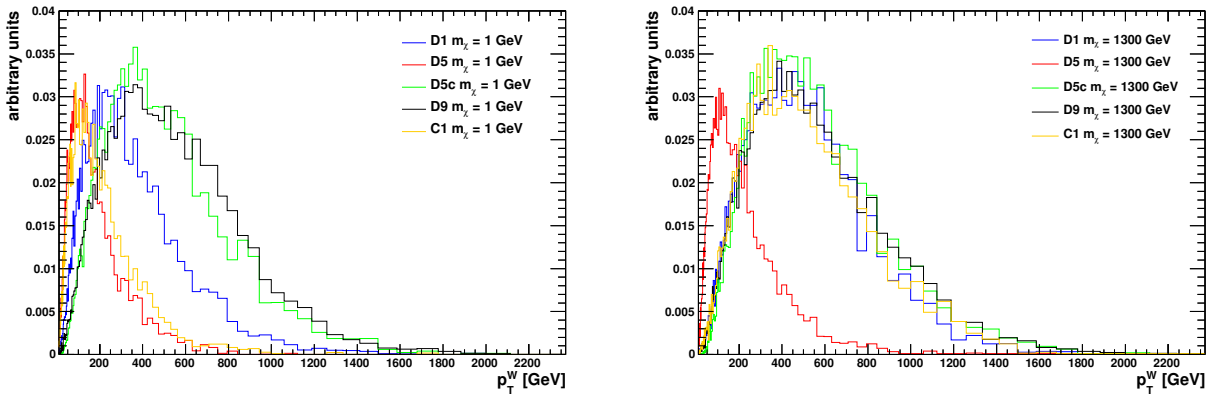


Figure 2.12: Comparison of different dark matter operators for two dark matter mass points, $m_\chi$=1 GeV (left) and $m_\chi$=1300 GeV (right). The spectrum of the W transverse momentum is shown before any selection criteria are applied. Besides the operators D1, D5 (considering both constructive and destructive modes) and D9, each treating the WIMP particles as Dirac fermions, also the operator C1 is visualized. The distributions are normalized to unity.

$L_{int}$ =20 fb$^{-1}$ ( [ATL14d]) derived in proton-proton collisions as combination of electron and muon decay channels. The limits of CDF refer to decays into electrons and neutrinos only, resulting out of proton–anti-proton collisions at a center-of-mass energy of $\sqrt{s}$ =1.96 TeV and a corresponding integrated luminosity of $L_{int}$ =5.3 fb$^{-1}$. They were determined in terms of a Bayesian approach, similar to the shown ATLAS searches, and quoted in terms of a 95 % coincidence level. The requirement of fermionic W′ couplings being identical to those of a SM W boson and the negligence of their interference is crucial for both, CDF and ATLAS. Table 2.4 summarizes additionally not only the visualized results of CDF and ATLAS but also those of other experiments referring to the same benchmark model of a SSM W′. Previous ATLAS results of W$^*$ searches are included in Table 2.4 as well.

Figure 2.14 visualizes the exclusion contours in context of a DM search with respect to SM W boson radiation [ATL14d]. The left side shows various ATLAS results referring to the mass scale $M_*$ of the unknown interaction in dependence of the WIMP mass, comparing especially to mono-Z (radiation of a SM Z) [ATL14g] or mono-jet analyses [ATL15b] as well as to searches involving events with hadronically decaying W or Z bosons [ATL14b]. Regarding the different operators, the values below the corresponding line are excluded. The right side demonstrates the limits in terms of the corresponding WIMP-nucleon scattering cross-section (splitted into spin-dependent and -independent operators) plotted versus the WIMP mass, too. It becomes obvious that the shown ATLAS results are still competitive with those of other direct searches. Both, the mass scale and scattering cross-section limits were commonly derived for a coincidence level of 90 % assuming each operator considered to be the only DM-SM interaction.

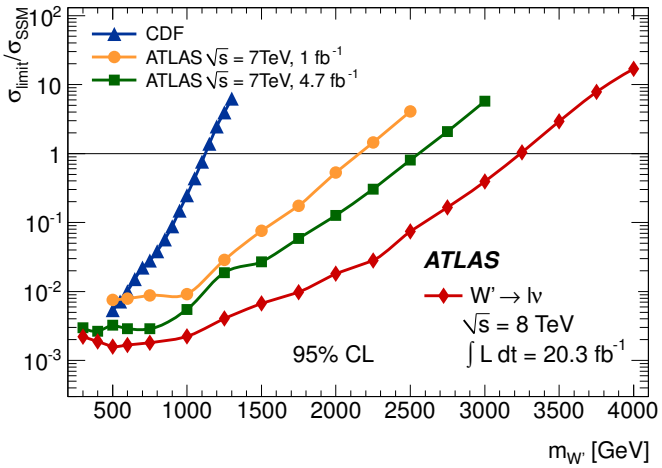


Figure 2.13: Comparison of exclusion limits to a SSM W′ for CDF and ATLAS. The observed cross-section limits are normalized to the prediction of a SSM W′ boson in dependence of the invariant W′ pole mass and shown in terms of a 95 % coincidence level [ATL14d].

| Experiment | Model | $m_{obs}$ [TeV] | $\sqrt{s}$ [TeV] | $L_{int}$ [fb$^{-1}$] |
|---|---|---|---|---|
| ATLAS (2014) [ATL14d] | W′ ($\rightarrow l\nu$) | 3.24 | 8 | 20.3 |
| ATLAS (2012) [ATL12g] | W′ ($\rightarrow l\nu$) | 2.55 | 7 | 4.7 |
| ATLAS (2011) [ATL11d] | W′ ($\rightarrow l\nu$) | 2.15 | 7 | 1.04 |
| ATLAS (2010) [ATL11c] | W′ ($\rightarrow l\nu$) | 1.49 | 7 | 0.036 |
| CDF II (2011) [CDF11] | W′ ($\rightarrow e\nu$) | 1.12 | 1.96 | 5.3 |
| CMS (2014) [CMS14] | W′ ($\rightarrow l\nu$) | 3.28 | 8 | 19.7 |
| CMS (2013) [CMS11b] | W′ ($\rightarrow l\nu$) | 2.90 | 7-8 | 5.0 + 3.7 |
| CMS (2010) [CMS11a] | W′ ($\rightarrow e\nu$) | 1.36 | 7 | 0.036 |
| D0 (2008) [D008] | W′ ($\rightarrow e\nu$) | 1.00 | 1.96 | 1 |
| ATLAS (2014) [ATL14d] | W* ($\rightarrow l\nu$) | 3.21 | 8 | 20.3 |
| ATLAS (2012) [ATL12g] | W* ($\rightarrow l\nu$) | 2.40 | 7 | 4.7 |
| ATLAS (2010) [ATL11c] | W* ($\rightarrow l\nu$) | 1.35 | 7 | 0.036 |

Table 2.4: Observed lower mass limits to a SSM W′ and a W* boson (95 % CL.) for previous experiments in comparison. The first two columns show the experiment name and the model (decay channel) regarded. The third column visualizes the observed lower mass limits at 95 % CL, followed by the experiment's center-of-mass energy and the corresponding integrated luminosity.

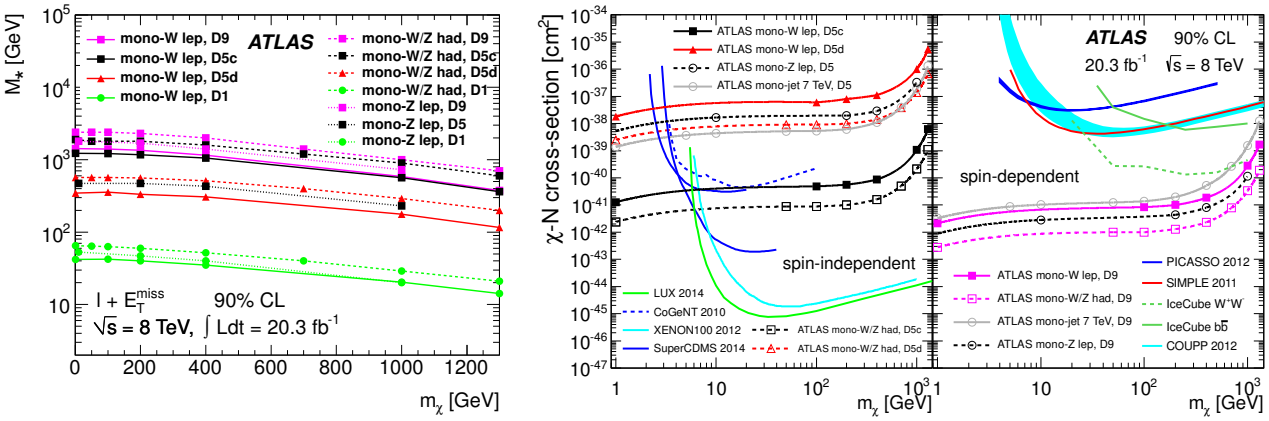


Figure 2.14: ATLAS exclusion contours to the mass scale $M_*$ of the unknown interaction (left) and to the corresponding WIMP-nucleon scattering cross-section (right), both in dependence of the WIMP mass and for a coincidence level of 90 %. They are competitive to those of other direct searches, shown here exemplarily for spin-dependent and -independent operators (D9, D5(c,d)) treating the WIMP as Dirac particle [ATL14d].

# 3 Experimental Setup

This section describes the basic setup of the ATLAS experiment located at the Large Hadron Collider in Geneva. Besides common construction details, also specific analysis tools shall be explained. The general reconstruction and identification of physical objects, as well as the need and usage of Monte Carlo simulations will be considered, too.

## 3.1 The Large Hadron Collider

The Large Hadron Collider (LHC, [Eva08]) with a length of 27 km is the world's largest circular accelerator. It is placed approximately 100 m below ground level at CERN, the European Organization for Nuclear Research, close to Geneva in Switzerland. On the basis of proton-proton-collisions, it provides the possibility to test the Standard Model of Particle Physics (SM) in new (p-p) spheres of action: with higher center-of-mass-energies and significant higher luminosities than previous experiments. It was designed such that protons grouped in bunches of about $O(10^{11})$ nucleons collide 40 million times per second reaching nominal center-of-mass-energies up to 14 TeV. To achieve instantaneous luminosities as high as possible (Sect. 2.3), the bunches are focused such that the width of the transverse particle distribution is minimized at the collision center (known as interaction point). In the sequel, the high particle density and the large inelastic cross-sections may cause multiple hadron-hadron collisions per bunch crossing (meaning the collisions of bunches). Thereby, besides the usual hard-scattering processes of interest, several soft (low-$p_T$) objects originating from further proton-proton collisions appear. The signals of these accompanying soft scatters superimpose with those of the usual hard-scattering particles and are, in the following, referred to as pile-up events.

After a difficult start in September 2008, the first stable proton-proton collisions were achieved in November of 2009 at a center-of-mass energy of 900 GeV. In 2010 and 2011, the energy was raised to $\sqrt{s}$ =7 TeV with steadily increasing instantaneous luminosities. In 2012, the LHC finally run in stable bunches with a center-of-mass-energy of 8 TeV and a bunch crossing time of 50 ns. With typically 1328 bunches on average during a physics run, the corresponding instantaneous luminosity reached $7.7\times 10^{33}$ cm$^{-2}$s$^{-1}$ in high p-p collisions at the end of 2012 and hence, values already close to the design parameters were achieved. Details of the precise luminosity measurements follow subsequently. In spring 2013, a long shut-down ("LS1") provided the opportunity for several upgrades to reach the full $\sqrt{s}$ =14 TeV in bunch crossing times of 25 ns during the next measurement periods. Besides proton-proton-collisions, also proton-lead (Pb) and Pb-Pb collisions were delivered during the first running period to analyze also parton energy losses in a medium by measuring high transverse momentum probes of photons, heavy bosons, jets, charged hadrons or correlations in between [ATL11b]. The center-of-mass energy was varied here from 2.76 to 5.02 TeV with corresponding luminosities up to $2\times 10^{25}$ cm$^{-2}$s$^{-1}$ (in Pb-Pb collisions).

## 3.2 The ATLAS Experiment at CERN Large Hadron Collider

At CERN, six experiments in total are located that make use of the LHC (Figure 3.1) whereby four of them are build for specific purposes ([ALI08], [LHC08a], [LHC08b], [TOT08]) like CP violation measurements or forward production of neutral particles, and two for general purposes

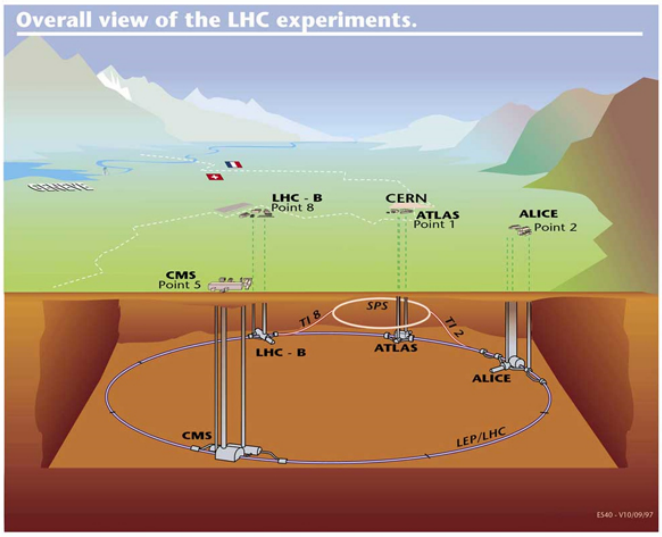


Figure 3.1: Large Hadron Collider at CERN, Geneva. The locations of the four major experiments are marked [LHC].

([ATL08a], [CMS08]). ATLAS [39] is with a length of 44 m, a diameter of 25 m and a mass of 7000 t in total the largest experiment. Consisting of three main components, it is constructed with an onion-shaped structure providing a multi-functional detector to determine particle energy and momentum (Figure 3.2). The innermost detector is used to determine the vertex position and particle track. It is followed by a large calorimeter system for energy measurements and, finally, by a muon spectrometer to identify charged particles passing through all components before without huge energy losses. The construction details will be explained after a brief introduction to luminosity measurements and the ATLAS coordinate system.

### 3.2.1 Luminosity Measurements

The instantaneous luminosity defined as in Sect. 2.3 (2.26) can be also expressed in terms of the smallest opening angle a beam might have (denoted as emittance $\varepsilon$) [40] and the beam amplitude at the interaction point $\beta^*$ [41]:

$$L = \frac{nf \cdot N_1 N_2}{2\varepsilon\beta^*} \tag{3.1}$$

Here, $n$ denotes the amount of colliding bunches, $N_{1/2}$ is the number of colliding protons per bunch and $f$ the bunch crossing frequency [42].

To determine the luminosity as precise as possible, ATLAS uses so-called van-der-Meer (vdM) scans at very large $\beta^*$ [Gra15]. As highly accurate measurements of the bunch population and dedicated calibrations are therefore necessary, luminosity measurements are usually performed with

[39] **A** **T**oroidal **L**HC **A**pparatu**S**
[40] The emittance provides a measure for the parallelism of a beam.
[41] The so-called "amplitude function" roughly denotes the beam width squared divided by the emittance: $\beta = \pi\sigma^2/\varepsilon$. The value of the amplitude function at the interaction point is denoted as $\beta^*$.
[42] With this, a nominal peak luminosity at the LHC would correspond to a $\beta^* \approx 0.55$ m.

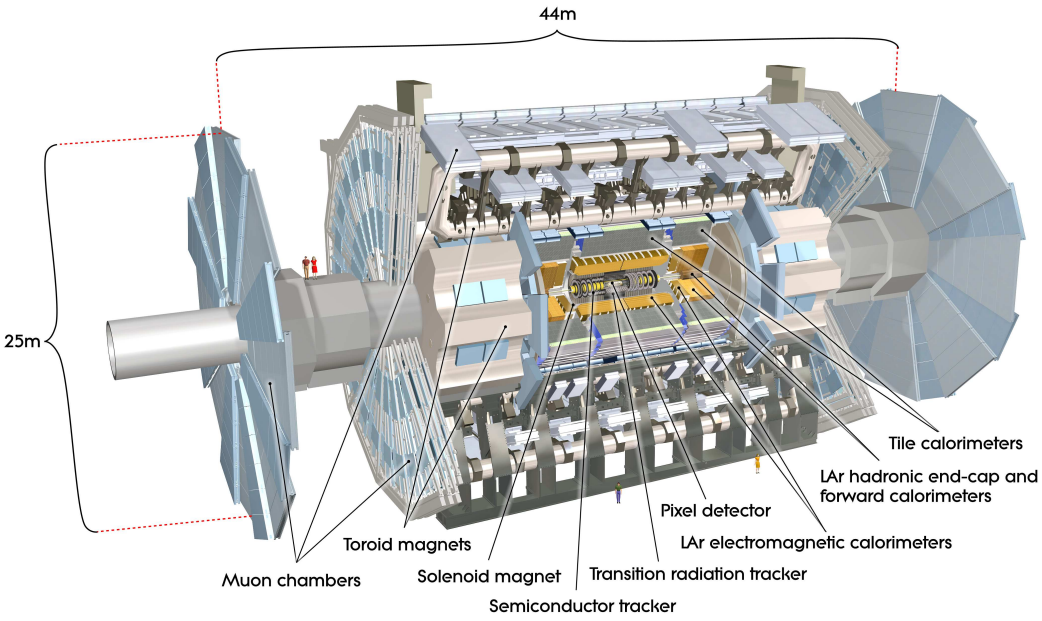


Figure 3.2: The ATLAS Experiment at CERN [ATL08a].

at most 50 bunches separated by a minimum of 1 $\mu$s (in contrast to typical physics runs). With this, problematic crossings of incoming and outcoming beams causing inefficiencies and shifts are avoided as well as systematic uncertainties minimized. Due to the same reasons, also the bunch intensity is lowered while still obtaining a usable counting rate over the whole range. In addition, the magnetic configuration near the interaction point is further adjusted to minimize the nominal beam crossing angle (ideally to zero) in order to reconstruct longitudinal displaced vertices and to minimize the impact due to the finite vertex resolution.

The vdM method itself comprises three important steps, namely the beam-separation scans for absolute luminosity calibration, the beam-displacement scans for absolute length-scale calibration and finally the visible cross-section determination [Gra15]. In order to determine the necessary quantities for calculating the instantaneous luminosity for each bunch separately, the single beams are shifted in x-direction while remaining centered in y (and vise-versa for a second scan) in typically 25 scan steps. The corresponding reaction rates are delivered by recording data for 20-30 s per step. To further determine the required beam sizes as accurately as possible, also the precise knowledge of beam separation is crucial (2.26). Therefor, the beams are shifted transversely in typically five steps by the same amount and in the same direction to perform dedicated length-scale calibration measurements close to the time of the first scans and using the same settings at the interaction point. The beams remain in collision whereby the actual position of the interaction point can be determined at each step quite exactly and the beam displacement may be calibrated with respect to the measured shift. Finally, the visible interaction rate is measured with respect to the actual beam separation. The resulting curves are fitted by modified Gaussian distributions (depending on the beam conditions) and their integrals determine the desired convolved beam widths $\Sigma_x$ and $\Sigma_y$. As the amount of particles per bunch and the beam sizes may vary, the measurements have to be performed separately for each colliding bunch pair.

The dominant uncertainties to the overall calibration during these vdM scans refer to the difficulty

of modelling and exactly reproducing the various beam conditions. Instrumental effects only play a minor role. Regarding the determination of the total integrated luminosity, also pile-up depending biases and the relative long-term stability of the luminosity are important. All in all, an uncertainty to the integrated luminosity quoted subsequently arises of 2.8 % for ATLAS data taking periods in 2012.

### 3.2.2 The ATLAS Coordinate System

The ATLAS coordinate system is based on a spherical coordinate system where the interaction point is chosen as its origin. The x-axis points in direction of the LHC ring center, the positive y-axis upwards. Perpendicular to the x-y plain defined as above, the z-axis leads counterclockwise along the beam pipe. Regarding the spherical coordinates in detail, the azimuth angle is determined in a range of [-$\pi$,+$\pi$] around the beam axis whereby the origin agrees with the positive x-axis. Instead of the usual polar angle $\theta \in [0,\pi]$, the so-called pseudo-rapidity $\eta$ is used (Figure 3.3). It is defined as

$$\eta = -\ln(\tan(\frac{\theta}{2}))$$

and coincides for mass-less particles with the common rapidity $y = \frac{1}{2}\ln(\frac{E+p_z}{E-p_z})$. The energy of the detected particle is named as $E$; $p_z$ describes the longitudinal component (in z direction) of its three-momentum. In many cases, the rapidity is preferred because the flux of produced particles per rapidity interval is nearly constant for hadron-hadron-collisions. Also the shape of the differential cross-section $\frac{d\sigma}{d\eta}$ is, similar to $\frac{d\sigma}{dy}$, in good approximation invariant under Lorentz boosts along the z-axis. The pseudo-rapidity is even easier to determine due to the fact that not the particle mass but its trajectory through the detector is taken into account.
The ATLAS experiment is located symmetrically at $\pm$240 m from the interaction point to measure very small angle elastic scattering and thus, determines trajectories of charged particles up to $|\eta| = 2.5$ [43], muon momenta up to $|\eta| = 2.7$ as well as electromagnetic and hadronic energy depositions up to $|\eta| = 5$.

### 3.2.3 The Inner Detector and Solenoid Magnet

The inner detector forms the tracking system of the ATLAS experiment. Figure 3.4 shows its onion-shaped structure. A silicon pixel system in its center is used for resolving trajectories and thus, the momentum of charged particles in high precision. Concentrically ordered around the beam axis, the pixel system is followed by a silicon microstrip tracker (SCT) and a transition radiation tracker (TRT) that will be explained explicitly subsequently.

Following the beam pipe, the inner detector itself is surrounded in a distance of about 120 cm (measured from the beam pipe) by a huge superconducting solenoid magnet. With a strength of 2 T, the

[43] This pseudo-rapidity corresponds to small opening angles of up to 9.4° relative to the beams.

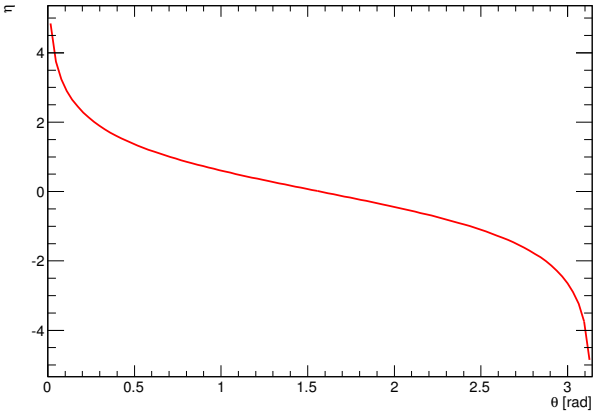


Figure 3.3: pseudo-rapidity $\eta$ in dependence of the polar angle $\theta$.

magnetic field causes a curved orbit of charged particles, so that their (transverse) momentum can be determined quite exactly [44]: A resolution of

$$\frac{\sigma(p_T)}{p_T} = 0.05\,\%(p_T[\mathrm{GeV}]) \oplus 1\,\% \tag{3.2}$$

is achieved within a coverage up to $|\eta| = 2.5$ whereby the first term refers to a finite spatial resolution of the measurements and the second to multiple scatterings due to the detector material [ATL08a].

**The pixel system** For precision measurements of short-lived processes, the innermost layer of the detector is ordered concentrically around the collision interaction point. Short-lived particles like b-quarks name this detector component the so-called "b-layer". Paralleling the beam pipe in a distance of 80 cm, the central region of the pixel system is attached in 5, 9 and 12 cm to the beam axis. Consisting of three wheels with radii between 9 and 15 cm that are arranged perpendicular to the axis, two end-caps surround this cylindrical central region to reach also high pseudo-rapidities. Typically, a particle transition involves three pixel layers. In total, the pixel system consists of 1456 modules in the barrel and 288 modules in the end-cap regions. With about 80 million pixels, the innermost detector system provides a very high granularity and is able to reach a position resolution up to 115 $\mu$m in z (R) direction within the barrel (end-caps) and up to 10 $\mu$m in (R-$\phi$) direction.

**SCT** Surrounding the innermost pixel system concentrically, a semi-conductor tracker composed of eight silicon-strip detector layers is arranged. On modules, the strips are assembled pairwise in four concentric layers around the beam axis (in the barrel). They provide a resolution of 17 $\mu$m in radial and 580 $\mu$m in beam direction. The single modules are arranged slightly turned by 40 $\mu$rad, so that a good spatial resolution can be ensured by response of two strips per layer while one particle transition. In addition, the end-caps of the SCT consist each of nine further layers assembled in the same manner but perpendicular to the beam axis, ensuring a comparable resolution. In total, 4088 single detector modules with about 6.3 million channels are used.

[44] The transverse momentum is given by $p = p_T / \sin\theta = p_T\sqrt{1+\cot^2\theta}$.

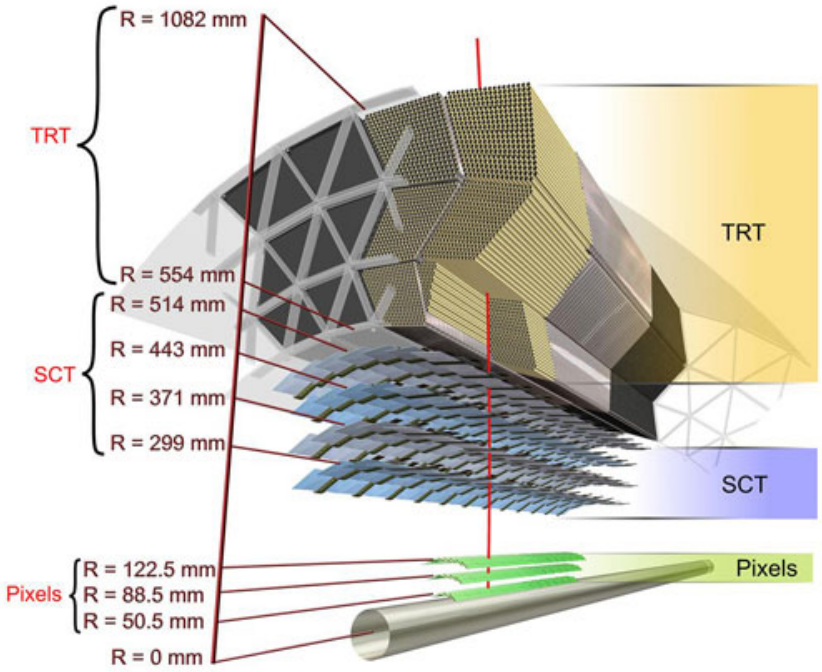


Figure 3.4: Scheme of constituents of the inner detector [LHC].

**TRT** Following the SCT, the transition radiation tracker (TRT) consists essentially of a drift chamber system. The single wires of the drift chamber lie in pipes filled with xenon gas that is ionized by charged particle transition or the produced transition radiation respectively. The pipes themselves have 4 mm in their diameter and lie, embedded in polyethylene foam, 144 cm collaterally in the central region along the beam axis. The end-caps contain 18 wheels each with 37 cm long tubes assembled radially. The so-called transition radiation is produced by charged particles crossing fibers with different refraction indices that are arranged in addition between the tubes. While traveling from one medium into the other (having a diversifying refraction index), the particles passing emit photons if their corresponding Lorentz factor, defined as $\gamma = \frac{E}{m}$, is sufficiently high. Since the intensity of the transition radiation is proportional to that Lorentz factor [45] and follows therefore out of the mass and energy of the detected particles, it can be used to identify the arising objects afterwards. So, it is possible to distinguish, for instance, electron signals (or positron signals respectively) from those of charged pions.
The TRT provides 420,000 channels in total, each providing a drift time measurement with a spatial resolution of 170 $\mu$m and two independent thresholds. With this a distinction between tracking hits passing the lower threshold only and transition radiation hits passing the higher threshold, is possible.

[45] The photons produced additionally also excite the gas and cause in the sequel higher signal amplitudes, compared to the case involving the pure ionization of the passing particle only.

### 3.2.4 The Calorimeter System

Before describing the ATLAS calorimetry in particular, the underlying structures and dedicated purposes of calorimeter systems in general shall be explained briefly as this detector part is the core of the ATLAS experiment. Calorimeters are usually used to determine the type and the energy of charged and uncharged particles [46] and need, therefore, a good spatial and direction resolution. Typical energy regions detectable at colliders are between about 100 MeV and a few TeV, so that the handling of even high event rates is crucial.

Particles passing the calorimeter system, interact with the detector material and loose their energy via effects like nuclear impacts (hadrons), bremsstrahlung, pair production or ionization. The energy depositions through electromagnetic or strong interactions happen stepwise forming so-called showers of secondary, tertiary or more particles until the energy of the shower particles is below a certain threshold. In general, two different types of calorimeter systems exist: homogeneous and heterogeneous calorimeters. The first includes detectors where the full absorber volume is sensitive but is only useful for electromagnetic interacting particles. The second refers to so-called sampling calorimeters which include passive absorber materials such as lead, iron or uranium (for shower formation), arranged alternating with active detector (scintillating) layers consisting typically of gas or liquid filled capacitors. The latter detector type has the advantage to choose an optimized absorber material together with an optimized choice of signal readout, even a fraction of the energy depositions is measured only (about 1-10 %) [47]. Therefore, ATLAS uses, like most of the collider experiments do, sampling calorimeters for the detection of both, electromagnetically and hadronically interacting particles. The active parts are usually connected to photomultipliers and optimized to measure the particle energy and the shower shapes in high precision by determining the current produced via ionization effects: incoming charged particles ionize the gas and the dissolved electrons are accelerated to the anode. The electrical current produced is converted into a voltage which is, hence, proportional to the energy of the incident particle [48]. However, the whole calorimeter system has to be thick enough to allow the particles to deposit all of their energy but should comprise also a high granularity (meaning the single layers have to be thin enough) for measuring the energies as precise as possible. Hence, various types of such detectors exist whereby their structure depends on the physical objects that should be detected. Usually, a further division into an electromagnetic and a hadronic sub-system is preferred to account for the different requirements of detectable objects. Electrons, for example, emit dominantly photons annihilating in an electron-positron pair. The processes known as Bremsstrahlung and pair production continue until the energy of the photon emitted is less than two times the electron mass. Then, ionization or Compton effects respectively dominate. The probability for such Bremsstrahlungs effects decreases as the mass of the incident particle increases. As a consequence, those lighter electromagnetically interacting particles are stopped earlier than hadrons of the same momentum being typically heavier. Also the cross-sections of processes being relevant for energy losses of the latter are much lower than that for Bremsstrahlung. To have a measure for the depth of the different detector parts needed, the so-called radiation and interaction lengths are derived. The first is relevant for electromagnetically interacting particles and is defined

[46] Indeed, calorimeters are the only detector system which is able to measure also uncharged particles. They provide the possibility to even identify the detected particles via their absorptions properties.

[47] This leads to fluctuations of the measurable energy fraction that are known as “sampling” or “partial” fluctuations.

[48] To be correct, not all of the particle energy is converted to such signals: a small part is transformed to heat but the change in temperature is negligible.

such that an highly energetic electron has deposited an average (1/e) of its initial energy $E_0$ on the path length $X_0$ within a certain material [49]. So, the particle energy remaining after a distance $x$ has been passed, is determined as $E(x) = E_0 e^{-\frac{x}{X_0}}$. The so-called interaction length gives the average absorption length defined as $\lambda = \frac{1}{\sigma_{in}\rho_N}$ with $\rho_N$ denoting the particle density and $\sigma_{in}$ the inelastic p-p cross-section [50]. Usually, the interaction length is about ten times larger than the radiation length and causes typically a higher granularity within the electromagnetic calorimeter.

Due to the reasons mentioned above, the calorimetry of ATLAS consists of three major parts: the electromagnetic calorimeter (ECAL), the hadronic calorimeter (HCAL) and the forward calorimeter (FCAL). The basic assembly of the single components is shown in Figure 3.5. Both, the ECAL and the HCAL are realized as sandwich calorimeters using liquid argon (ECAL) or scintillating tiles (HCAL) as active material. They are composed of a central barrel region and two linked end-caps, so that a total coverage up to pseudo-rapidities of $|\eta| < 4.9$ can be achieved in association with the FCAL. The central region reaches up to $|\eta| < 2.5$ providing the opportunity to distinguish between charged and uncharged particles, whereas the common forward region belongs to a pseudo-rapidity of $2.5 < |\eta| < 4.9$. In fact, the central region contains not only the barrel region but also a part of the end-caps that is also covered by the tracking detector system. The rest of the end-caps belongs to the forward region since here, no tracking information is available. The single components of the calorimeter system are explained in detail subsequently.

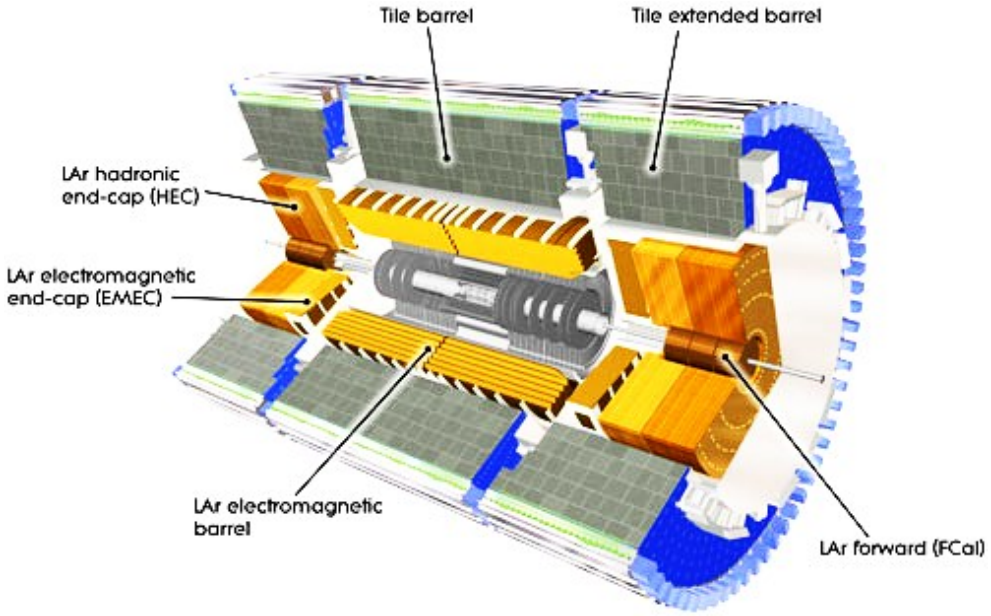


Figure 3.5: Scheme of calorimeter structure [ATL08a].

**The electromagnetic calorimeter** The innermost part of the calorimeter system is comprised of the electromagnetic calorimetry (ECAL) containing a central barrel region ($|\eta| < 1.475$) followed by two end-caps ($1.375 < |\eta| < 3.2$). Both, barrel and end-caps are composed of a wavelike design

[49] The mean free path corresponding to photons is given by $(9/7)X_0$ for pair production processes.
[50] So, the interaction length is the average length a particle travels before an interaction takes place.

which mainly consists of 1.9 mm thick lead layers coated with high-grade steel as absorber. Between the single layers, liquid argon (LAr) serves as active medium to detect charged particles interacting electromagnetically. The alternating active and passive media are arranged in a wavelike geometry described as above and form a so-called sampling calorimeter. Because of this special symmetry, it is possible to ensure a uniform detector response independently from the incoming particle direction. The undulate layers parallel the beam pipe within the barrel region while they lie perpendicular to the beam axis for the end-caps. Providing the opportunity to merge calorimeter cells running projectively to the primary interaction point, especially the $\phi$ direction is covered almost totally homogeneously.
Inside the electromagnetic calorimeter, another detector, namely the presampler, is assembled to correct the energy deposited in non-sensitive material in front of the calorimetry. Its granularity is about $0.025\times\ 0.0982$ in $\Delta\eta \times \Delta\phi$.

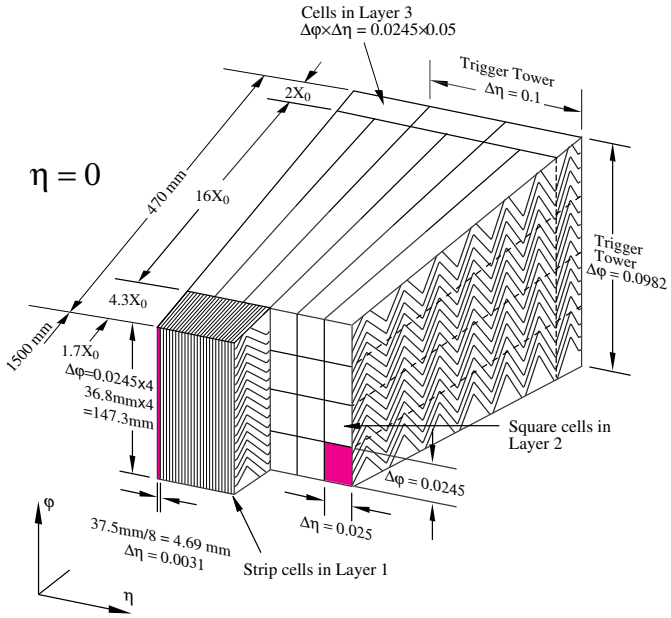


Figure 3.6: Granularity of the electromagnetic calorimeter [ATL08a].

The electromagnetic calorimeter itself consists of three different layers within the central barrel, each serving another purpose. The granularity of the first layer is with $0.0031 \times 0.0982$ in $\Delta\eta \times \Delta\phi$ segmented finer than the two following to achieve a good shower resolution especially in $\eta$ direction. That is important to ensure an effective suppression of possibly arising backgrounds such as due to $\pi^0$ decays, for instance (meaning $\pi^0 \rightarrow \gamma\gamma$). Single cells within the second layer comprise $0.025 \times 0.0245$ in $\Delta\eta \times \Delta\phi$ to determine most of the deposited energy as well as its position as accurately as possible. The outermost layer serves as correction to showers overlapping behind the sensitive calorimeter regions and has a lower granularity of $0.050 \times 0.0245$ in $\Delta\eta \times \Delta\phi$ (see Figure 3.6). The central barrel region comprises in total a depth varying between 22 and 33 radiation lengths whereby 16 radiation lengths are kept constantly up to the second layer. The granularity as described before leads to an energy resolution within the central region of the electromagnetic calorimeter of:

$$\frac{\sigma(E)}{E} = \frac{10\,\%}{\sqrt{E[\mathrm{GeV}]}} \oplus 0.7\,\% \tag{3.3}$$

Here, the first term corresponds to stochastic uncertainties whereas the latter belongs to noise and calibration issues [ATL08a].

The end-cap region is assembled similarly but with two layers only within the transition region (1.37 $< |\eta| <$1.52) and the outermost range not covered by the tracking system. Here, the purpose of the first central layer belongs effectively to the second end-cap layer, in order to correct for energy depositions behind the electromagnetic calorimetry. In front of the end-caps another presampler is located providing a granularity of 0.025 $\times$ 0.1 in $\Delta\eta \times \Delta\phi$ and a coverage of 1.52 $< |\eta| <$1.81. Within the end-cap region in total, the depth varies between 24 and 38 radiation lengths whereby it is kept as constant as possible up to the end of the major layer. The energy resolution is about [ATL08a]:

$$\frac{\sigma(E)}{E} = \frac{10\,\%}{\sqrt{E[\mathrm{GeV}]}} \oplus 0.2\,\% \tag{3.4}$$

**The hadronic calorimeter** The hadronic calorimeter (HCAL) surrounds the electromagnetic and measures the energy of hadrons interacting mainly strongly and thus, passing the ECAL without loosing all of their energy. At higher rapidities, it has a depth up to 10 interaction lengths and consists of barrel and end-cap regions, too. The barrel is further divided into a barrel section with two enhanced parts, denoted as extended-barrel, covering $|\eta| <$1.0 and 0.8$< |\eta| <$1.7. Also the hadronic calorimeter uses the sampling method as described above but with alternating ferric-absorbers and synthetic tiles as scintillators that are readout by secondary multipliers. The structuring into three layers is kept within the hadronic barrel calorimeter. In addition, the hadronic end-caps consist of two parts utilizing copper plates varyingly thick as absorbers and liquid argon as active detecting medium. In a range of 1.52$< |\eta| <$2.47, a granularity of 0.1 $\times$ 0.1 in $\Delta\eta \times \Delta\phi$ is provided that is made coarser to 0.2 $\times$ 0.2 in $\Delta\eta \times \Delta\phi$ for 2.47$< |\eta| <$3.2.
In total, the tile calorimeter comprises a few thousand cells whereas the LAr calorimetry has about 180,000 channels (in association with the electromagnetic region). Together with the electromagnetic (about two absorption lengths) and the hadronic end-caps (about ten absorption lengths), jets originating from a proton-proton collision with a center-of-mass energy of up to 14 TeV can be fully detected. Thus, the resolution related to jets is about [ATL08a]:

$$\frac{\sigma(E)}{E} = \frac{50\,\%}{\sqrt{E[\mathrm{GeV}]}} \oplus 3\,\% \tag{3.5}$$

**Forward calorimeter** The liquid argon forward calorimeter (FCAL) has been designed in order to detect hadronic jets at small scattering angles (about 1 to 5 degrees) relative to the beams. Similar to the other calorimeter systems, it uses sampling detectors with liquid argon as active medium but copper or tungsten rods as absorber (because it has to withstand intense radiation). In total, about 10,000 tubes are used that are arranged in a hexagonal structure (instead of being structured wavelikely). With a granularity of about 0.2$\times$0.2 in $\Delta\eta \times \Delta\phi$, a maximum resolution in $\Delta$x$\times\Delta$y of (3.0$\times$2.6) cm can be reached.

### 3.2.5 Muon System and Toroidal Air-Core Coil Magnet System

Passing the calorimeter system defined as above without being stopped, muons are detected in the outer regions of the ATLAS detector. A separate muon system provides a tool to measure muon paths and momenta with high precision. With eight superconducting coils in the central barrel and eight coils in each end-cap region, a toroidal air-core coil magnet system is the basis of this detector part. An effective field strength of about 1 T at each coil center [51] is produced. The air-core coils provide the advantage to not include a magnetic core but simply a non-magnetic structure fixing the superconducting wires. Similar to the inner detector system, the toroidal magnetic field surrounds the muon spectrometer which consists in turn of three sub-components. The central barrel region comprises three layers assembled by monitored drift tubes (MDT) that are used for high precision measurements, and Resistive Plate Chambers (RPC) utilized for quick trigger decisions. The end-caps are attached to the barrel region and consist of three wheels which include certain cathode strip chambers (CSC) for precise momentum measurements [52] and thin gap chambers (TGC) less resolving for trigger purposes.
All in all, the muon spectrometer covers a range up to $|\eta|$ <2.7. It is designed to measure transverse muon momenta ($p_T$ >3 GeV) with a resolution of 4% up to $p_T$ =100 GeV rising to 10% for $p_T$ =1 TeV track momenta. The single MDTs provide a resolution of below 100 $\mu$m in drift direction whereas an overall resolution of a multi-layer is approximately 50 $\mu$m. The track resolution in the bending plain is designed to be about 40 $\mu$m.

### 3.2.6 Trigger and Data Acquisition

As already mentioned before, the Large Hadron Collider is designed for colliding proton bunches with an orbital frequency of about 40 MHz and a luminosity up to $10^{34}\,\mathrm{cm}^{-2}\mathrm{s}^{-1}$ such that bunches collide every 25 ns and multiple pp collisions take place. A maximum event rate of about 1 GHz would result so that recording each p-p reaction is nearly impossible. Up to 2012, the bunch crossing time was 50 ns and thus the resulting rate lower than expected with the design values but still huge. However, only a small amount of occurring events is of physical interest and due to further technical limitations such as the possible detector readout, a separation of interesting processes is needed. In 2012 (that is before LS1), the trigger system of ATLAS consists of three parts (namely the level 1, level 2 and event filter) that ensured a reasonable treatment of the recordable event rate. Selecting data step by step, the time to decide increases with the trigger level and the decisions can be based on more elaborate analyses. To clarify, the single trigger components shall be described briefly.

**L1** The first trigger level (denoted as L1) is, in contrast to the following two, hardware based and consists of a calorimeter trigger, a muon trigger and a central trigger processor. At each of the first two L1 trigger parts mentioned (calorimeter and muon trigger), various multiplicities and trigger thresholds with programmable parameters can be applied. So, the calorimeter trigger distinguishes already between local and global energy depositions and uses multiplicities for electrons/photons, hadrons/taus and jets isolation criteria or flags to the transverse energies whereas the muon trigger

[51] The field is non-uniform, especially in the transition regions.
[52] Due to an increased rate, especially in the end-cap inner layer, MDTs would have occupancy problems.

level includes conditions for track related hits in special muon detectors. In particular, these requirements to the (calorimeter) threshold related quantities like the transverse energy, the window size regarded or specific isolation conditions, can be dependent on the angular position in $\eta$ and $\phi$. In addition, the calorimeter trigger comprises eight trigger threshold sets for each of electrons/photons, hadrons/taus and jets that can operate concurrently whereas six trigger threshold sets are implemented for muon tracks at the muon trigger stage. The central trigger processor finally combines the different requirements under inclusion of prescaling factors [53], the generation of deadtime and further triggers (e.g. for calibration issues).
All in all, using a coarse detector granularity, 2.5 $\mu$s are available at L1 to decide if and where interesting energy deposition may be found such that about 0.19 % of the original data remain.

**HLT** The regions of interest (ROI) are passed on to the two following software based trigger level, namely L2 and the final event filter (EF). Due to their similar structure, they are commonly combined to a so-called high level trigger (HLT) system. In contrast to L1, it uses the full detector granularity whereby at L2 10 ms and at EF a few seconds are available for dedicated decisions. The second stage reduces the amount of recorded data up to 1.3-4 %. The EF reconstructs subsequently the remaining events with respect to calibration and various correction issues in order to decide such that 7-20 % survive [54]. For both, L2 and EF, tracking information as well as reconstruction and identification algorithms are already available, so that dedicated distinctions are possible and certain physical candidate objects of interest may be selected. So, after the last step, a data rate of about 300 Hz is left and the events finally accepted are recorded. Using particular algorithms, the raw data can be reconstructed subsequently and resided in various data formats with different information depth.

## 3.3 Monte Carlo Simulations

ATLAS uses so-called Monte Carlo simulations to better estimate and understand the processes occurring during the detector operations. The simulations follow pre-defined conditions and probabilities that are realized via different generators. In fact, it is possible to concern not only the known physics parameters but also to simulate signatures indicating new physics scenarios beyond the SM. The basic principles of detection as well as several surrounding parameters are defined and generated such that the respective particles can collide at a given center-of-mass energy and specific processes of interest follow subsequently. Also allowed decay channels and existing restrictions to single parameters have to be accounted for. Hence, it is not only possible to calculate corrections to pre-defined surroundings such as the acceptance but also to estimate the uncertainties in the current state of physics modelling. The conjunction of the various event parts starting with the hard scattering process, multiple interactions or beam remnants, jet fragmentation and decay processes is a challenge that is realized in dedicated generators depending on the specific need of analyzers. Also

[53] As with increasing luminosity also the amount of events passing the pre-defined trigger thresholds rises, the event rate exceeds the recordable trigger rate at a certain time. However, to achieve the desired reduction, it might be necessary to suppress single trigger objects by definable factors. These factors are commonly known as prescales.
[54] The amounts in percent always refer to the remaining data after passing the previous trigger level.

QCD and higher-order QED corrections play an important role in the structure of event simulation that need to be taken into account.

**Simulation Data Flow** Simulating physical processes happens in different steps, starting with a general event generation. After certain particle filter requirements are applied, the data objects representing Monte Carlo truth information are, then, read by simulation algorithms and processed into so-called Raw Data Objects (RDOs). Common reconstruction methods may be used in addition with these RDOs as input. The single event generation and simulation steps shall be described briefly in the following section. Common particle reconstruction and identification methods are explained afterwards.

**Common event generators** To model physical processes like hard interactions or subsequent decays initially at LO, three "general-purpose" tools are commonly used: Herwig [Cor01], Pythia [Sjö08] and Sherpa [Gle09]. The first includes the original framework for cluster fragmentation and is usually utilized to receive a full simulation of events involving angular ordered parton showers and spin-correlated decay chains. Pythia is originated in hadronization studies and plays an important role for the development of multiple interaction models. It also includes parton shower simulations using a new procedure of merging (high-multiplicity) LO matrix elements and parton showers ("ME⊗PS"). Sherpa comprises an automated framework for NLO calculations and provides complete hadronic final states in the simulation of high-energy particle collisions.

Despite the choice of the event generator, a cross-section calculation of the hard scattering process is performed initially. With respect to the appropriate probability densities (Sect. 2.2), it is used in the sequel as input for random generators to determine also the four-vectors of the involved particles [55]. In some cases, kinematic requirements or phase space restrictions respectively to the latter are reasonable and can be applied additionally already for generation. The underlying matrix elements can be estimated for any physics model, usually at LO or NLO, using different tools in addition. Examples are: MadGraph [Alw14] or CompHEP [56] [Boo04] for the implementation of Feynman diagrams and AlpGen [Man03] especially for the generation of multi-parton processes in hadronic collisions [57]. Generally, on the basis of certain model files or automated implementations of arbitrary higher-dimensional operators, vertices are extracted for a particular process from the appropriate Lagrangian using minimal information about a particles content. Initial- and final-state-radiation effects involving parton showers are included iteratively up to the energy scale where the perturbation breaks down and need to be harmonized with the generator specific matrix elements. The final-state photon radiation from leptons, for instance, is simulated via PHOTOS [Gol06]. By converting the output into a common format (HepMC (a C++ event record) [Dob01]), the final four-vectors of the particles involved may be passed on to the next simulation instance [58]. Thereby, besides, the so-called underlying event and decays of unstable particles, also hadronization processes

[55] Due to this, the generators are known as Monte Carlo generators. To achieve smooth spectra in the sequel, usually, a large amount of generated events is needed.

[56] **Comp**utation in **H**igh **E**nergy **P**hysics.

[57] NLO generators are combined with LO generators to calculate the outgoing particles whereby the interference of NLO and LO processes is handled by additional event weights (e.g. JIMMY and MC@NLO, Sect. 6.1).

[58] These so-called truth quantities (without any detector response simulated) are, commonly, referred to as "generator level" results.

demonstrating the transition from parton showers to color neutral particles (Sect. 2) have to be, finally, implemented. Certain interactions with the required detector material are accounted for within the last simulation step that will be explained afterwards.

The subsequent analysis utilizes mainly simulations generated by a POWHEG [Fri07] implementation interfaced with PYTHIA8. Using the first, the event generation for processes in next-to-leading order (NLO) is derived while the latter handles the parton showering and hadronization. Further generators utilized are Sherpa, JIMMY [59], Acer [Ker12], MadGraph and CalcHEP [Bel12]. Details of the appropriate fields of application follow in the sections describing the background (6) and signal (8.2) sample usage.

**Final event simulation** To account in the final step also for the various detector states and conditions, ATLAS makes use of different simulation environments, namely GEANT4 [Ago03] and ATLFAST ([Yam11],[Luk12]), to simulate the interactions of the generated particles with matter, meaning the single detector components. While the first reconstructs a particle's track and its various interactions in detail, the latter uses parametrizations of shower shapes to estimate the most probable distribution of the particle's energy depositions. Since a simulation of the response of each detector component can be very time-consuming, the use of ATLFAST provides a reasonable way to get a first approximation. Both environments are briefly described below. However, the final simulation results are stored in a format compatible to that used for recorded data wherewith the object reconstruction can ensued also in the same manner. So, after this last step, the Monte Carlo sets include not only a pure event generation but also a (detailed) detector simulation and thus, not only effects like common energy losses due to bremsstrahlung, but also the finite detector energy resolution.

**GEANT4** As already mentioned above, GEANT4 provides a full ATLAS simulation comprising particle transitions through the whole detector material, involved interactions and the corresponding secondary particles. Also the object behavior with respect to the surrounding magnetic field is accounted for, as well as for inefficiencies arising due to defects or misalignment. The so-called underlying event (Sect. 2) is realized within the ATLAS tune AUET2B [ATL12a]. Multiple interactions or beam remnants (pile-up), are estimated via minimum-bias events generated with PYTHIA and overlayed with the common hard-scattering collision events. To correct for possible deviations between the simulations and the observed data, subsequent weighting of events within the scope of analysis may be applied (Sect. 5.5).

**ATLFAST** The environment ATLFAST is an ATLAS fast simulation program to simulate physics events with respect to detector response and software reconstruction. It is used to analyze stable particles with four-vectors provided by dedicated event generators whereby these vector inputs are smeared by appropriate functions. Also jet finding and energy smearing algorithms are applied and provide output for further analyses. The general calorimeter response is realized in ATLFAST by summing the transverse energies of the particles in total. Also track quantities and the total missing transverse energy may be determined with the fast simulation program. But in contrast to the full detector simulation of GEANT4, not every appearing interaction and the corresponding secondary

[59] https://jimmy.hepforge.org/

particles are included. Simplifications in the geometry of the calorimeter cells and a parametrization of the shower shapes reduce the time-consuming processes by an order of magnitude compared with the full treatment realized in GEANT4. Nevertheless, the derived distributions are comparable to those of GEANT4 and a combination of both is possible if an urgent analysis is needed. Also the treatment of pile-up events is similar with ATLFAST and a subsequent event weighting applicable.

### 3.3.1 PDFs and Higher Order Corrections

In general, the tools for the common event generation described as before, usually, use matrix elements at LO or NLO. Depending on the various analysis challenges, the simulation sets may be corrected afterwards by applying additional weights event-wise in order to receive also higher order equivalents (briefly described below). Also certain parton distribution functions used in convolution with the matrix elements are an opportunity to influence the distribution shapes of the underlying kinematics (Eq. 2.15, Sect. 2.2). Ideally, the PDFs would fully describe physical scenarios and such cross-section measurements were independent of the PDF choice. But, because of limitations in their time-consuming calculations, it is not possible to give exact theoretical descriptions over the whole kinematic regions and slight deviations in the shapes appear. Usually, the PDFs are extracted out of collider or fixed target experiments by introducing a functional form whose free parameters are fixed for a given momentum scale by fits to the data [60]. Deviations due to the choice of momentum scale, $Q^2$, or factorization scale, respectively, are compensated via different coefficients in the particle distribution functions [61]. Depending on the matrix elements convoluted with the functions, the resulting PDFs are referred to as LO or NLO. Well-known PDF sets were derived by the MSTW [Mar09], CTEQ [Lai10] and HERA [H1Z10, H1Z12] collaborations whereby all slightly differ due to the use of different data sets and parametrizations. To estimate the corresponding fitting uncertainties, the fit parameters are, usually, varied separately up and down within one or two standard deviations (68 % or 90 % confidence level) such that multiple PDF sets are derived for a certain choice of parametrization and momentum scale. The difference resulting by using various PDF sets, can be quoted as theoretical uncertainty in cross-section measurements, for instance.

**k-factors** To derive kinematic distributions for a certain physical process at a higher order (e.g. NNLO), correction factors, commonly denoted as k-factors, are usually applied event-wise (depending on the analysis and the regarded processes). Defined as ratios of NNLO to (N)LO cross-sections, the correction factors are derived for higher order QCD and EW effects separately and combined afterwards.
Exemplified by SM W and Z boson expectations, the method used for the subsequent analysis demonstrates a common way of proceeding. Therefor, a (boson) mass-dependent correction was derived, accounting also for the boson charges, whereby the general calculation and parametrization were performed by the ATLAS W′ and Z′ working groups ([ATL14d], [ATL14a]).

[60] Higher Bjørken-x regions are better described with aid of fixed target experiments (deep inelastic scattering) like [Lai97] while good results for low values of x are achieved, for example, by H1 and Zeus [H1Z10].
[61] The momentum distributions of partons can be transfered to other scales with the aid of so-called DGLAP functions if the kinematics are known for any scale $Q^2$ [Dok77, Gri72, Alt77, Bor13].

Regarding higher order QCD effects, the corresponding k-factor is defined as ratio of NNLO and (N)LO cross-sections with PDF sets chosen as NNLO MSTW2008 in the numerator and (N)LO CT10 in the denominator [Lai10]. The cross-section derivation is performed using ZWPROD [Ham91], the appropriate validation compares to FEWZ [Gav13] and VRAP [62]. Due to significant deviations, the correction factors are calculated separately for $W^+$ and $W^-$ (shown in Figure 3.7).

The EW k-factors, instead, are defined as ratios of $\frac{d\sigma}{dm}$ distributions calculated by MCSANC [Bon13]. They account for higher order effects such as initial state radiation, the interference between initial and final state radiation as well as so-called Sudakov logarithm single-loop corrections.

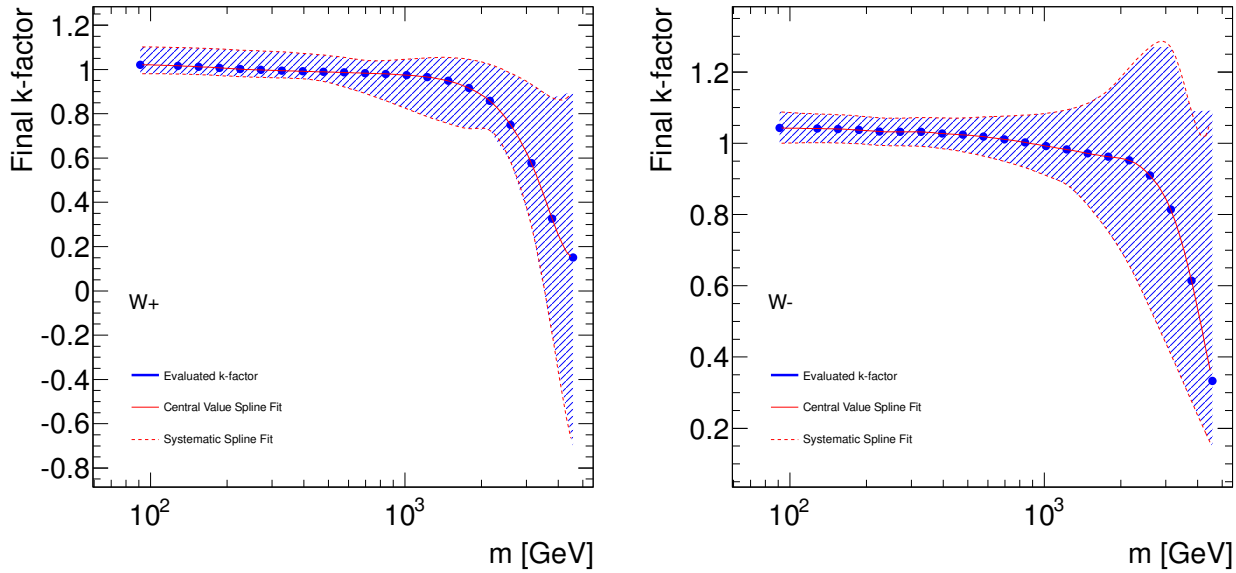


Figure 3.7: Final k-factors as function of the invariant lepton-neutrino mass calculated for processes $W^+ \to \ell^+\nu$ (left) and $W^- \to \ell^-\nu$ (right), derived by the W′ working group [ATL14d].

## 3.4 Signatures in ATLAS

The following section describes the various methods to reconstruct and distinguish particles in ATLAS. They are based mainly on information according energy depositions detected with aid of the calorimeters, as well as on kinematic effects and the momentum determination within the tracking system. The central region of ATLAS covers $|\eta|$ <2.47. Before explaining the different reconstruction variations, a short introduction to certain signatures follows at this stage.

### 3.4.1 Reconstruction and Identification of Physical Objects

Depending on the kind of certain particles, the signatures recorded within the tracking and calorimeter systems differentiate. Various factors like the particle mass and charge, as well as the kind of

[62] http://www.slac.stanford.edu/ lance/Vrap

interaction within the detector play a role. Electrons, for instance, interact electromagnetically and deposit their energy via ionization mechanisms within the material passed or via emission of photons due to bremsstrahlung. Also photons can loose their energy through excitation or ionization of atoms respectively, or convert, during the transition, to an electron-positron pair that behaves subsequently as described before. That difference leads essentially to a slightly larger average penetration depth of the shower caused by the photon (assuming the same electron and photon momentum). The single shower shapes give some indication of the object interacting hadronically or electromagnetically, the observed showering originates from. In fact, those showers corresponding, for instance, to single hadrons are wider than those of an object interacting electromagnetically. In addition, hadrons carry larger masses and follow mainly the strong interaction mechanisms, so that a wider distance between two interactions may be traveled due to the lowered probability of arising ionization. This aspect is reflected in a longer particle shower compared to that of an electron or photon. Jets, on the other hand, built by bunches of electromagnetically or hadronically interacting particles, have already a certain width. Therefore, the related shower runs wider than a comparable electromagnetic one.

The ATLAS data recorded consists of raw detector information only, comprising, for instance, certain hits in the tracking or single energy depositions within the calorimeter system. Dedicated algorithms allow to reconstruct properties like the four-momentum of the related physical objects and hence, a precise identification. Essential for a good particle reconstruction, is the matching of a well constructed particle track to the corresponding energy deposition within the calorimetry. The details of the fundamental track reconstruction are considered generally subsequently, followed by more specific object reconstruction and identification methods.

**Track reconstruction** The general track reconstruction is based on hit information of the pixel system and the semi-conductor tracker (SCT) that impart a three-dimensional view of the particle's trajectory. So, two hits within consecutive pixel layers are commonly taken as starting-point of the track and give a hint to the possible direction of the trajectory. Additional tracking points situated in that direction are assumed to belong to the track. Fitting a parametrized function through these points, the compatibility with a possible trajectory is assessed. To receive a reconstruction as complete as possible, also hits within the TRT are taken into account in sequel to the information from pixel and SCT system.
After reconstructing all such tracks within an event detected, their most probable origins within the beam pipe are determined by extending the various trajectories. The common geometrical intersection points within the interaction zone are denoted as vertices. To ensure the correctness, the tracks are fitted anew using the information of a common vertex they are pointing approximately to.
In order to estimate also their impact within the calorimeter systems, the trajectories reconstructed as described above are extended beyond the inner detector and used to reconstruct and identify specific physical objects such as electrons. Descriptions of certain reconstruction algorithms follow briefly and can be read in more detail in [ATL14e].

**Identification of physical objects** The precise identification of certain particles is a challenge that requires the coverage of a wide energy range. Particles may be determined as positively or negatively charged depending on their deviation and the resulting curved orbit due to the solenoid magnetic field. As already described before, also their charge leads to an ionization of the passed material

producing an electric signal. Quite often, false identification happens since a precise determination of the charge sign is difficult, especially regarding high energies. For instance, bremsstrahlung emitted by an electron passing the detector causes the production of a new electron-positron pair due to the photon radiated. The trajectory of such a positron may cross or be combined to that of the initial electron and hence, result in a misidentification of the electron's charge. Figure 3.8 visualizes the effect exemplified for electrons (respectively positrons) and muons in dependence of the particle's transverse momentum and its position in $\eta$ ([ATL10a],[ATL14e]). Obviously, an increase with the direction in $\eta$ is apparent due to the higher amount of passed material. The effect becomes also less crucial for lower transverse momenta as the intrinsic resolution of the position measurement improves.

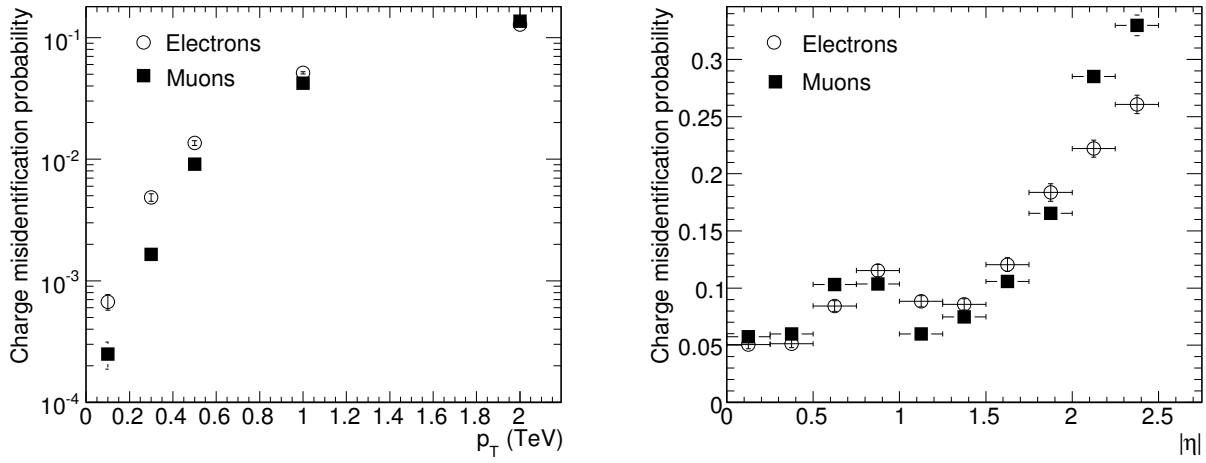


Figure 3.8: Charge misidentification probability as function of the transverse lepton momentum $p_T$ for particles with $|\eta| < 2.5$ (left), and in dependence of $|\eta|$ for particles with $p_T = 2$ TeV (right) [ATL08a].

Since the particle identification aims to identify objects involved in the hard scattering process, it is not sufficient to classify the shower shapes into electromagnetic or hadronic energy depositions only. It is rather important to be able to distinguish an electron [63] from a photon converted into an electron-positron pair within the tracking system as origin of an electromagnetic shower. Although photons themselves do not leave a trace, the combination of possible electron candidate tracks with photon showering is conceivable. A track candidate would be built by combination of certain tracking points originating not necessarily from the same particle. Most of the time, those reconstructed tracks would have bad quality only and are suppressed by applying further requirements to the tracking properties.
Also the differentiation between a photon and a neutral pion decaying subsequently nearly instantaneously into two photons is necessary. A look into the first calorimeter layer may help to distinguish as a pion decay would cause two higher energy depositions.

Finally, the so-called disastrous bremsstrahlung caused by muons passing the calorimeter system should be mentioned. Usually, muons would pass the detector up to the muon system where

[63] Referring subsequently to electrons, both electrons and positrons are meant. A further distinction is not made as electrons and positrons simply differ in their charge signs and the resulting opposing direction of their trajectories.

they would deposit their energy in total. Within the calorimetry before, bremsstrahlung effects would arise at most that could be used for latter background estimation. Talking about disastrous bremsstrahlung on the other hand, a muon cannot pass the inner calorimeter system and may be identified as electron candidate since a corresponding track within the outer muon detector is missed.

### 3.4.2 Electron Reconstruction

The reconstruction of electron candidates can be realized via two different algorithms - the so-called *eGamma* standard algorithm and the alternative *soft*e algorithm - that are based on common definitions of certain aspects. Those will be explained in the following:
Energy depositions covering certain regions of the electromagnetic sections in the calorimeter system are known as cluster. They are determined via a sliding-window algorithm that tries to find a preferably high energy deposition within a pre-defined window. In general, a cluster can be reconstructed in case an transverse energy [64] of at least 2.5 GeV has been deposited within $3 \times 3$ cells of the central layer in the calorimeter. Similarly, corresponding track candidates are evaluated on the basis of several positions within the tracking system (see Section above).
The standard eGamma algorithm tries to match a found cluster to an existing track and thus has been optimized within a broad energy range. Whereas the alternative *soft*e algorithm follows an approach of low energetic electrons and tries to find a corresponding electromagnetic cluster to a determined track candidate.
This thesis refers mainly to the eGamma based reconstruction whereby an electron candidate exists if the energy cluster has a matched track pointing towards its position within $0.05 \times 0.10$ in $\Delta\eta \times \Delta\phi$. In case several track candidates exist, that enclosing the smallest distance (defined as $\Delta R = \sqrt{(\eta_{electron} - \eta_{track})^2 - (\phi_{electron} - \phi_{track})^2}$ ) is chosen. The energy contributions within the single calorimeter layers are recomputed afterwards, summing up the single energy depositions within a pre-defined window of cells in the second calorimeter layer. As the granularity variies for the other layers, a matching algorithm is used to recompute the contributions with respect to the appropriate energy fractions, too. A detailed description of these procedure follows within the section concerning the electron identification. Geometrical effects or inefficiencies due to the detector construction are accounted for within a certain energy calibration [ATL14f]. Corrections to the predefined scaling are finally applied in context of a dedicated analysis and explained more in detail in Section 5.5.

### 3.4.3 Electron Identification

The general three-momentum of an electron candidate is derived from the common energy calculation described as before and its position in $\eta$ and $\phi$ taken from the track if at least four hits within the silicon detector can be assigned [65]. The electron mass is assumed to be negligible compared to the energy region considered within this analysis.
To identify physical objects as electrons, information in different depths are used that go beyond the basic reconstruction step. One distinguishes between three identification level, namely loose,

[64] The transverse energy $E_T$ is defined as $E_T = \sqrt{E_x^2 + E_y^2}$.

[65] If not, those of the energy weighted cluster position in the calorimeter are chosen in case of tracks with lower quality.

medium and tight, that will be explained in detail in the following ([ATL10a], [ATL14e]). Since the nomenclature of most of the variables utilized subsequently is not immediately obvious, those identification variables are introduced before, separated in calorimeter based, track based and those carrying information of both. For the electron identification itself, the related quantities are optimized in ten regions according the cluster pseudo-rapidity and eleven bins with respect to the transverse energy to account, in particular, for the various detector conditions. Diversifying the transverse energy in steps of 5 GeV from 5 to 20 GeV and in steps of 10 GeV up to energies of above 80 GeV, a good separation between isolated (signal) electrons and the background occurring due to hadrons misidentified as electrons, non-isolated electrons (e.g. from heavy-flavor particles decaying semi-leptonically) and those originating from photon conversions, can be ensured. The related optimization in $\eta$ is motivated by the detector geometry, consolidating significant detector regions such as the transition region of barrel and end-caps or the changing in granularity of the calorimeter layers.

**Calorimeter based quantities** Both, the electromagnetic and the hadronic calorimeter are composed of various layers accounting for different purposes. They provide information allowing an itemization of particular energy depositions in certain depths. Commencing with the first layer of the ECAL, the distance, for instance, of a second energy deposition to the shower position regarded can be analyzed. Therefor, the variable denoted as $\Delta E_s$ is used which provides information about the energy difference between the second maximum ($E_{max2}$) and the first determined minimum ($E_{min}$). The total shower width with respect to strip cells of the first calorimeter layer is described by the variable $w_{stot}$ that gives a first idea of the shower. It is:

$$w_{stot} = \sqrt{(\sum E_i(i-i_{max})^2)/(\sum E_i)} \tag{3.6}$$

where $i$ runs over all stripes within a window of $0.0625 \times 0.2$ in $\Delta\eta \times \Delta\phi$, corresponding typically to 20 strips in $\eta$. The index of the strip comprising the highest energy deposition is denoted as $i_{max}$.

Further information about the shower shape can be derived with aid of the second calorimeter layer. The lateral shower width, namely $w_{\eta 2}$, is determined as

$$w_{\eta 2} = \sqrt{(\sum E_i \eta_i^2)/(\sum E_i) - ((\sum E_i \eta_i)/(\sum E_i))^2} \tag{3.7}$$

whereby $E_i$ denotes the energy and $\eta_i$ the pseudo-rapidity of cell $i$. The corresponding sum is derived for a window of $3 \times 5$ cells. In order to retrieve also information according the hadronic leakage, meaning the overlap of an electromagnetic showering into the hadronic calorimeter, the transverse energy ($E_{Thad}$) in the HCAL is adduced. In addition, also the ratio ($R_{Had}$) of the transverse energy deposited in total within the HCAL and that of the EM cluster is regarded.

**Track based quantities** The tracking system of ATLAS is dominated by the inner detector whereby the momentum of charged particles can be determined. The consequent variables convey information about the track quality and thus, may be utilized in addition for particle identification. Thereby, both the identified hits within the pixel system, denoted as $n_{Pixel}$, and those within the semiconductor strip modules, $n_{Si}$, as well as those of the innermost layer of the pixel system ($n_{Blayer}$), known as b-layer, are processed separately. Displaying not only the amount of hits belonging to

a certain track in total ($n_{TRT}$) but also those exceeding a certain threshold, the TRT contributes further information to the track quality determination. In addition, the odds are to retrieve the impact parameters describing the distance of radiated particles to the interaction point separately. The variable $d_0$, for instance, denotes the smallest transverse distance to a track originating from a certain vertex.

**Combination of both** To combine calorimeter and track based quantities, the main emphasis of the energy deposition is compared to an extrapolated direction of the track candidate. In fact, to avoid the impact due to hard bremsstrahlung effects causing possibly huge deviations between track and cluster, the track is extended from its outer monitoring points within the inner detector to the calorimeter system. The deviations are determined with respect to differences in $\eta$ (meaning $\Delta\eta$) and $\phi$ (meaning $\Delta\phi$).

The various identification levels are explained in the following with respect to the aforementioned quantities and are, finally, summarized in Table 3.4.3.

**loose** The first level of electron identification ensues over a few cuts referring to limited information of the calorimeter. Thus, it is the simplest of the three selections considered and causes, in spite of a good electron identification efficiency, a low background suppression only. Mainly, information about the shower shape are used with respect to the first and second layers of the ECAL like $R_\eta$ or the lateral shower width $w_{\eta 2}$. To reject, for instance, arising objects originating from neutral pion decays, the energy difference between the first and second largest maximum are regarded in comparison to their sum ($E_{ratio}$) [66]. Also the hadronic leakage is tolerated up to a certain energy threshold only and quality requirements are applied to the electron track and the electron-cluster matching to further reject the hadronic backgrounds while still ensuring a high identification efficiency.

**medium** At this stage, the identification at loose level is refined by tightening the existing cut selection and regarding further discriminating variables like the presence of hits measured within the innermost pixel layer (to reject electrons originating from photon conversions). Additional restrictions are included with respect to the allowed transverse distance to the center of the interaction point, $d_0$, and the identification of transition radiation in the TRT to suppress also the dominant background contributions due to charged hadrons.
In general, the medium cut selection improves the background rejection by an order of magnitude with respect to loose identification, even the actual identification efficiency is slightly reduced by about 10 %.

**tight** The identification at tight level is the most precise one. It uses nearly all quantities and information available for a particle identification and comprises the loose and medium selection. In fact, the restrictions previously mentioned are tightened further and additional requirements are comprised according the track quality in the presence of a track extension in the TRT. Furthermore, to achieve also a higher suppression of the background contributions due to photon conversions, a veto on reconstructed photon conversion vertices in association with the cluster is introduced and

[66] Two high separable energy depositions within the first calorimeter layer would indicate such a process

the energy depositions within the electromagnetic calorimeter are compared to the corresponding track momenta.
All in all, the rejection power can be even increased by a factor of two with respect to the medium identification level.

Despite the level of identification, no isolation requirement is included for a general electron identification described as above and thus, no restrictions are set to the presence of other particles causing additional tracks or energy depositions outside the electromagnetic cluster. Depending on the physical process regarded, each subsequent analysis is free to apply additional conditions to suppress these effects.

### 3.4.4 Reconstruction of Missing Transverse Energy $E_T^{miss}$

Because this dissertation concerns especially decays into a highly energetic electron with a potential neutrino, not only the reconstruction of particles interacting electromagnetically should be described but also that of so-called missing transverse energy, $E_T^{miss}$. As the neutrino momentum is not detectable directly within ATLAS, it is calculated indirectly as missing transverse energy. In fact, regarding the longitudinal component of the neutrino momentum, no statement to the corresponding longitudinal momentum fraction of the initial quark composition can be made whereas their fraction within the transverse plain should be negligible small. Assuming the neutrino to be the only particle not interacting with the detector material (and thus, to be the only undetected object), the transverse component of the neutrino momentum follows as remnant of the total transverse energy subtracted by the already known contributions due to previously reconstructed physical objects or detector effects [67]. The calculation procedure of the missing transverse energy shall be explained subsequently in detail.

Reconstructing the neutrino contribution, a refined calibration with respect to the missing transverse energy is taken as basis. Thereby, already reconstructed and identified high energetic objects are matched to calorimeter cells in a predefined order to increase the accuracy in calibration. The matching regards firstly electrons, photons, hadronically decaying tauons followed by jets and muons, and is stored afterwards in a specific map. Also unused (meaning cells not included within the reconstruction of any highly energetic object) or damaged calorimeter cells are regarded. Within the map, not only the various objects are listed but also the corresponding cluster components and the final cell allocation within the predefined ordering. In case a cell can belong to more than one object, the first possibility only is stored. But, if a cell can be matched to different particles of the same type, each possibility is considered weighted with respect to the cell geometry. So, cell double counting can be avoided while a correct allocation of each energy fraction within a cell can be ensured. Using a pre-defined calculation algorithm [68], the final missing transverse energy is derived event-wise and called "MET_RefFinal". The jets regarded within the $E_T^{miss}$ determination are reconstructed via a so-called "anti-$k_t$" algorithm using local calibrated topological clusters [69] (which include hadronic calibration, dead material and out-of-cluster corrections) ("LC Topo" jets). Details of the basic jet reconstruction and calibration are briefly described subsequently. The underlying scheme of the

[67] Momentum conservation is assumed.
[68] Provided by the ATLAS JetEtmiss analysis group: METUtility/01-02-05, https://twiki.cern.ch/twiki/bin/view/AtlasProtected/EtMissRefFinal.
[69] Cells are grouped together to form topological clusters that are calibrated afterwards.

| Layer | Cut definition | Cut variables |
|---|---|---|
| | Loose | |
| Acceptance | - Central (barrel) region | $\|\eta\|$ <2.47 |
| HCAL | - Ratio of $E_T$ deposited in the HCAL (first layer) $E_T$ to of the EM clusters ($\|\eta\| < 0.8$, $\|\eta\| > 1.37$) | $R_{had,1}$ |
| | - Ratio of $E_T$ deposited in the whole HCAL $E_T$ to of the EM clusters ($0.8 < \|\eta\| < 1.37$) | $R_{had}$ |
| | - Ratio of $E_T$ deposited in the HCAL (first layer) $E_T$ to of the EM clusters | $R_{had}$ |
| middle layer of ECAL | - Ratio of energies within 3×7 vs. 7×7 cells | $R_\eta$ |
| | - Lateral shower width | $w_{\eta 2}$ |
| front layer of ECAL | - Total shower width | $w_{stot}$ |
| | - Energy difference of the largest and second largest energy deposits in the cluster divided by their sum | $E_{ratio}$ |
| Track quality and track-cluster matching | - Number of hits in the pixel detector | $n_{Pixel} > 0$ |
| | - Number of hits in the silicon detectors | $n_{Si} \geq 7$ |
| | - $\|\Delta\eta\|$ between the cluster position in the first layer and the extrapolated track | $\|\Delta\eta\| < 0.015$ |
| | Medium (composing Loose) | |
| Tracking variables | - Smallest distance between track and vertex | $\|d_0\| < 5$ mm |
| | - $\Delta\eta$ between cluster and track | $\|\Delta\eta\| < 0.005$ |
| | - Number of hits within pixel detector ($\|\eta\| > 2.01$) | $n_{Pixel} > 1$ |
| | - Number of b-layer hits ($\|\eta\| < 2.01$) | $n_{Blayer} > 0$ |
| TRT | - Loose cut on high-threshold fraction in TRT | |
| | Tight (composing Medium) | |
| Tracking variables | - Smallest distance between track and vertex | $\|d_0\| < 1$ mm |
| | - Asymmetric cut on $\Delta\phi$ between cluster position in the middle layer and the extrapolated track | $\|\Delta\phi\|$ |
| | - Ratio of cluster energy to track momentum | E/p |
| TRT | - Total amount of hits within the TRT | $n_{TRT}$ |
| | - Tighter cut on high-threshold fraction in TRT | |
| Conversions | - Reject electron candidates matched to reconstructed photon conversions | |

Table 3.1: Summary of identification cut selections. Single cut values are mentioned explicitely if they are kept constant within all regions considered [ATL14e].

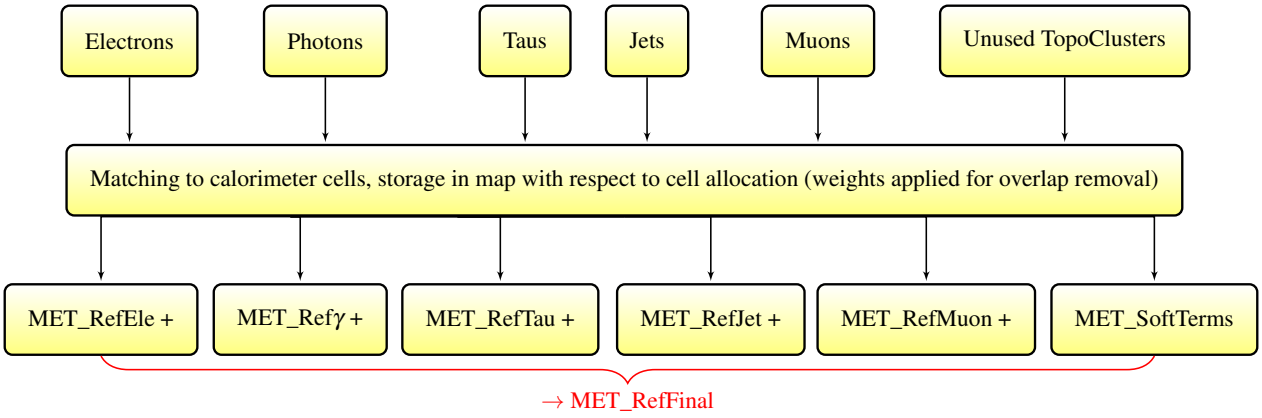


Figure 3.9: Scheme of MET_RefFinal calculation.

$E_T^{miss}$ calculation is shown in Figure 3.4.4. The nomenclature of the final cell allocation is combined using the term "MET_Ref" and the name of the object it refers to. "Soft terms" includes, thereby, both, soft (low-$p_T$) jets and cell out contributions whereby the latter uses not only the local hadronic calibration but also tracking information [70].

### 3.4.5 Jet Reconstruction and Calibration

Because jets are important to reconstruct a full picture of a hard scattering event, especially for multiparticle dynamics occuring and the calculation of the missing transverse energy, the corresponding reconstruction algorithm shall be explained briefly. The challenge, here, is to decide which particles belong to the same jet and how the corresponding momenta have to be recombined to obtain the jet-momentum. The procedure known as "anti-$k_t$" algorithm [Cac08] has been designed not to recombine soft (low-$p_T$) particles together and is based on the determination of distances from detected particles to the beam axis and in between. Identifying the smallest distance to the beam ($d_{iB}$) and to the following objects ($d_{ij}$), particles are recombined to a jet, the remaining distances are recalculated and the procedure repeated until no objects are left within a predefined cone. The distance parameter takes not only the rapidity ($y$) and azimuth angle ($\Phi$) between two particles into account, but also their transverse momenta ($k_t$). It is:

$$d_{ij} = min(k_{ti}^{2p} k_{tj}^{2p}) \frac{\Delta_{ij}^2}{R^2} \quad with \quad \Delta_{ij}^2 = (y_i - y_j)^2 + (\Phi_i - \Phi_j)^2 \tag{3.8}$$

$$d_{iB} = k_{ti}^{2p} \tag{3.9}$$

The impact of the relative power of the energy compared to the angular properties going into $\Delta_{ij}$, is realized with the parameter $p$ [71]. The radius of a mostly conical jet is denoted as R.

[70] Only tracks are considered which do not belong to any hard object already reconstructed. The remaining tracks extrapolated to the second layer of the ECAL and matched to clusters.

[71] For $p = 1$ the known $k_t$ algorithm is reproduced; $p = 0$ corresponds to the inclusive Cambridge/Aachen algorithm. The new properties of the anti-$k_t$ algorithm follow for $p = -1$.

If, now, two hard particles are found within a radius R [72] (meaning $\Delta_{12} < R$), they are recombined to a single jet. If, thereby, the transverse momentum of the first, $k_{t1}$, is, for instance, much larger than that of the second particle, the jet is conical and centered on $k_{t1}$. In the case of two hard particles appearing with a larger distance in between, such that $R < \Delta_{12} < 2R$, two separated hard jets are formed, each centered on the corresponding particle depositions whereby the jets wouldn't be necessarily perfectly conical. Another conceivable scenario is having an event with a single hard particle and several soft objects involved. Here, the derived distance $d_{1i}$ between the hard and a soft particle is dominated by the transverse momentum of the hard object, $k_{t1}$, and the angular separation visualized in $\Delta_{1i}$. Because of much larger distance parameters for soft particles involved only, they would therefore always cluster to a hard particle firstly. In fact, if no further object of a hard process is present, the single hard particle is recombined with soft objects until a perfectly conical jet with radius R is derived.

Hence, the shape of a reconstructed jet does not rely on the influence of soft particles but on the occurrence of objects originating from the hard process. So, in contrast to the sliding window algorithm used for electron reconstruction, the obtained jet clusters are allowed to comprise varying numbers of cells whereby hard jets are usually circular (softer jets would result in slightly more complex shapes). Details of the corresponding jet areas and further properties can be find in [Cac08].

**Jet calibration** Because of an highly increased amount of particles appearing due to the underlying event or pile-up effects (effects increase for higher luminosities), it becomes necessary to account for these and recalibrate the physics jet to interaction level. To achieve a jet momentum to be measured as precisely as possible, also non-instrumented detector parts and regions where not all energy deposits can be determined (tile calorimeters), have to be regarded. Starting with so-called calorimeter jets (detection of energy clusters and first jet reconstructions) [73], cell weights are applied with respect to the energy density and pile-up dependent offsets. After additional origin corrections to the jet direction (the energy is not influenced), the jet energy and pseudorapidity are recalibrated to the particle jet scale (corrections derived from MC only). Using in-situ measurements subsequently, a residual calibration is derived by balancing the transverse jet momentum by that of a well-measured reference object. The corrections are applied on data only such that a refined physics jet at interaction level is determined which can be used, in the following, as proxy of final state partons [74]. The underlying scheme is visualized in Figure 3.10.

[72] For this thesis, a cone of $R = 0.4$ is used to identify jets with the anti-$k_t$ algorithm.

[73] Only clusters are taken into account that comprise significantly higher energy depositions than underlying noise effects.

[74] The weights are commonly provided by an official ATLAS working group, https://twiki.cern.ch/twiki/bin/viewauth/ AtlasProtected/ ApplyJetCalibration2012.

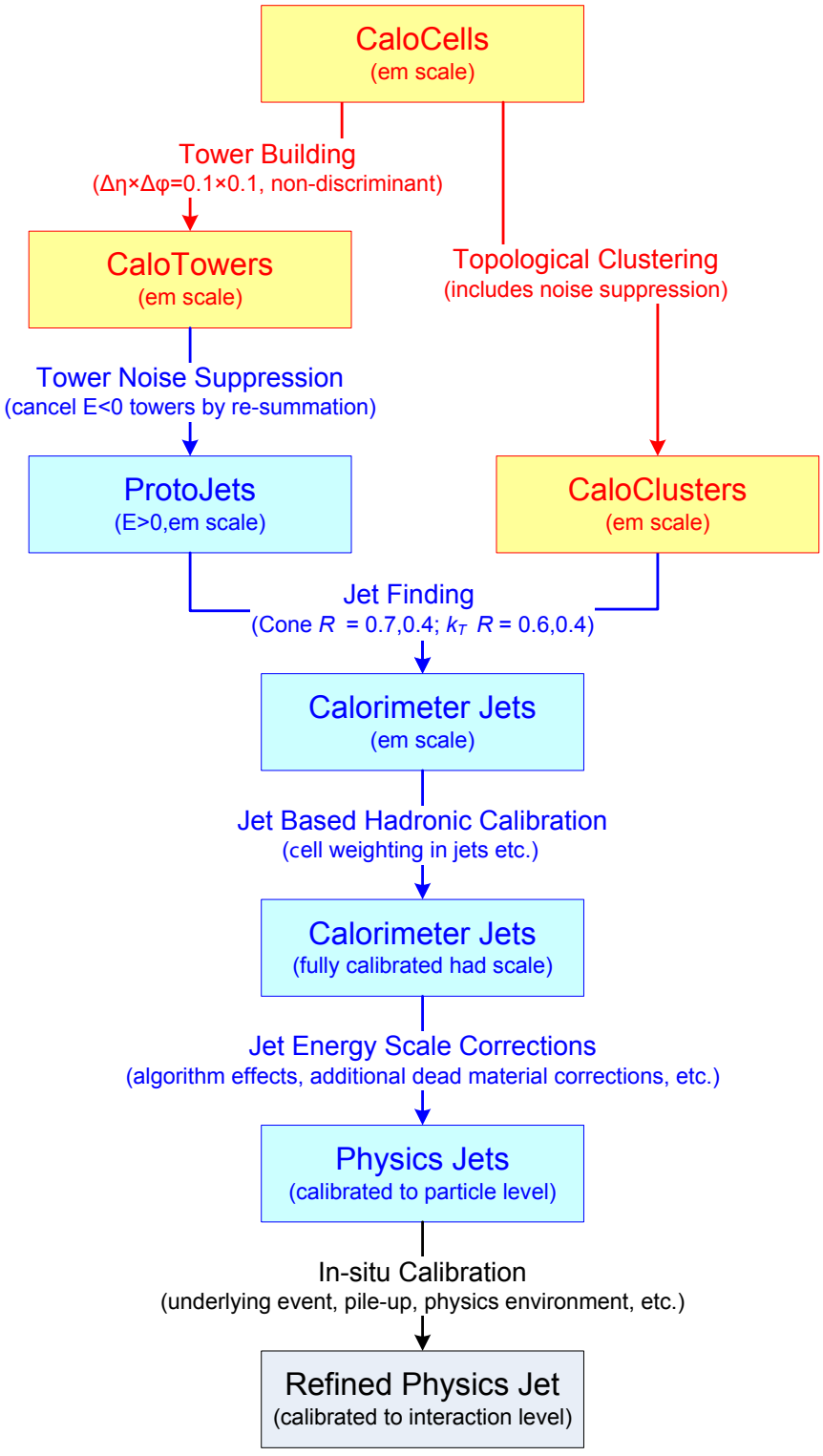


Figure 3.10: Scheme of jet calibration [ATL08a].

# 4 Trigger Performance Studies

The wide variety of ATLAS analyses as well as certain calibration and efficiency measurements bring along the need also for a wide variety of dedicated triggers.

Regarding the general electron reconstruction and identification, for instance, scale factor derivations (as described in Sect. 5.5) are necessary to adapt predicted efficiencies found in Monte Carlo simulations to data. Referring to clean electron sources such as W or Z decays, such corrections can be derived via so-called tag- and probe methods referring to fractions of candidate events passing a selection with a certain signal trigger involved.
Combining different decay channels, the precision in measurements can be even increased. So, besides different electron or photon triggers, also special missing transverse energy, $E_T^{miss}$, or so-called W tag&probe triggers are designed to study the reconstruction and identification performance of particles with different transverse momenta [75].

In each case, the trigger performance has to be studied carefully and, due to changed conditions in data taking, also re-optimized to control the appropriate rates while ensuring stable signal selection efficiencies over the whole data acquisition.

The following sections refer in particular to the purity of the lowest unprescaled single electron trigger used as primary trigger for most physics analyses and the underlying performance studies of the W tag&probe triggers enabled in 2012. The appropriate results were developed within the context of the official ATLAS electron and photon trigger performance measurements [ATL14h].

## 4.1 Single Electron Trigger

During most of the data taking periods in 2012 [76], the trigger named `e24vhi_medium1` was kept as the lowest unprescaled single electron trigger. The "v" marks the L1 $p_T$ threshold to be $\eta$ dependent, the "h" visualizes a cut applied to the hadronic leakage at the first trigger level (L1). A relative track isolation within a cone of $\Delta R < 0.2$ required at EF stage (that is $\frac{p_{T,iso}}{E_T} < 0.1$) is indicated by an "i" in the trigger name. In addition, the medium identification criteria are applied to electron candidates at HLT [77]. Since the selection criteria of this trigger had to be tuned several times to maintain the signal efficiency and to keep the appropriate rate within the allocated bandwidth, it is interesting and important to look into its purity.

Studies were performed using the whole data set recorded in 2012 at a center-of-mass energy of $\sqrt{s} = 8\,\text{TeV}$ and a corresponding integrated luminosity of about $L_{int} = 20\,\text{fb}^{-1}$. The fraction of triggered events that satisfy $W \to e\nu$ or $Z \to ee$ is interpreted as trigger purity whereas the rate of those

[75] Low $E_T$ measurements up to $E_T < 20\,\text{GeV}$ are dominated by J/$\psi$ statistics while a higher statistical precision is achieved by Z/W tag&probe measurements for the higher transverse energy region.

[76] For all periods following since period B.

[77] Requirements on the calorimeter shower shapes, the reconstructed track quality, the electron identification information provided by the TRT and on the matching between the energy deposition in the calorimeter and the measured track.

events stored by the ATLAS Trigger and Data Acquisition (TDAQ) system is determined as

$$R_i = R_0 \cdot \frac{N_i}{N_0}. \tag{4.1}$$

Here, the (peak) rate of the `e24vhi_medium1` trigger is denoted as $R_0$ (96 Hz obtained at the beginning of a typical run [78] in 2012 at an instantaneous luminosity of about $7 \times 10^{33}\,\mathrm{cm}^{-2}\mathrm{s}^{-1}$), $N_i$ is the number of triggered (trigger matched respectively) events passing (additional) disversified $p_T$ thresholds, and $N_0$ is the number of events selected by the `e24vhi_medium1` trigger in data. The purity at each trigger level describes the contribution of prompt electrons originating from W and Z production and follows by dividing the predicted fraction of pure W or Z events (derived out of Monte Carlo simulations) by those observed in data, thus assuming the simulations to fully describe W or Z production mechanisms in data:

$$purity = \frac{N_{i,MC}}{N_{i,Data}}. \tag{4.2}$$

Figure 4.1 shows the output rate (left) and the purity (right) at EF level as a function of the electron transverse energy thresholds for data and MC simulation sets. The single fractions of pure W or Z events ($N_i$) are compared to data and shown in the appendix (Section A.2). The predicted MC contributions are derived separately for W and Z decays into electrons (plus missing transverse energy), scaled to the appropriate data luminosity and visualized as stacked histograms. They demonstrate a similar behavior to that observed for the `mu24i` single muon trigger [79]. Shown uncertainties are estimated using a simple Poissonian approach for the event numbers, $\Delta N = \sqrt{N}$, and are distributed to the final rate or purity. The ATLAS operating point for the `e24vhi` trigger is shown in the first bin with a low edge of 24 GeV. The distributions are inclusive meaning that the event rate for $p_T$ above a certain value is plotted at that $p_T$ point. The rates determined for data as well as those for predicted W and Z events show the expected exponential slope with increasing transverse energy thresholds. In the peak region of the purity distribution, the contribution of prompt electrons originating from W and Z productions collected after the trigger selection are almost half of that observed in data (about 40-50 %) and thus, quite high for a single trigger applied [ATL14h]. Increasing the energy requirement at EF, the purity decreases, such that it seems to be convenient to keep (or only slightly rise) the current energy threshold applied at trigger level in upcoming trigger menus.

Comparable studies performed at the first two trigger level, namely L1 and L2, show similar results. Figures 4.2 and 4.3 show the appropriate rates and purities for the L1 (`L1_EM18VH`) and L2 (`L2_e24vhi_medium1`) trigger stages corresponding to the `e24vhi_medium1` trigger [80]. As the selection requirements tighten from level to level, the amount of remaining background events reduces. This becomes obvious also in an (slightly) increased purity regarding L1, L2 and EF distributions in comparison. The typical exponential tail due to the background contamination and the non-exponential behavior for the signal are visible in each.

Commonly, the `e24vhi_medium1` single electron trigger had been designed to select good isolated electrons with very low background contamination in order to control the rates. In fact, the

[78] The data acquisition at the LHC is splitted into various data periods whereby each period is subdivided into single runs each acquiring data within about six hours.

[79] ATLAS Muon Trigger Public Results: https://twiki.cern.ch/twiki/bin/view/AtlasPublic/MuonTriggerPublicResults.

[80] At L1, the corresponding $R_0$ is 17000 Hz, at L2 about 1030 Hz.

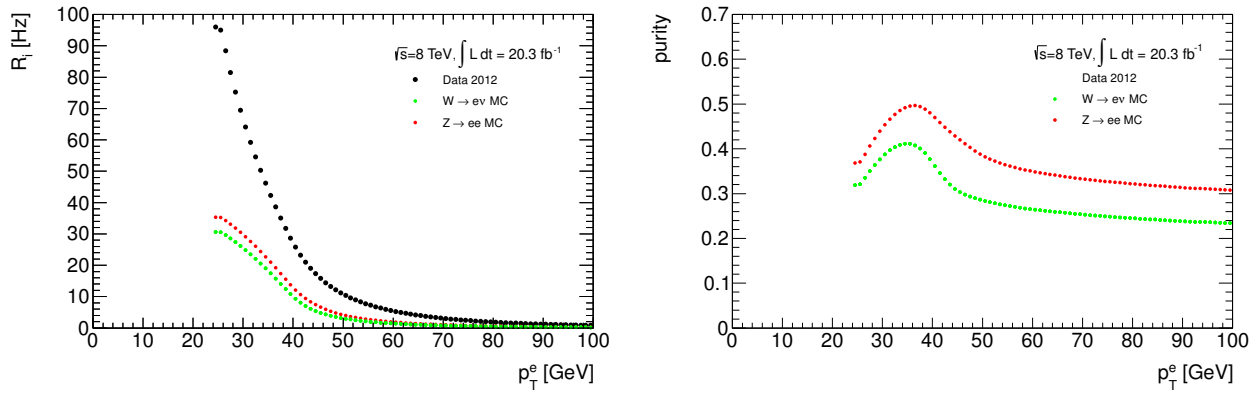


Figure 4.1: Rate in Hz (left) and purity (right) as function of $p_T$ at EF level. The contributions due to W and Z decays derived out of MC simulations are scaled with the predicted cross-sections to data luminosity and shown as stacked histograms. The purity distributions are determined by dividing the single rates by the total data rate.

trigger efficiency is relatively high for medium or tight selections. Figure 4.4 shows the rate (left) and purity (right) after requiring the `e24vhi_medium1` trigger with disversified energy thresholds at EF level. Estimated uncertainties are derived by using a Poissonian approach, too. As expected, the trigger rate for offline medium selections is about 83 Hz at maximum, for an offline tight selection the rate decreases to about 56 Hz. Tight selections are quite pure whereas the medium distributions still include more electron fakes.

Summarizing, the `e24vhi` is the lowest unprescaled electron trigger chosen as primary trigger for most ATLAS analyses and scale factor derivations, demonstrating a good overall purity. Raising the energy threshold applied at trigger level would not cause significant improvements with respect to the contribution of prompt electrons originating from W and Z production mechanisms. The performance of the `e24vhi` trigger with respect to different offline identification criteria achieved high efficiencies. In fact, comparing medium to tight electron selections, quite pure electron samples can be obtained in both cases whereby a medium identification still allows about 20 % more fake electron candidates.

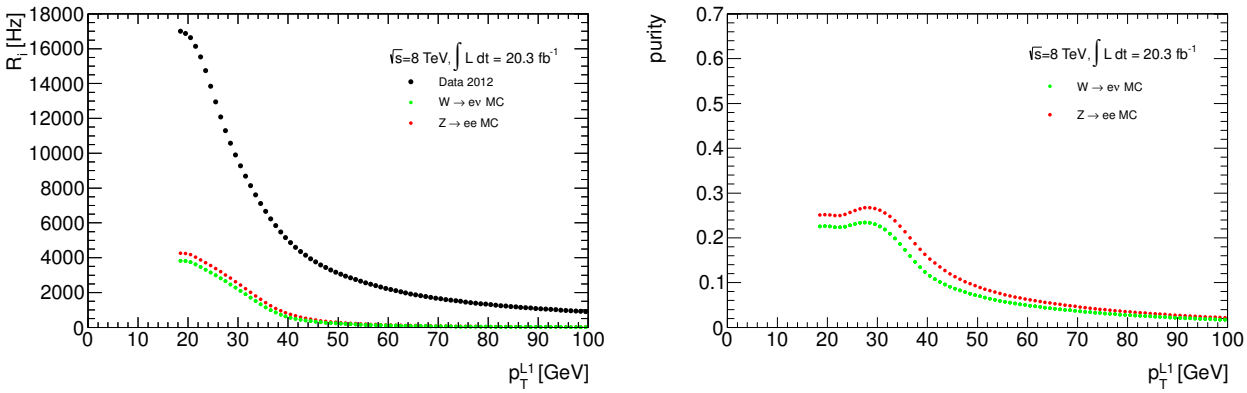


Figure 4.2: Rate in Hz (left) and purity (right) as function of $p_T$ at L1 level. The expected contributions due to W and Z decays derived by MC simulations are scaled with the predicted cross-sections to data luminosity and shown as stacked histograms. The purity distributions are derived by dividing the single rates by the total data rate.

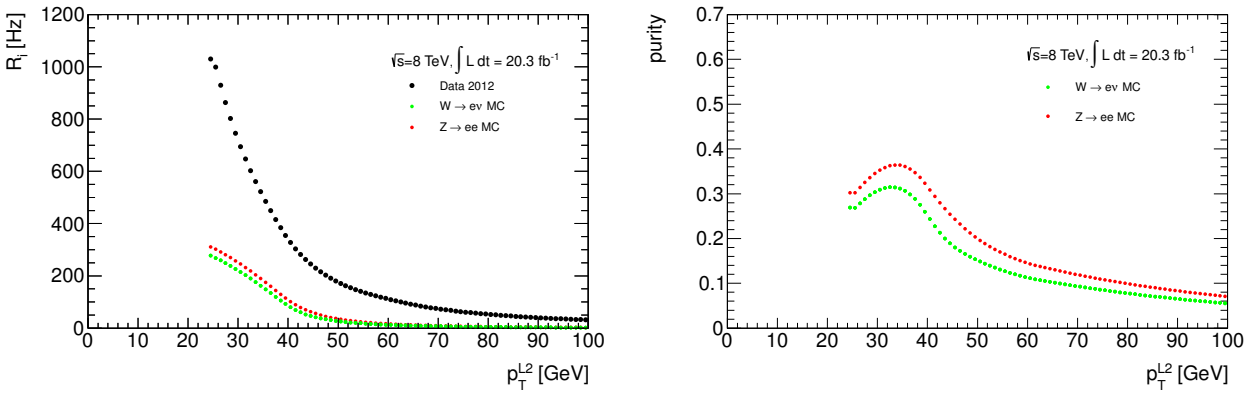


Figure 4.3: Rate in Hz (left) and purity (right) as function of $p_T$ at L2 level. The expected contributions due to W and Z decays derived by MC simulations are scaled with the predicted cross-sections to data luminosity and shown as stacked histograms. The purity distributions are derived by dividing the single rates by the total data rate.

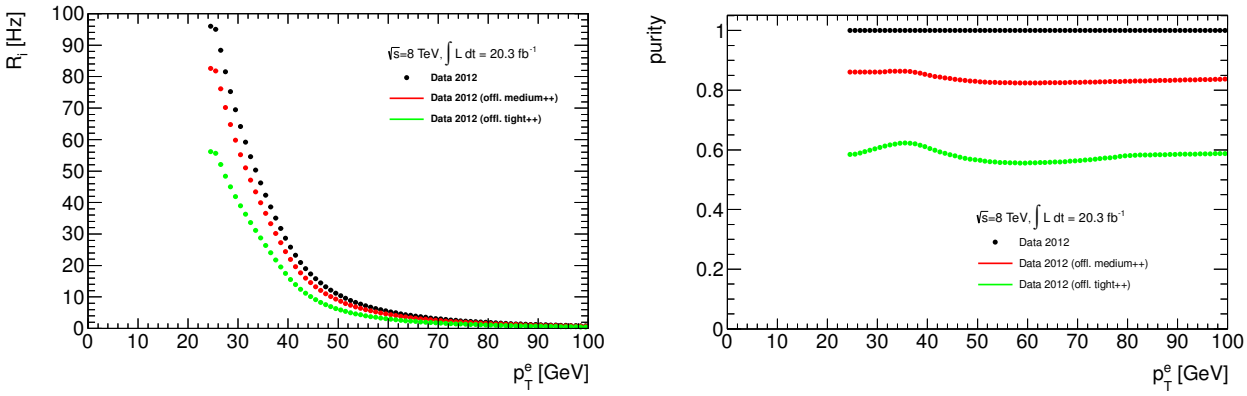


Figure 4.4: Rate in Hz (left) and purity (right) as function of the $p_T$ threshold at EF level. The fraction of offline medium and tight electrons in data after varying the $p_T$ thresholds are shown in red (med.) and green (tight). The purity distributions are derived by dividing the single rates by the total data rate.

## 4.2 W Tag&Probe Trigger

As already mentioned, the wide variety of ATLAS analyses as well as certain calibration and efficiency measurements bring along the need also for a wide variety of dedicated triggers. So, besides certain electron analyses, many interesting physics processes are based on the signature of missing transverse energy, $E_T^{miss}$. But, due to the complexity in measuring or calculating the total momentum of particles that don't interact within the detector, it is a challenge to design dedicated triggers selecting interesting events without being dominated by fake sources of missing transverse energy such as calorimeter cracks or defective cells.

So-called W tag&probe triggers are, in particular, designed to select electron candidates with very loose conditions applied to probe the performance while a tighter requirement should be applied to arising missing transverse energy. With this, such $W \to e\nu$ events selected could also be used for (electron) identification efficiency measurements, even slightly softer electron distributions compared to those of Z decay products, for instance, may be expected.

But, with the increased luminosity in 2012, pileup effects became more frequent that also may cause additionally large transverse energy deposits in calorimeter cells. So, also the probability of measurement fluctuations is increased and large values of fake missing transverse energy can arise. Therefore, accounting for an output rate growing non-linearly with luminosity, the W tag&probe triggers do not include a cut on the missing transverse energy directly. Instead, a cut on electron transverse momenta and a requirement on the so-called $E_T^{miss}$ significance are used to improve their performance and to select mainly W candidates decaying into an electron and a neutrino. The significance is denoted as `xs` and defined as follows:

$$\texttt{xs} = \frac{E_T^{miss}}{(a\sqrt{\sum E_T} + b)} \tag{4.3}$$

where $\sum E_T$ is the sum of the transverse energies of all electron candidates in the event, and $a$ and $b$ denote some constant values. The significance is computed at all trigger levels, introducing different parametrizations to the $E_T^{miss}$ resolution as developed in the ATLAS electron/$\gamma$ trigger working group. Table 4.1 lists the different trigger levels with the corresponding values of $a$ and $b$ for 2011 [ATL12h] and 2012 performances whereby the L1 parametrization derived in 2011 was used until end of May 2012 (before run 204187 in period B). Regardless of the trigger level, typically the missing transverse energy needs to be above 80-100 GeV, $\sum E_T$ between 16 GeV and 4 TeV to obtain reasonable results.
In addition to the requirements on electron transverse momenta and the $E_T^{miss}$ significance, a cut on the angle between a jet and the direction of the missing transverse energy, $\Delta\phi$, is applied on EF level to suppress QCD multi-jet backgrounds. This requirement is reflected in the trigger name such as "dphi2j15xe20", meaning a $\Delta\phi > 2.0$ was checked against two highest $p_T$ jets with a transverse momentum of at least 15 GeV [81].

[81] The term "xe20" refers to a missing transverse energy above 20 GeV.

| | 2011 | | 2012 | |
|---|---|---|---|---|
| | *a* | *b* | *a* | *b* |
| offline | 0.5 | 0 | 0.5 | 0 |
| L1 | 1.12 | -1.4336 | 1.15 | -1.886 |
| L2 | 1.12 | -1.4336 | 0.57315 | -0.898 |
| EF | 0.46 | -0.23 | 0.2966 | 4.265 |

Table 4.1: Values used for $a$ and $b$ to compute $E_T^{miss}$ significance at each trigger level, 2011 in comparison with 2012. In 2012, the L1 parametrization has changed since run 204187; before, the 2011 parametrization was used.

The original trigger menu of 2012 data acquisition included four different W tag&probe triggers, namely [82]

- `e13_etcutTrk_xs60` (← `L2_e13_etcutTrk_xs45` ← `L1_EM6_XS45`)
- `e13_etcutTrk_xs60_dphi2j15xe20` (← `L2_e13_etcutTrk_xs45` ← `L1_EM6_XS45`)
- `e20_etcutTrk_xs60_dphi2j15xe20` (← `L2_e20_etcutTrk_xs45` ← `L1_EM16V_XS45`)
- `e20_etcutTrk_xe30_dphi2j15xe20` (← `L2_e20_etcutTrk_xe25` ← `L1_EM16V_XE20`).

The `etcutTrk` in the trigger names indicates that only a loose cut on track quality and a cut on $E_T$ are used for the electron selection (applied on L2, EF). Especially, no requirements on the cluster shower shapes influence the trigger selection.

In order to study the appropriate trigger performances, the corresponding overall efficiencies are determined in the following with respect to an offline selection of $W \to e\nu$ events triggered by the lowest unprescaled single electron trigger `e24vhi_medium1`. Thereby, the W boson is reconstructed from an electron having a transverse momentum of at least 25 GeV which is reconstructed within the central detector region ($|\eta|$ <2.47), and the missing transverse energy (also $E_T^{miss}$ >25 GeV). The combined transverse mass is defined as $m_T = \sqrt{2p_{T,e}E_T^{miss}(1-\cos\phi_{e,E_T^{miss}})}$ and required to be larger than 50 GeV. So, the efficiencies should be interpreted as the acceptance of the W tag&probe triggers relative to the current $W \to e\nu$ identification on ATLAS data and represent the performance of the $E_T^{miss}$ significance selection at trigger level (with respect to the $W \to e\nu$ event selection):

$$\varepsilon = \frac{\#Wevents + Wtag\&probetrigger}{\#Wevents} \tag{4.4}$$

[82] Upper case notation "XS45" in the trigger name refers to a cut on $E_T^{miss}$ significance > 4.5 applied at L1, while lower case "xs" refers to a cut on $E_T^{miss}$ significance > 6.0(4.5) applied at EF (L2) level.

While calculation, also the fact is taken into account that the e13+xs60 triggers are prescaled at L1 with a prescale reduced as the luminosity falls and thus, a bandwidth allocation increasing towards the end of a fill. It is:

- e13_etcutTrk_xs60: 1.28 % - prescale included
- e13_etcutTrk_xs60_dphi2j15xe20: 1.28 % - prescale included
- e20_etcutTrk_xs60_dphi2j15xe20: 7.66 % - unprescaled

Even after general menu configuration changes (introduced by official ATLAS working groups) [83], these overall efficiencies stayed low. This is mainly caused by inefficiencies due to changes in the L2 parametrization during the very first data acquisition runs (Tab. 4.1, in order to introduce the additional $E_T^{miss}$ calculation at L2). Also the high xs cut of 6.0 at EF level leads to such reduced efficiencies.

So, to collect statistics throughout a fill and to minimize the pile-up bias of the collected event sample, it is necessary to reduce the rates especially at L1 while increasing the L1 XS thresholds. New (prescaled) triggers were enabled during a short break at the end of June 2012 (since run 206481) with xs thresholds of XS50, XS55 and XS60 at L1 and L2. These thresholds were kept equal at L1 and L2, and the EF thresholds were also lowered to recover the efficiency. The new triggers are listed in Table 4.2 with the appropriate efficiencies derived relatively to the $W \to e\nu$ selection as described before. Errors are statistical only and no background subtraction was used.

| Trigger chain | efficiency (%) |
|---|---|
| e13_etcutTrk_xs60_dphi2j15xe20 | 6.90±0.03 |
| e20_etcutTrk_xs60_dphi2j15xe20 | 6.86±0.03 |
| e13_etcutTrk_xs45_L1XS50_dphi2j15xe20 | 34.83±0.05 |
| e13_etcutTrk_xs50_L1XS50_dphi2j15xe20 | 23.22±0.05 |
| e13_etcutTrk_xs45_L1XS55_dphi2j15xe20 | 28.51±0.05 |
| e13_etcutTrk_xs45_L1XS60 | 20.80±0.04 |
| e13_etcutTrk_xs45_L1XS60_dphi2j15xe20 | 20.01±0.04 |
| e20_etcutTrk_xs45_L1XS45_dphi2j15xe20 | 38.76±0.05 |
| e20_etcutTrk_xe30_dphi2j15xe20 | 64.77±0.05 |

Table 4.2: Integrated efficiencies of W tag&probe triggers relative to a $W \to e\nu$ selection.

The corresponding rates (Table 4.3) are estimated by emulating the trigger selection over a sample of events triggered first by the L1_EM6_XS45 (50, 55, 60) which selects electromagnetic cluster with $E_T$ >6 GeV and XS>4.5 (5.0, 5.5, 6.0). The number of accepted events is scaled to the corresponding L1 rate. The final output rate is calculated as before (Equation 4.1).

In order to investigate the single trigger performances in detail, the efficiency distributions are analyzed with respect to various kinematic quantities. Figure 4.5 shows the appropriate efficiency versus

[83] An accidentally high $E_T^{miss}$ cut was applied for all L2 xs triggers so that events with a missing transverse energy of above 80 GeV could pass only (fixed since run 203719). Since run 204416, a L2 rate reduction of about 25 % was achieved due to an additional L2 $E_T$ cut (11 GeV for e13_etcutTrk_xs60 chain and 18 GeV for e20_etcutTrk_xs60 chain).

| Trigger chain | L1 rate [kHz] | L2 rate [Hz] | EF rate [Hz] |
|---|---|---|---|
| e13_etcutTrk_xs60_dphi2j15xe20 | 7.5 | 360 | 2 |
| e20_etcutTrk_xs60_dphi2j15xe20 | 1.5 | 270 | 2 |
| e13_etcutTrk_xs45_L1XS50_dphi2j15xe20 | 2.8 | 150 | 11 |
| e13_etcutTrk_xs50_L1XS50_dphi2j15xe20 | 2.8 | 150 | 6 |
| e13_etcutTrk_xs45_L1XS55_dphi2j15xe20 | 1.1 | 70 | 6 |
| e13_etcutTrk_xs45_L1XS60 | 0.4 | 30 | 20 |
| e13_etcutTrk_xs45_L1XS60_dphi2j15xe20 | 0.4 | 30 | 3 |
| e20_etcutTrk_xs45_L1XS45_dphi2j15xe20 | 1.5 | 270 | 9 |

Table 4.3: W tag&probe trigger rates given at an instantaneous luminosity of $6 \times 10^{33}\text{cm}^{-2}\text{s}^{-1}$.

the transverse momentum, $p_T$ (right), and the position in $\eta$ (left) of the selected offline medium electron candidate. Corresponding statistical uncertainties are derived assuming binomial distributions. As expected, the behavior in $\eta$ is flat for all triggers regarded. Also the $p_T$ spectra show the typical slope commonly passing into a plateau at around 70 GeV. Obviously, the overall efficiencies for the triggers involving the high xs cut of 6.0 at EF level (visualized in blue and red) are lower than those with the improved selection criteria applied. So, increasing the $E_T^{miss}$ significance requirement at L1 and the reduction of the appropriate EF threshold in particular show the desired efficiency recovery (comparing the violet and yellow distributions to the blue, for instance).

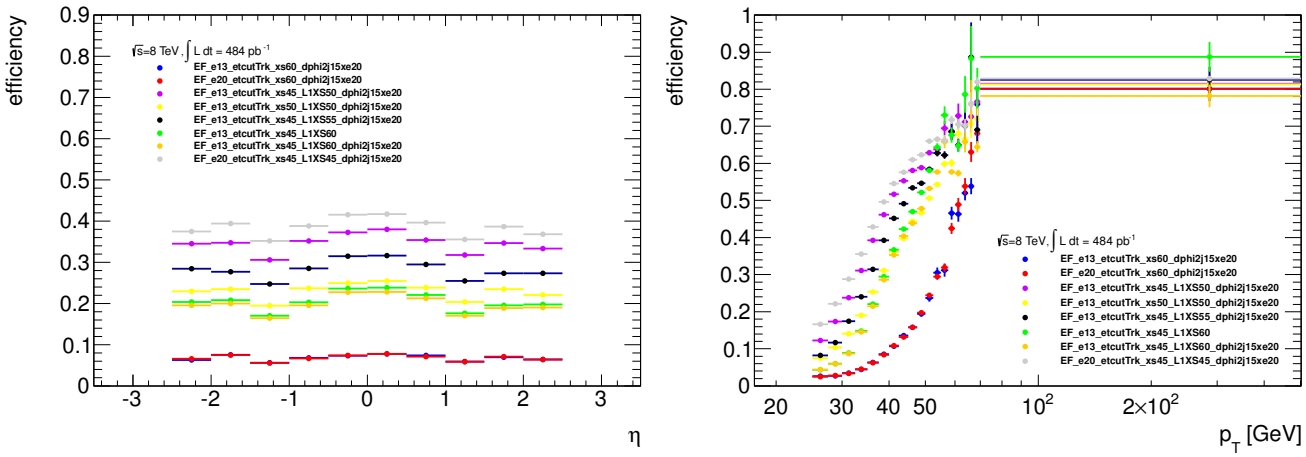


Figure 4.5: Trigger efficiencies relative to a $W \to e\nu$ identification as a function of $\eta$ (left) and the transverse electron momentum of the offline electron (right).

The efficiencies as functions of the offline missing transverse energy, $E_T^{miss}$, and xs are shown in Figure 4.6 whereby an $E_T^{miss}$ significance parametrization as described in Equation 4.3 has been used for the latter (with parameters $a = 0.5$ and $b = 0$). Both, the $E_T^{miss}$ (left) and xs (right) distributions also show the predicted slopes and saturate, as expected, for higher values in a plateau. The different behavior of the e13+xs60 triggers is visible, too, and confirm the statements before. All efficiencies obtained include a correction due to the trigger prescales since these triggers are not executed in re-run mode.

The effect of pile-up on the trigger efficiency has been studied additionally by measuring the efficiency as a function of the number of reconstructed primary vertices relative to the $W \to e\nu$ identifi-

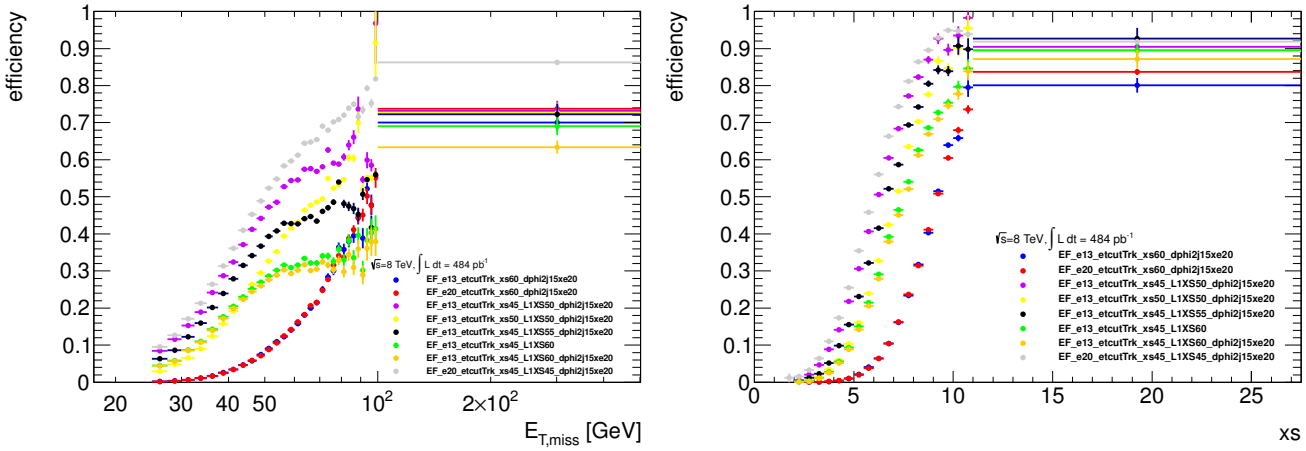


Figure 4.6: Trigger efficiencies with respect to a $W \to e\nu$ identification as a function of the offline missing transverse energy, $E_T^{miss}$, (left) and the $E_T^{miss}$ significance, denoted as xs (right).

cation (Figure 4.7). As expected, a strong dependence is visible in form of a steeply falling efficiency curve whereby the trigger efficiency could be recovered at least by introducing the increased $E_T^{miss}$ significance cuts at L1 and lowering the appropriate `xs` cut values at EF level. Also obvious, increased threshold requirements at EF or L1 lead to slightly lower overall efficiencies, as it can be expected.

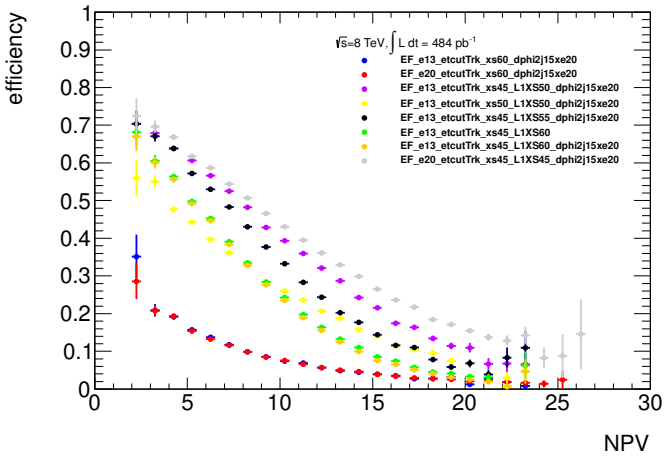


Figure 4.7: Efficiencies of W tag&probe triggers relative to a $W \to e\nu$ identification as a function of the number of primary vertices.

After these performance studies, the `e13_etcutTrk_xs45_L1XS55_dphi2j15xe20` with a high overall efficiency of $\sim 28.5\%$ and low L1 and L2 rates, has been finally kept unprescaled while all other `xs` triggers were disabled.
The `e20_etcutTrk_xe30_dphi2j15xe20` trigger with an overall efficiency of about 64.8% has been kept for later cross-checks of the $E_T^{miss}$ significance, too.

# 5 Selection Criteria

At hadron colliders like the LHC, SM W bosons are produced through quark coupling vertices and decay afterwards hadronically or leptonically. Due to a large amount of QCD jet background processes, leptonical decay channels involving an electron or a muon, for instance, together with the appropriate neutrino partner in the final state, provide the cleanest signature. As the muon efficiency and thus, the related energy resolution are less efficient compared to that for electron signatures, this dissertation simply focuses on the latter only. In fact, the s-channel production of a SM W boson may lead to a highly energetic electron detectable within the central region of the ATLAS detector. Therefore, searching for new physics in final states with one electron and high missing transverse energy, SM W decays constitute the main background and have to be reconstructed as exactly as possible. So, aiming for a signal efficiency as high as possible while ensuring a reasonable background subtraction, certain selection criteria are needed to reduce at least the remaining background sources. Since also further electroweak processes have not reducible contributions like those of top production [84], especially so-called QCD processes as mis-identified jets originating from multi-jet events or semi-leptonic hadron decays are of particular interest. Selection requirements should reduce these processes as much as possible while keeping them assessable. Also sources of non-conformances as failures in the electromagnetic calorimeter should be mostly excluded.
The event selection is grouped in two major sections, following the common ATLAS W′ performance: a pre-selection ensuring a good data quality, and specific requirements on the particles found within the remaining events to select possible electron candidates. With an additional cut on the missing transverse energy, mainly W decay like processes are detected. Table 5.4 shows the event reduction due to various selection requirements exemplified by the observed data set. The criteria themselves are described in detail afterwards. The total impact of applying such a selection as described is visualized in addition in the $\eta$-$\phi$ phase space for the whole data set recorded in 2012 whereby the data includes all events relevant for physics with at least one electron having a transverse momentum of above 110 GeV (Figure 5.2).

## 5.1 Quality Criteria

To ensure high quality, the recorded data has to fulfill already certain requirements while data acquisition. The following paragraphs concern not only general conditions like stable collisions, but also correction factors resulting for subsequent analyses.

### Data Acquisition and “Good Runs Lists”

The data acquisition at the LHC is splitted into various data periods, namely periods A to M in 2012 [85], whereby the recorded luminosity, respectively the amount of recorded data, increases with time. Each period itself is subdivided into single runs each acquiring data within about six hours. In addition, these sections are ordered in so-called luminosity blocks whereby one block is defined as an interval of two minutes. To ensure full efficiency of each detector component, control histograms

[84] Due to well-known cross-sections and its comparably small contribution
[85] Up to and including period M, data with an integrated luminosity of about $L_{int} \approx 20\,\text{fb}^{-1}$ has been recorded.

are created permanently, showing the operating status of single parts. In case of failures, a prompt reaction in form of fault removal or at least notification in subsequent analyses follows [86].
Various analysis groups monitor and summarize these criteria within a separate list known as "Good Runs List" (GRL), including all data runs relevant for physics and taken under good beam and detector quality conditions such as the presence of a stable magnetic field [87].
In addition, the recorded data events are grouped within various streams depending on the fired triggers they originate from [88].

### Trigger

As already described in Section 3.2.6, the trigger system of ATLAS comprises three different levels (before the LS1). At the first, namely L1, calorimeter data is read out using a coarser granularity. Different aspects like the presence of one or two clusters, minimal (missing transverse) energy thresholds or the isolation of certain energy depositions may be required to distinguish and preselect different trigger signatures or possible regions of interest. The following high level trigger system (HLT) regards these regions under inclusion of further restrictions, using the full calorimeter granularity. Required energy thresholds raise, thereby, from one trigger level to another to ensure a fully efficient trigger activity and to avoid the loss of events possibly passing subsequent selections. So, the HLT thresholds are increased compared to the L1 requirements to leave the behavior during the initial slope of certain triggers out of consideration for energy measurements. Also possible deviations in the energy scales due to the transition between hardware (L1) and software (HLT) based data formats might be avoided by those varied (increased) thresholds.

The subsequent analysis is based on events selected by an unprescaled trigger [89] called `EF_g120_loose` that refers to trigger decisions on event filter level ("EF"). The appropriate precedent levels are, namely, the `L1_EM30` and `L2_g120_loose` triggers. So, at L1, electromagnetic clusters ("EM") comprising energy depositions exceeding a minimal transverse energy threshold of 30 GeV per object passing, are regarded only and the interesting regions are passed on to the HLT. At L2 and EF, the trigger requires already the presence of an electromagnetic cluster with an energy corresponding to an electron transverse momentum of above 120 GeV and at least a loose identification of selected particles (Sect. 3.4.3). The letter "g" in the trigger name refers to photon triggers, meaning no requirements on corresponding tracks are applied [90]. Inferences about the shower origin and thus, existing electrons, follow afterwards via analysis specific selection criteria like requirements on appearing tracks (Section 5.2) or the corresponding position in $\eta$ and $\phi$ (5.2). An advantage of the loose identification level is, in addition, the opportunity for further data-driven background determinations under usage of the signal trigger. However, while at L1, a peak rate of 7 kHz at an

[86] Via so-called express streams, randomly chosen events are reconstructed promptly (Tier-0). A first analysis of the corresponding runs is performed within 36 hours.

[87] This analysis uses the GRL named *data12_8TeV.periodAllYear_DetStatus-v61-pro14-02_DQDefects-00-01-00_PHYS_StandardGRL_All_Good.xml*.

[88] This analysis uses the so-called egamma stream that is defined to contain collision data with electron and photon candidates only.

[89] To not refuse events which might be interesting for a search of new physics scenarios, the usage of an unprescaled trigger is reasonable. In 2012, the EF_g120_loose is the unprescaled single photon trigger comprising the lowest energy threshold.

[90] The trigger, itself, uses the same identification algorithm for both, electrons and photons, with common requirements on the appearing shower shapes as the resulting showers are quite similar.

instantaneous luminosity around $7 \times 10^{33}\,\mathrm{cm}^{-2}\mathrm{s}^{-1}$ could be obtained at the beginning of 2012 runs, the rate was reduced at L2 (`L2_g120_loose`) to about 45 Hz and at EF (`EF_g120_loose`) to about 11 Hz.

Choosing a trigger together with a particular GRL, the expected integrated luminosity can be calculated with a tool named "ilumicalc" tool which has been provided by ATLAS, [91]. Based on a high rate L1 trigger and the used physics trigger, the calculated integrated luminosity for this analysis is about $20.3\,\mathrm{fb}^{-1}$ with a corresponding systematic uncertainty of 2.8 % [ATL11a] [92].

### TTC restart, LAr and Tile Error

Detector problems concerning noise bursts and defective liquid argon (LAr) cells are monitored per event. Also increasing fluctuations in high voltage due to the increasing luminosity are taken into account. A dedicated flag marks every event as "standard", "warning" or "error" while a set of 28 bits indicates additionally the reasons for the detector problems. So, for instance, if the LAr event flag shows values equal to two ("error"), events should be totally rejected. Especially in the treatment of the missing transverse energy, it is important to avoid mistaking noise as energy deposition within the calorimeter system. Figure 5.1 shows the values of the bit-mask in dependence of $\eta$ for the whole data set of 2012 recorded at a center-of-mass energy of $\sqrt{s} = 8\,\mathrm{TeV}$ and a corresponding integrated luminosity of about $L_{int} \approx 20\,\mathrm{fb}^{-1}$. The data set includes an underlying skim that requires events to have at least one electron with a transverse momentum of above 110 GeV.

Similar to the procedure concerning defective LAr cells, also in-activities (as tripped and unpowered tile modules) within the tile calorimeter are considered. While trips within the tile calorimeter are tolerable defects as the energy in an unpowered module is extrapolated from its neighbors, events with several consecutive unpowered (or not recording) tile modules are rejected by the GRL. Further data corruption from particular tile channels are listed per event. Thus, regarding each run and the corresponding luminosity blocks, events can be checked for saturation in a tile cell. To avoid those effects contributing falsely as missing transverse energy, the particular events are removed.

In addition to the previously mentioned effects, also events are rejected where a high energetic jet [93] points to the $\eta$,$\phi$ region of a hot tile calorimeter cell which has not been masked within the reconstruction of particular data runs [94].
However, a complete restart and reconfiguration of single detector parts may be needed as last resort without a total run-restart. This procedure may introduce larger dead-times to the experiment, thus, events with incomplete detector information can occur within a luminosity block following a

[91] https://atlas-lumicalc.cern.ch, Internal tool.

[92] In 2012, the L1_EM30 trigger is recommended for computing the fraction of delivered luminosity which ATLAS actually recorded. To account for dead-times or other interruptions, the fraction is calculated using the amount of triggered events before and after applying corresponding vetoes. However, any trigger having a high rate after prescale can be used, ensuring to keep the statistical uncertainty per luminosity block low.

[93] The jet should have deposit most of its energy in the Tile second layer.

[94] The following runs were affected: 202660, 202668, 202712, 202740, 202965, 202987, 202991, 203027, 203169 (data period B1 and B2).

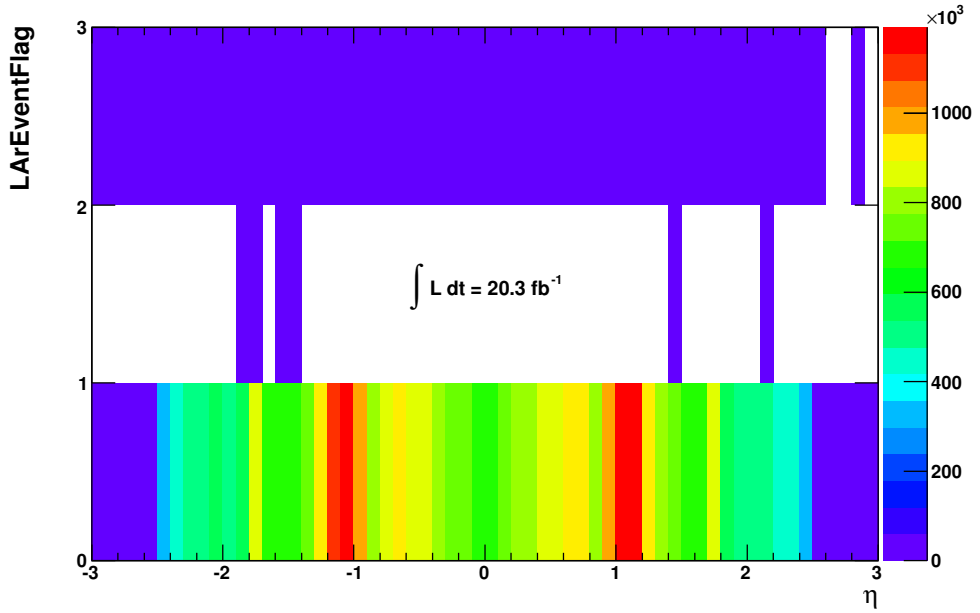


Figure 5.1: The so-called "LAr event flag" is shown in dependence of $\eta$ for the whole (skimmed) data set of 2012 (before selection cuts). Values equal to zero indicate "standard" detector conditions, those equal to one show already critical sections ("warnings"). Values equal to two indicate serious errors and the corresponding events should be rejected.

TTC [95] restart. In less than one percent of the regarded data set, those events occur and are removed completely from the analysis.

### Vertex Requirement

To ensure selecting particles only that originate from a hard scattering process, primary vertices with at least three tracks and a z-position within 200 mm from the center of the interaction point are taken into account. Primary vertices are, namely, those involving the highest transverse momentum of the outgoing particles in total (that is $\sum_i p_{T,i}$).

### Jet Cleaning

Taking a so-called "bad jet cleaning" into account, events are also rejected in case they include "bad" jets with a transverse energy of above 20 GeV. Here, a jet is denoted as bad if it originates mainly from hardware problems, bad beam conditions or cosmic rays and is, hence, not matched to a well-defined energy deposition within the calorimeter system. Requiring a particular set of cuts, a selection of such events is avoided and arising corresponding inefficiencies due to out-of-time pileup effects are reduced.

[95] Timing, Trigger and Control

### Debug Stream

Events not passing the HLT systems due to trigger timeout or crashes are recorded within a specific "debug stream". Running the whole performance on this particular stream as well, it can be ensured that none of these events would have passed the required selection criteria. Otherwise, the remaining events passing the HLT offline are reconstructed as for the normal physics streams [96].

## 5.2 Electron Selection

### Defective Detector Regions

Failures within beam periods can not always be removed promptly. Usually, breakdowns or interruptions of different detector components are repaired within longer shutdowns and have to be notified explicitly during data acquisition. Thus, physics analyses make use of a bit-mask consisting of 32 bits which is commonly known as "Object Quality Flag" (OQ flag). Cluster cells are monitored for each electron candidate and, in case of failures, the corresponding bit is set to unity. To refuse such particles with an energy deposition in a problematic detector region, the object quality is checked separately for each candidate in an event.

### Author Requirement

The "author" of a particle describes the place of its highest energy deposition and ensures that the corresponding reconstruction is consistent such that a given energy deposition in the calorimeter corresponds to an observed track. Requiring the corresponding bit-mask (namely "el_author") to be equal to unity or equal to three, it is ensured to have central electrons only, meaning electrons loosing their energy totally within the central region of the electromagnetic calorimeter. Thus, the so-called *eGamma* algorithm is used (Section 3.4.2).

### $\eta$ Requirement

In addition to the previous criteria, the allowed calorimeter regions are further constraint for definite particle identification. Since this analysis refers to the central region of the calorimeter, a pseudo-rapidity of a detected cluster of $|\eta_{cluster}| < 2.47$ is required. Due to a loss in the energy resolution, the calorimeter transition region between barrel and end-cap ($1.37 < |\eta_{cluster}| < 1.52$) is removed which is poorly instrumented only.

[96] The debug stream has been checked for all data periods but no events survived after applying a high transverse momentum threshold criteria.

### $p_T$ Requirement

Since SM W decays are the dominant background processes, the W resonance should be visible for a better estimation in the transverse mass spectrum (even in case of a search for new high mass states). But, as a trigger with a threshold of 120 GeV is used, selected electron candidates are required to have at least a transverse momentum of above 125 GeV. To avoid the initial trigger slope and to ensure a fully efficient trigger activity, a value within the trigger plateau is chosen. Even the previously mentioned aspect of keeping the W resonance visible is not fulfilled, the right tail of the spectrum remains still visible and the background well assessable.
In addition, the transverse momentum is corrected in order to adjust the cluster energy to the corresponding track position. In case of at least four hits in SCT and pixel detector, the energy in the transverse plain is defined as:

$$E_T = \frac{E_{cluster}}{\cosh(\eta_{track})} \tag{5.1}$$

where $E_{cluster}$ is the magnitude of the energy deposition (corrected according energy calibration and resolution 5.5) and $\eta_{track}$ denotes the $\eta$ position of the corresponding track [97].

### EM Identification

To ensure a good quality of particle identification, electron candidates of the remaining events have to fulfill at least an identification based on medium criteria (Sect. 3.4.3). The background reduction efficiency is about 95 %.

### Impact Parameters

The remaining particles should pass the detector as close to the primary vertex as possible to guarantee the origin in a hard scattering process of proton-proton collisions. Therefore, the electron candidates are required to have a track position within 5 mm along the beam axis and a radial distance to the reconstructed interaction point smaller than 1 mm.

### Triggermatching

To ensure that the chosen trigger has been fired certainly by a particular object, meaning that the object has indeed passed the trigger, a triggermatching is applied. Since a photon trigger is used, first, all photon trigger objects are analyzed that have passed the trigger. Afterwards, a so-called $\Delta R$ matching is performed matching electron objects to the photon objects. The $\Delta R$ is defined as $\Delta R = \sqrt{\Delta\eta^2 + \Delta\phi^2} < 0.15$ whereby $\eta$ and $\phi$ of the cluster position is used for both electrons and photons (since photons do not have any track information). The cut value of 0.15 is derived to achieve a high matching efficiency and thus, a stable requirement according to the event filter can be expected.

[97] In case of more than three hits in SCT and pixel detector, the track position in $\eta$ and $\phi$ is used; otherwise, those of the cluster.

### Electron Isolation

To reduce, for instance, the background contamination out of QCD events further, the remaining electron candidates are required to have an isolation energy less than a particular threshold varying with the corrected transverse energy of the electron. It is: $(E_{iso} < (0.007 * E_T + 5.))$ with $E_{iso}$ and $E_T$ in GeV. This dependence has been derived in order to ensure an overall efficiency for real electrons of above 90 % [98]. The isolation energy refers to the sum of all energy depositions (transverse energies respectively) within a cone of $\Delta R < 0.2$ around the central cluster deposition whereby the energy corresponding to the electron candidate is not taken into account. The latter is determined within a window of $3 \times 7$ ($5 \times 5$) calorimeter cells of the barrel (end-caps). The derived isolation energy is corrected, in addition, with respect to soft processes and a certain leakage of the central electron energy into the surrounding cone. Thereby, the correction according energy depositions out of pileup interactions is based on the amount of primary interaction points of an event [99].

### Electron Veto

Additionally to the previous cut selection, also events are rejected if a second isolated electron with a transverse momentum of above 20 GeV and medium identification is present. The cut value is lowered for further electron candidates in order to refuse also events out of QCD or Z decay processes.

## 5.3 $E_T^{miss}$ Criteria

To select mainly SM W decay-like processes, a missing transverse energy of above 125 GeV is required [100]. The cut value is chosen symmetrically to the lepton momentum since a neutrino momentum in the absence of new physics can be expected to balance the lepton contribution.

## 5.4 Blinding - Additional $m_T$ Requirement

Regarding events with low transverse masses only, no new physics scenarios should be visible. Therefore, to ensure a stable performance and to demonstrate a good understanding of all effects expected within the SM, just events with transverse masses below 400 GeV are considered firstly [101].

[98] The procedure is chosen identically to the ATLAS dilepton working group [ATL14a] (for electrons with the highest transverse momentum).

[99] The common isolation energy calculation is provided by an official ATLAS tool, https://twiki.cern.ch/twiki/bin/view/AtlasProtected/CaloIsolationCorrections.

[100] The $E_T^{miss}$ calculation is performed with aid of the "METUtility" tool described in Section 3.4.4 and based on the MET_RefFinal_et definition.

[101] This procedure is known as "blinding".

| selection cuts | events | fraction [%] | w.r.t. triggered events [%] |
|---|---|---|---|
| pre-selection | | | |
| Egamma stream | 732026805 | N/A | N/A |
| Skimm | 39265109 | 5.36 | N/A |
| GRL | 37479324 | 95.45 | N/A |
| Trigger | 29316613 | 78.22 | N/A |
| Vertex | 29312071 | 99.98 | 99.98 |
| Hot Tile Calo | 29312070 | 99.99 | 99.98 |
| Jet cleaning | 29217444 | 99.68 | 99.66 |
| Tile error | 29217441 | 99.99 | 99.66 |
| LAr error | 29155323 | 99.79 | 99.45 |
| TTC restart | 29155297 | 99.99 | 99.45 |
| Tile Trip Reader | 29155295 | 99.99 | 99.45 |
| electron specific cuts | | | |
| Author | 29150321 | 99.98 | 99.43 |
| Central $\eta$ | 29149470 | 99.99 | 99.43 |
| Crack excluded | 29123118 | 99.91 | 99.34 |
| OQ check | 29121060 | 99.99 | 99.33 |
| $\lvert d_0 \rvert < 1\,\text{mm}$ | 29024478 | 99.67 | 99.00 |
| $\lvert z_0 \rvert < 5\,\text{mm}$ | 28881198 | 99.51 | 98.51 |
| $p_T > 20\,\text{GeV}$ | 27481176 | 95.15 | 93.74 |
| $p_T > 125\,\text{GeV}$ | 20047164 | 72.95 | 68.38 |
| EM identification | 1480944 | 7.39 | 5.05 |
| Isolation | 710075 | 47.95 | 2.42 |
| Trigger matching | 709905 | 99.98 | 2.42 |
| Electron veto | 669543 | 94.31 | 2.28 |
| selection | | | |
| $E_T^{miss} > 125\,\text{GeV}$ | 25433 | 3.80 | 0.09 |
| $m_T < 400\,\text{GeV}$ | 22887 | 89.99 | 0.08 |

Table 5.1: Overview of selection criteria exemplified by the data selection. The event numbers shown in the table demonstrate those data events passing the corresponding cut. The fraction in % shown in the third column is calculated relatively to the previous cut. The last column shows the remaining amount of events with respect to all triggered events.

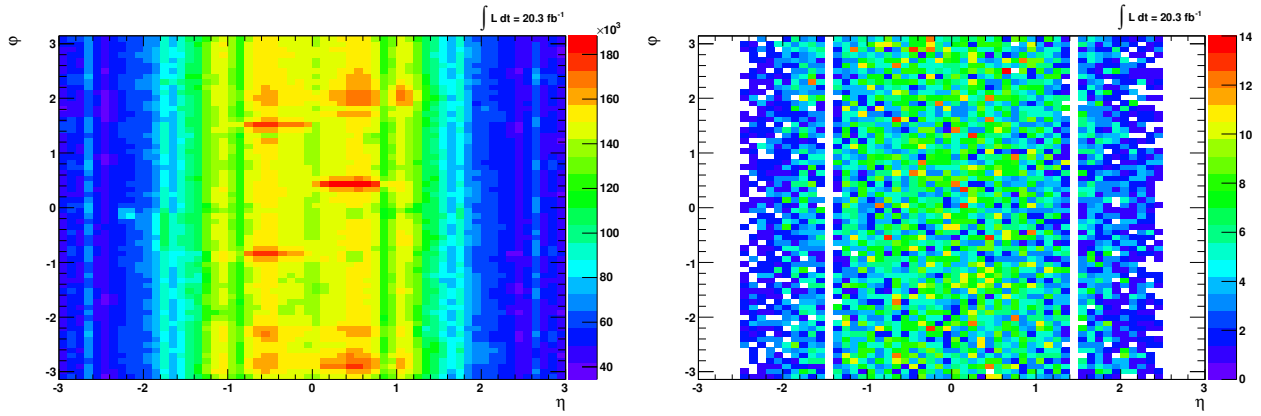


Figure 5.2: Two-dimensional $\eta$,$\phi$ spectrum before (left) and after final event selection (right) derived by the whole data set of 2012. The latter one is shown for events in a potential signal region ($m_T > 252\,\text{GeV}$). The data set includes an underlying skim that requires events to have at least one electron with a transverse momentum of above 110 GeV. The energy scale has been corrected as described in Section 5.5. The exclusion of the barrel-endcap transition region is visible for $1.37 < |\eta_{cluster}| < 1.52$.

## 5.5 Correction Factors

Different effects appearing while data acquisition as well as those due to the difficulty of simulating complex physical processes, have to be corrected subsequently with aid of various correction factors. Comparing energy measurements in the calorimeter systems to the reproduction via Monte Carlo simulations, a need for data recalibration and corrections of the simulated data sets becomes obvious. Also effects like multiple proton-proton collisions per bunch-crossing have to be accounted for and will be explained in the following.

### Pileup and Vertex z-position Reweighting

Due to the high instantaneous luminosities obtained during the LHC data taking periods, multiple proton-proton collisions per bunch-crossing can be detected (Sect. 3). Besides hard scattering processes which are used for physics analyses, there are also additional interactions in the same bunch-crossing possible, namely (in-time) "pile-up" events [102]. In fact, these events lead to further tracks and additional energy depositions within the calorimeter system. To involve those effects correctly also in Monte Carlo simulations, the data acquisition is monitored within an average number of interactions $< \mu >$. By an additional scaling of that certain $< \mu >$ in case of the simulation sets, the average activity of an event can be reproduced [103]. But however, due to a difference in the beamspot size along the beam line between data and Monte Carlo simulations [104], a larger amount of merged

[102] "Out-of-time" pileup refers to events leaking from one bunch crossing into the following so that the signal of an incident particle of interest superimposes with that of another passing the calorimeter cells regarded a few bunch-crossing before or after.

[103] Characteristic distributions of that average activity are shown for the different data periods of 2012 data taking in the appendix, Section A.5.

[104] With a $\sigma_z$ of 66 mm in MC, compared to data 47 mm.

vertices and a reduction of reconstructed vertex multiplicities (namely $N_{vtx}$) in data compared to MC follows. Thus, the pileup vertex distributions do not agree well but a further scaling would cause an underestimation of the event activity [105]. Figure 5.3 compares the effect due to pileup reweighting in case of the average interactions per bunch crossing (left) to that for the number of primary vertices (right), exemplified for the prediction out of W decays to electrons and tauons with large missing transverse energy involved, before and after applying selection criteria. The bottom panels show the appropriate data to MC ratios and visualize the deviation due to applying the correction weights. In both cases, the corrected distributions demonstrate an improved agreement to the measured data values. In fact, in the peak regions, an improvement of up to 1.5 % can be reached, while it is even larger regarding the tails.

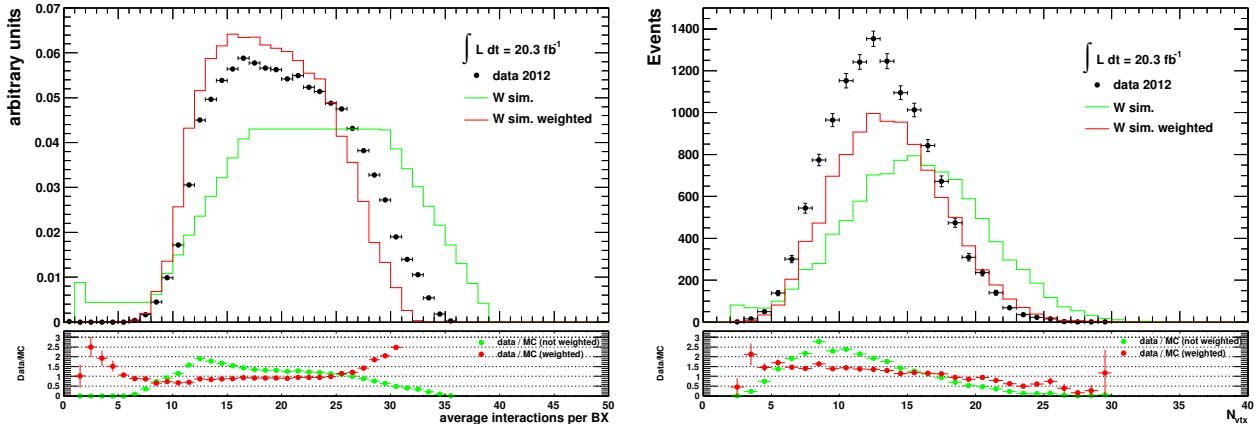


Figure 5.3: Average interactions per bunch crossing (left) in data compared to the prediction out of W decays to electrons and tauons before any selection criteria applied. The distributions are normalized to unity. The right side shows the number of primary vertices in data compared to the prediction out of W decays to electrons and tauons after final selection for events with $m_T > 252\,\text{GeV}$. The effect due to pileup reweighting is demonstrated.

To account also for differences in the z vertex position distributions between reconstructed data and Monte Carlo simulation sets, a further reweighting is applied. The effect is shown in Figure 5.4 for W decay processes involving electrons in the final state (not taking pileup reweighting effects into account) before any selection criteria are applied. Obviously, both distributions follow a Gaussian shape but with a deviation in the distribution width. An additional comparison is shown in the appendix (Sect. A.5) comparing data to the prediction out of W decays after all selection requirements have been applied.

### Energy Corrections in Data and MC

Comparing energy measurements in the calorimeter systems to the reproduction via Monte Carlo simulations, a need for data recalibration and corrections of the simulated data sets becomes obvious. On the basis of reconstructed Z or J/Ψ resonances and E/p studies of isolated electrons out of W

[105] The common pileup reweighting procedure is provided by an official ATLAS working group, https://twiki.cern.ch/twiki/bin/viewauth/AtlasProtected/ExtendedPileupReweighting.

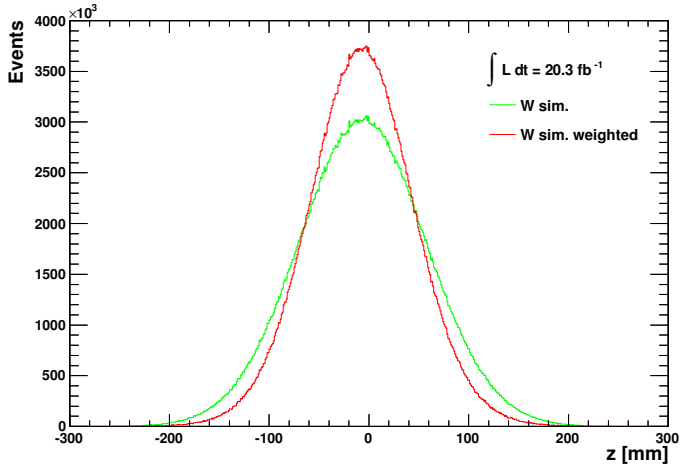


Figure 5.4: Vertex reweighting. The figure shows the z position of the primary vertex before any selection cuts. The distributions are derived by W decays to electrons and tauons and scaled to an integrated luminosity of $20\,\mathrm{fb}^{-1}$. Pileup reweighting is not applied.

boson decays, a correction factor can be evaluated in dependence of $\eta$, $\phi$ and the measured (uncorrected) cluster energy [ATL14f]. The true (corrected) energy value follows as $E_{true} = \frac{E_{measure}}{1+f}$. Fitting the invariant mass distribution of both, simulations and recorded data, within different $\eta$ bins, the deviation around the mass peak and thus the correction factor can be derived. Calibration constants known from previous data taking periods had been applied already in 2012 Monte Carlo production. Multiple calibration iterations during the whole data acquisition result, therefore, in small rescaling factors only.
To account in addition for an underestimation of the energy resolution in Monte Carlo simulations, the (simulated) energy values are smeared by the aid of a normal distribution. The effect lies within a few percent and can be applied similarly to the calibration correction using a tool provided by the Electron-Gamma Combined Performance group [106].

Figure 5.5 visualizes the effects of data rescaling and energy smearing of the analysis background simulation sets, exemplified for the prediction out of W decays to electrons and tauons after applying the final event selection. Obviously, the difference between the rescaled data distribution (green points) and that obtained directly (black points) is nearly negligible small. The bottom panel shows the deviation due to energy smearing as ratio of the scaled data distributions to the smeared (pink), respectively not smeared (gray) MC predictions. Also here, the difference is small but at least up to nearly half a percent in the peak region.

[106] egammaAnalysisUtils-00-04-46, Internal tool.

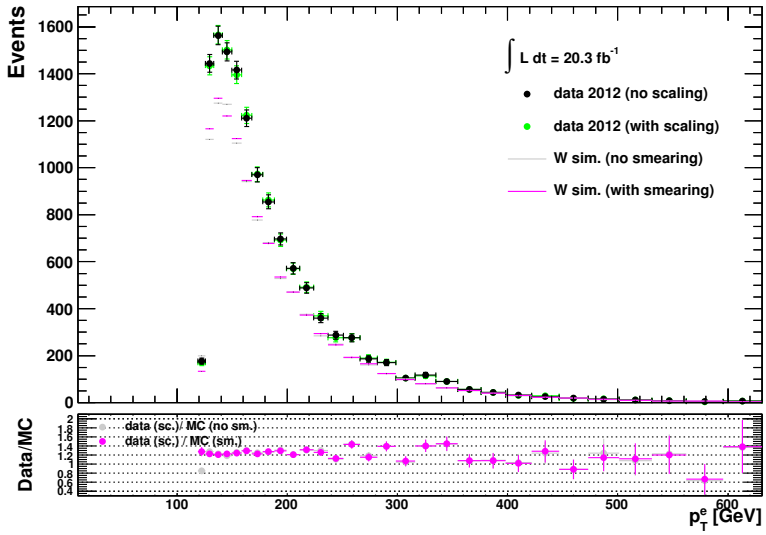


Figure 5.5: Spectrum of the transverse electron momentum after final event selection. The effects of data rescaling and energy smearing in Monte Carlo simulations are visualized.

### Identification, Reconstruction and Trigger Scales

To further correct instrumentation inefficiencies related to the particle identification and reconstruction, or the required trigger, the corresponding efficiencies are determined in different tag-and-probe methods. These regard known resonances such as those of Z, J/$\psi$ or W decays with at least one electron in the final state (performed by the Egamma working group [ATL14e]).

Due to the dependence of electron shower shapes on both, the corresponding candidate energy and the material traversed before reaching the calorimeter, the efficiency factors are derived in bins of $\eta$ and the transverse energy $E_T$ (one bin from 7 to 10 GeV and eight bins of 5 GeV from 10 to 50 GeV) as fraction of candidates passing a particular selection [107]. A fine binning in $\eta$ comprises, thereby, 50 bins with a granularity of 0.1 [ATL14e].

By combining the different decay channels (that are statistically independent), the precision of the measurements can be increased. Comparing the efficiency distributions so obtained in data to those simulated separately for the different decay channels, discrepancies arise that originate mainly in mismodelling of shower shapes and increase with the tightness of applied selection criteria. To correct for these, so-called scale factors are obtained bin-wise as data-to-MC ratios.

Exemplified by the Z tag&probe analysis, the procedure of deriving the identification scale factors shall be described. Within the Egamma working group, the related measurements were performed up to a transverse energy of 50 GeV due to limited statistics, so that the W′ working group had to derive scale factors in a similar way for a medium identification in correspondence with an isolation requirement of electron candidates carrying high transverse momenta ([ATL14d]). This dis-

[107] Low $E_T$ measurements up to $E_T$ <20 GeV are dominated by J/$\psi$ statistics while a higher statistical precision is achieved in the higher transverse energy region by Z/W tag&probe measurements. Systematic uncertainties on the scale factors due to the MC generator choice are, commonly, assumed to be negligible.

sertation uses the scale factors as derived for the official W′ performance. Thereby, the baseline selection concerns reconstructed electron candidates triggered by the `e24vhi_medium1`and the `e60vhi_medium1` respectively in the central $\eta$ region (crack excluded). Selected events are required to have at least one primary vertex with at least three corresponding tracks and at least two electrons having a transverse momentum of above 25 GeV and passing object quality criteria. One of the electron candidates has to fulfill a tight identification and should be matched to the applied triggers (so-called *tag* electron). Requiring the second (opposite charged) electron to pass further trigger (`g120_loose`) and track quality requirements (so-called *probe* electrons), pairs with an invariant mass between 80-100 GeV are considered only and the identification efficiency is evaluated as follows: $\varepsilon = \frac{N_{probespassingselection}}{N_{allprobes}}$. Since no additional identification criterion is applied to probe electrons, the arising background contribution has to be subtracted. Therefore, opposite sign tag and probe pairs are constructed whereby the probe fails specific identification cuts. Subtracting the original Drell-Yan contribution between 120-180 GeV in the corresponding invariant mass tail, the resulting template is scaled afterwards to data luminosity.
The final scaling factor is defined as the ratio of data to Monte Carlo efficiencies and amounts a few percent [108].

Using the eGamma algorithm as described in Section 3.4.2, electrons depositing an energy of at least 2.5 GeV within the central layer of the calorimeter are reconstructed [109]. The efficiency or probability to reconstruct such an electron or energy cluster respectively, is measured for both data and simulated Drell-Yan processes. The final reconstruction corrections are derived by the Egamma working group and follow as ratio of data to MC efficiencies. In general, they are close to unity [ATL14e].

In addition, a so-called trigger scale factor is derived using the Z tag&probe method as described before. The tag electron has to fulfill tight identification criteria whereas the opposite charged probe electron should be isolated and follows medium identification requirements. Electron pairs with an invariant mass between 80-100 GeV are considered only and, since a quite clean sample of electrons follows, no further background subtraction is needed. Varying the baseline selection such as tightening or loosening the tag selection or varying the invariant mass window for electron pairs, the central efficiency values are derived as average. Calculating in addition the root mean square (RMS) of baseline and all variations the corresponding systematic uncertainties are determined [ATL14d]. The final efficiency is then obtained as the ratio of probe electrons passing the `g120_loose` trigger compared to all selected probes.

Finally, the single scaling factors are combined by multiplication and result in an overall correction of a few percent.

The stability versus reconstruction and trigger efficiencies is demonstrated in appendix Section A.3.

[108] Due to limited statistics, the correction factor could be derived up to 400 GeV; for values above, the scaling factor of the previous bin is used.

[109] To talk about electron candidates, the energy cluster has to have a corresponding track pointing towards its position within $0.05 \times 0.10$ in $\Delta\eta \times \Delta\phi$.

# 6 Background Determination

As already described before, selecting events with one high momentum electron plus high missing transverse energy, SM W decays constitute the main background. The next largest that can have real missing transverse energy and isolated leptons arises due to so-called diboson (WW, WZ, ZZ) decays, followed by $t\bar{t}$ and single top production which is most important for describing low transverse masses. Z boson decays where one lepton could not be reconstructed and is therefore mimicking real $E_T^{miss}$ result in a minor background contribution. Strong-interaction processes such as heavy-flavour decays or misidentification of jets as electrons contribute as so-called multi-jet or QCD background. Due to their complexity and the difficulty to generate a sufficient amount of events, these processes are, in contrast to the previously mentioned electroweak background processes, estimated out of data via a so-called matrix method. The others are estimated with aid of Monte Carlo simulations that are explained in the following.

## 6.1 Simulated Processes

The simulated data sets utilized are listed in detail in the appendix (Section A.1). Typical cross-sections and the corresponding integrated luminosities are listed for each background sample in the appendix, Table A.1.
In order to compare subsequently the simulations of various processes expected due to the SM to the observed data distributions, a scaling of the simulation sets to the corresponding data luminosity is needed. Therefore, an additional weight is applied event-wise, accounting not only for the underlying process cross-section but also for the restrictions made while generating. It is:

$$w_{lumi} = \frac{L_{int}^{data}}{L_{int}^{MC}} = L_{int}^{data} \frac{\sigma B \cdot \varepsilon_{fil}}{N_{gen}} \tag{6.1}$$

Here, $L_{int}^{data}$ denotes the integrated luminosity corresponding to the regarded data set and, accordingly, $L_{int}^{MC}$ that of the used Monte Carlo simulation. The latter is derived by the amount of generated events devided by the appropriate cross-section and the related branching fraction. The restrictions to the process simulated with a specific generator are taken into account as additional filter efficiency $\varepsilon_{fil}$.

### W Background

Selecting events with one high momentum electron plus high missing transverse energy, SM W decays constitute the main background. Besides direct decays into an electron and a neutrino, also processes involving tauons which decay further into an electron and a neutrino, are considered. To ensure enough statistics, Monte Carlo simulations are generated separately for various invariant mass ranges and combined afterwards. For invariant masses below 200 GeV, not only data sets including all invariant mass and transverse momentum ranges but also simulations including all mass regions but filtered for different ranges of the lepton transverse momentum are used in addition. All samples utilized are generated on next-to-leading order (NLO) using a Powheg implementation interfaced with Pythia 8 (short: “PowhegPythia”) including a full detector simulation via GEANT4.

They are corrected afterwards to next-to-next-to-leading order (NNLO) using k-factors provided by the ATLAS W′ performance group [ATL14d]. So, higher order electroweak and QCD corrections like final state radiation of a photon are accounted for (Section 3.3.1). For common event generation, the mass of a SM W boson is assumed to be 80.399 GeV with a resonance width of 2.085 GeV [110]. Finally, the distributions derived separately for each mass region are scaled to an integrated luminosity of $L_{int} \approx 20.3\,\text{fb}^{-1}$ as described before. The correct treatment of the single simulation sets is shown in Figure 6.1 demonstrating a smooth transition between each contribution. Additional control histograms are shown in the appendix (Section A.3).

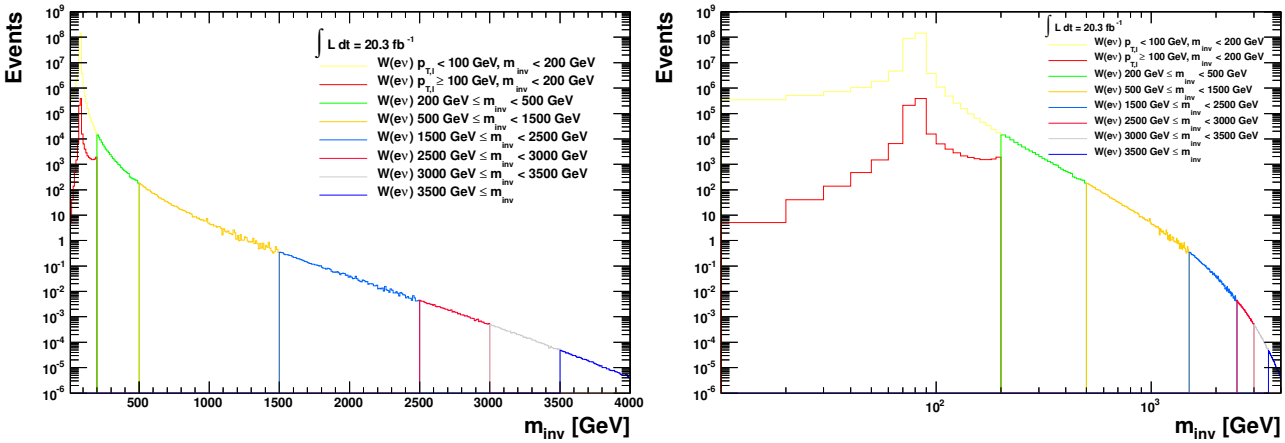


Figure 6.1: Spectrum of the invariant mass before selection (truth level) (left: linear, right: logarithmic notation). The distributions of the single mass filtered simulation sets are shown in particular, demonstrating a smooth transition between each contribution. Below 200 GeV unfiltered and $p_T$ filtered samples are combined. For better visibility, only direct decays to electrons and neutrinos are shown.

[110] These parameters are common to all event generators, except PYTHIA6 and Pythia8 where the width is calculated perturbatively.

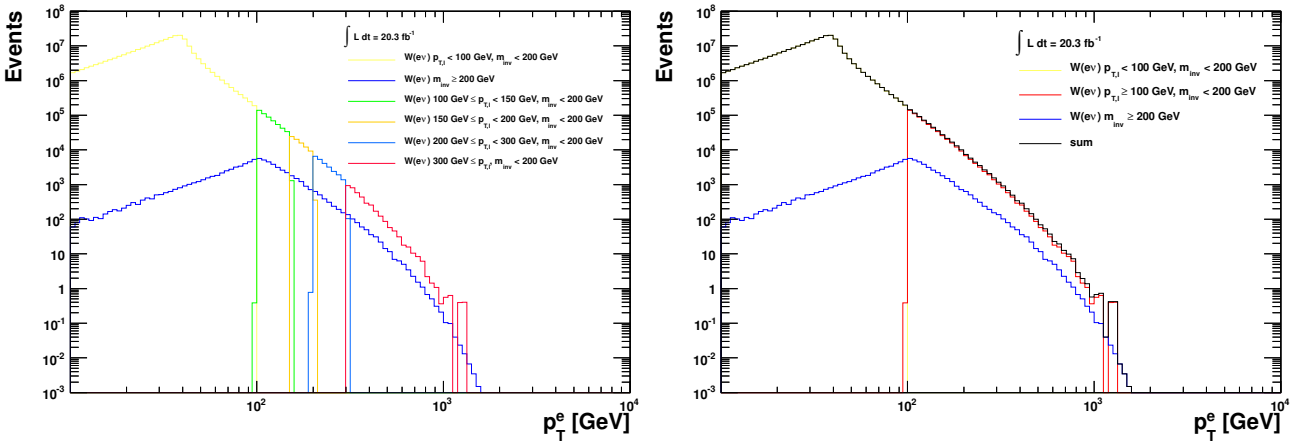


Figure 6.2: Spectrum of the transverse electron momentum before selection (truth level). The distributions of the single $p_T$ binned simulation sets in combination with unfiltered samples for $m_{inv}$ below 200 GeV are compared to the contribution of all mass filtered simulations. The right side shows explicitly the summed contributions due to mass filtered, $p_T$ filtered and unfiltered (used below 200 GeV only) samples and visualizes the resulting background contribution in total as black curve. For better visibility, only direct decays to electrons and neutrinos are taken into account.

## Z Background

A minor background contribution refers to SM Z boson decays where one lepton has not been reconstructed and is therefore mimicking real missing transverse energy. Here, not only direct decays into two electrons but also those into two tauons are considered, since one of the tauons can decay in turn involving a highly energetic electron (and two neutrinos $\nu_e$, $\nu_\tau$) while the other one decays hadronically.
Similar to the background out of SM W decays, also the contribution corresponding to neutral Drell-Yan (DY) processes is combined out of various mass and $p_T$ binned simulation sets. Data sets including all invariant mass and transverse momentum ranges for neutral DY processes are also used for invariant dilepton masses below 250 GeV whereas $p_T$ filtered simulations are taken additionally into account in case of electron decays only. All samples utilized are also generated on NLO with PowhegPythia, including a full detector simulation (GEANT4), too. For MC production, the Z boson mass is assumed to be equal to 91.1876 GeV with a resonance width of 2.4952 GeV [111]. Applying separate k-factors [ATL14d] as event weights, the single distributions are corrected to NNLO as well (Sect. 3.3.1). The final contributions are derived separately for each mass region and scaled to an integrated luminosity of $L_{int} \approx 20.3\,\text{fb}^{-1}$. The correct treatment of the single simulation sets is demonstrated in Figure 6.3. As already seen for the SM W background, a smooth behavior can be recognized for the transition between each contribution.

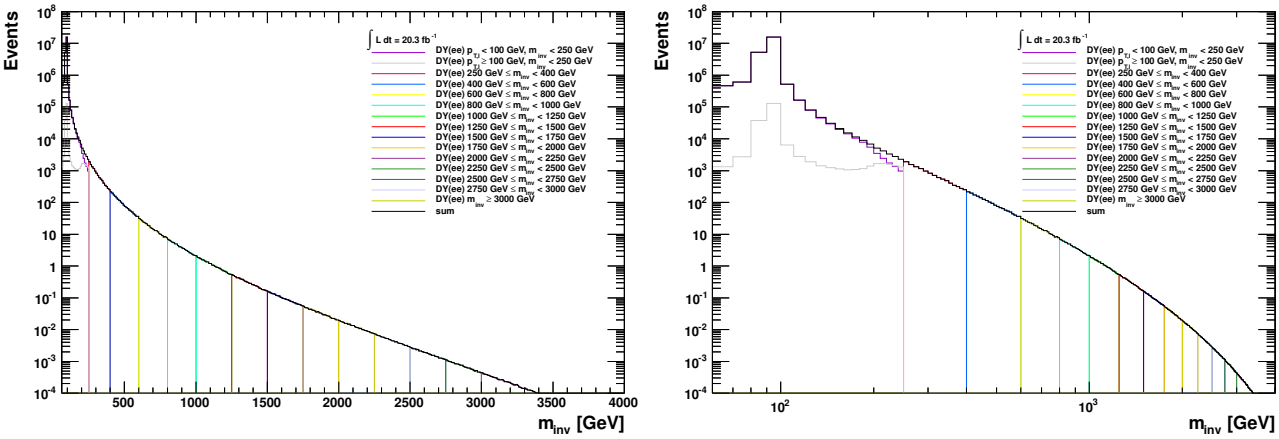


Figure 6.3: Spectrum of the invariant mass before selection (truth level) (left: linear, right: logarithmic notation). The distributions of the single mass filtered simulation sets are shown in particular; below 250 GeV unfiltered and $p_T$ filtered samples are combined. For better visibility, only DY processes with two electrons in the final states are shown (meaning no $Z \to \tau\tau$ decays contribute here).

[111] These parameters are common to all event generators, except PYTHIA6 and Pythia8 where the width is calculated perturbatively.

### Dibosons

After regarding the contributions due to single SM W or Z decays, processes including two SM vector bosons (SM W or Z) are considered. In general, these are known as "diboson" events, refering to processes like $pp \to V_1V_2 + X$ (where $V_i$ denote a SM W or Z). The corresponding production mechanisms are demonstrated in Figure 6.4 including s-, t- and u-channel. Besides leptonical decays only, also scenarios including a leptonically decaying boson and a hadronically decaying are considered. Therefore, final states involving up to four electrons can be detected whereby electrons can arise either out of direct decays or indirect via tauons. In contrast to the previously mentioned simulated backgrounds, the corresponding Monte Carlo simulations are not split into various mass or $p_T$ ranges. Sherpa is used as event generator providing processes in (N)LO.

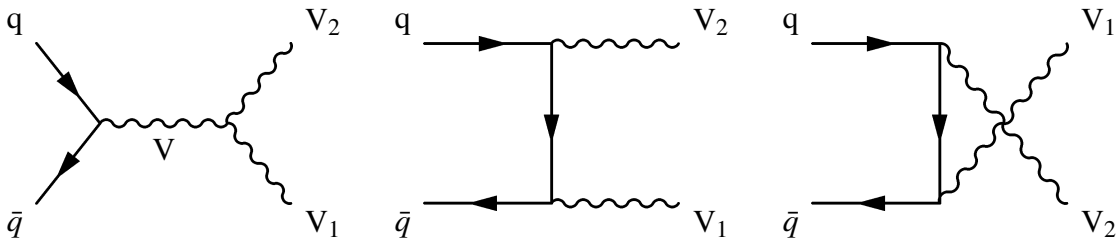


Figure 6.4: Diboson production in LO. The s-channel, t-channel and u-channel are shown, whereby $V_1$, $V_2$ and V denote the SM bosons W, Z or $\gamma$.

Figure 6.5 shows the diboson contributions taken into account for further analysis steps. Both, the distributions due to the single diboson background sources as well as the sum of all are visualized.

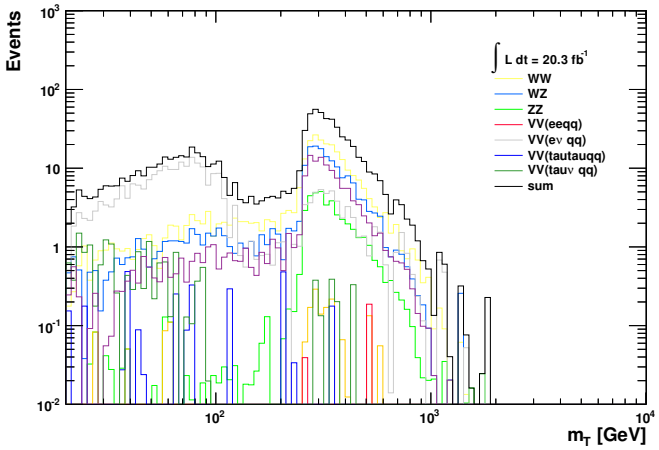


Figure 6.5: Spectrum of the transverse mass after selection.

Additional diboson candidates which are considered within the SM are selected via so-called $W\gamma$ (or $Z\gamma$) production processes, namely $pp \to \ell\nu\gamma + X$ with ($\ell = e, \mu$), $pp \to \ell^+\ell^-\gamma + X$ and $pp \to \nu\bar{\nu}\gamma + X$. They include the production of SM W (or Z) bosons not only in context of photon bremsstrahlung

from SM W (or Z) decays, but also in context of photon radiation from initial-state quarks or directly from W bosons. Also photons from fragmentation of secondary quarks and gluons into isolated photons are considered [ATL13a]. The single mechanisms are visualized in Figure 6.6. Since s-, t- and u- channel are included already in the previously described diboson samples and the final state radiation is also considered within the applied k-factor corrections of the SM W background, the contribution due to fragmentation is neglected and the $W\gamma$ simulations are not taken into account for further analysis steps to avoid double-counting effects.

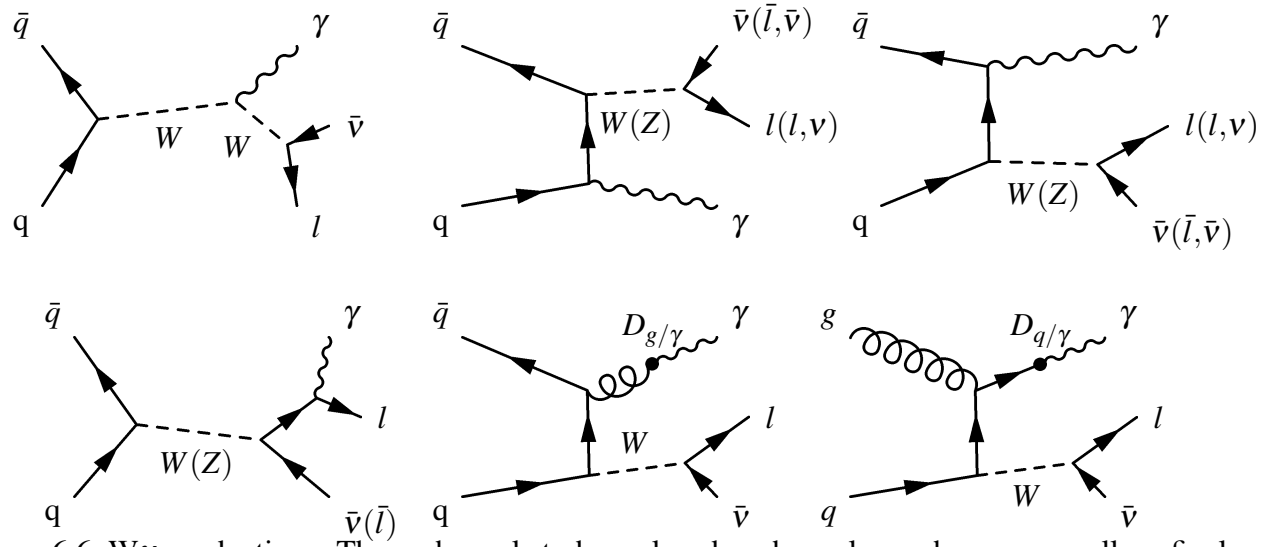


Figure 6.6: W$\gamma$ production. The s-channel, t-channel and u-channel are shown, as well as final state photon radiation from W decay processes and contributions from fragmentation processes.

### Top Background

In general, top quarks decay via weak interaction, emitting a SM W together with a bottom-, strange- or down-type quark. To estimate the resulting background contribution, not only top pair production from strong interaction effects [112] but also single top quarks produced due to weak interactions are considered. The mechanisms causing the latter processes are shown in LO in Figure 6.7. The s-channel refers to quark-antiquark annihilation to a top-antibottom pair via a SM W boson whereas a bottom quark annihilates a gluon and decays afterwards into a SM W and a top quark in the Wt-channel. The t-channel instead embraces two processes: Once an incoming bottom quark (mostly originating from gluon decays) transforms into a single top quark via radiation of a SM W, or the incoming bottom interacts with a gluon via a top quark propagator emitting a SM W and a top. However, background contributions include both, electrons from direct SM W boson decays as well as those originating from top-quark decays.

[112] Top-antitop pairs have their origin in highly virtual gluons out of pp collisions and build the most frequent form of top production.

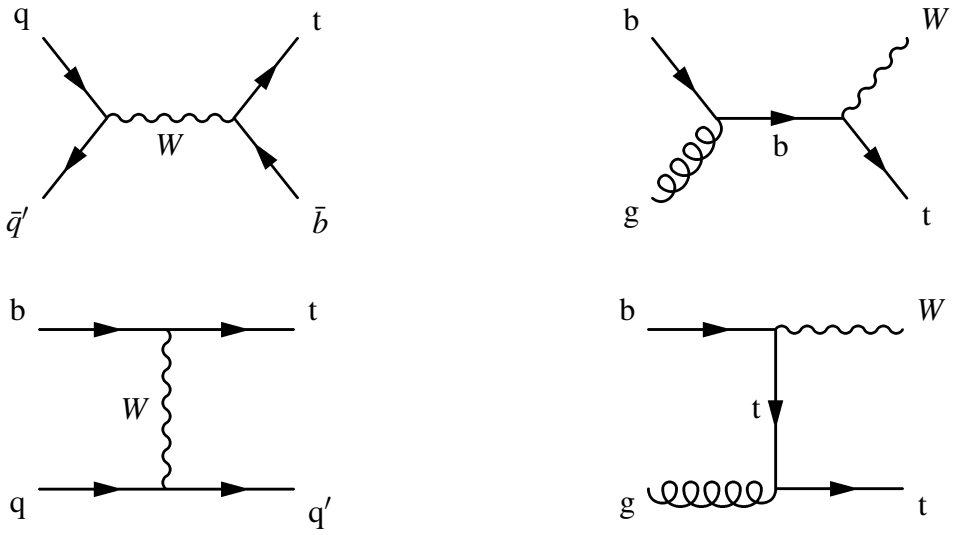


Figure 6.7: Single top production in LO. The s-channel, Wt-channel (top left and right) and t-channel (bottom) are shown.

Regarding processes in NLO, contributions due to top pair and single top Wt-channel production interfere. This can cause problems in case the initial states with two gluons or a quark-antiquark should be distinguished (Figure 6.8). Therefore, in contrast to other background contributions, top event generators mainly make use of a MC@NLO method that avoids double-counting due to initial states [Nas12]. Here, MC@NLO generates NLO matrix elements that are combined with information about multiple particle interactions provided by Jimmy. Particularly derived event weights avoid double-counting of final states according to NLO matrix elements and NLO radiation corrections [113] (Sect. 3.3).
However, top pair processes are generated using PowhegPythia whereas single top s- and Wt-channel events are simulated with MC@NLO and Jimmy. AcerMCPythia is used in case of single top t-channel production. The top pair contribution due to PowhegPythia has been checked against that derived by MC@NLO and Jimmy but no significant deviation has been observed. The top quark mass is assumed to be equal to 172.5 GeV [114].

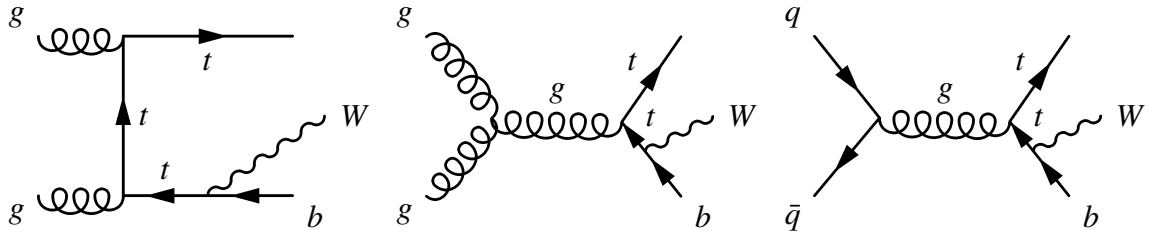


Figure 6.8: NLO contributions to Wt production.

Figure 6.9 shows the distributions due to the various top production mechanism considered as well as the resulting SM background contribution in total.

In contrast to the official W′ performance, the top contribution is extrapolated to higher masses due to missing statistics for events with a transverse mass above 1 TeV. Two different functional forms

[113] These weights are equal to $\pm$ unity.
[114] This parameter is common to all event generators.

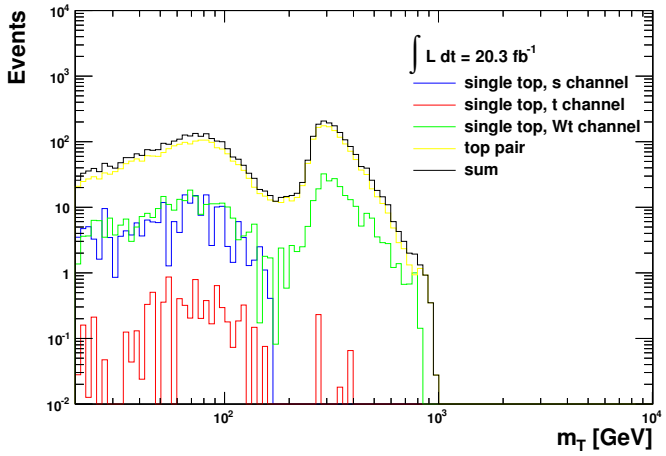


Figure 6.9: Spectrum of the transverse mass after selection.

are fitted to the background distribution and the derived result is stitched at 700 GeV to the original top spectrum. A function originally evaluated for dijet mass measurements

$$f_1 = a(1-x)^b x^{c+d\log(x)} \tag{6.2}$$

with $x = m_T/\sqrt{s}$ ($\sqrt{s} = 8$ TeV) and fitted in the range of 360 to 3000 GeV is used as baseline, whereby a power law function

$$f_2 = ax^b \tag{6.3}$$

with $x = m_T/\sqrt{s}$ and $\sqrt{s} = 8$ TeV is used as alternative. The variables $a$, $b$, $c$, $d$ denote constants varied in each fit anew while the fitting procedure is executed inductively using the derived parameters as starting point for further adjustments. A log-likelihood method is used for the estimates. In addition, the integral of the distribution in each bin is taken instead of the value at the particular bin center and errors estimation is performed using the MINOS technique ([Ead71], pp. 204-205). To estimate further systematic uncertainties on the fitting procedure itself, the fit range is varied up (400-3000 GeV) and down (320-3000 GeV). The final top background estimates derived for several choices of lower integration boundaries and the corresponding uncertainties are listed in Table 6.1. Figure 6.10 shows the different fitting approaches for varied fit ranges.

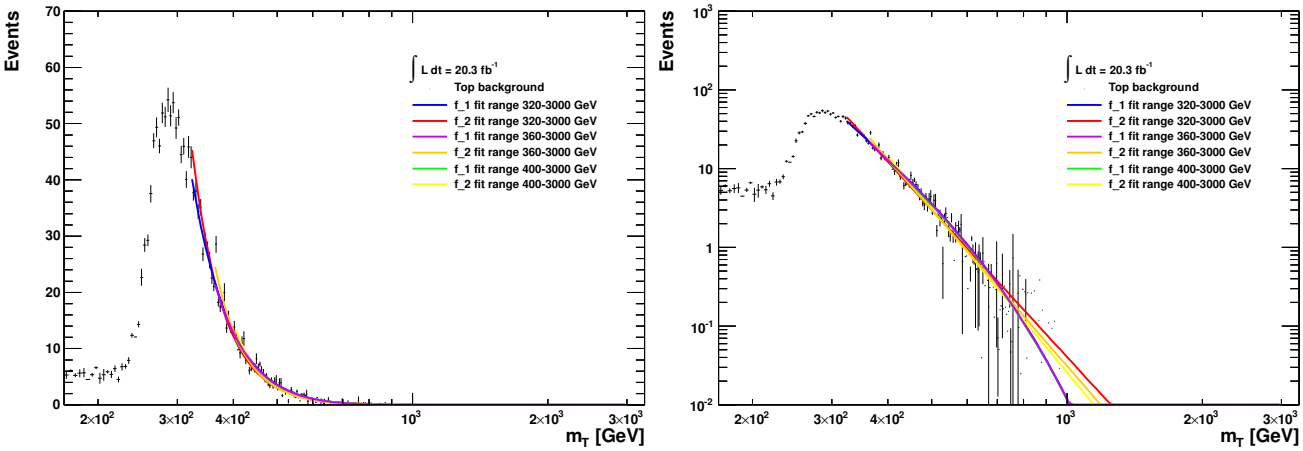


Figure 6.10: Transverse mass spectrum after final event selection (linear binning!). Two fitting approaches in different fit ranges are shown.

| $m_{Tmin}$ [GeV] | Top (w/o estimate) | Top estimate | Systematic fit uncertainties |
|---|---|---|---|
| 252 | 1522±17 | 1527±11 | 3.73 |
| 317 | 778±12 | 784±8.2 | 3.73 |
| 336 | 593±11 | 596±7.4 | 3.73 |
| 377 | 335±8.3 | 339±6.4 | 3.73 |
| 423 | 179±6.1 | 184±5.4 | 3.73 |
| 448 | 135±5.4 | 140±5.1 | 3.73 |
| 474 | 93.2±4.5 | 99±4.8 | 3.73 |
| 564 | 32.1±2.7 | 37.9±4.1 | 3.73 |
| 597 | 20.7±2.2 | 26.4±3.96 | 3.73 |
| 710 | 6.73±1.2 | 11.57±3.27 | 3.25 |
| 796 | 2.66±0.65 | 4.74±1.69 | 1.68 |
| 843 | 1.28±0.43 | 2.89±1.87 | 1.87 |
| 1002 | 0±0 | 0.52±1.41 | 1.41 |
| 1062 | 0±0 | 0.27±1.16 | 1.16 |
| 1191 | 0±0 | 0.06±0.72 | 0.72 |
| 1337 | 0±0 | 0.01±0.42 | 0.42 |
| 1416 | 0±0 | 0.004±0.31 | 0.31 |
| 1500 | 0±0 | 0.002±0.23 | 0.23 |
| 1683 | 0±0 | 0.0002±0.13 | 0.13 |
| 1888 | 0±0 | 0.00001±0.07 | 0.07 |

Table 6.1: Final estimates of the top background contribution for different choices of lower integration boundaries. The background is scaled to an data luminosity of about $20\,\mathrm{fb}^{-1}$. The listed systematics according the fit are obtained as maximum deviation while varying the fit range and function.

## 6.2 Data-driven Background - QCD

Due to its complexity, the SM background, consisting of particles mis-identified as electrons, is estimated via a data-driven matrix method. In contrast to real electron contributions, where the term "real" refers to electron candidates being identified as electrons, those mis-identified particles are denoted as "fakes". They can originate either out of multi-jet processes or semi-leptonic hadron decays into quark-antiquark pairs and arise mainly as mis-identified jets with certain topologies. Single $\pi^0$s, for example, that carry most of the corresponding jet energies, would decay nearly exclusively into two photons creating in turn electromagnetic showers. These showers closely resemble those induced by electrons and lead to a mis-identification of the corresponding jets. Since such neutral pions do not leave any track within the inner detector, it is sufficient to regard certain event selection and identification criteria to suppress these signatures. The matrix method takes use of this behavior and will be described in the following.

### Matrix Method

To estimate the number of fakeable objects, respectively the number of QCD events, the rate of events passing a looser electron identification is measured. Determining further the probability of these to pass also the tighter signal selection in comparison to the one derived for real electrons, the fake contribution can be calculated.
Measurable observables as the number of electron candidates passing the loose and/or tight criteria (denoted as $N_L$ respectively $N_T$) are related to the corresponding truth quantities $N_R$ (for real electrons) and $N_F$ (for fakes) as follows:

$$\begin{pmatrix} N_T \\ N_L \end{pmatrix} = \begin{pmatrix} \varepsilon_R & \varepsilon_F \\ 1-\varepsilon_R & 1-\varepsilon_F \end{pmatrix} \begin{pmatrix} N_R \\ N_F \end{pmatrix} \tag{6.4}$$

Since the truth quantities are not correlated, also the corresponding measurable observables are independent of each other. The looser criterion means therefore a loose identification without fulfilling also tight requirements (that is "loose but not tight"). The connecting matrix contains the probabilities for looser objects to pass also tighter requirements, concerning both real and fake particles. These efficiencies are defined subsequently:

$$\varepsilon_F = \frac{N_{tight}^{fake}}{N_{loose}^{fake}}, \qquad \varepsilon_R = \frac{N_{tight}^{real}}{N_{loose}^{real}}. \tag{6.5}$$

The QCD contamination is already given within the first line of Equation 6.4 whereby the amount of electron candidates passing the tight criteria is composed of real electrons and a contribution due to fakes:

$$N_T = \varepsilon_R N_R + \varepsilon_F N_F \,,$$

In addition, the truth quantities can be expressed by inverting the matrix (Equ. 6.4) so that:

$$\begin{pmatrix} N_R \\ N_F \end{pmatrix} = \frac{1}{\varepsilon_R(1-\varepsilon_F) - \varepsilon_F(1-\varepsilon_R)} \begin{pmatrix} 1-\varepsilon_F & -\varepsilon_F \\ \varepsilon_R - 1 & \varepsilon_R \end{pmatrix} \begin{pmatrix} N_T \\ N_L \end{pmatrix}$$

Via insertion, the amount of fake electrons passing the selection criteria, follows in dependence of measurable quantities only:

$$N_{QCD} = \varepsilon_F N_F = \frac{\varepsilon_F}{\varepsilon_R - \varepsilon_F} (\varepsilon_R(N_L + N_T) - N_T) \tag{6.6}$$

### Fake Rate Estimation

To receive a QCD enriched sample, specific cuts are required. In order to select not only jets matched to electrons ($\Delta R < 0.1$) but also to suppress events from SM W or Z decays, the missing transverse energy criterion is lowered (and inverted) to $E_T^{miss} < 25\,\text{GeV}$ and an additional requirement concerning the invariant dielectron mass applied ($|m_{ee} - m_Z| > 20\,\text{GeV}$ for electron pairs with loose identification and $p_T > 20\,\text{GeV}$). Furthermore, only events having one single medium identified electron with a transverse momentum of $p_T > 20\,\text{GeV}$ are selected. All other cuts are identical to the signal selection (except, of course, that for $E_T^{miss}$).

Applying these requirements not only to data but also to the Monte Carlo simulations of all SM background processes, the real electron contamination within the enriched sample is estimated. For determining the final fake efficiency, the latter is subtracted from the corresponding amount of fakes in data. Figure 6.11 shows the single contributions in comparison (left), the final efficiency in dependence of $\eta$ (upper right side) and the ratios of MC to data contributions (lower right side). Since the fake efficiency behavior is not constant in all ranges, an optimization is performed in $p_T$ and four broad $\eta$ bins. The four bins in $\eta$ are chosen with respect to the rate behavior: The lower covers the barrel region up to $|\eta| < 1.37$, the next reaches up to $|\eta| < 2.01$ (excluding the barrel-endcap transition region), followed by two broad bins splitting the endcap region further: $2.01 < |\eta| < 2.37$ and $2.37 < |\eta| < 2.47$. While the first two bins show a quite flat distribution in the same order of magnitude, an increase in the third bin indicates changed detector conditions as the transition radiation tracker does not cover this $\eta$ region any more. Regarding the outermost $\eta$ values, another increase in the amount of fake candidates accounts for the end of the innermost pixel detector. The corresponding $p_T$ dependencies are demonstrated in Figure 6.12 with respect to each $\eta$ bin.

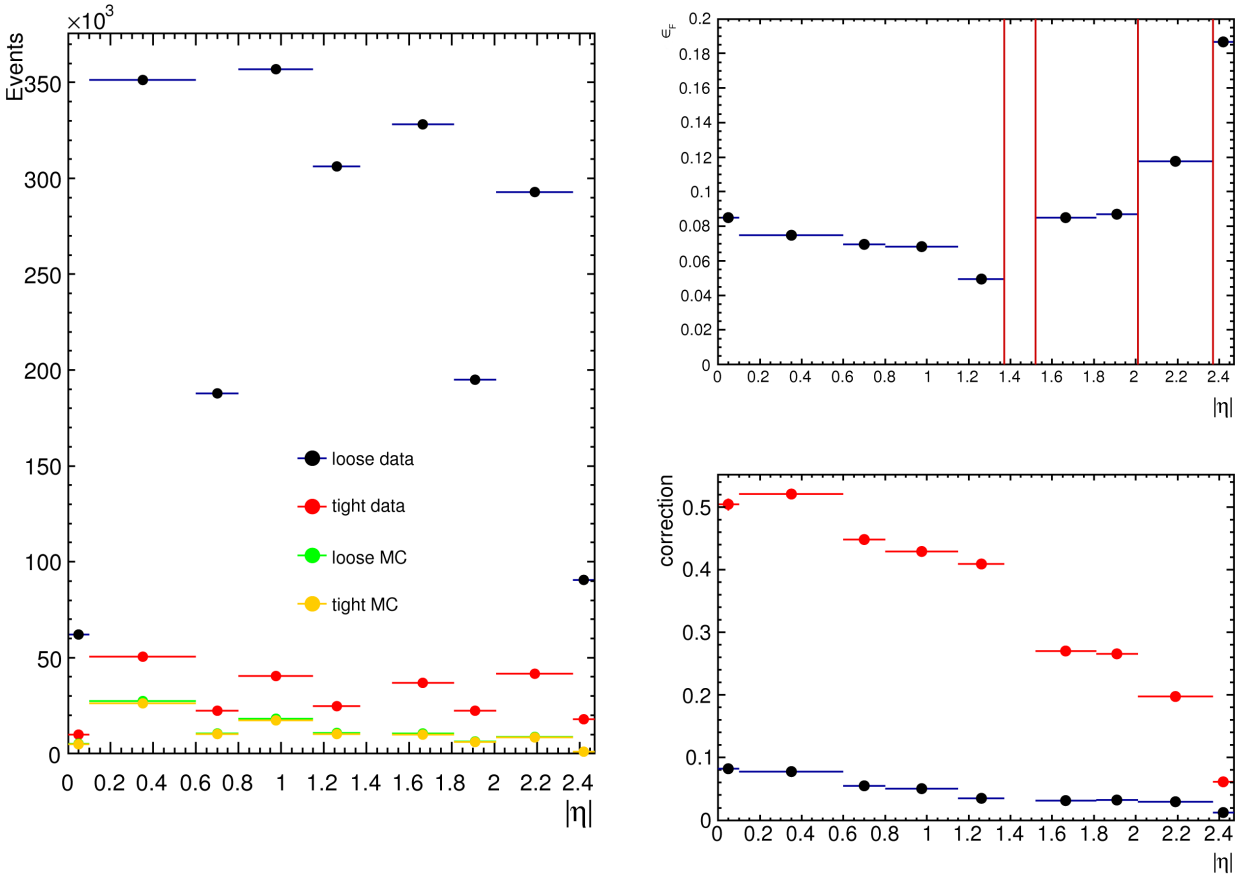


Figure 6.11: On the left side, the single contributions of (possible) fakes in data and simulated background processes (real electron contamination) are shown with respect to the loose and tight selection applied. The fake efficiency in dependence of $\eta$ is shown on the upper right side. The four red vertical lines indicate the course $\eta$ binning chosen for an optimization in $\eta$ and $p_T$. The lower right side demonstrates the correction that would need to be applied: The red markers show the MC-to-data ratio with respect to tight candidates whereas that concerning loose candidates is shown in black.

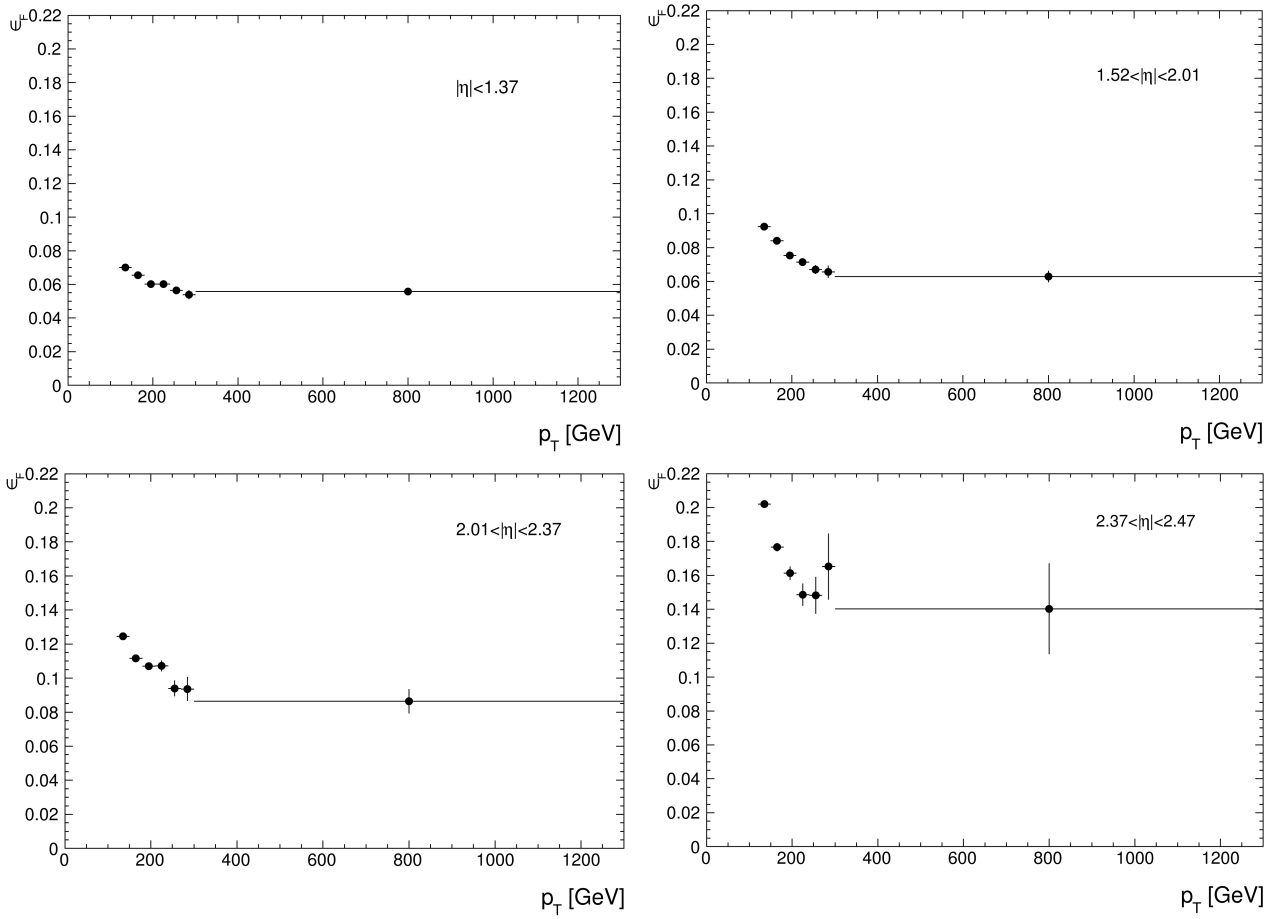


Figure 6.12: The $p_T$ dependence of the fake efficiency shown for different $\eta$ ranges.

### Real Efficiency Estimation

Counting real electron candidates passing the loose or tight selection, the real efficiency is obtained. To ensure to have indeed real electrons, W Monte Carlo simulations are used. In addition, a truth matching is applied matching a generated particle to the reconstructed electron candidate within $\Delta R$ <0.1. The resulting real efficiency is shown in Figure 6.13, its dependence in $p_T$ is demonstrated in Figure 6.14. The coarse $\eta$ binning is chosen identically to the fake efficiency estimation and visualized in Figure 6.13 as red vertical lines. Despite a slight drop in efficiency at a transverse electron momentum of about 250 GeV, the overall high efficiency indicates a good electron identification such that 5 % the highest of real electron candidates are rejected with the current selection criteria.

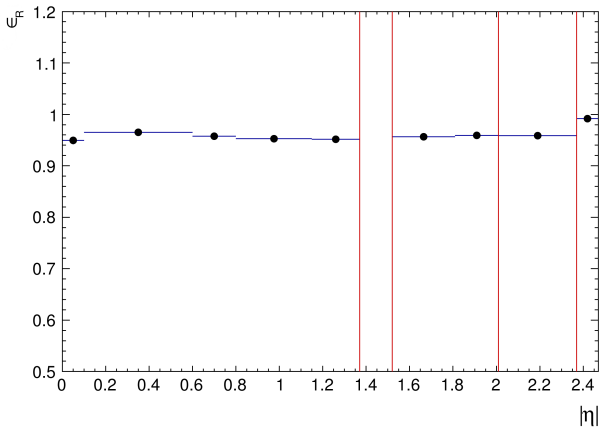


Figure 6.13: The real electron efficiency in dependence of $\eta$ is shown. The four red vertical lines indicate the course $\eta$ binning chosen for an optimization in $\eta$ and $p_T$.

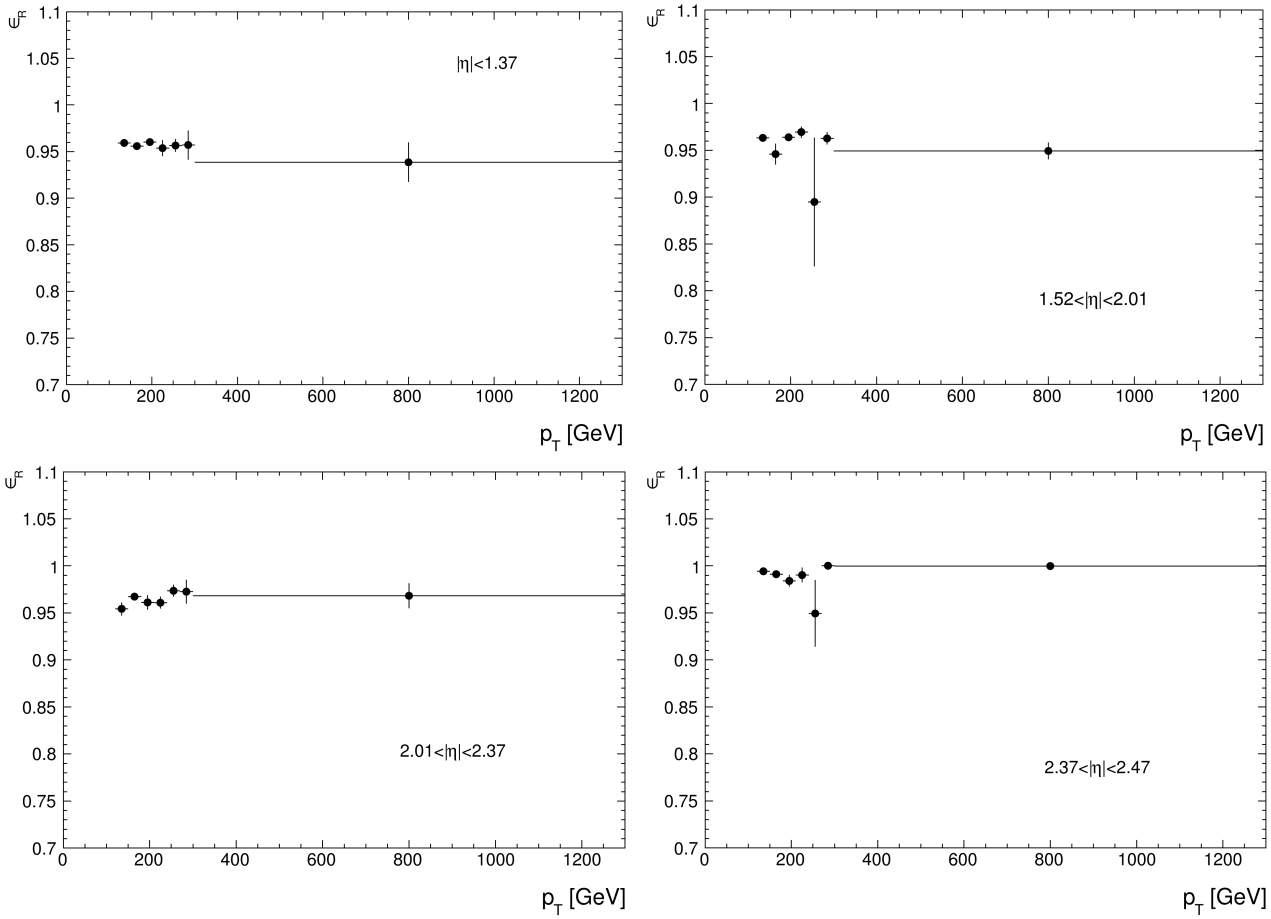


Figure 6.14: The $p_T$ dependence of the real electron efficiency shown for different $\eta$ ranges.

### Systematic Variations

Varying the cut selection for receiving the QCD enriched template, an estimation of the correlated systematic uncertainty can be obtained. In fact, the missing transverse energy requirement is varied up and down (35 GeV and 20 GeV respectively) as well as the choice of the invariant mass window to select electron pairs (10 GeV and 30 GeV respectively, or left out completely). In addition, also the impact of the electron veto rejecting events with more electrons having a $p_T > 20$ GeV, is investigated. The deviations of the resulting fake efficiency variations to the selection chosen as default are shown for all $\eta$ bins in Figure 6.15. As the varied missing transverse energy requirements and the statistical fluctuations have the largest impact, these are used for quoting the systematic uncertainty on the QCD contribution only.

### Estimation of the Transverse Mass Spectrum in QCD

In order to obtain the final QCD background distributions, the previously derived efficiencies are combined. Following Equation 6.6, weights result that are applied to the respective “loose not tight”

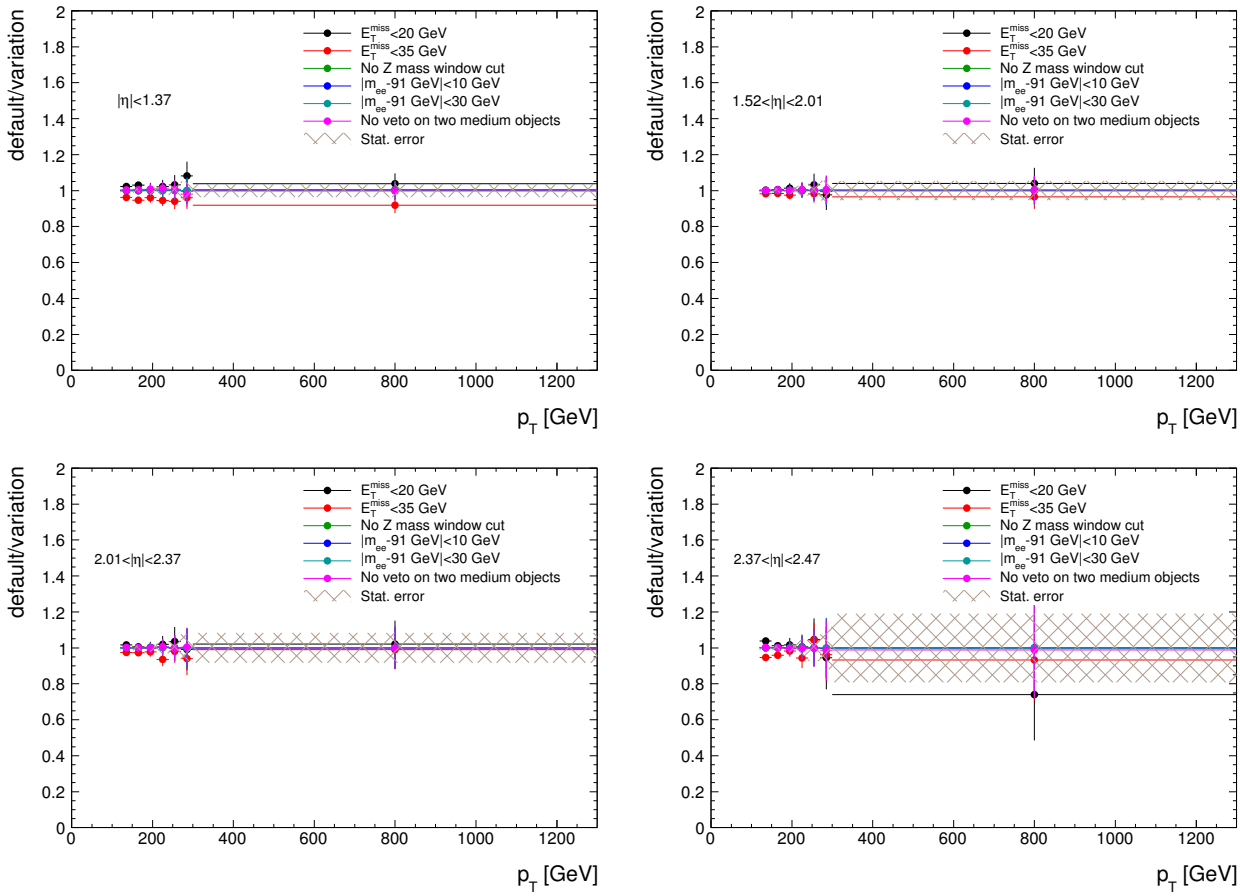


Figure 6.15: The deviations of the fake efficiency variations to the default selection are shown in dependence of $p_T$ for different $\eta$ bins. Also the impact of statistical fluctuations is demonstrated.

and tight candidates following the standard selection in data.

$$w_L = \frac{\varepsilon_F \varepsilon_R}{\varepsilon_R - \varepsilon_F}, w_T = \frac{\varepsilon_F (\varepsilon_R - 1)}{\varepsilon_R - \varepsilon_F} \tag{6.7}$$

Figure 6.16 shows the resulting QCD contribution in dependence of the transverse mass. The sharp edge at 250 GeV results due to the symmetrically chosen lepton $p_T$ and $E_T^{miss}$ cuts at 125 GeV and the related topologies. The expected falling behavior for higher transverse masses is also clearly visible (Sect. 2.2).

### Extrapolation to Higher Transverse Masses

Nevertheless, to account for the still low statistics of the QCD contribution, the need for an extrapolation to higher transverse masses arises. Similar to the top background, the final QCD distribution is derived by fitting two functional forms as described before. Also here, the power law function as

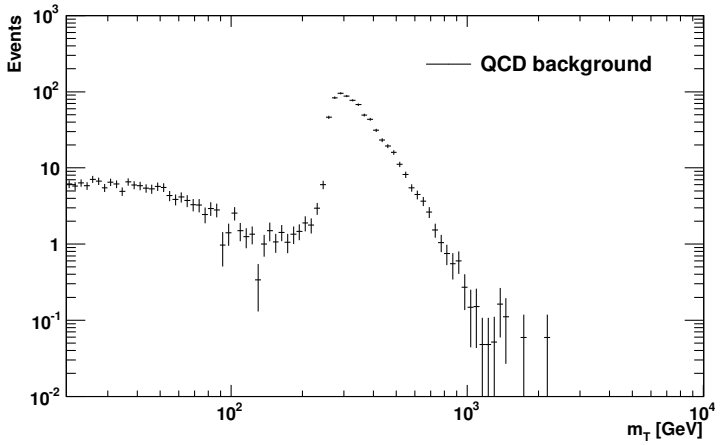


Figure 6.16: QCD contribution in the transverse mass spectrum showing the typical falling behavior in higher mass regions.

well as a modified version of that determined for dijet mass measurements are used. It is

$$f_1 = e^{-a} x^{b+c\log(x)} \tag{6.8}$$

with $x = m_T/\sqrt{s}$ ($\sqrt{s} = 8\,\text{TeV}$) the "dijet function" as baseline and the power law function

$$f_2 = ax^b \tag{6.9}$$

with $x = m_T/\sqrt{s}$ and $\sqrt{s} = 8\,\text{TeV}$ used as alternative. The variables $a$, $b$, $c$ denote constants varied in each fit anew using a so-called $\chi^2$ method. To ensure enough statistics needed for executing the $\chi^2$ method, the unweighted QCD contribution (that is without weights applied, Equ. 6.7) is adduced to find a binning guaranteeing a sufficient amount of events per bin. In addition to the different functional forms, various fit ranges are tested. Diversifying the lower fit border between 350 GeV and 700 GeV, and using a range of 600 GeV to 1200 GeV for the upper border, about 43 converged fits can be obtained. The mean of all converged fits is chosen as default and shown in Figure 6.17 (left) using one standard deviation as common uncertainty. Having a fit probability around 90 % for most of the succeeded fits (visible in Figure 6.17 (right)), a good description of the QCD background processes is ensured. The good agreement between fit and "raw" QCD distribution is, especially, obvious in a range of 400 GeV to 800 GeV and a corresponding small uncertainty band (due to enough statistics and thus, a well described distribution). At higher transverse masses, the existing amount of data points becomes less and thus, the corresponding uncertainties larger. That is also visualized in the fit uncertainty band since the fit values are now allowed to spread in a bigger range. The deviations for lower transverse masses are due to the original distribution shape caused by the high transverse lepton momentum and missing transverse energy requirements.
Stitching the fitted (default) distribution to the originally derived QCD contribution at a transverse mass of 850 GeV, the final QCD extrapolation can be determined (shown in Figure 6.18). Corresponding integrated numbers of QCD background events are listed in Table 6.2 for various integration intervals. The systematic uncertainties are splitted into their single sources and visualized in Table 6.3 with respect to various transverse mass regions, too. The given $m_T$ values denote the lower integration boundaries.

In addition to the previously discussed uncertainties of the matrix method itself, a comparison to an alternative method (called “Inverse Id” method) has been performed which is described in detail in the appendix (Section A.4). Slight deviations between both approaches are taken as further systematic uncertainty while evaluating the QCD estimation and are given in Table 6.3, too.

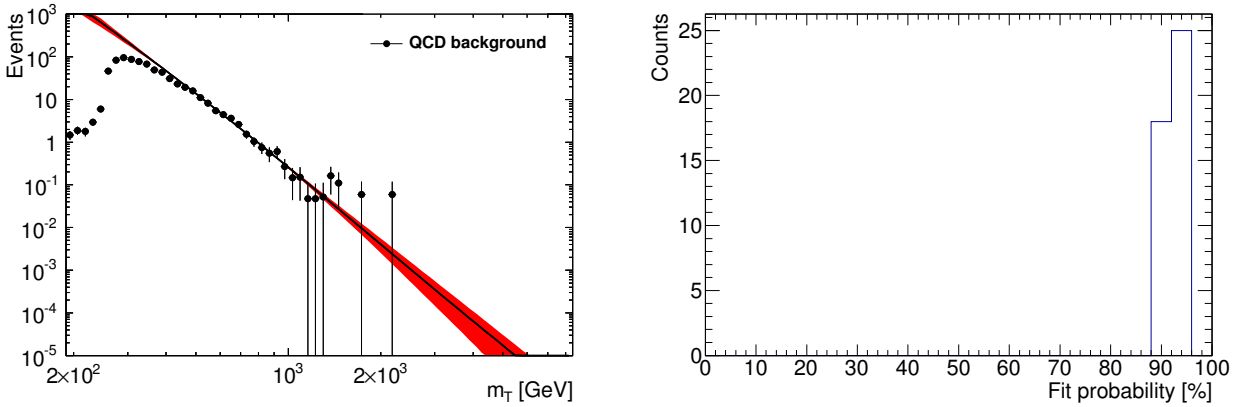


Figure 6.17: The mean of all converged fits is shown on the left side using one standard deviation as uncertainty; the related fit probability (shown on the right) demonstrates a good background description.

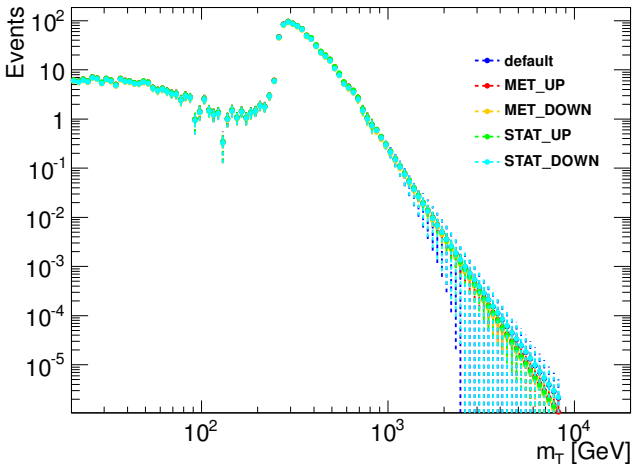


Figure 6.18: Final QCD contribution obtained by fitting the default distribution and stitching both (fit and default) at a transverse mass of 850 GeV. Distributions resulting in the same manner out of control region variations are shown, too.

| $m_T[GeV]$ | QCD background |
|---|---|
| 252 | $681.6 \pm 7.9$ (stat)$^{+75.1}_{-70.9}$ (total) |
| 317 | $368.7 \pm 5.6$ (stat)$^{+20.4}_{-14.0}$ (total) |
| 336 | $290.0 \pm 4.8$ (stat)$^{+18.2}_{-13.6}$ (total) |
| 377 | $173.6 \pm 3.6$ (stat)$^{+19.0}_{-17.3}$ (total) |
| 423 | $99.0 \pm 2.6$ (stat)$^{+17.0}_{-16.3}$ (total) |
| 448 | $76.0 \pm 2.3$ (stat)$^{+13.7}_{-13.1}$ (total) |
| 474 | $57.09 \pm 1.96$ (stat)$^{+12.43}_{-12.05}$ (total) |
| 564 | $21.61 \pm 1.169$ (stat)$^{+5.538}_{-5.388}$ (total) |
| 597 | $16.132 \pm 0.994$ (stat)$^{+5.025}_{-4.926}$ (total) |
| 710 | $5.413 \pm 0.481$ (stat)$^{+2.427}_{-2.395}$ (total) |
| 796 | $2.833 \pm 0.241$ (stat)$^{+0.567}_{-0.527}$ (total) |
| 843 | $2.079 \pm 0.09$ (stat)$^{+0.208}_{-0.138}$ (total) |
| 1002 | $0.728 \pm 0.0$ (stat)$^{+0.345}_{-0.346}$ (total) |
| 1062 | $0.513 \pm 0.0$ (stat)$^{+0.312}_{-0.312}$ (total) |
| 1191 | $0.257 \pm 0.0$ (stat)$^{+0.209}_{-0.21}$ (total) |
| 1337 | $0.129 \pm 0.0$ (stat)$^{+0.121}_{-0.121}$ (total) |
| 1416 | $0.092 \pm 0.0$ (stat)$^{+0.089}_{-0.089}$ (total) |
| 1500 | $0.066 \pm 0.0$ (stat)$^{+0.065}_{-0.065}$ (total) |
| 1683 | $0.034 \pm 0.0$ (stat)$^{+0.034}_{-0.034}$ (total) |
| 1888 | $0.018 \pm 0.0$ (stat)$^{+0.018}_{-0.018}$ (total) |

Table 6.2: Expected number of QCD events with corresponding uncertainties for different $m_T$ regions.

| $m_T[GeV]$ | $N_{QCD}$ | stat [%] | $sys_{fit}$ [%] | $sys_{up}$ [%] | $sys_{down}$ [%] | diff. to inv. id. [%] | $sys^{tot}_{up}$ [%] | $sys^{tot}_{down}$ [%] |
|---|---|---|---|---|---|---|---|---|
| 252 | 681.62 | 1.164 | 0.0 | 4.6 | 2.9 | 9.92 | 11.0 | 10.4 |
| 317 | 368.7 | 1.509 | 0.01 | 5.3 | 3.5 | 0.25 | 5.5 | 3.8 |
| 336 | 289.98 | 1.67 | 0.01 | 5.6 | 3.8 | 2.23 | 6.3 | 4.7 |
| 377 | 173.57 | 2.08 | 0.01 | 6.3 | 4.4 | 8.67 | 10.9 | 9.9 |
| 423 | 99.0 | 2.666 | 0.02 | 7.1 | 5.0 | 15.42 | 17.2 | 16.4 |
| 448 | 75.98 | 3.0 | 0.03 | 7.4 | 5.2 | 16.1 | 18.0 | 17.2 |
| 474 | 57.09 | 3.434 | 0.03 | 7.6 | 5.4 | 20.11 | 21.8 | 21.1 |
| 564 | 21.61 | 5.409 | 0.1 | 8.3 | 5.8 | 23.64 | 25.6 | 24.9 |
| 597 | 16.13 | 6.164 | 0.1 | 8.5 | 5.8 | 29.34 | 31.2 | 30.5 |
| 710 | 5.41 | 8.882 | 0.4 | 8.9 | 5.2 | 43.03 | 44.8 | 44.2 |
| 796 | 2.83 | 8.522 | 0.7 | 8.8 | 4.7 | 15.82 | 20.0 | 18.6 |
| 843 | 2.08 | 4.331 | 0.9 | 8.7 | 4.5 | 2.06 | 10.0 | 6.6 |
| 1002 | 0.73 | 0.0 | 1.6 | 7.0 | 7.1 | 46.88 | 47.4 | 47.4 |
| 1062 | 0.513 | 0.0 | 1.9 | 6.5 | 7.8 | 60.44 | 60.8 | 61.0 |
| 1191 | 0.257 | 0.0 | 2.3 | 6.0 | 8.4 | 81.08 | 81.3 | 81.5 |
| 1337 | 0.129 | 0.0 | 2.7 | 6.6 | 7.3 | 92.98 | 93.3 | 93.3 |
| 1416 | 0.092 | 0.0 | 2.9 | 7.4 | 6.2 | 96.15 | 96.5 | 96.4 |
| 1500 | 0.066 | 0.0 | 3.0 | 8.4 | 4.6 | 98.06 | 98.5 | 98.2 |
| 1683 | 0.034 | 0.0 | 3.2 | 11.2 | 1.8 | 99.62 | 100.3 | 99.7 |
| 1888 | 0.018 | 0.0 | 3.3 | 16.1 | 1.9 | 99.95 | 101.3 | 100.0 |

Table 6.3: Expected number of QCD events and uncertainties in different transverse mass regions. Uncertainties are separated in that arising from variations of the fit function and range and that due to fake rate variations (marked as sys up and sys down). In addition, a comparison to an alternative method (called "Inverse Id" method) has been performed that is described in detail in appendix (Section A.4). Slight deviations between both approaches are taken as further systematic uncertainty.

# 7 First summary

## 7.1 Common Uncertainties

As already shown, the data analysis in total consists of many different parts, each involving some "difficulties". In fact, not only the data reconstruction itself and the corrections applied introduce uncertainties but also systematic uncertainty sources exist.

The following section considers such uncertainties arising in the different analysis steps. Their impact is shown with respect to various transverse mass regions and summarized in Table 7.1. Explaining general uncertainty sources firstly, detailed descriptions of particular background related sources follow. The systematic uncertainties listed with respect to the data-driven contribution have been described already before (Section 6.2) resulting mainly out of variations in the choice of the QCD control region.

The first general uncertainty source considered refers to the common luminosity measurement (Sect. 3.2.1). The luminosity is defined as $L = \frac{nfI_1I_2}{2\pi\Sigma_x\Sigma_y}$ whereby n denotes the amount of colliding bunches, $f$ the orbital frequency at the LHC and $I_{1/2}$ the amount of particles per bunch. The dimension of the colliding area is described further by $\Sigma_x$ and $\Sigma_y$ which are determined via so-called Van-der-Meer scans. Thereby, the single beams are shifted in x- and y-direction step by step and the corresponding reaction rates are delivered (Sect. 3.2.1). In case of the integrated luminosity (that is $\int Ldt$), an systematic uncertainty of 2.8 % follows due to the uncertainty in determining the amount of colliding particles and the method itself [Gra15].

Systematic uncertainties arising with respect to higher-order QCD corrections (Section 3.3.1), include not only deviations due to the choice of the PDF set and the values used for $\alpha_s$ but also those due to renormalization and factorization scales. The uncertainties resulting of the $\alpha_s$ choice are, especially, derived by using different values (e.g. 68 % or 90 % confidence level) consistently in the PDF and the underlying matrix element for calculating the cross-sections corresponding to a certain process. Then, the deviation to the nominal can be quoted as systematic uncertainty. The envelope of the final uncertainty (derived by adding all previously mentioned uncertainties in quadrature) and deviations with respect to k-factors determined with different PDF sets, is reported as final uncertainty. Using both, an additive and factored approach, mass-dependent systematic uncertainties with respect to EW corrections are estimated in addition, assuming either that NLO EW and NNLO QCD add up or that NLO EW and NNLO QCD factorize. The original development has been performed within the official W′ working group [ATL14d].

Regarding, furthermore, the colliding beams in detail, each is designed to have an energy of 4 TeV. The deviation in the actual beam energy to that nominal one is measured during data acquisition in 2012 [Wen13]. Similar to the k-factor corrections provided by the W′ working group [ATL14d], it is propagated to the W background contribution using VRAP at NNLO using CT10 NNLO PDFs with $\alpha_s$ =0.117. The beam energy uncertainty is also calculated as a function of the generated invariant lepton-neutrino mass for both positive and negative charges separately and propagated (with aid of an official ATLAS tool) to the transverse mass spectrum in order to receive an additional systematic uncertainty. The resulting deviations are listed for various transverse mass regions in Table 7.1 ([ATL14d]).

Considering in contrast to the official W′ performance also the influence due to pileup corrections, a conservative estimation is performed by comparing the distributions with and without weights applied.

Also scaling the Monte Carlo simulation distributions to data luminosity causes systematic uncertainties. Similar to those according k-factor corrections, cross-section uncertainties are commonly calculated by varying the PDF choice and scales. Exemplified by the corresponding top cross-sections, the influence to the transverse mass spectrum is evaluated and listed below.

Investigating also calibration and resolution effects, further uncertainties up to 3.9 % arise. Varying the correction factors within one standard deviation, uncertainty sources such as statistics, the common measurement itself and material inefficiencies are considered separately.

The dominant uncertainty to the applied in-situ calibration applied for the jet energy scale (Section 3.4.5) is based on the calorimeter response whereby not only the global energy scale or the E/p response and acceptance are involved, but also noise threshold effects and the neutral hadrons response play a role. Their single impact to the final uncertainty is estimated via pseudo-experiments using nuisance parameters for the various uncertainty sources that are assumed to be uncorrelated (performed with aid of an official ATLAS tool). The systematic uncertainty to the jet energy calibration in total follows by determining the quadratic sum of the relative uncertainties derived by diversifying the various parameters. The resulting variations in the jet scale are propagated to the calculation of the missing transverse energy and thus, to the transverse mass. The impact of the jet resolution is quantified by applying a smearing correction (provided by the official ATLAS jet performance group) to the Monte Carlo simulations and deriving the resulting deviation for the various $m_T$ regions. Due to the good agreement between data and background contributions, the smearing correction is used for systematic evaluation only.

Calculating the missing transverse energy, leptonic and non-leptonic contributions are taken into account that lead to different systematic uncertainties (Section 3.4.4). Especially in case of decaying particles carrying high energies like a potential W′ boson, most of the missing transverse energy arises due to the lepton and thus, the leptonic part is highly correlated to the transverse momentum of the electron. In fact, the corresponding uncertainty is mainly included already within the electron energy scale and resolution uncertainties [115].
The non-leptonic part consists of summed contributions from the rest of the calorimeter. To treat the impact of each correctly, a package provided by the ATLAS jet and $E_T^{miss}$ performance group is used and the uncertainties propagated to the transverse mass spectrum. Since the corresponding uncertainties are assumed to be uncorrelated, they are added in quadrature.

Finally, assuming no correlations between identification, reconstruction and trigger scale factors, the corresponding relative uncertainties are derived by variations up and down (within one standard deviation) and added up quadratically (named as “Efficiency” uncertainty in Table 7.1).

[115] Deviations should be in the order of magnitude of a few GeV due to $E_T$ differences between the electron and local cluster depositions.

Table 7.1 summarizes the impact of certain uncertainty sources with respect to various transverse mass regions. The numbers given are calculated relatively to the nominal value derived by integration of the background contributions in total. The upper listed uncertainties (up to "Pileup") refer to experimental sources whereas the lower listed involve theoretical or model depending parts. Obviously, the experimental side is dominated over the whole transverse mass regions by corrections due to the energy scale (up to 3.9 %). Scaling factor variations (due to identification, reconstruction and trigger scales) are mainly in the order of 2.5 % and thus, constitute the next highest uncertainty. The theoretical deviations are clearly characterized by the k-factor uncertainties reaching values up to 20 % (for the highest transverse mass region). In comparison, those show also the strongest correlation to the transverse mass region regarded and even MC statistics play a minor role.

| | $m_{Tmin}$ [GeV] | | | | | | | | | |
|---|---|---|---|---|---|---|---|---|---|---|
| Source | 252 | 317 | 336 | 377 | 423 | 448 | 474 | 564 | 597 | 710 |
| Efficiency | 2.5 | 2.5 | 2.5 | 2.5 | 2.6 | 2.6 | 2.6 | 2.5 | 2.5 | 2.5 |
| Resolution | 0.022 | 0.1 | 0.17 | 0.11 | 0.31 | 0.8 | 0.28 | 0.26 | 0.28 | 0.26 |
| Scale | 1.7 | 3 | 3.4 | 2.7 | 3.9 | 3.9 | 3 | 3.3 | 3.6 | 3.5 |
| $E_T^{miss}$ | 0.31 | 0.23 | 0.41 | 0.17 | 0.38 | 0.44 | 0.13 | 0.21 | 0.14 | 0.35 |
| Jet resolution | 0.23 | 0.39 | 0.29 | 0.087 | 0.5 | 0.18 | 0.087 | 0.11 | 0.14 | 0.3 |
| Jet scale | 0.65 | 0.46 | 0.41 | 0.25 | 0.36 | 0.17 | 0.28 | 0.33 | 0.076 | 0.4 |
| Pileup | 0.60 | 0.88 | 0.81 | 0.95 | 0.14 | 0.010 | 0.16 | 0.26 | 0.12 | 0.49 |
| All experimental | 3.2 | 4.0 | 4.4 | 3.8 | 4.7 | 4.7 | 3.9 | 4.2 | 4.5 | 4.4 |
| MC statistics | 0.92 | 1.2 | 1.3 | 1.4 | 1.5 | 1.4 | 1.1 | 1 | 1.1 | 1.7 |
| $K$-factor | 5.3 | 5.1 | 5.1 | 5.2 | 5.2 | 5.6 | 6.2 | 7.9 | 8.6 | 11 |
| Top cross section | 0.66 | 0.65 | 0.62 | 0.55 | 0.46 | 0.43 | 0.38 | 0.28 | 0.23 | 0.17 |
| Beam energy | 0.85 | 0.91 | 0.93 | 0.99 | 1.1 | 1.1 | 1.1 | 1.3 | 1.3 | 1.5 |
| QCD | 0.58 | 0.32 | 0.36 | 0.58 | 0.83 | 0.85 | 1 | 0.96 | 1.1 | 1.2 |
| Total | 6.3 | 6.8 | 6.9 | 6.7 | 7.3 | 7.6 | 7.6 | 9.2 | 9.9 | 12 |
| | $m_{Tmin}$ [GeV] | | | | | | | | | |
| Source | 796 | 843 | 1002 | 1062 | 1191 | 1337 | 1416 | 1500 | 1683 | 1888 |
| Efficiency | 2.5 | 2.5 | 2.5 | 2.5 | 2.5 | 2.6 | 2.7 | 2.7 | 2.9 | 2.4 |
| Resolution | 0.93 | 0.52 | 0.64 | 0.77 | 0.72 | 3 | 1.2 | 1.9 | 0.37 | 0.29 |
| Scale | 3.6 | 3.6 | 3.8 | 3.6 | 2.9 | 3.1 | 3.3 | 3.5 | 3.1 | 3.9 |
| $E_T^{miss}$ | 0.37 | 0.38 | 0.83 | 0.21 | 1.3 | 0.26 | 0.74 | 1.2 | 0.08 | 0.12 |
| Jet resolution | 0.43 | 0.35 | 0.28 | 0.61 | 0.3 | 3 | 0.98 | 0.072 | 0.079 | 0.13 |
| Jet scale | 0.33 | 0.15 | 0.63 | 0.18 | 0.54 | 0.62 | 0.94 | 0.025 | 0.14 | 0.092 |
| Pileup | 0.82 | 1.3 | 0.98 | 0.73 | 1.1 | 3.8 | 1.4 | 4.6 | 7.0 | 2.8 |
| All experimental | 4.7 | 4.7 | 4.9 | 4.6 | 4.2 | 7.0 | 4.9 | 6.8 | 8.2 | 5.4 |
| MC statistics | 2.1 | 2.4 | 3.7 | 4.3 | 5.1 | 6.7 | 7.2 | 8.5 | 17 | 1.8 |
| $K$-factor | 12 | 13 | 15 | 16 | 17 | 17 | 18 | 18 | 16 | 20 |
| Top cross section | 0.14 | 0.095 | 0 | 0 | 0 | 0 | 0 | 0 | 0 | 0 |
| Beam energy | 1.7 | 1.8 | 2 | 2.1 | 2.4 | 2.5 | 2.7 | 2.8 | 2.8 | 3.9 |
| QCD | 0.53 | 0.27 | 0.98 | 1.2 | 1.6 | 1.8 | 2 | 2.2 | 2.5 | 4.2 |
| Total | 13 | 14 | 16 | 17 | 19 | 19 | 20 | 21.5 | 25 | 21.6 |

Table 7.1: Systematic uncertainties in % listed for various transverse mass regions, referring to different background related uncertainty sources. For all, the maximum deviation derived by up or down variation and subsequent integration over a certain transverse mass region is given only (and so, taken as resulting symmetric uncertainty). The value $m_{Tmin}$ denotes the lower integration boundaries.

## 7.2 First Résumé

As a first summary, the following section presents the kinematic distributions comparing data with a corresponding integrated luminosity of about $20\,\text{fb}^{-1}$ to the expected SM background contributions (Figures 7.1 to 7.3). The data set includes the whole data recorded in 2012 with the ATLAS detector at a center-of-mass energy of $\sqrt{s} = 8\,\text{TeV}$. The selection criteria as well as the correction factors as described before are applied to both, data and Monte Carlo samples, such that a clear signature with good object quality and detector conditions can be expected. Due to the blinding requirement explained in Section 5.2, no new physics scenario will be considered in the following and arising deviations would indicate mis-calibration effects, mis-modeling in the Monte Carlo simulations or even mistakes in the performance.

For comparison reasons, the expected SM contributions are scaled to data luminosity and shown as stacked histograms such that each background considered is added up to the one previously shown. Arising differences between the observed data distribution and the prediction are illustrated as ratios in corresponding lower panels whereby statistical fluctuations are shown only.

As expected, the SM W decay processes constitute the dominant background in all subsequent histograms (Figures 7.1 to 7.3). The next largest arise due to $t\bar{t}$ and single top production (commonly denoted as "top" background) which is most important for describing low transverse masses, followed by so-called diboson (WW, WZ, ZZ) decays. Z boson decays where one lepton could not be reconstructed and is therefore mimicking real $E_T^{miss}$ result in a minor background contribution, as well as the QCD background.

The spectra of the electron position in $\eta$ and $\phi$ (Figure 7.1) and its transverse momentum (Figure 7.2) demonstrate a good overall understanding of the predicted background processes.
Especially, the exclusion of the barrel-endcap transition regions becomes obvious in the $\eta$ spectrum as well as the expected falling behavior in the outer $\eta$ regions (that is $1.52 < |\eta| < 2.47$). The common distribution shape is mainly caused by the detector geometry and the correlated dependence on the polar angle $\theta$ as described already in Sect. 3.2.2.
The $\phi$ distribution shows an overall flat behavior in both data and predicted SM background distribution. Few fluctuations result mainly due to low statistics in the simulation of $W \to \tau\nu$ decays.

Due to the high trigger threshold, the maximum of the $p_T$ spectrum lies around 130 GeV and falls sharply in the sequel, as expected and described in Sect. 2.2. The spectrum is shown in a logarithmic binning to account for lower statistics at higher energy scales. This procedure keeps the relative bin width - defined as $(p_T^{i,max} - p_T^{i,min})/p_T^{i,center}$ ($i$ is the bin number) - constant while the absolute enlarges with increasing $p_T$. Slight deviations between data and SM backgrounds above 400 GeV arise probably due to mis-modeling of boosted W bosons in the Monte Carlo simulations (Section A.5). A reweighting procedure based on the transverse momentum of the decaying W boson has been evaluated but shows tiny effects on the transverse electron spectrum only and is therefore not applied in the following. Also the usage of different MC generators for the SM W and diboson contributions showed no satisfying change and is therefore not followed up further.

Similar to the $p_T$ spectrum, also the spectra of the missing transverse energy and the combined transverse electron-neutrino mass are visualized with aid of a logarithmic binning. The shape of the missing transverse energy distribution (Figure 7.3, left) shows a nearly identical behavior to that corresponding to the transverse electron momentum: as expected due to the kinematic predictions

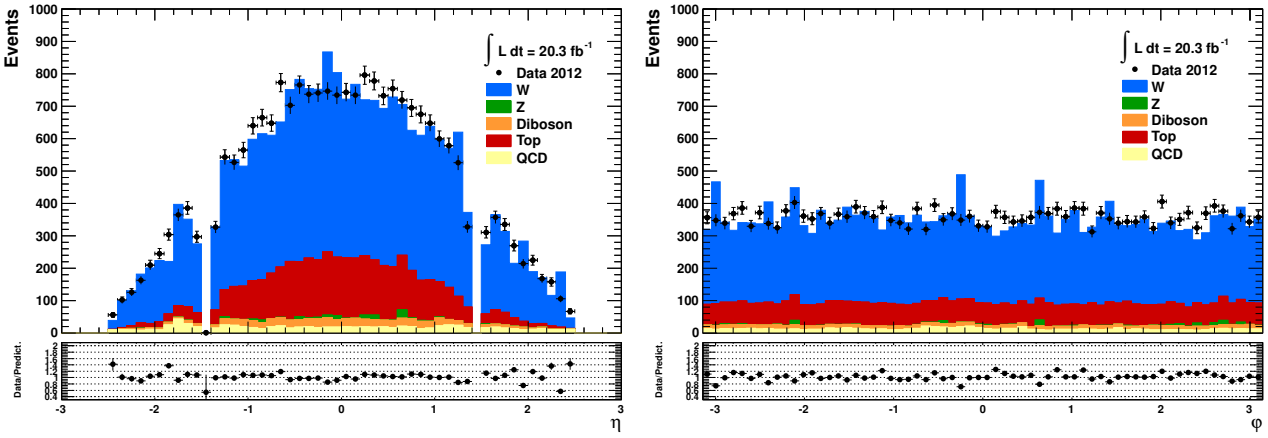


Figure 7.1: Blinded electron $\eta$ (left) and $\phi$ (right) spectra after final event selection.

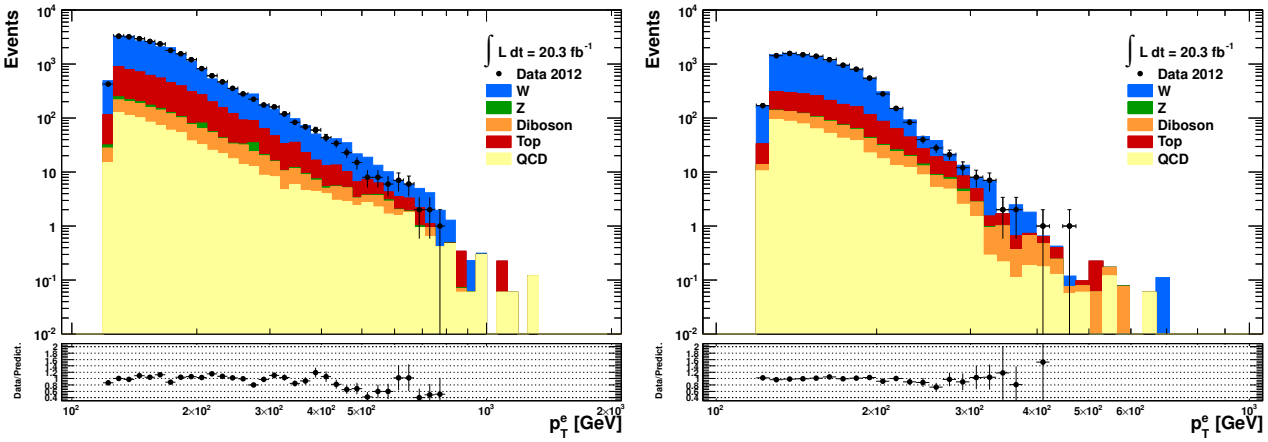


Figure 7.2: Blinded electron $p_T$ spectrum after final event selection (left). On the right side, the data in comparison to the background expectation is shown for events with transverse masses above 252 GeV involved (still including the blinding requirement).

for the decay products (Sect. 2.2) and the $E_T^{miss}$ cut chosen symmetrically to the electron $p_T$, the spectrum has a maximum at around 130 GeV and falls sharply in the sequel. The overall agreement between observed data and all known SM background processes is good and even does not show the same deviations above 400 GeV as visible in the electron transverse momentum spectrum.

The blinded transverse mass spectrum is shown in Figure 7.3 on the right side. The sharp edge at around 250 GeV results due to the symmetrically chosen $p_T$ and $E_T^{miss}$ cut values and visualizes the energy region above which the decay products are produced nearly back-to-back. Below, the remaining SM W bosons have to be highly boosted (in the transverse plain) to still fulfill the transverse electron momentum and missing transverse energy requirements. Nevertheless, the expected Jacobian peak is clearly visible and well described at around 81 GeV, followed by a steeply falling distribution (Sect. 2.2). Despite the blinding cut of $m_T < 400$ applied, the cut is not exactly visible as sharp edge. This effect is caused by the logarithmic binning and corresponding bin migration.

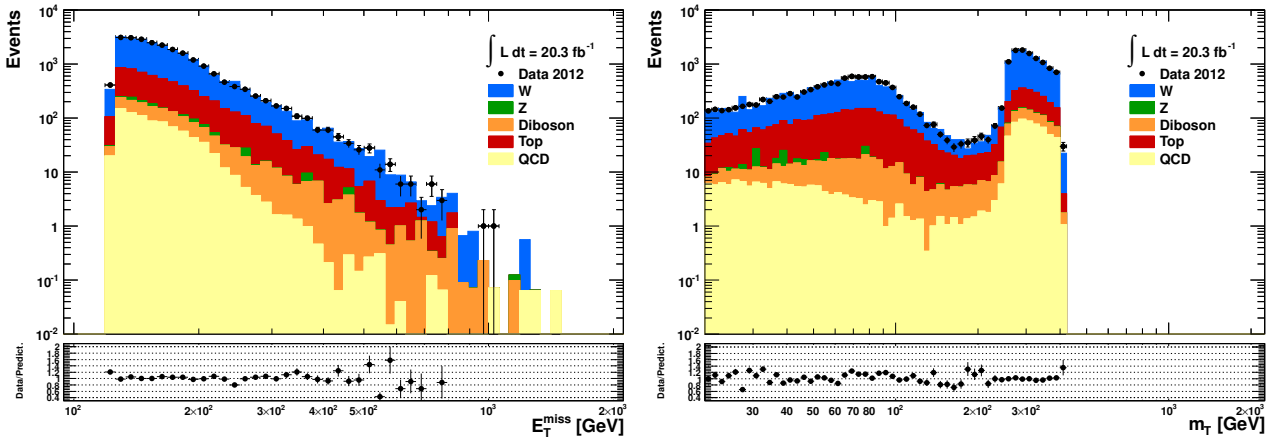


Figure 7.3: Blinded spectra of the missing transverse energy (left) and the transverse mass (right) after final event selection.

All in all, the considered SM background contributions describe the observed data in a good manner. Single bins show slightly higher SM predictions than observed data (e.g. in $E_T^{miss}$, $m_T$ spectra) but the effects are still within one or two standard deviations and mainly refer to statistical fluctuations and bin migration effects. So, arising differences are understood and in the following, it is possible to look into the whole data set without any blinding cut applied.

# 8 Exotic Processes

With respect to the precedent studies, it is now reasonable to take the whole data recorded into account and look for any excess not describable within the previously considered SM expectations. Therefore, the blinding cut of $m_T$ <400 GeV is removed in the following.

Figure 8.1 shows an event display of the ATLAS detector corresponding to the highest energy deposition selected with the previously described analysis criteria: with an electron momentum of $p_T$= 840.3 GeV and missing transverse energy of $E_T^{miss}$=723.0 GeV, the highest transverse mass $m_T$=1551.5 GeV can be reconstructed in event 351815822 of run 213754. The corresponding electron position in $\phi$ is determined as about 0.97 whereas the missing transverse energy points into $\phi \approx$-1.98 direction. Thus, the electron and the neutrino decay nearly back-to-back as expected for high energies and clearly visible in Figure 8.1. Making the event display, the impact parameter and track quality criteria as well as the requirements on $p_T$ for medium electron candidates and $E_T^{miss}$ were accounted for. Jets are shown if they have a transverse momentum of above 20 GeV.

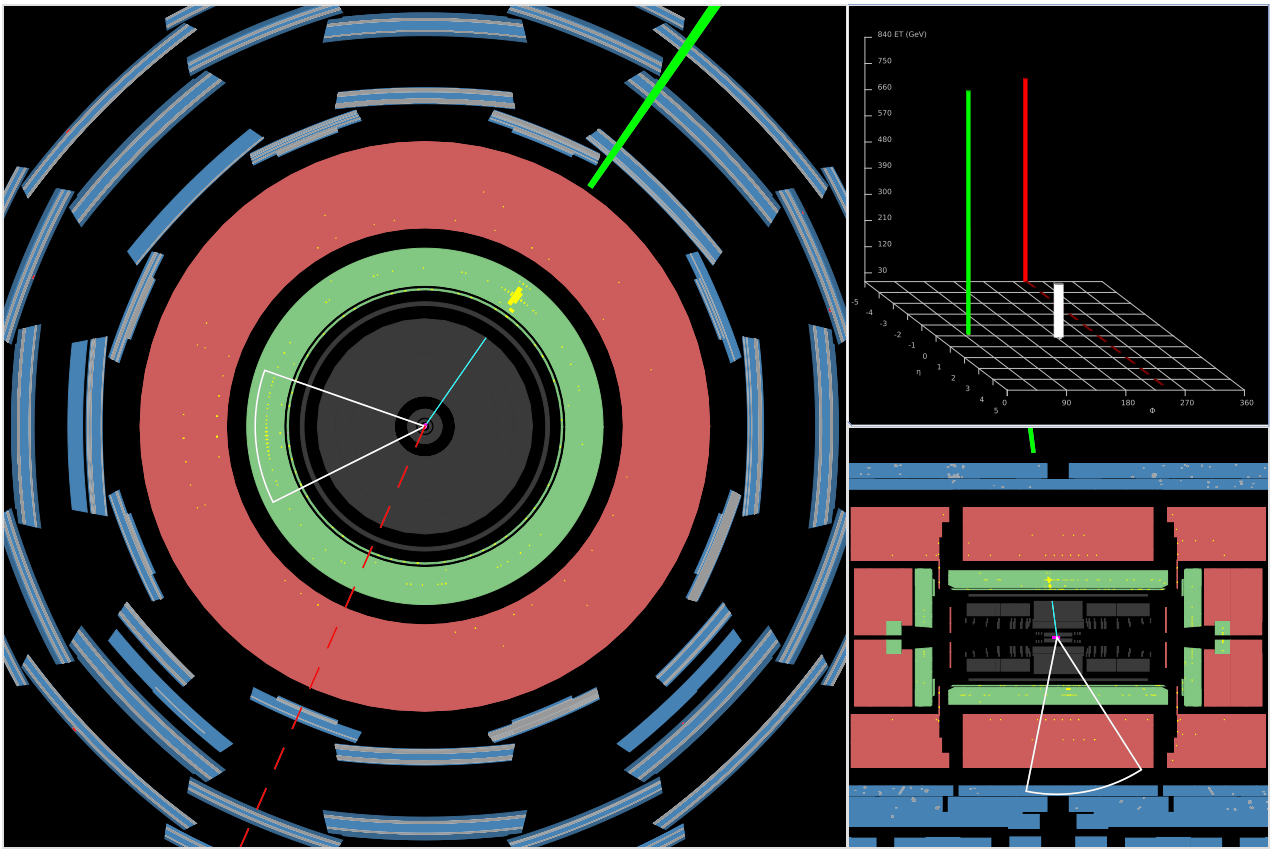


Figure 8.1: Event display demonstrating the highest transverse mass event after final event selection. A track corresponding to a medium electron candidate is shown in blue, pointing to the highest energy deposition within the electromagnetic calorimeter (yellow). The direction of the missing transverse energy is shown as red dashed line. The white cone visualizes a jet. Shown are the xy- (left) and $\rho$z (bottom right) projections, as well as the transverse energy in dependence of $\eta$ and $\phi$ as lego plot (top right).

## 8.1 Interpretation of Unblinded Results

Due to the high transverse electron momentum and the corresponding high missing transverse energy required (at least 125 GeV each), clean signal signatures comprising an electron and a neutrino in the final state might be expected for transverse masses of at least 250 GeV. To ensure sufficient statistics per bin also in the high energy regions, a logarithmic binning is chosen in the spectra of the discriminating variables ($p_T$, $E_T^{miss}$, $m_T$) as already described before [116]. So, the subsequent signal regions commonly regarded lie above $m_T$ >252 GeV as this is the corresponding lower bin border.

The whole data set recorded in 2012 with the ATLAS detector at a center-of-mass energy of $\sqrt{s} =$ 8 TeV comprises a corresponding integrated luminosity of about 20 fb$^{-1}$. The selection criteria as well as the correction factors are applied as described before to both, data and Monte Carlo samples, whereby the latter are commonly scaled to data luminosity (for Figures 8.2 to 8.4). As before, the expected SM contributions are shown as stacked histograms such that each background considered is added up to the one previously shown. Arising differences between the observed data distribution and the prediction are illustrated as ratios in corresponding lower panels whereby statistical fluctuations are shown as well as systematic uncertainties (visualized as smooth band for discriminating variables). All kinematic quantities considered subsequently are shown for transverse masses above 252 GeV for the above mentioned reasons.

As already shown before, the SM W decay processes constitute the dominant background also within the following histograms (Figures 8.2 up to 8.4). The next largest arise due to $t\bar{t}$ and single top production, followed by so-called diboson (WW, WZ, ZZ) decays. Z boson decays and QCD events result in a minor background contribution.

Figure 8.2 shows the observed data in comparison to SM expectations in the unblinded spectra of the electron $\eta$ position (left) and its transverse momentum (right) after final selection. As before, a good overall agreement between data and expected background contributions is visible. The exclusion of the barrel-endcap transition regions as well as the falling behavior for larger $\eta$ values are visible. The $p_T$ spectrum has again a maximum at around 130 GeV and falls sharply in the sequel. Removing events with $m_T < 252$ GeV, even the discrepancies for $p_T > 400$ GeV vanished and thus, the previous suggestion of mis-modeled boosted W bosons is supported.

Figure 8.3 shows the unblinded spectra of the missing transverse energy and the transverse mass after final event selection for transverse masses above 252 GeV. As before, the missing transverse energy distribution demonstrates the same behavior as the electron momentum. A maximum at around 130 GeV with a slope thereafter shows the expected and well described shape. The combined transverse mass spectrum starts at 252 GeV and falls as predicted. Single bins in the previously presented histograms also show slightly higher SM contributions than observed data due to statistical fluctuations and bin migration effects.

Additionally, Figure 8.4 shows the difference between the electron position in $\phi$ and the direction of the corresponding missing transverse energy after final selection with (right) and without (left) an additional transverse mass cut of 252 GeV. Obviously, the events with $m_T$ <252 GeV involved are well distinguishable from those high mass events concentrated in the outer regions. Thus, the corresponding SM W bosons are actually strongly boosted resulting in small opening angles of the decay

[116] The binning is justified as the focus is on the search for significant resonances ("bumps").

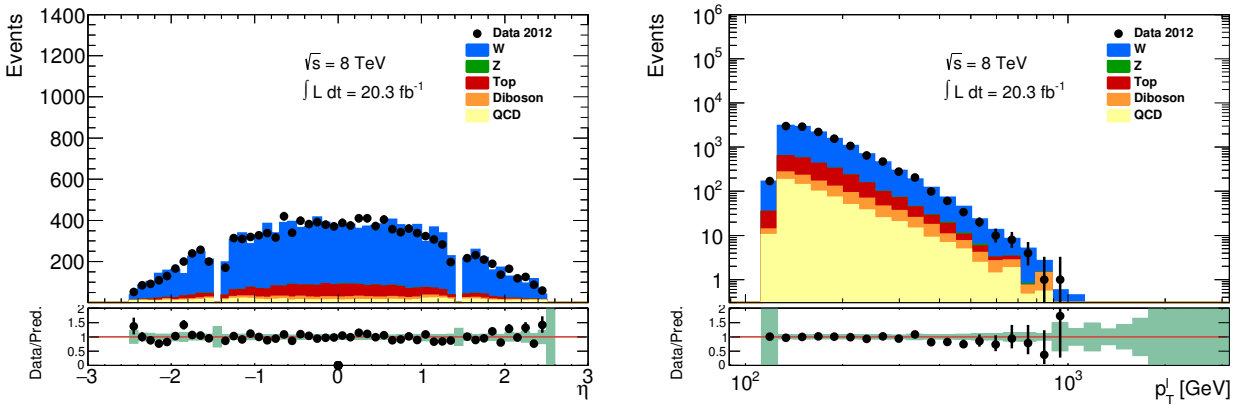


Figure 8.2: Unblinded spectra of the electron $\eta$ position (left) and its transverse momentum (right) after final selection for transverse masses above 252 GeV. Systematic uncertainties are visualized as smooth band and shown in addition to statistical fluctuations in the lower panel.

products (as discussed before). By contrast, the high energy candidates (corresponding to events with high transverse masses involved) decay nearly back-to-back, meaning large angles between electrons and neutrinos. The data observed are well described by the predicted SM background contributions, except for small fluctuations covered by statistical and systematic uncertainties.

All spectra show the expected kinematic behavior and a good overall agreement between the data observed and the considered SM background contributions. Unfortunately, no significant excess can be observed and exclusion limits will be derived in the following for three new physics scenarios (Sect. 2.3). These are namely additional charged vector gauge bosons in the context of a Sequential Standard Model (SSM), called W′, charged chiral bosons (W*) and the occurrence of WIMP pair production with initial-state radiation of a SM W boson. In the following, the signal simulation sets used are explained first, followed by the principles of different limit setting approaches and the underlying calculation principles.

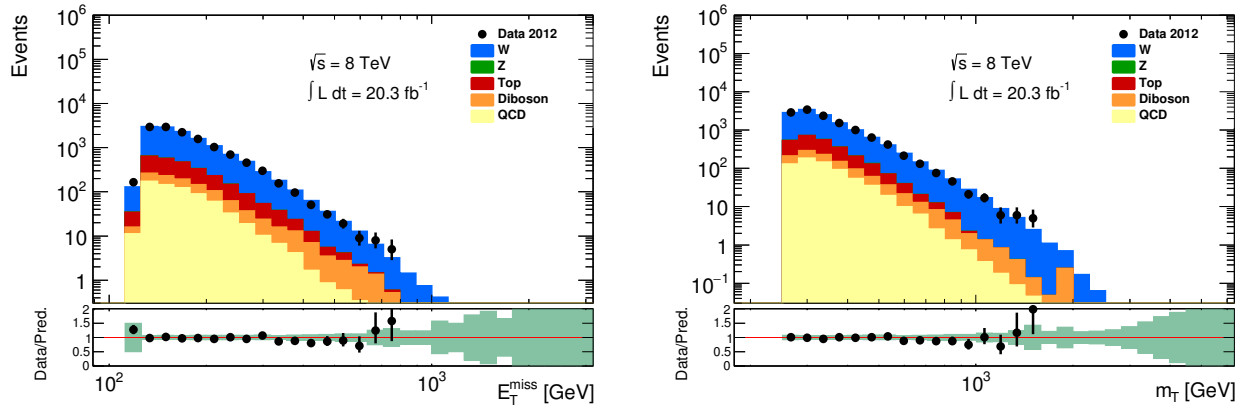


Figure 8.3: Unblinded spectra of the missing transverse energy and the transverse mass after final event selection. The comparisons of data to SM expectations are shown for events with a transverse mass of above 252 GeV. Systematic uncertainties are visualized as smooth band and shown in addition to statistical fluctuations in the lower panel.

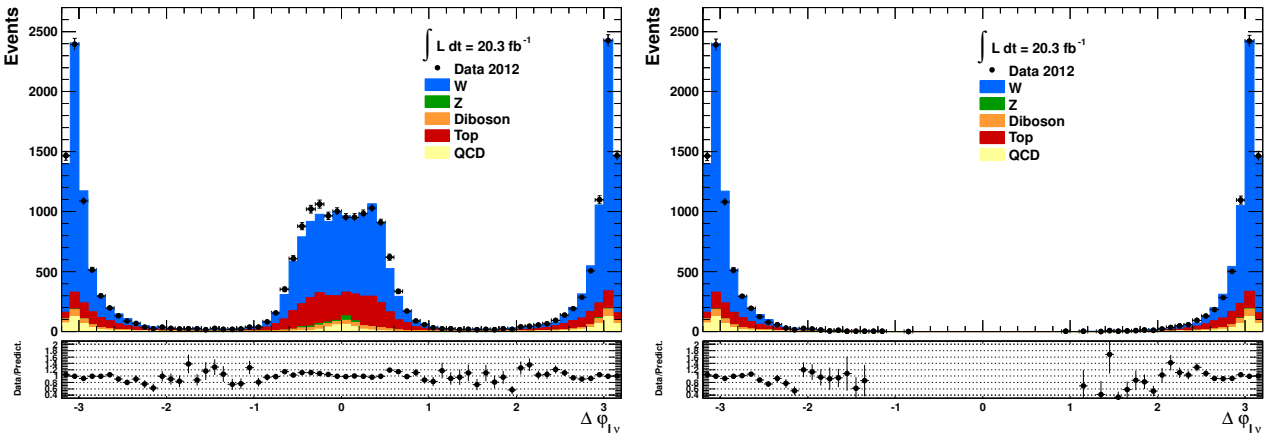


Figure 8.4: The difference between the electron position in $\phi$ and the direction of the corresponding missing transverse energy is shown after final event selection with (right) and without (left) an additional transverse mass cut of 252 GeV (unblinded data set). Statistical uncertainties are shown in the lower panel only.

## 8.2 Signal Samples

Simulating signatures of heavier charged gauge bosons, denoted as W′, PYTHIA 8 is used as event generator including a full detector simulation via GEANT4. While generation, processes are determined at LO using a MSTW2008 LO PDF set. In contrast to the previously discussed background processes, signal samples are used that are generated flat in the invariant boson mass, meaning no resonance shape is simulated, to ensure high statistics in all transverse mass ranges. In fact, removing the common Breit-Wigner dependence and dividing the matrix element by $f(m_{l\nu}) = \exp(-p_1 m_{l\nu}/8000)(m_{l\nu}/8000)_2^p$ ($p_1$, $p_2$ are derived by fitting) while event generation, a flat mass spectrum can be obtained and an associated loss in the cross-section avoided. In order to receive signatures distinguishable for different W′ pole masses, a reweighting with the correct line shape is applied event-wise afterwards by using $\Gamma = 0.03382870 * (3. + (1. + 0.5 * r) * (1. - r)^2)/4.$ with $r = (\frac{174.3}{M_{W'}})^2$ and $M_{W'}$ as the desired pole mass ($M_{W'} > 174.3 (= m_{top})$). It is:

$$\begin{aligned} w &= 1.0 * 10^{12}/((m_{l\nu}^2 - M_{W'}^2)^2 + (m_{l\nu}^2 * \Gamma)^2) \\ \omega_{W'} &= w/(121.88 * \exp(13.0 * (\frac{m_{l\nu}}{8000.}))), (\frac{m_{l\nu}}{8000.}) < 0.0375 \\ \omega_{W'} &= w/\exp(18.5 * (\frac{m_{l\nu}}{8000.}) - 1.4 * \log(\frac{m_{l\nu}}{8000.})), (\frac{m_{l\nu}}{8000.}) \geq 0.0375 \end{aligned} \tag{8.1}$$

As described in Section 2.3, the W′ fermionic couplings are assumed to be identical to those of a SM W boson, so that PYTHIA default settings for V-A couplings have been implemented for both SM W and W′ bosons. An interference between both is not taken into account. Comparing to different samples simulated for certain W′ pole masses, the reweighting procedure has been validated. Figure 8.5 shows the invariant mass distributions as well as the total transverse mass spectrum (derived on truth level) for W′ pole masses of 1000 GeV and 3000 GeV derived by the signal sample generated flat in the invariant boson mass in comparison to those derived by direct simulation sets. A good overall agreement is visible. Further validation plots are shown in appendix, Sect. A.6.

Similar to the W′ signal sample, also the W* simulation is generated flat in the invariant boson mass. CalcHEP is used for generating initial kinematics at LO (CTEQ6L1 PDF set) while the general event generation is done via PYTHIA. The appropriate reweighting procedure is defined as follows [117], using $\Gamma_{W^*} = 0.03382870 * (1 + (1. - 4.) * r^2 * (3. - 2. * r)/12.)$ and $r = (\frac{m_{top}}{M_{W^*}})^2 = (174.3/M_{W^*})^2$:

$$\begin{aligned} w &= 1.0 * 10^{12}/((m_{l\nu}^2 - M_{W^*}^2)^2 + (M_{W^*}^4 * \Gamma_{W^*}^2)) \\ \omega_{W^*} &= w * \exp(-18.5 * (\frac{m_{l\nu}}{8000.}) + 1.35 * \log(\frac{m_{l\nu}}{8000.})) * \exp(4. * \log(\frac{m_{l\nu}}{M_{W^*}})) \end{aligned} \tag{8.2}$$

Similar to the background samples, PHOTOS is used to simulate final-state photon radiation from leptons in all signal samples.

[117] Both, the reweighting procedure for a SSM W′ and that for W* bosons, have been developed by Misha Chizhov and are based on Pythia modifications introduced by Daniel Hayden (https://twiki.cern.ch/twiki/bin/viewauth/AtlasProtected/WprimeFlatTemplate#Re_weighting_Back_to_Resonance_p, Internal page.) .

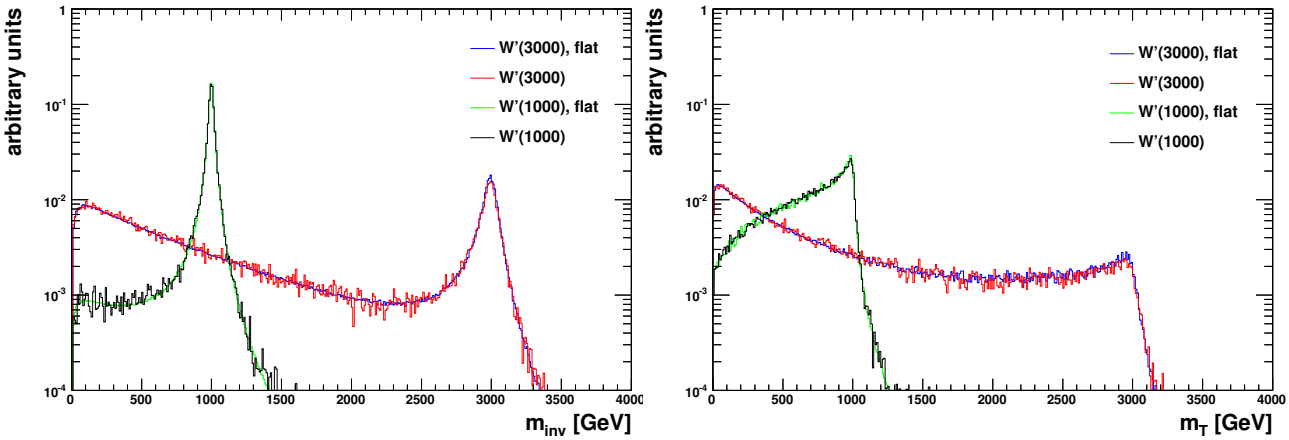


Figure 8.5: Validation of W′ reweighting procedure exemplified for W′ pole masses of 1000 GeV and 3000 GeV. The comparisons are shown in the spectra of the invariant mass (left) and the total transverse mass (right) (truth level) before any selection criteria are applied. The single distributions are normalized to unity to better compare the shapes.

Table 8.1 shows the LO and NNLO cross-sections and associated uncertainties (using the flat sample) for decays of those heavier gauge bosons (W′) whereby the corresponding values are reported not only for the full phase space but also for a so-called fiducial volume that is defined by $m_{l\nu} > 0.4 m_{W'/*}$. The latter one has been chosen to investigate especially the influence due to PDF uncertainties on the subsequent limit setting procedure in comparison to exclusions derived with respect to the full phase space. The Monte Carlo simulation sets utilized are also listed in the appendix Section A.1. The amount of events simulated with the corresponding integrated luminosities $L = \frac{N}{\sigma B}$ are listed in Table A.2 for both, W′ and W* bosons. The flat W′ sample includes decays into electrons or muons and the related neutrinos only. Decays to other final states such as $\tau\nu$, $ud$, $sc$ or $tb$ are not considered as further signal or background processes and contribute only calculating the related decay width. Their impact has been investigated with aid of the samples simulated for particular pole masses. In general, the branching fractions to the various lepton decay channels are about 8.2 % each (with respect to high W′ pole masses above 1 TeV).

The selection required is identical to that described before and also the appropriate corrections are applied (Section 5).

In order to correct the distributions of the heavier vector gauge bosons (W′) to NNLO, k-factors are used that have been provided by the W′ working group (Figure 8.6). The k-factor corrections are calculated in the same manner as those in case of SM W boson decays (Sect. 3.3.1, except that the electroweak corrections beyond final-state radiation are not included (since they are not adaptable directly). Uncertainties are considered for the renormalisation and factorisation scales, the choice of the parton distribution function (PDF) and PDF+$\alpha_s$ variations as done for the SM W contribution. Figure 8.7 shows the expected SM processes overlaid with the signal distribution of a W′ boson with 3 TeV pole mass in the transverse mass spectrum. The appropriate Jacobian peak and the characteristic falling behavior above the W′ resonance mass are visible.

| W′ [GeV] | LO $\sigma B$ [fb] | LO $\sigma B^{\text{fid}}$ [fb] | QCD k-factor | QCD Fid. k-factor | NNLO $\sigma B$ [fb] | Δ PDF+ [%] | Δ PDF− [%] | NNLO $\sigma B^{\text{fid}}$ [fb] | Δ PDF+ [%] | Δ PDF− [%] |
|---|---|---|---|---|---|---|---|---|---|---|
| 300 | 114000 | 112000 | 1.310 | 1.310 | 149000 | 3.5 | 2.9 | 147000 | 3.5 | 2.9 |
| 400 | 38400 | 38000 | 1.306 | 1.307 | 50200 | 3.8 | 3.0 | 49600 | 3.8 | 3.1 |
| 500 | 16500 | 16300 | 1.298 | 1.299 | 21400 | 4.0 | 3.2 | 21100 | 4.0 | 3.2 |
| 600 | 8080 | 7930 | 1.289 | 1.289 | 10400 | 4.3 | 3.4 | 10200 | 4.3 | 3.4 |
| 750 | 3270 | 3200 | 1.273 | 1.273 | 4160 | 4.7 | 3.6 | 4070 | 4.8 | 3.6 |
| 1000 | 930 | 901 | 1.250 | 1.249 | 1160 | 5.6 | 4.0 | 1130 | 5.7 | 4.1 |
| 1250 | 316 | 302 | 1.230 | 1.227 | 389 | 6.6 | 4.7 | 371 | 6.8 | 4.8 |
| 1500 | 120 | 113 | 1.212 | 1.207 | 146 | 7.8 | 5.5 | 136 | 8.1 | 5.7 |
| 1750 | 48.7 | 44.4 | 1.194 | 1.185 | 58.1 | 8.9 | 6.4 | 52.6 | 9.5 | 6.7 |
| 2000 | 20.7 | 18.0 | 1.174 | 1.158 | 24.3 | 10.0 | 7.2 | 20.9 | 11.1 | 7.9 |
| 2250 | 9.34 | 7.55 | 1.155 | 1.125 | 10.8 | 10.9 | 7.9 | 8.49 | 12.8 | 9.2 |
| 2500 | 4.46 | 3.23 | 1.140 | 1.085 | 5.09 | 11.4 | 8.4 | 3.50 | 14.8 | 10.9 |
| 2750 | 2.28 | 1.40 | 1.133 | 1.040 | 2.58 | 11.4 | 8.5 | 1.45 | 17.2 | 12.7 |
| 3000 | 1.26 | 0.623 | 1.138 | 0.993 | 1.44 | 10.8 | 8.2 | 0.618 | 19.9 | 14.9 |
| 3250 | 0.765 | 0.284 | 1.156 | 0.950 | 0.885 | 9.6 | 7.5 | 0.270 | 22.4 | 17.3 |
| 3500 | 0.497 | 0.133 | 1.181 | 0.923 | 0.587 | 8.3 | 6.6 | 0.123 | 24.2 | 19.4 |
| 3750 | 0.348 | 0.0661 | 1.206 | 0.911 | 0.419 | 7.1 | 5.8 | 0.0602 | 24.8 | 20.7 |
| 4000 | 0.255 | 0.0342 | 1.226 | 0.918 | 0.312 | 6.2 | 5.1 | 0.0314 | 24.0 | 20.5 |

Table 8.1: LO and NNLO cross-sections and associated uncertainties for W′ decays to a single lepton plus missing transverse energy reported for both, the full phase space and for a fiducial volume defined by $m_{l\nu} > 0.4 m_{W'}$. PDF uncertainties are for 90% CL PDF variations using MSTW2008 NNLO PDFs. [ATL14d]

Regarding chiral W* bosons, no uncertainties and further NNLO corrections have been calculated since the W* interactions are non-renormalizable and thus, any higher order (QCD) corrections are meaningless. Thus, Table 8.2 shows the LO cross-sections only.

In order to include a dark matter interpretation, too, the processes $pp \to \chi\chi W$ were generated using a MADGRAPH5 implementation interfaced with PYTHIA8 for the parton shower and hadronization. Similar to the W′ signal samples, a MSTW2008 LO PDF set has been used while generating. But in contrast to the Monte Carlo simulation sets of the heavier gauge (and chiral) bosons, various mono-W samples are produced for an effective scale, M*, of 1000 GeV and different WIMP masses (varied between 1 GeV and 1300 GeV). The decays included are leptonical only. The amount of generated events, the corresponding cross-sections and effective integrated luminosities are summarized for four characteristic operators (namely D1, D5(c), D9) in Table A.2 (appendix Sect. A.1). Typical kinematic distributions are additionally shown in Section A.8.

| W* $[GeV]$ | LO $\sigma B$ [fb] | LO $\sigma B^{\text{fid}}$ [fb] |
|---|---|---|
| 400 | 37600 | 37600 |
| 500 | 16200 | 16200 |
| 600 | 7950 | 7950 |
| 750 | 3170 | 3170 |
| 1000 | 882 | 882 |
| 1250 | 294 | 294 |
| 1500 | 108 | 108 |
| 1750 | 42.3 | 42.3 |
| 2000 | 17.1 | 17.1 |
| 2250 | 7.0 | 7.0 |
| 2500 | 2.9 | 2.9 |
| 2750 | 1.2 | 1.2 |
| 3000 | 0.49 | 0.489 |
| 3250 | 0.199 | 0.198 |
| 3500 | 0.0797 | 0.0788 |
| 3750 | 0.0317 | 0.0310 |
| 4000 | 0.0126 | 0.0122 |

Table 8.2: LO cross-sections and associated uncertainties for W* decays to a single lepton and missing transverse energy reported for both, the full phase space and for a fiducial volume defined by $m_{l\nu} > 0.4 m_{W^*}$. NNLO cross-sections and uncertainties are not listed due to non-renormalizability at higher orders in QCD [ATL14d].

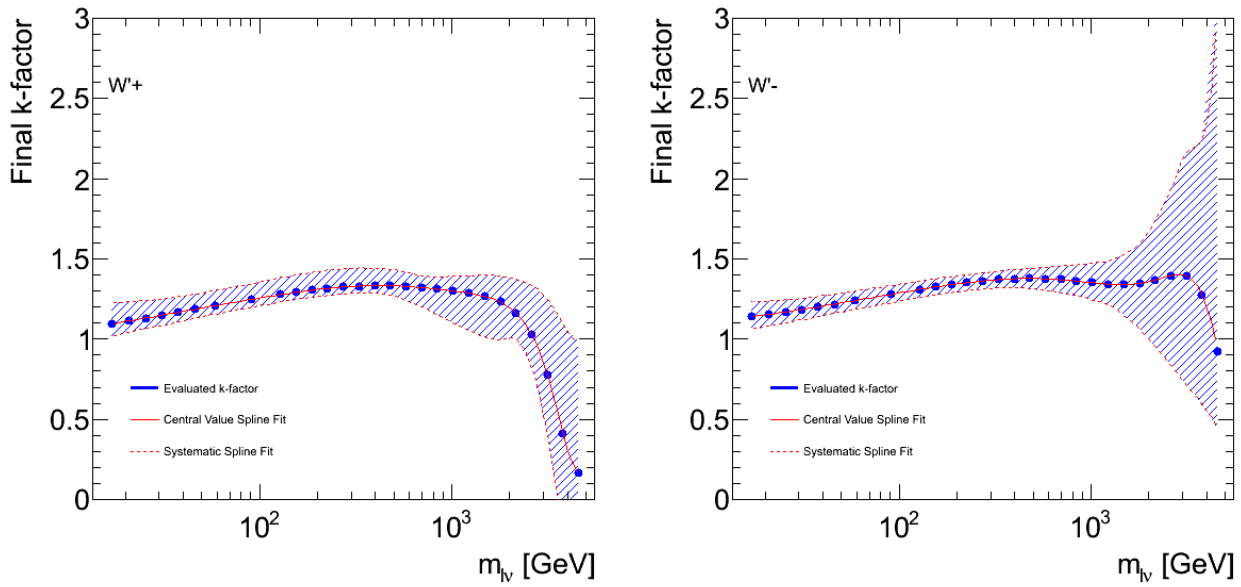


Figure 8.6: Final k-factors as function of the invariant lepton-neutrino mass calculated for signal processes $W'^{+} \to \ell^{+}\nu$ (left) and $W'^{-} \to \ell^{-}\nu$ (right), derived by the W′ working group [ATL14d].

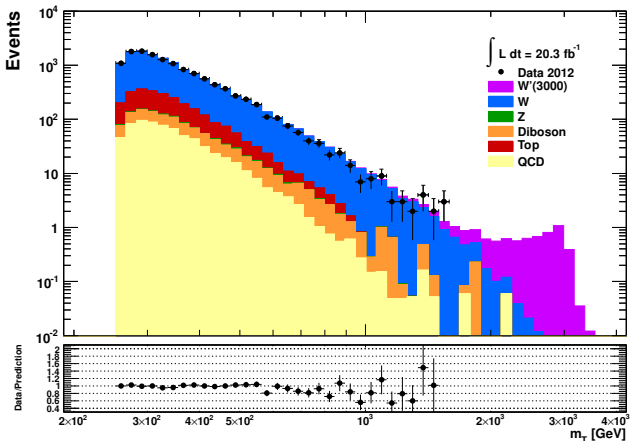


Figure 8.7: Unblinded spectrum of the transverse mass above 252 GeV after final event selection. The contribution of a W′ boson with a pole mass of 3000 GeV is shown in addition to the expected SM processes. The characteristic sharp edge above the resonance mass is visible.

**SSM W′ vs. chiral W* bosons** Also after selecting events involving a highly energetic electron and high missing transverse energy, the differences in the kinematic distributions originating from different production mechanisms are visible (compare Sect. 2.3.1). Comparing to predictions involving charged gauge bosons in the context of the SSM (W′), the helicity vanishing for charged chiral bosons causes a lepton production preferably at higher pseudo-rapidities, visible in Figure 8.8 (top left). Section A.3 (appendix) shows in addition two-dimensional $\eta$,$\phi$ spectra derived by both, W′ and W* decays. While an emission of the final-state lepton-pair is forbidden for the latter in the plain perpendicular to the beam axis in the parton rest frame, an emission probability not vanishing in the lab frame occurs due to longitudinal boosts of the colliding partons. As a consequence, the chiral bosons are produced already with negligible longitudinal momenta and thus, the lepton pseudo-rapidity distribution has a minimum around $\eta$ =0 (Sect. 2.3.1). Furthermore, the anomalous couplings to leptons for charged chiral bosons lead to broad smooth bumps (instead of the Jacobian peak typical for SM W and SSM W′ bosons) in both, the spectra of the transverse electron momentum (Figure 8.8, top right) and the missing transverse energy (Figure 8.8, bottom left). Hence, also the distribution of the combined transverse mass (Figure 8.8, bottom right) differs significantly.

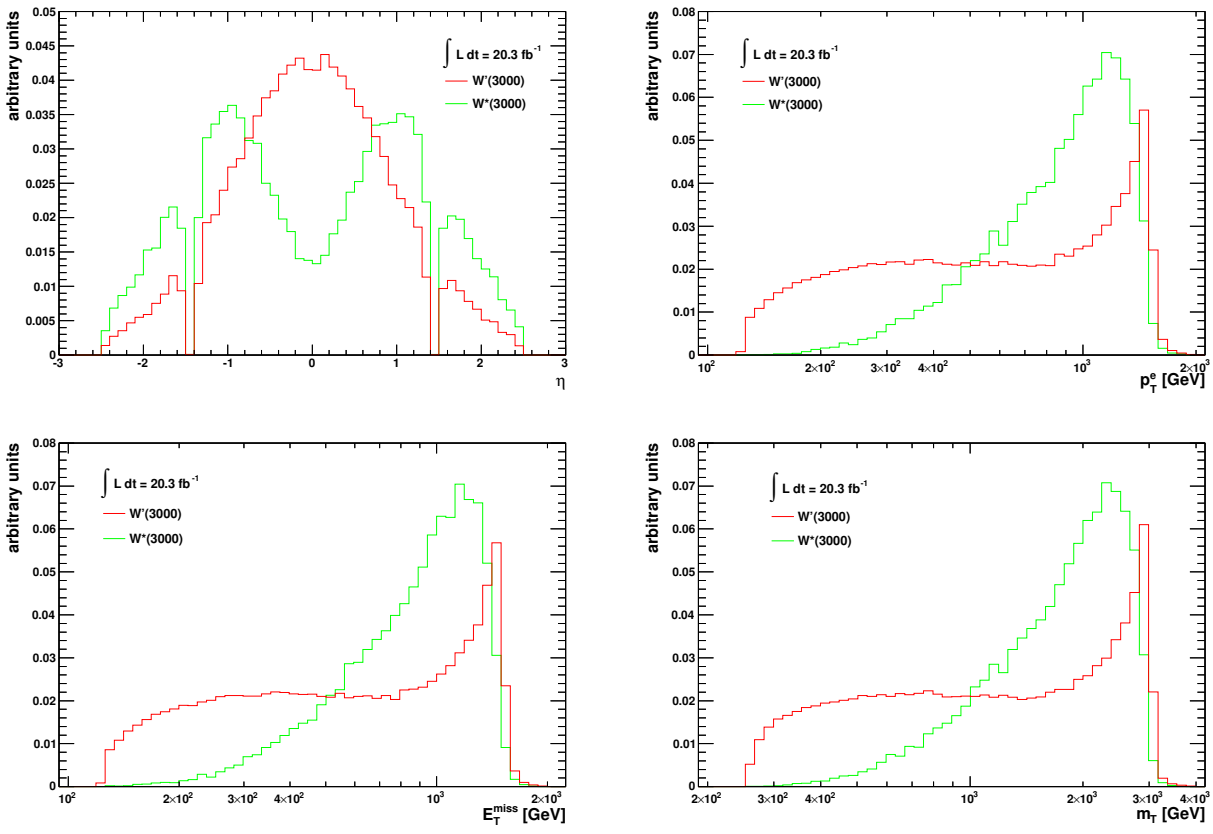


Figure 8.8: W′ vs. W* after final event selection for events with $m_T$ >252 GeV. The single distributions are scaled to unity for both, W′ and W*.

## 8.3 Efficiency Determination

For each of a series of W′ or W* pole masses and various WIMP masses, the signal efficiency $\varepsilon_{sig}$ is derived in the appropriate Monte Carlo simulation considering the fraction of events passing all selection criteria. Thus, the efficiency is obtained as follows:

$$\varepsilon_{sig} = \frac{N_{sel}}{N_{total}} \tag{8.3}$$

whereby $N_{sel}$ denotes the signal events selected with respect to a certain $m_{Tmin}$ value and $N_{total}$ the total amount of (generated) signal events before any selection requirement applied. For both, the impact of the previously discussed correction factors (namely pileup, vertex z-position and k-factors) is considered. In addition, the amount of selected signal events is corrected with respect to electron reconstruction and identification scales as well as for general energy adjustments (energy resolution corrections, Sect. 5.5). The appropriate uncertainties on the signal efficiency are obtained subsequently by varying the correction values by one standard deviation up and down and evaluating the difference between the resulting signal efficiency to the nominal. Regarding both, up and down variation, the larger deviation is chosen as systematic. Finally, the separate uncertainties are obtained as relative uncertainties and added in quadrature. The separate values are summarized for each new physics scenario considered and listed in Tables 8.3 to 8.5. A detailed description of the common systematic uncertainties can be found in Sect. 7.1.

To account for the different signal production processes considered, the $m_{Tmin}$ values vary in dependence on the signal pole masses and with respect to the different new physics scenarios considered. In fact, the lowest integration interval in the search for heavier vector gauge bosons (W′) starts at 252 GeV for the reasons described before. Due to the change in kinematics, the integration borders slightly deviate in the case of chiral bosons. In the dark matter case involving a highly boosted SM W boson and large missing transverse energy, four strongly increased transverse mass regions are considered only (one for each operator). Details of the $m_{Tmin}$ optimization follow in Section 8.5.

Regarding the signal efficiency uncertainties for W′ bosons, a huge increase in the k-factor systematic uncertainty becomes obvious. The reason for this is based on the W′ production mechanisms. Figure 8.9 shows the invariant W′ boson mass derived before any selection criterion is applied (on generator level), such that a distortion of the line shapes for higher W′ pole masses is visible. That is mainly caused by steeply falling parton distribution functions at high values of Bjørken-x (Sect. 2.3.1).

In order to account for the high fraction of signal events produced far off-shell and the related high PDF uncertainties, not only the full phase space is considered in the following but also a fiducial volume. For the latter, only signal events that fulfill the requirement $m_{l\nu} > 0.4 m_{W'/*}$ contribute to $N_{total}$ meaning only events are included that lie in a region where the invariant mass is above 40 % of the W′ pole mass. That criterion was investigated and optimized in the W′ working group [ATL14d].

Figure 8.10 shows the W′ signal efficiency in dependence of the W′ pole mass for both the fiducial (left) and the full phase space (right). Since the efficiency calculation takes only events into account that passed the selection criteria and lie above a certain $m_{Tmin}$ value, a steeply falling behavior arises especially with respect to the full phase space (due to the distortion at higher pole masses).

| Source | $m_{W'}$, $m_{Tmin}$ [GeV] | | | | | | | | |
|---|---|---|---|---|---|---|---|---|---|
| | 300 | 400 | 500 | 600 | 750 | 1000 | 1250 | 1500 | 1750 |
| | 252 | 336 | 423 | 474 | 597 | 796 | 1002 | 1191 | 1416 |
| Efficiency | 2.7 | 2.7 | 2.7 | 2.6 | 2.6 | 2.5 | 2.5 | 2.5 | 2.5 |
| Resolution | 0.096 | 0.19 | 0.25 | 0.096 | 0.19 | 0.1 | 0.12 | 0.13 | 0.15 |
| Scale | 2.2 | 2.4 | 2.8 | 1.8 | 1.7 | 1.5 | 1.5 | 1.6 | 1.5 |
| $E_T^{miss}$ | 1.3 | 0.11 | 0.06 | 0.14 | 0.056 | 0.087 | 0.034 | 0.081 | 0.051 |
| Jet resolution | 0.52 | 0.17 | 0.028 | 0.12 | 0.073 | 0.064 | 0.06 | 0.09 | 0.029 |
| Jet scale | 0.7 | 0.25 | 0.073 | 0.21 | 0.12 | 0.022 | 0.043 | 0.091 | 0.021 |
| Pileup | 0.047 | 0.079 | 0.19 | 0.022 | 0.18 | 0.038 | 0.13 | 0.067 | 0.096 |
| All experimental | 3.8 | 3.6 | 3.9 | 3.2 | 3.1 | 3 | 2.9 | 3 | 2.9 |
| MC stats | 1.4 | 1.2 | 1.2 | 1.1 | 1 | 1 | 0.97 | 0.93 | 0.94 |
| k-factor | 0.13 | 0.13 | 0.21 | 0.45 | 0.49 | 0.69 | 1.2 | 1.9 | 2.5 |
| Beam energy | 0.012 | 0.015 | 0.018 | 0.02 | 0.03 | 0.056 | 0.1 | 0.17 | 0.31 |
| Total | 4.1 | 3.8 | 4.1 | 3.4 | 3.3 | 3.2 | 3.3 | 3.6 | 3.9 |

| Source | $m_{W'}$, $m_{Tmin}$ [GeV] | | | | | | | | |
|---|---|---|---|---|---|---|---|---|---|
| | 2000 | 2250 | 2500 | 2750 | 3000 | 3250 | 3500 | 3750 | 4000 |
| | 1500 | 1683 | 1888 | 1888 | 1888 | 1888 | 1888 | 1888 | 1888 |
| Efficiency | 2.5 | 2.5 | 2.5 | 2.5 | 2.5 | 2.5 | 2.5 | 2.5 | 2.5 |
| Resolution | 0.19 | 0.13 | 0.11 | 0.018 | 0.048 | 0.091 | 0.04 | 0.049 | 0.041 |
| Scale | 1.2 | 1.1 | 1.3 | 1.2 | 1 | 0.96 | 1 | 1.2 | 1.5 |
| $E_T^{miss}$ | 0.068 | 0.027 | 0.043 | 0.026 | 0.02 | 0.03 | 0.014 | 0.015 | 0.018 |
| Jet resolution | 0.062 | 0.024 | 0.065 | 0.019 | 0.022 | 0.0064 | 0.0084 | 0.0089 | 0.018 |
| Jet scale | 0.022 | 0.007 | 0.036 | 0.018 | 0.022 | 0.024 | 0.0064 | 0.016 | 0.0035 |
| Pileup | 0.078 | 0.0064 | 0.015 | 0.083 | 0.21 | 0.26 | 0.13 | 0.03 | 0.055 |
| All experimental | 2.8 | 2.8 | 2.8 | 2.8 | 2.7 | 2.7 | 2.7 | 2.8 | 2.9 |
| MC stats | 0.85 | 0.87 | 0.9 | 0.85 | 0.81 | 0.78 | 0.73 | 0.65 | 0.54 |
| k-factor | 2.9 | 3.6 | 5.9 | 9.7 | 15 | 26 | 39 | 51 | 56 |
| Beam energy | 0.52 | 0.9 | 1.5 | 2.3 | 3.3 | 4.3 | 5.1 | 5.4 | 5.2 |
| Total | 4.2 | 4.7 | 6.8 | 10 | 16 | 27 | 40 | 52 | 57 |

Table 8.3: W′ event selection efficiency uncertainties [%].

| Source | $m_{W^*}$, $m_{Tmin}$ [GeV] | | | | | | | | |
|---|---|---|---|---|---|---|---|---|---|
| | 400 | 500 | 600 | 750 | 1000 | 1250 | 1500 | 1750 | 2000 |
| | 317 | 377 | 448 | 564 | 710 | 843 | 1062 | 1191 | 1337 |
| Efficiency | 2.9 | 3 | 3 | 2.9 | 2.8 | 2.8 | 2.7 | 2.7 | 2.7 |
| Resolution | 0.22 | 0.28 | 0.24 | 0.23 | 0.094 | 0.21 | 0.18 | 0.17 | 0.36 |
| Scale | 3.4 | 2.7 | 2.7 | 2.6 | 2.8 | 2.4 | 2.4 | 2.4 | 2.4 |
| $E_T^{miss}$ | 0.15 | 0.25 | 0.13 | 0.076 | 0.17 | 0.12 | 0.087 | 0.12 | 0.083 |
| Jet resolution | 0.84 | 0.083 | 0.35 | 0.058 | 0.019 | 0.077 | 0.085 | 0.17 | 0.066 |
| Jet scale | 0.53 | 0.32 | 0.14 | 0.14 | 0.15 | 0.053 | 0.074 | 0.094 | 0.091 |
| Pileup | 0.24 | 0.67 | 0.25 | 0.23 | 0.60 | 0.17 | 0.16 | 0.33 | 0.019 |
| All experimental | 4.6 | 4.1 | 4 | 3.9 | 4 | 3.7 | 3.6 | 3.6 | 3.6 |
| MC stats | 1.7 | 1.6 | 1.5 | 1.6 | 1.4 | 1.3 | 1.3 | 1.3 | 1.2 |
| k-factor | 0.81 | 0.58 | 0.53 | 0.5 | 0.24 | 0.16 | 0.18 | 0.2 | 0.23 |
| Beam energy | 0.079 | 0.051 | 0.045 | 0.044 | 0.036 | 0.033 | 0.044 | 0.049 | 0.059 |
| Total | 4.9 | 4.4 | 4.3 | 4.2 | 4.2 | 3.9 | 3.9 | 3.9 | 3.9 |

| Source | $m_{W^*}$, $m_{Tmin}$ [GeV] | | | | | | | |
|---|---|---|---|---|---|---|---|---|
| | 2250 | 2500 | 2750 | 3000 | 3250 | 3500 | 3750 | 4000 |
| | 1416 | 1683 | 1888 | 1888 | 1888 | 1888 | 1888 | 1888 |
| Efficiency | 2.7 | 2.6 | 2.6 | 2.6 | 2.6 | 2.6 | 2.6 | 2.6 |
| Resolution | 0.074 | 0.15 | 0.2 | 0.14 | 0.055 | 0.17 | 0.18 | 0.088 |
| Scale | 2.1 | 2.4 | 2.5 | 2.1 | 1.9 | 1.7 | 1.5 | 1.3 |
| $E_T^{miss}$ | 0.044 | 0.031 | 0.071 | 0.077 | 0.038 | 0.054 | 0.013 | 0.031 |
| Jet resolution | 0.16 | 0.06 | 0.098 | 0.044 | 0.057 | 0.086 | 0.037 | 0.068 |
| Jet scale | 0.079 | 0.076 | 0.076 | 0.083 | 0.066 | 0.018 | 0.037 | 0.096 |
| Pileup | 0.069 | 0.99 | 0.11 | 1.3 | 0.39 | 0.74 | 0.15 | 0.45 |
| All experimental | 3.4 | 3.7 | 3.6 | 3.6 | 3.3 | 3.2 | 3 | 2.9 |
| MC stats | 1.1 | 1.2 | 1.3 | 1.2 | 1.2 | 1.3 | 1.3 | 1.4 |
| k-factor | 0.27 | 0.48 | 0.89 | 1.4 | 2.2 | 3.9 | 10 | 30 |
| Beam energy | 0.068 | 0.1 | 0.15 | 0.2 | 0.28 | 0.43 | 0.66 | 1 |
| Total | 3.6 | 3.8 | 4 | 3.9 | 4.1 | 5.2 | 11 | 31 |

Table 8.4: $W^*$ event selection efficiency uncertainties [%].

| D1 Operator | | | | | | |
|---|---|---|---|---|---|---|
| | $m_\chi$, $m_{Tmin}$ [GeV] | | | | | |
| Source | 1 | 100 | 200 | 400 | 1000 | 1300 |
| | 796 | 796 | 796 | 796 | 796 | 796 |
| Efficiency | 2.6 | 2.6 | 2.5 | 2.5 | 2.5 | 2.6 |
| Resolution | 0.71 | 0.75 | 0.59 | 0.42 | 0.26 | 1.1 |
| Scale | 3.8 | 1.6 | 3.4 | 1.2 | 1.8 | 1.3 |
| $E_T^{miss}$ | 0.91 | 0.5 | 0.96 | 0.21 | 0.31 | 0.33 |
| Jet resolution | 1.1 | 0.38 | 0.57 | 0.78 | 0.23 | 0.4 |
| Jet scale | 0.68 | 0.87 | 0.48 | 0.38 | 0.084 | 0.39 |
| Pileup | 0.37 | 3.3 | 1 | 2.3 | 3.2 | 3.2 |
| All experimental | 4.9 | 4.7 | 4.5 | 3.8 | 4.5 | 4.5 |
| MC stats | 6.4 | 5.6 | 4.9 | 4.1 | 3.5 | 3.6 |
| k-factor | 13 | 11 | 9.7 | 8.6 | 9.2 | 8.6 |
| Beam energy | 0 | 0 | 0 | 0 | 0 | 0 |
| Total | 15 | 13.2 | 11.8 | 10.3 | 10.8 | 10.4 |
| D5d Operator | | | | | | |
| | $m_\chi$, $m_{Tmin}$ [GeV] | | | | | |
| Source | 1 | 100 | 200 | 400 | 1000 | 1300 |
| | 597 | 597 | 597 | 597 | 597 | 597 |
| Efficiency | 2.7 | 2.6 | 2.5 | 2.5 | 2.4 | 2.5 |
| Resolution | 1.8 | 2.2 | 0.92 | 1.9 | 0.88 | 1.2 |
| Scale | 2.9 | 4 | 3.4 | 4.5 | 3 | 2.4 |
| $E_T^{miss}$ | 0.88 | 2.3 | 0.82 | 1.4 | 0.92 | 0.28 |
| Jet resolution | 1.2 | 1.8 | 0.64 | 0.97 | 0.79 | 1.4 |
| Jet scale | 0.99 | 1.3 | 0.8 | 2 | 1.4 | 0.91 |
| Pileup | 2.9 | 7.9 | 1 | 9.1 | 0.89 | 5.9 |
| All experimental | 5.5 | 10 | 4.6 | 11 | 4.9 | 7.1 |
| MC stats | 9.1 | 8.9 | 9 | 7.8 | 6.6 | 6.5 |
| k-factor | 4.4 | 3 | 2.9 | 3.5 | 4.2 | 5.6 |
| Beam energy | 0 | 0 | 0 | 0 | 0 | 0 |
| Total | 11.5 | 13.7 | 10.5 | 13.9 | 9.2 | 11.1 |
| D5c Operator | | | | | | |
| | $m_\chi$, $m_{Tmin}$ [GeV] | | | | | |
| Source | 1 | 100 | 200 | 400 | 1000 | 1300 |
| | 843 | 843 | 843 | 843 | 843 | 843 |
| Efficiency | 2.6 | 2.5 | 2.5 | 2.5 | 2.5 | 2.5 |
| Resolution | 0.49 | 0.14 | 0.47 | 0.41 | 0.24 | 0.11 |
| Scale | 1.9 | 1.7 | 1.4 | 2.2 | 1.7 | 1.6 |
| $E_T^{miss}$ | 0.29 | 0.076 | 0.32 | 0.31 | 0.26 | 0.073 |
| Jet resolution | 0.16 | 0.5 | 0.084 | 0.39 | 0.13 | 0.17 |
| Jet scale | 0.15 | 0.11 | 0.02 | 0.19 | 0.083 | 0.16 |
| Pileup | 1.3 | 3.4 | 1.8 | 3.6 | 0.072 | 1.1 |
| All experimental | 3.5 | 4.6 | 3.5 | 5 | 3 | 3.2 |
| MC stats | 4.1 | 3.9 | 4 | 3.7 | 3.5 | 3.4 |
| k-factor | 3.7 | 3.7 | 4.1 | 4 | 8.1 | 8.3 |
| Beam energy | 0 | 0 | 0 | 0 | 0 | 0 |
| Total | 6.5 | 7.1 | 6.7 | 7.4 | 9.3 | 9.5 |
| D9 Operator | | | | | | |
| | $m_\chi$, $m_{Tmin}$ [GeV] | | | | | |
| Source | 1 | 100 | 200 | 400 | 1000 | 1300 |
| | 843 | 843 | 843 | 843 | 843 | 843 |
| Efficiency | 2.5 | 2.5 | 2.5 | 2.5 | 2.5 | 2.5 |
| Resolution | 0.98 | 0.15 | 0.81 | 0.074 | 0.51 | 0.36 |
| Scale | 2.1 | 2.1 | 1.6 | 1.5 | 1.7 | 1.3 |
| $E_T^{miss}$ | 0.27 | 0.29 | 0.42 | 0.11 | 0.15 | 0.31 |
| Jet resolution | 0.52 | 0.18 | 0.29 | 0.34 | 0.3 | 0.42 |
| Jet scale | 0.26 | 0.24 | 0.27 | 0.079 | 0.078 | 0.18 |
| Pileup | 0.46 | 0.063 | 1.9 | 0.44 | 1.4 | 0.067 |
| All experimental | 3.5 | 3.3 | 3.7 | 3 | 3.4 | 2.8 |
| MC stats | 3.8 | 3.6 | 3.4 | 3.4 | 3.4 | 3.4 |
| k-factor | 3.6 | 3.4 | 3.7 | 4.6 | 7.3 | 9 |
| Beam energy | 0 | 0 | 0 | 0 | 0 | 0 |
| Total | 6.3 | 5.9 | 6.2 | 6.4 | 8.7 | 10 |

Table 8.5: WIMP event selection efficiency uncertainties [%].

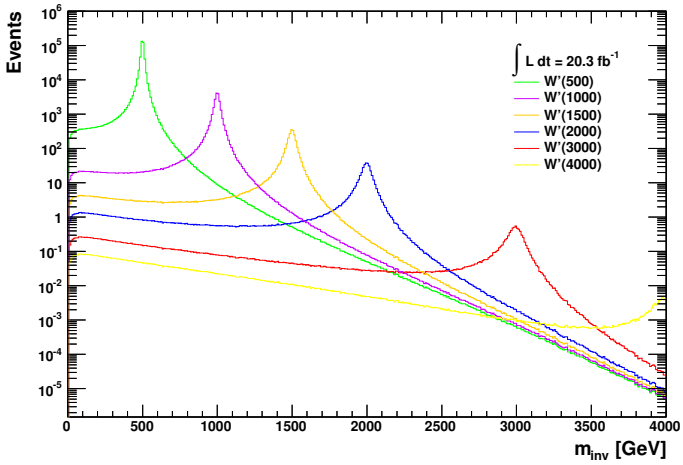


Figure 8.9: Spectrum of the invariant mass for different W′ pole masses (derived on generator level before any further selection criteria applied).

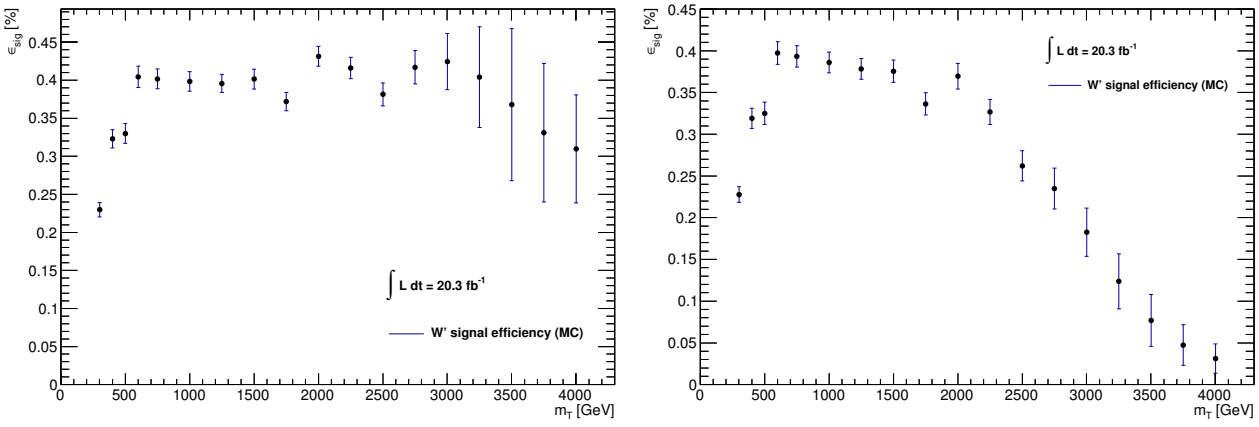


Figure 8.10: W′ signal efficiency in dependence of the W′ pole mass in the fiducial (left) and the full phase space (right). Both, statistical and systematic uncertainties are shown.

## 8.4 Bayes vs. Frequentist Limit Approaches

Due to the absence of any significant deviation in the comparisons of observed data distributions to the expected SM contributions, limits on the cross-section times branching fraction $\sigma B$ at each of a series of W′ or W* pole masses are set by counting events with $m_T > m_{T\,min}$. To investigate the influence of different limit setting approaches, both a conservative Bayesian and a Frequentist formalism are derived and compared. While exclusions based on the theorem of Bayes regard, in general, the degree of belief in the appropriate model parameters and, thus, assign a probability to a theory, the Frequentistic strategy tries to give for each theory the probability of an observation as function of the (unknown) model parameters in order to describe the experimental outcomes.
In the following, the different approaches are explained in detail.

### Bayes Analysis

Determining the exclusion contours with aid of a Bayesian approach, a single-bin likelihood analysis is performed. Here, the number of events observed above a certain minimal transverse mass value (denoted as $m_{T,min}$) is compared to the expectation due to the SM. Based on this, it can be decided if the recorded data advocate the discovery of a new physics scenario. To clarify, the unblinded spectrum of the transverse mass is shown again (Figure 8.11) visualizing the observation in data compared to the SM expectation overlaid with a signal of a potential heavier gauge boson.

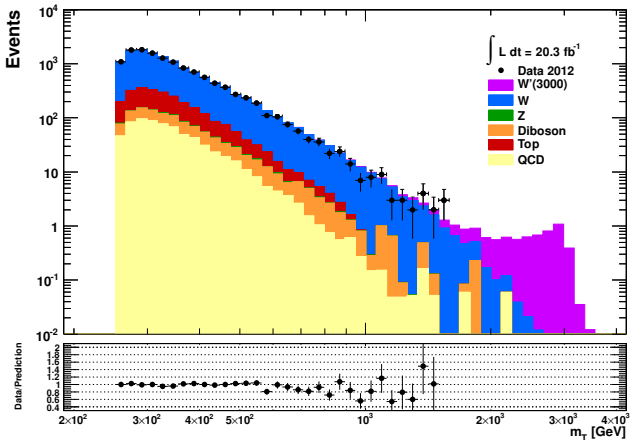


Figure 8.11: Unblinded spectrum of the transverse mass above 252 GeV after final event selection. The contribution of a W′ boson with a pole mass of 3000 GeV is shown in addition to the expected SM processes. The characteristic sharp edge above the resonance mass is visible.

Following the theorem of Bayes, the conditional probability for a certain event A to happen can be obtained as:

$$P(A|B) = \frac{P(B|A) \cdot P(A)}{P(B)} \tag{8.4}$$

where $P(B) > 0$. Thereby, P(A) (respectively P(B)) is denoted as a-priori probability (that is the initial probability for event A (respectively B)), P(B|A) is the (conditional) probability for a certain event B to happen upon condition that A has already entered. The probability P(B) functions as normalization.
In case of determining exclusion limits for a new physics scenario, not a single event B is regarded but a decomposition into disjoint events $B_i$ ($i = 1,...,N$) that correspond to a set of measurements. The underlying theory is then denoted as A (to stay with the formula above). Hence, P($B_i$|A) denotes the probability for measuring $B_i$ upon condition that the theory is true, and vise versa. In fact, P(A|$B_i$) is called a-posteriori probability since it describes the knowledge *after* a measurement and follows with respect to the a-priori probability.

To obtain in that manner the probability for a signal strength of a new physics scenario having the predicted value $\sigma B$, the a-priori (or shortly called prior) probability $P_{prior}(\sigma B)$ is chosen to be flat and equal to unity (and thus, independent of the signal strength) in order to not influence the final result with subjective informative priors. The wanted a-posteriori (shortly posterior) probability follows as:

$$P_{post}(\sigma B) = NL_B(\sigma B)P_{prior}(\sigma B) \tag{8.5}$$

whereby N denotes the normalization factor that is chosen such that $\int_0^\infty P_{post}(\sigma B)d(\sigma B) = 1$. A so-called likelihood function, $L_B(\sigma B)$, considers the single model parameters distinguished in those of interest such as the signal strength and those that are uncertain but not "of interest". The latter ones are called nuisance parameters and are associated to the systematic uncertainty sources like the integrated luminosity $L_{int}$, the signal efficiency $\varepsilon_{sig}$ and background estimation $N_{bkg}$ [118]. In the following, they are denoted as $\theta_i$. Hence, it is:

$$L_B(\sigma B) = \int d(\theta_1...\theta_N)L(\sigma B, \theta_1,...,\theta_N) \tag{8.6}$$

The likelihood function $L(\sigma B, \theta_1,...,\theta_N)$ contains not only the treatment of the experimental observation but also the arising systematic uncertainty sources. The number of observed events, $N_{obs}$, is handled with Poisson statistics to account for the rare appearance of these processes, while the uncertainties are taken into account by multiplying the corresponding probability density function (pdfs) to the likelihood for observing $N_{obs}$ events:

$$L(\sigma B, \theta_1,...,\theta_N) = L(\sigma B) \cdot \Pi g_i(\theta_i) \tag{8.7}$$

with $L(\sigma B)$ the likelihood for observed events:

$$L(\sigma B) = \frac{(L_{int}\varepsilon_{sig}\sigma B + N_{bkg})^{N_{obs}} e^{-(L_{int}\varepsilon_{sig}\sigma B + N_{bkg})}}{N_{obs}!} \tag{8.8}$$

Here, $L_{int}$ denotes the integrated luminosity, $\varepsilon_{sig}$ the signal efficiency and $N_{bkg}$ the sum of all background contributions also counted above a certain $m_{T,min}$ value. It is $g_i(\theta_i)$ the pdf for parameter $\theta_i$. Those pdfs can be interpreted as the prior probabilities related to the different uncertainty sources and described with aid of a log-normal distribution [Dem02].

[118] The word nuisance refers to something annoying. Within the Bayesian limit setting procedure, not only systematic uncertainties are taken into account but also limitations in MC statistics contribute in the summarized signal or background uncertainty.

As their determination is quite difficult, a subsequent integration prevents a dependence of these in the limit setting (Equ. 8.6).

The expected amount of events per decay channel consists of the predicted number of signal events, $N_{sig}$ with $N_{sig} = L_{int}\varepsilon_{sig}\sigma B$, and the expected contributions due to the underlying SM processes, $N_{bkg}$.

$$N_{exp} = N_{sig} + N_{bkg} \tag{8.9}$$

The final exclusion limit on $\sigma B$ should be within a certain credibility level (CL) such that:

$$CL_{bayes} = \int_0^{\sigma B} P_{post}(x)dx = 1 - p \tag{8.10}$$

The so-called p-value denotes an implicit significance level that describes the probability with that the background-only hypothesis can still be rejected mistakenly. Following this, the Bayesian limit setting approach aims to exclude a set of theories such that the posterior probability of the excluded theories is $1 - CL$.

### Frequentist's Point of View

In order to cross-check the Bayesian exclusions and to find approach based dependencies, limits will be derived also using one-sided hypothesis tests based on a so-called profile likelihood ratio.

Similar to the Bayesian limit setting formalism explained before, a single-bin likelihood analysis is performed to set limits on the cross-section times branching fraction $\sigma B$ at each of a series of W′ masses by counting events with $m_T > m_{Tmin}$. The thresholds are chosen identical to those used for the Bayesian analysis. Also the definition of the expected number of signal events is retained unchanged ((8.9)). The number of observed events is still treated with Poisson statistics.
In contrast to the Bayesian approach, the Frequentist hypothesis test is performed using the signal strength $\mu$ as parameter of interest. Thus, the expected number of events in total can be derived as $n_{exp} = \mu \cdot s + b$, where s is the signal contribution, b the background contribution. The histograms showing the cross-section times branching fraction $\sigma B$ versus the W′ mass can be obtained afterwards by multiplying the SSM cross-section to the signal strength. Theoretical uncertainties on the signal cross-section are not taken into account for calculating the limits as they are model-dependent.

As test statistics, the profile likelihood ratio [Ran12] is used:

$$\lambda = \frac{L_{s+b}(\mu, \hat{\hat{\theta}})}{L_{s+b}(\hat{\mu}, \hat{\theta})} \tag{8.11}$$

where the likelihood is defined as

$$L = Poisson(n_{obs}|\mu, \theta) Gaussian(\theta_0|\theta, \sigma_\theta). \tag{8.12}$$

The parameter of interest is defined as $\mu$, $\theta$ describes the nuisance parameters. The number of events in the data set is named $n_{obs}$. Using the nuisance parameters at their conditional estimate ($\theta = \hat{\theta}_\mu$),

many pseudo-experiments are generated by fitting them to the observed number of events. The constraint terms (e.g. systematic uncertainties) are treated as auxiliary measurements and introduced as global observables that are varied for each toy ($\theta_0$, considered constant while fitting). The profile likelihood ratio is evaluated by maximizing the likelihood function over the nuisance parameters (keep $\mu$ fixed and fit $\theta$) and normalized by maximizing the likelihood function with respect to all parameters (fit both $\mu$ and $\theta$). It is then a function of the parameter of interest alone that is broadened by the influence of the nuisance parameters. Since $\lambda$ has a Gaussian shape here, the negative logarithm of the profile likelihood ratio is a parabola. Multiplied with a factor of two, its asymptotic behavior is similar to a $\chi^2$ distribution with one degree of freedom (one parameter of interest only). The function $q = -2\ln(\lambda(\mu))$ is used afterwards to determine the p-value.
For each W′ mass point, a given interval of the parameter of interest $\mu$ is run through and a hypothesis test is performed at each value of $\mu$. The hypothesis test results are then inverted to obtain a confidence interval for the parameter of interest. The null hypothesis contains therefore a model including signal and background contributions, the alternative hypothesis is a background-only model.

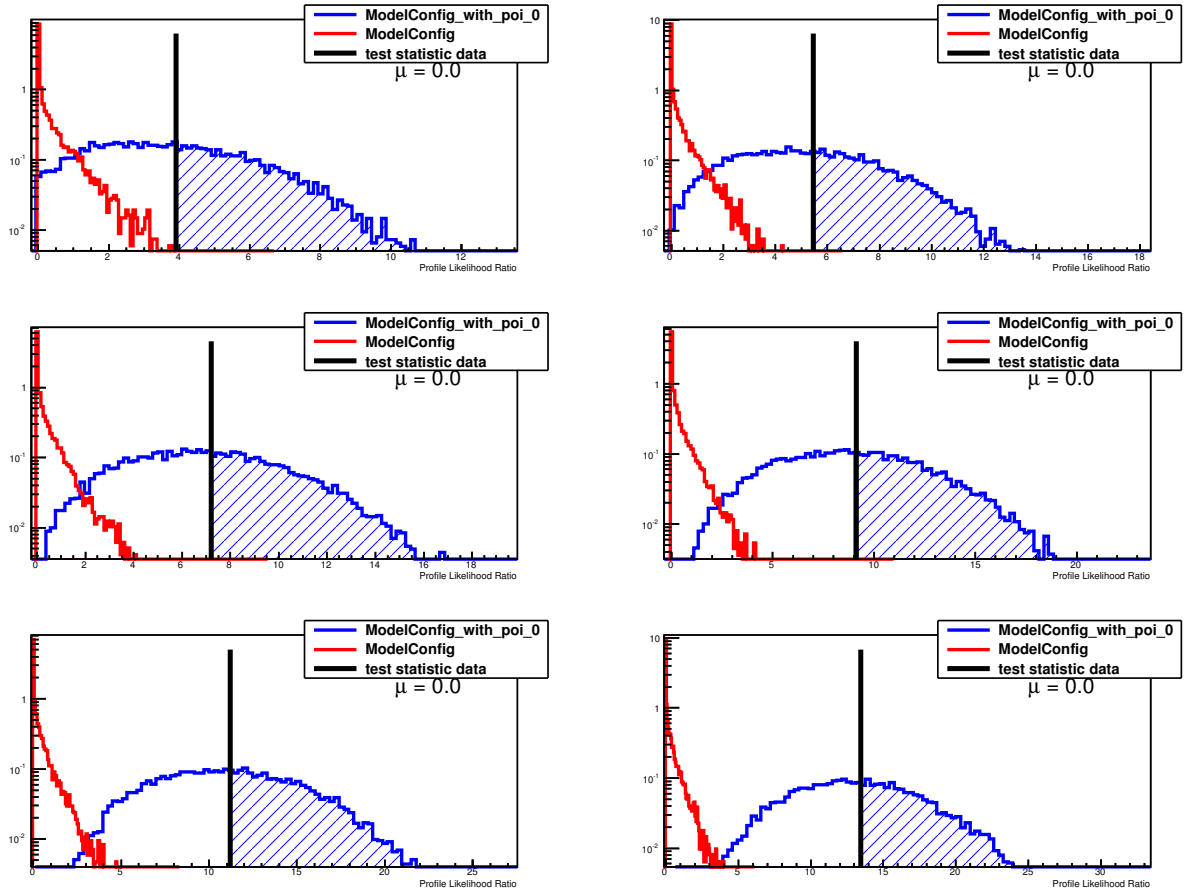


Figure 8.12: Example of hypothesis test results for a W′ mass point of 1250 GeV. The red curve describes the test statistics distribution of the signal hypothesis, the blue one shows the background-only result. The black line marks the data value ($n_{obs}$) from which the distributions will be integrated to obtain the corresponding p-value.

Figure 8.12 shows the hypothesis test results for a W′ mass point of 1250 GeV. The red curve is derived by the signal hypothesis, the blue distribution shows the background-only result. By integrating these test statistic distributions from the data value ($n_{obs}$), the p-value (and thus $CL_{s+b}$ and $CL_b$) can be derived. Figure 8.13 shows the Frequentist CL scan obtained with these hypothesis test results. Expected limit bands are evaluated by replacing the test statistics data value with quantiles of the background-only test statistics distribution.

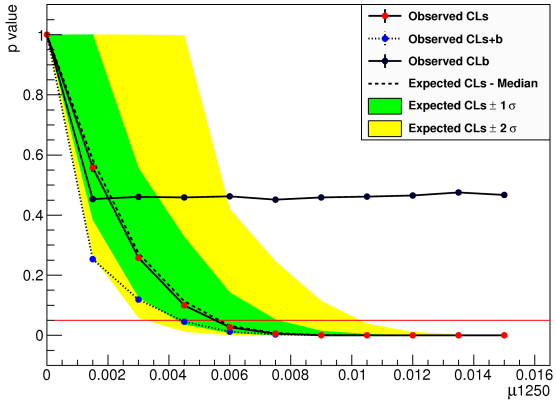


Figure 8.13: Frequentist CL scan for a W′ mass point of 1250 GeV.

The signal hypothesis is excluded above a certain signal strength value such that the statistical significance (p-value) is smaller than $\alpha$=5 % (i.e. 95 % confidence level (CL)). The so-called upper limit is, in fact, the largest value of the parameter of interest for which the probability of a signal under-fluctuation is above $\alpha$, i.e. $p \geq \alpha = 1 - CL$. In other words, the Frequentistic limits exclude all theories which produce the data at a probability less than $\alpha$.
To avoid limits that are too good, the $CL_s$ p-value distribution is used to obtain the point of intersection.

## 8.5 $m_{T\,min}$ Optimization

For calculating the various signal efficiencies and SM background contributions, events are counted in the transverse mass spectrum above a certain $m_{T\,min}$ value. This threshold has been evaluated by scanning the transverse mass spectrum and optimized on the expected significance of a given mass (adapting the Bayesian limit setting procedure). The scan granularity is defined here by the binning of the appropriate $m_T$ histogram.
The $m_{T\,min}$ values used subsequently are equal to those of the official ATLAS W′ working group. They had been optimized for electron and muon decays separately, and combined afterwards by always choosing the lowest border to not refuse any event of further interest [119].

[119] The single values were very close and the resulting deviations negligible small.

## 8.6 Limits

Both, the sum of all SM background contributions, $N_{bkg}$, and the amount of expected signal events (entering via the expected signal efficiency, $\varepsilon_{sig}$) are considered within the limit setting procedure. The number of observed events, $N_{obs}$, is thereby treated Poisson-distributed and determined by counting events above a certain $m_{T,min}$ value (as done for the SM and signal selections). That lower integration border varies for different W′ or W* pole masses as well as for the four considered DM operators (D1, D5(c), D9). In the following, the exclusion limits are determined and shown for the different new physics scenarios considered. Table 8.6 shows the various contributions to the SM background level for each transverse mass region; the resulting limit calculation inputs are listed and summarized additionally for each scenario separately in Tables 8.7, 8.8 and 8.9. To account for the different signal production mechanisms considered, the $m_{Tmin}$ values vary in dependence on the signal pole masses and with respect to the different new physics scenarios. In fact, the lowest integration interval in the search for heavier vector gauge bosons (W′) starts at 252 GeV for reasons as mentioned before. Considering the existence of charged chiral bosons (W*), the first lower integration border is set to 317 GeV. In the dark matter case involving a highly boosted SM W boson and large missing transverse energy, four strongly increased transverse mass regions are regarded only (one for each operator).

| $m_{Tmin}$ [GeV] | $N_{\mathrm{EW}}$ | $N_{\mathrm{top}}$ | $N_{\mathrm{QCD}}$ | $N_{bkg}$ | $N_{obs}$ |
|---|---|---|---|---|---|
| 252 | 1.07e+04 ±1.2e+02 | 1.53e+03 ±10.6 | 682 ±12 | 1.29e+04 ±1.2e+02 | 12717 |
| 317 | 5.48e+03 ±76 | 783 ±8 | 369 ±8.4 | 6.63e+03 ±77 | 6448 |
| 336 | 4.4e+03 ±65 | 596 ±7 | 291 ±7.3 | 5.28e+03 ±67 | 5176 |
| 377 | 2.82e+03 ±46 | 339 ±6.4 | 174 ±5.2 | 3.32e+03 ±47 | 3275 |
| 423 | 1.8e+03 ±30 | 184 ±5.4 | 99.3 ±3.7 | 2.08e+03 ±30 | 2017 |
| 448 | 1.42e+03 ±21 | 140 ±5.1 | 76.1 ±3.1 | 1.63e+03 ±22 | 1582 |
| 474 | 1.11e+03 ±14 | 99 ±4.8 | 56.8 ±2.6 | 1.27e+03 ±15 | 1214 |
| 564 | 539 ±5.3 | 37.9 ±4.1 | 21.6 ±1.4 | 593 ±6.1 | 524 |
| 597 | 419 ±4.7 | 26.4 ±4.0 | 16.1 ±1.1 | 461 ±5.3 | 414 |
| 710 | 191 ±3.2 | 11.6 ±3.3 | 5.39 ±0.53 | 203 ±3.4 | 177 |
| 796 | 111 ±2.3 | 4.74 ±1.69 | 2.81 ±0.29 | 118 ±2.4 | 101 |
| 843 | 82.2 ±2 | 2.89 ±1.87 | 2.06 ±0.17 | 85.6 ±2.1 | 79 |
| 1002 | 34.6 ±1.3 | 0.52 ±1.41 | 0.727 ±0.098 | 35.8 ±1.3 | 34 |
| 1062 | 25.3 ±1.1 | 0.27 ±1.16 | 0.513 ±0.081 | 25.8 ±1.1 | 26 |
| 1191 | 12.9 ±0.68 | 0.06 ±0.72 | 0.257 ±0.053 | 13.2 ±0.68 | 14 |
| 1337 | 6.62 ±0.45 | 0.01 ±0.42 | 0.13 ±0.033 | 6.75 ±0.45 | 9 |
| 1416 | 4.47 ±0.33 | 0.004 ±0.31 | 0.0925 ±0.025 | 4.57 ±0.33 | 5 |
| 1500 | 2.92 ±0.25 | 0.002 ±0.23 | 0.0662 ±0.02 | 2.99 ±0.25 | 3 |
| 1683 | 1.34 ±0.23 | 0.0002 ±0.13 | 0.0342 ±0.011 | 1.38 ±0.23 | 0 |
| 1888 | 0.415 ±0.0078 | 0.00001 ±0.07 | 0.0179 ±0.0066 | 0.432 ±0.01 | 0 |

Table 8.6: Single background contributions for $L_{int} = 20.3$ fb$^{-1}$ for each of the background samples separated (combined EW, top and QCD), and their sum. The given uncertainties are due to statistics only. The last column shows the observed number of events.

| $m_{W'}$ [GeV] | $m_{Tmin}$ [GeV] | $\varepsilon_{sig}^{fid}$ | $\varepsilon_{sig}$ | $N_{sig}$ | $N_{bkg}$ | $N_{obs}$ |
|---|---|---|---|---|---|---|
| 300 | 252 | 0.230±0.0094 | 0.228±0.0093 | 6.88e+05±2.8e+04 | 1.29e+04±8.2e+02 | 12717 |
| 400 | 336 | 0.323±0.012 | 0.319±0.012 | 3.25e+05±1.2e+04 | 5.28e+03±3.6e+02 | 5176 |
| 500 | 423 | 0.330±0.013 | 0.325±0.013 | 1.41e+05±5.7e+03 | 2.08e+03±1.5e+02 | 2017 |
| 600 | 474 | 0.404±0.014 | 0.397±0.014 | 8.38e+04±2.9e+03 | 1.27e+03±96 | 1214 |
| 750 | 597 | 0.402±0.013 | 0.393±0.013 | 3.32e+04±1.1e+03 | 461±45 | 414 |
| 1000 | 796 | 0.398±0.013 | 0.386±0.012 | 9.08e+03±2.9e+02 | 118±15 | 101 |
| 1250 | 1002 | 0.396±0.012 | 0.378±0.012 | 2.98e+03±98 | 35.8±5.8 | 34 |
| 1500 | 1191 | 0.401±0.013 | 0.376±0.014 | 1.11e+03±40 | 13.2±2.5 | 14 |
| 1750 | 1416 | 0.372±0.012 | 0.336±0.013 | 396±16 | 4.57±0.92 | 5 |
| 2000 | 1500 | 0.431±0.013 | 0.37±0.015 | 183±7.7 | 2.99±0.61 | 3 |
| 2250 | 1683 | 0.416±0.014 | 0.327±0.015 | 71.5±3.3 | 1.38±0.33 | 0 |
| 2500 | 1888 | 0.381±0.015 | 0.262±0.018 | 27.1±1.8 | 0.432±0.091 | 0 |
| 2750 | 1888 | 0.417±0.022 | 0.235±0.024 | 12.3±1.3 | 0.432±0.091 | 0 |
| 3000 | 1888 | 0.424±0.037 | 0.183±0.029 | 5.33±0.86 | 0.432±0.091 | 0 |
| 3250 | 1888 | 0.404±0.066 | 0.124±0.033 | 2.22±0.59 | 0.432±0.091 | 0 |
| 3500 | 1888 | 0.368±0.099 | 0.0769±0.031 | 0.917±0.36 | 0.432±0.091 | 0 |
| 3750 | 1888 | 0.331±0.091 | 0.0474±0.024 | 0.403±0.21 | 0.432±0.091 | 0 |
| 4000 | 1888 | 0.310±0.071 | 0.0311±0.018 | 0.197±0.11 | 0.432±0.091 | 0 |

Table 8.7: Inputs for the W′ limit calculations using data recorded with an integrated luminosity of $L_{int} \approx 20.3\,\text{fb}^{-1}$. The first two columns show the W′ pole mass and the $m_T$ threshold used for integration. The next two give the corrected signal selection efficiency, $\varepsilon_{sig}$, of the fiducial and the full phase space, followed by the prediction of the number of signal events, $N_{sig}$, obtained with the latter. The expected number of background events, $N_{bkg}$, and the number of events observed in data, $N_{obs}$, are shown in the last two columns. The uncertainties for $N_{sig}$ and $N_{bkg}$ include contributions from the uncertainties in the cross sections but not from the integrated luminosity.

| $m_{W^*}$ [GeV] | $m_{Tmin}$ [GeV] | $\varepsilon_{sig}^{fid}$ | $\varepsilon_{sig}$ | $N_{sig}$ | $N_{bkg}$ | $N_{obs}$ |
|---|---|---|---|---|---|---|
| 400 | 317 | 0.196±0.0097 | 0.196±0.0097 | 1.49e+05±7.4e+03 | 6.63e+03±4.4e+02 | 6448 |
| 500 | 377 | 0.246±0.011 | 0.246±0.011 | 8.09e+04±3.5e+03 | 3.32e+03±2.2e+02 | 3275 |
| 600 | 448 | 0.257±0.011 | 0.257±0.011 | 4.14e+04±1.8e+03 | 1.63e+03±1.2e+02 | 1582 |
| 750 | 564 | 0.248±0.011 | 0.248±0.011 | 1.59e+04±6.8e+02 | 593±54 | 524 |
| 1000 | 710 | 0.302±0.013 | 0.302±0.013 | 5.39e+03±2.3e+02 | 203±24 | 177 |
| 1250 | 843 | 0.337±0.013 | 0.337±0.013 | 2.01e+03±79 | 85.6±12 | 79 |
| 1500 | 1062 | 0.296±0.011 | 0.296±0.011 | 648±25 | 25.8±4.4 | 26 |
| 1750 | 1191 | 0.324±0.013 | 0.324±0.013 | 278±11 | 13.2±2.5 | 14 |
| 2000 | 1337 | 0.342±0.013 | 0.341±0.013 | 118±4.6 | 6.75±1.3 | 9 |
| 2250 | 1416 | 0.391±0.014 | 0.391±0.014 | 55.5±2 | 4.57±0.92 | 5 |
| 2500 | 1683 | 0.338±0.013 | 0.337±0.013 | 19.8±0.76 | 1.38±0.33 | 0 |
| 2750 | 1888 | 0.323±0.013 | 0.322±0.013 | 7.84±0.31 | 0.432±0.091 | 0 |
| 3000 | 1888 | 0.384±0.015 | 0.382±0.015 | 3.8±0.15 | 0.432±0.091 | 0 |
| 3250 | 1888 | 0.440±0.018 | 0.437±0.018 | 1.77±0.073 | 0.432±0.091 | 0 |
| 3500 | 1888 | 0.479±0.025 | 0.474±0.025 | 0.766±0.04 | 0.432±0.091 | 0 |
| 3750 | 1888 | 0.508±0.055 | 0.498±0.055 | 0.32±0.035 | 0.432±0.091 | 0 |
| 4000 | 1888 | 0.505±0.15 | 0.487±0.15 | 0.124±0.038 | 0.432±0.091 | 0 |

Table 8.8: Inputs for the W$^*$ limit calculations using data recorded with an integrated luminosity of $L_{int} \approx 20.3\,\text{fb}^{-1}$. The first two columns show the W$^*$ pole mass and the $m_T$ threshold used. The next two give the corrected signal selection efficiency, $\varepsilon_{sig}$, for the fiducial and full phase space, followed by the prediction of the number of signal events, $N_{sig}$, obtained with the latter. The expected number of background events, $N_{bkg}$, and the number of events observed in data, $N_{obs}$, are shown in the last two columns. The uncertainties for $N_{sig}$ and $N_{bkg}$ include contributions from the uncertainties in the cross sections but not from the integrated luminosity.

| $m_\chi$ [GeV] | $m_{Tmin}$ [GeV] | $\varepsilon_{sig}$ | $N_{sig}$ | $N_{bkg}$ | $N_{obs}$ |
|---|---|---|---|---|---|
| | | D1 Operator | | | |
| 1 | 796 | 0.0294±0.0044 | 8.72e-08±1.3e-08 | 118±15 | 101 |
| 100 | 796 | 0.0396±0.0052 | 8.89e-08±1.2e-08 | 118±15 | 101 |
| 200 | 796 | 0.0484±0.0057 | 6.58e-08±7.7e-09 | 118±15 | 101 |
| 400 | 796 | 0.0709±0.0071 | 3.09e-08±3.1e-09 | 118±15 | 101 |
| 1000 | 796 | 0.0989±0.01 | 1.07e-09±1.1e-10 | 118±15 | 101 |
| 1300 | 796 | 0.0964±0.0095 | 1.38e-10±1.4e-11 | 118±15 | 101 |
| | | D5d Operator | | | |
| 1 | 597 | 0.0148±0.0016 | 0.723±0.08 | 461±45 | 414 |
| 100 | 597 | 0.0158±0.0018 | 0.758±0.085 | 461±45 | 414 |
| 200 | 597 | 0.0147±0.0015 | 0.585±0.061 | 461±45 | 414 |
| 400 | 597 | 0.019±0.002 | 0.422±0.044 | 461±45 | 414 |
| 1000 | 597 | 0.0281±0.0025 | 0.045±0.0041 | 461±45 | 414 |
| 1300 | 597 | 0.0291±0.0028 | 0.00893±0.00085 | 461±45 | 414 |
| | | D5c Operator | | | |
| 1 | 843 | 0.0737±0.0047 | 30.3±1.9 | 85.6±12 | 79 |
| 100 | 843 | 0.0798±0.005 | 31±1.9 | 85.6±12 | 79 |
| 200 | 843 | 0.0762±0.0049 | 25.1±1.6 | 85.6±12 | 79 |
| 400 | 843 | 0.0857±0.0055 | 16.2±1 | 85.6±12 | 79 |
| 1000 | 843 | 0.0987±0.0091 | 1.28±0.12 | 85.6±12 | 79 |
| 1300 | 843 | 0.101±0.0095 | 0.24±0.023 | 85.6±12 | 79 |
| | | D9 Operator | | | |
| 1 | 843 | 0.085±0.0053 | 55.5±3.5 | 85.6±12 | 79 |
| 100 | 843 | 0.095±0.0056 | 55.8±3.3 | 85.6±12 | 79 |
| 200 | 843 | 0.104±0.0062 | 48.9±2.9 | 85.6±12 | 79 |
| 400 | 843 | 0.103±0.0067 | 25.5±1.6 | 85.6±12 | 79 |
| 1000 | 843 | 0.107±0.0092 | 1.63±0.14 | 85.6±12 | 79 |
| 1300 | 843 | 0.102±0.01 | 0.285±0.029 | 85.6±12 | 79 |

Table 8.9: Inputs for the mono-W limit calculations using data recorded with an integrated luminosity of $L_{int} \approx 20.3\,\text{fb}^{-1}$ and the operators D1, D5, D5c and D9. The first two columns show the WIMP mass $m_\chi$ and the $m_{Tmin}$ threshold used. The next two give the corrected signal selection efficiency, $\varepsilon_{sig}$, and the prediction for the number of signal events, $N_{sig}$, obtained with this efficiency. The expected number of background events, $N_{bkg}$, and the number of events observed in data, $N_{obs}$, are shown in the last two columns. The uncertainties for $N_{sig}$ and $N_{bkg}$ include contributions from the uncertainties in the cross sections but not from the integrated luminosity.

In order to determine the various exclusion limits, the Bayesian approach is utilized as described before. Figure 8.14 demonstrates the evaluation of the posterior probability and the derived cross-section times branching fraction limit versus the appropriate p-value for a W′ with pole mass of 3 TeV.

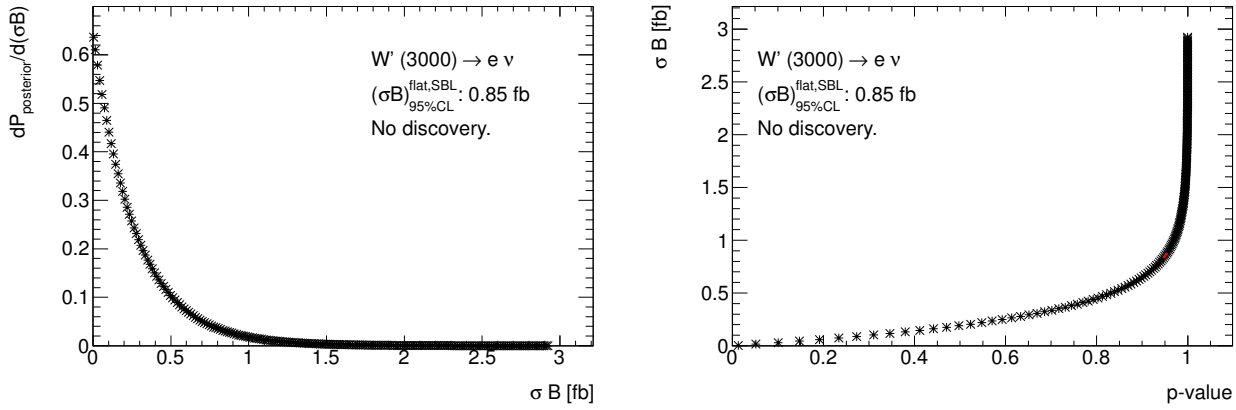


Figure 8.14: Derived posterior probability (left) and p-value dependence (right) shown for a W′ mass point of 3000 GeV. Signal efficiency, background level and integrated luminosity uncertainties are taken into account.

### Search for Heavier Charged Gauge Bosons (W′)

The Bayesian derived exclusion limits on the cross-section times branching fraction of a new heavier charged gauge boson, denoted as W′, are determined at a credibility level (CL) of 95 % in dependence of the signal pole mass as shown in Figure 8.15. For both, the fiducial ($m_{e\nu} > 0.4 m_{W'}$) and full phase space, the observed limit curve is visualized as black solid line, the black dashed lines show the expected exclusions. The corresponding ranges of one and two standard deviations are drawn additionally as green and yellow bands. Small fluctuations around the expected limit are visible in both, fiducial and full phase space distributions, but do not exceed the two $\sigma$ bands. Thus, also no significant excess is visible in these exclusion contours.
The final lower mass limits are derived using the signal cross-sections of a SSM W′ at next-to-next-to-leading order (NNLO) and are visualized as blue stars at the crossing point of theory prediction and observed (expected) limit curves. Theoretical uncertainties from variations of the renormalisation and factorisation scales, the choice of the parton distribution function (PDF) and PDF+$\alpha_s$ variations are shown in addition as width of the predicted theory band.
As already discussed in Sect. 2.3.1 and 8.3, steeply falling parton distribution functions at high values of Bjørken-x lead to significant distortions of the line shapes at high W′ pole masses. As a consequence, the derived cross-section limits increase again at high pole masses. The effect is strongly visible regarding the full phase space whereas the fiducial limit curve remains much more flat. Nevertheless, the lower mass limits to a SSM W′ boson are still in the same order of magnitude as shown in Table 8.6.

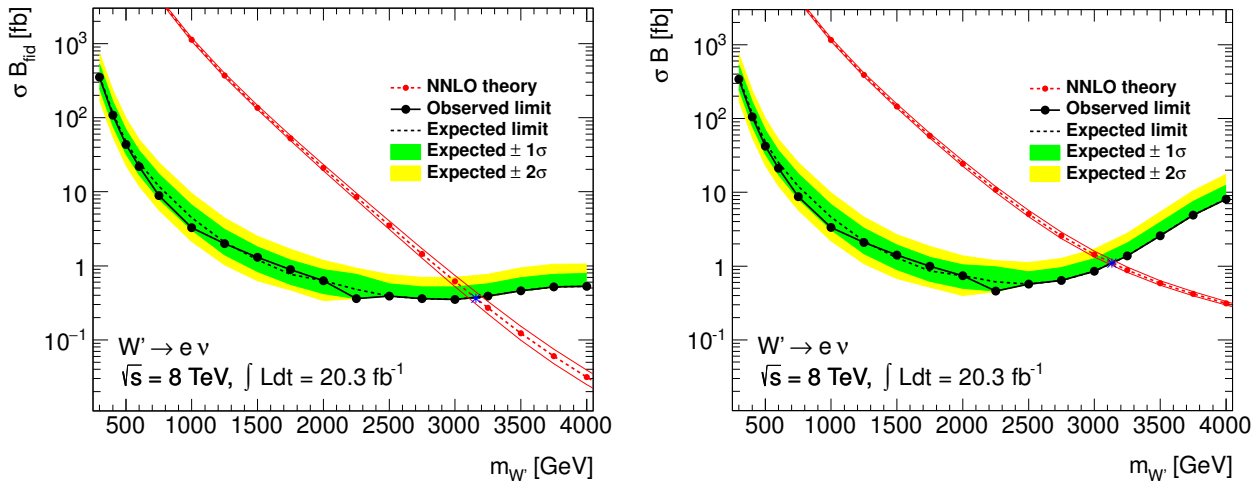


Figure 8.15: Observed and expected exclusion limits on the cross-section times branching fraction for an additional heavier charged vector gauge boson (W′) derived for a fiducial (left) and in the full phase space (right) at 95 % CL. The lower mass limits are visualized as blue stars.

| | $m_{W',exp}$ [TeV] | $m_{W',obs}$ [TeV] |
|---|---|---|
| fid. | 3.16 | 3.16 |
| full | 3.13 | 3.13 |

Table 8.10: Lower mass limits in terms of a SSM W′ derived at 95 %CL using a Bayesian approach.

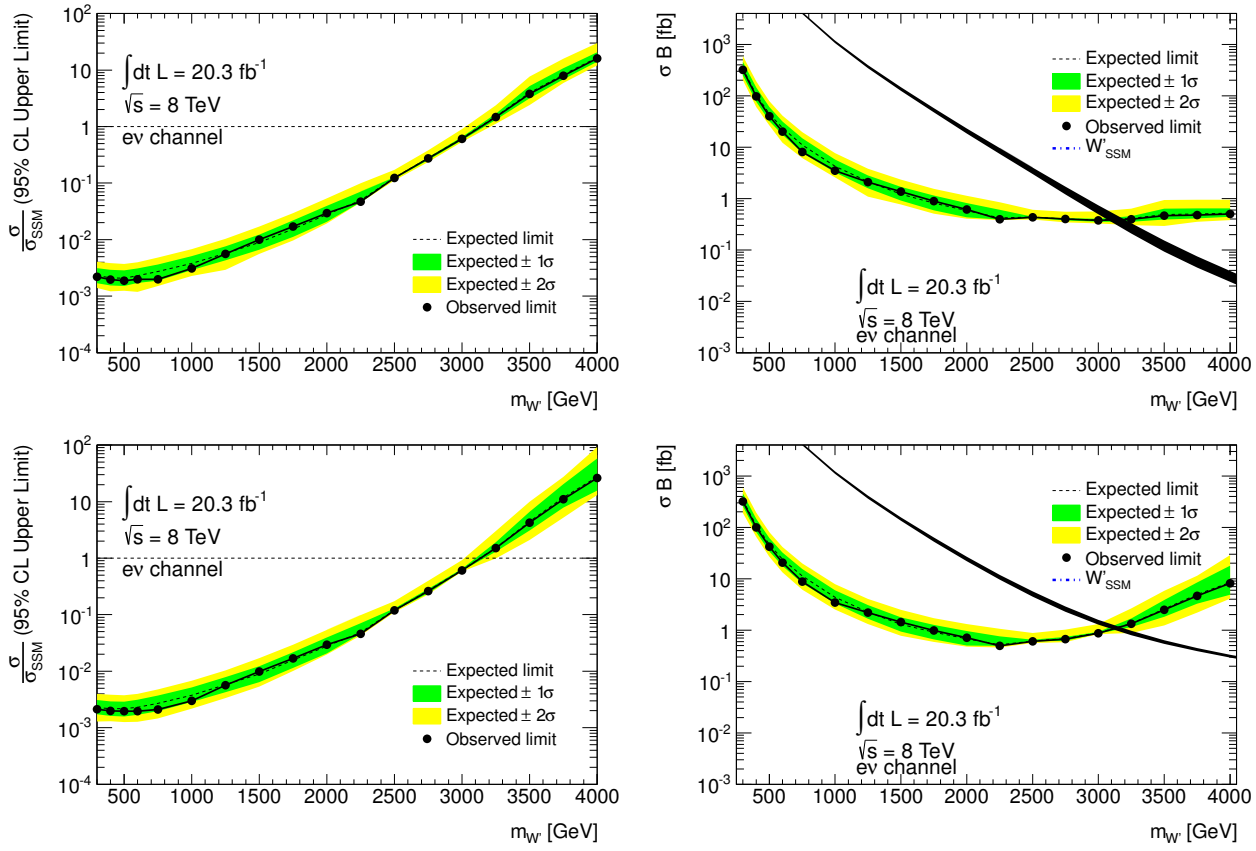


Figure 8.16: Exclusion limits obtained by using a profile likelihood ratio based analysis. The upper plots show the limit strength (left) and the limits on the cross-section times branching fraction $\sigma B$ (right) for a fiducial phase space defined as before; the lower ones include the total cross-section volume. The histograms showing the cross-section times branching fraction $\sigma B$ versus the W′ mass are obtained by multiplying the SSM cross-section to the signal strength. Theoretical uncertainties on the signal cross-section are drawn as theory band only and do not enter the limit calculation at all.

As already described before, the Frequentistic strategy is used to investigate the dependence on limit setting approaches. In contrast to the Bayesian one, the signal strength $\mu$ serves here as parameter of interest. The resulting signal strength and exclusions on the cross-section times branching fraction $\sigma B$ versus the W′ pole mass are shown in Figure 8.16. The latter are obtained by multiplying the SSM cross-section to the signal strength. Theoretical uncertainties on the signal cross-section are not taken into account for calculating the limits as they are model-dependent.

The agreement of the limits derived once with Bayesian and with Frequentist formalisms is within 10 % across the whole mass range (Figure 8.17). The Frequentistic approach used Gaussian-distributed nuisance parameters while the Bayesian considered nuisance parameters constrained by truncated log-normal distributions. However, the impact of the pdf (or constraint term) choice was investigated and shown in appendix, Sect. A.7. For Frequentistically derived limits, the impact is negligible and thus, comparing those to Bayesian exclusions with nuisance parameters constrained by truncated log-normal distributions involved, nearly no difference can be obtained.

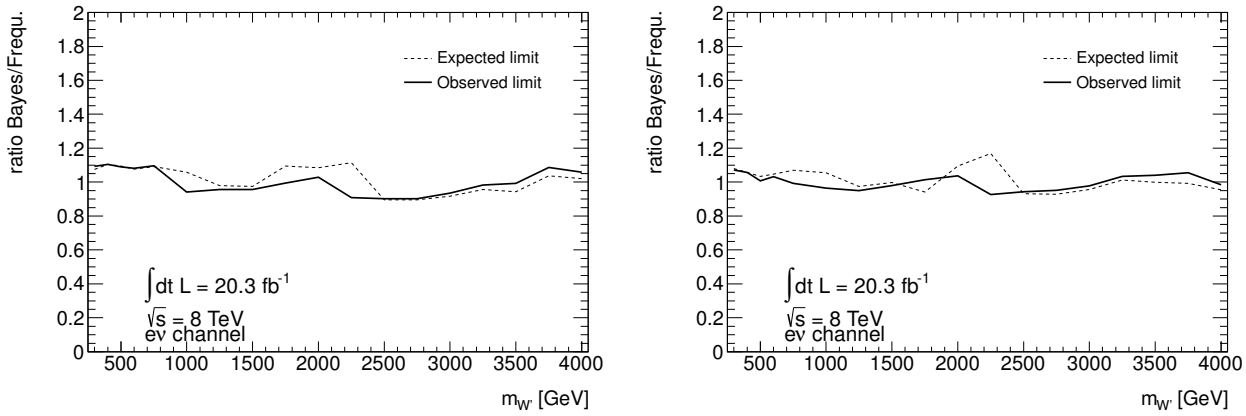


Figure 8.17: Observed and expected limits obtained with a Bayesian approach for both fiducial (left) and total phase space (right) in comparison to Frequentistic limits. Setting Bayesian limits, a truncated log-normal prior for pdf sets was used; nuisance parameters were constrained by a Gaussian distribution in the Frequentist formalism.

To be fully correct, interference effects between SSM W′ and SM W bosons should be accounted for (Sect. 2.3.1).

### Search for Charged Chiral Bosons (W*)

In contrast to additional heavy gauge bosons in context of the SSM, W′, new tensor interactions involving charged chiral bosons (W*) would not conserve the chirality. As a consequence, the new bosons would have to be doublets and so, would not mix with SM gauge bosons (before the symmetry breaking) [Chi00]. Hence, interference effects with SM W bosons must not be considered in the following.
Deriving the exclusion limits on the cross-section times branching fraction and the mass of such charged chiral bosons, the Bayesian approach has been used as introduced before. The limit inputs were shown in Table 8.8 and the resulting observed (black solid line) and expected (black dashed line) cross-section limits are given at 95 % CL in dependence of the boson pole mass for both, a fiducial (Fig. 8.18, left) and the full phase space volume (Fig. 8.18, right). The corresponding ranges of one and two standard deviations are drawn additionally as green and yellow bands around the expected limit curves. Also here, small fluctuations in the observed limit curves occur but, as before, do not exceed the two $\sigma$ bands and thus, no significant excess can be observed.
The theory prediction is visualized as red line, considering LO effects as discussed in Sect. 8.2. The blue stars indicate the lower mass limits on a new charged W* boson at the crossing point of theory prediction and observed (expected) limit curves.
In contrast to the exclusions derived for a SSM W′ boson, the difference between fiducial and full phase space cross-section limits is negligible small. The different shapes follow due to the totally different kinematic behavior of the W* compared to a SSM W′, especially in high mass regions (Sect. 2.3.1). Because of the missing tail dependency comparing fiducial to full cross-section limits and its fundamental different kinematic properties, it is important to consider such charged chiral bosons in addition to the commonly used SSM W′.

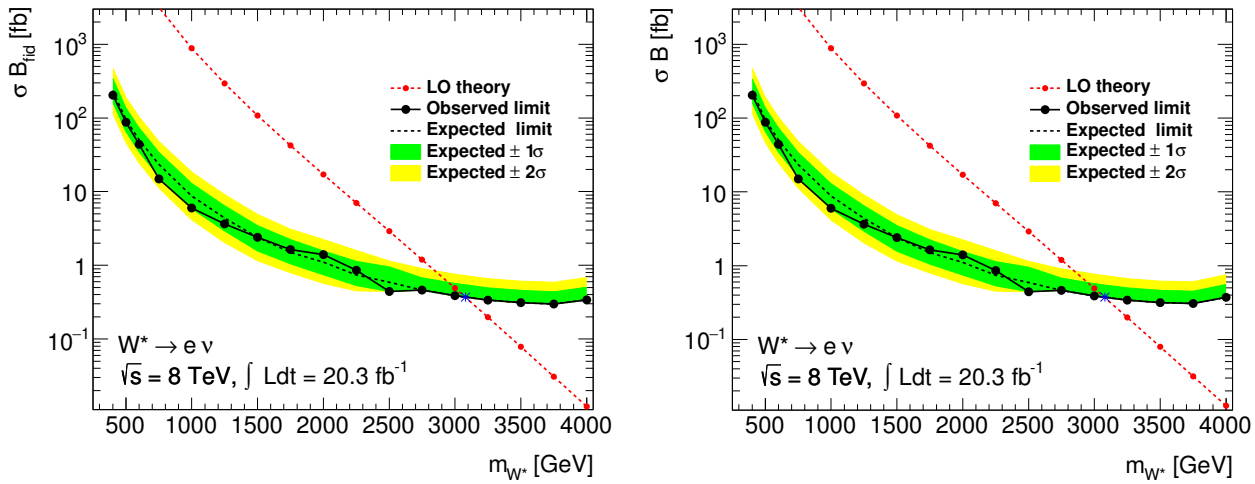


Figure 8.18: Observed and expected exclusion limits on the cross-section times branching fraction for a new charged chiral boson (W*) derived for a theory prediction at LO (95 % CL). The exclusions have been calculated with respect to both, a fiducial (left) and the full phase space (right). The lower mass limits are visualized as blue stars.

| | $m_{W^*,exp}$ [TeV] | $m_{W^*,obs}$ [TeV] |
|---|---|---|
| fid. | 3.08 | 3.08 |
| full | 3.08 | 3.08 |

Table 8.11: Lower mass limits in terms of a chiral $W^*$ boson derived at 95 %CL using a Bayesian approach.

### Dark Matter Interpretation ("mono-W")

Regarding WIMP pair production via initial-state radiation of a SM W boson, various operators might be used to describe the interactions occurring. However, as already described before, only a few characteristic kinematic distributions exist. To consider both, operators accounting for the spin-dependent and spin-independent parts of the elastic WIMP-nucleon scattering cross-section, not only the operator D9 but also D1 and D5 (constructive and desctructive mode) are regarded that treat each the WIMP as Dirac fermions.

Figure 8.19 shows the observed exclusion contours obtained using a Bayesian approach as described before for both, the mass scale $M_*$ of the unknown interaction (left) and the corresponding WIMP-nucleon scattering cross-section (right) in dependence of the WIMP mass. The exclusions were commonly derived for a coincidence level of 90 % assuming each operator considered to be the only DM-SM interaction (thus, the amount of expected events is slightly under-estimated). Referring to Equation 2.34, the $M_*$ limits are converted into $\sigma_{\chi-N}$ exclusions whereby the following dependencies are accounted for [Goo10]:

- for D1: $\sigma_{\chi-N} \propto \frac{\mu_\chi^2}{M_*^6}$
- for D5 (c,d) and D9: $\sigma_{\chi-N} \propto \frac{\mu_\chi^2}{M_*^4}$

where $\mu_\chi$ is the reduced mass of the WIMP-nucleon system. Regarding the limits on the mass scale $M_*$ of the unknown interaction (Fig. 8.19, left), the values below the line corresponding to an operator are excluded. For the corresponding WIMP-nucleon scattering cross-section limits, it is vise-versa.

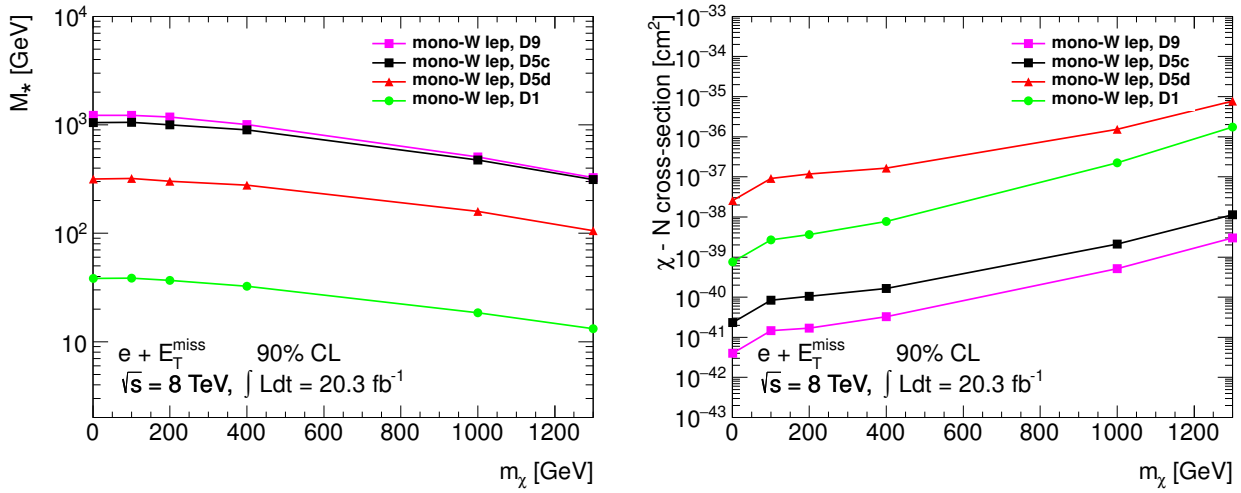


Figure 8.19: Observed limits obtained with a Bayesian approach for a dark matter (mono-W) search. Setting Bayesian limits, a truncated log-normal prior for pdf sets was used. The left side shows the exclusion contours in context of $M_*$, the WIMP-nucleon cross-section limits are shown on the right.

## 8.7 Comparison to Previous Experiments

Previously placed ATLAS exclusions from 2011 could be strongly improved and the lower observed (expected) exclusion limits on the pole mass raised to 3.13 TeV (3.13 TeV) for a SSM W′ boson considering the full phase space. In contrast to the most recent ATLAS publication, also an observed (expected) limit has been provided with respect to a fiducial volume: the lower mass limit to a SSM W′ boson is set to 3.16 TeV (3.16 TeV). Concerning also charged chiral bosons, denoted as W*, the lower mass limits are set to 3.08 TeV (3.08 TeV) for both, the full and the fiducial phase space. Although some analysis details had been changed for this dissertation (as providing a fitting procedure to estimate the top contribution at high transverse masses or the conservative treatment of the pileup related uncertainties), these results are in a very good agreement with the most recent published limits of ATLAS [ATL14d] and the CMS Collaboration [CMS08]. Additionally, the Bayesian derived exclusions have been cross-checked with respect to a SSM W′ boson using a Frequentistic approach, demonstrating a stable performance and a good agreement between both.
Also the dark matter exclusions derived with respect to initial-state radiation of a SM W boson are competitive with previous results. Table 8.12 and Figure 8.20 show again the previously placed exclusion contours in context of a SSM W′, a charged chiral W* and a dark matter search as described already in Section 2.3.3 [ATL14d].

| Experiment | Model | $m_{obs}$ [TeV] | $\sqrt{s}$ [TeV] | $L_{int}$ [fb$^{-1}$] |
|---|---|---|---|---|
| ATLAS (2014) [ATL14d] | W′ ($\rightarrow e\nu$) | 3.13 | 8 | 20.3 |
| ATLAS (2012) [ATL12g] | W′ ($\rightarrow e\nu$) | 2.50 | 7 | 4.7 |
| ATLAS (2011) [ATL11d] | W′ ($\rightarrow e\nu$) | 2.08 | 7 | 1.04 |
| ATLAS (2010) [ATL11c] | W′ ($\rightarrow e\nu$) | 1.37 | 7 | 0.036 |
| CDF II (2011) [CDF11] | W′ ($\rightarrow e\nu$) | 1.12 | 1.96 | 5.3 |
| CMS (2014) [CMS14] | W′ ($\rightarrow e\nu$) | 3.22 | 8 | 19.7 |
| CMS (2010) [CMS11a] | W′ ($\rightarrow e\nu$) | 1.36 | 7 | 0.036 |
| D0 (2008) [D008] | W′ ($\rightarrow e\nu$) | 1.00 | 1.96 | 1 |
| ATLAS (2014) [ATL14d] | W* ($\rightarrow e\nu$) | 3.08 | 8 | 20.3 |
| ATLAS (2012) [ATL12g] | W* ($\rightarrow e\nu$) | 2.35 | 7 | 4.7 |
| ATLAS (2010) [ATL11c] | W* ($\rightarrow e\nu$) | 1.26 | 7 | 0.036 |

Table 8.12: Observed lower mass limits to a SSM W′ and a W* boson (95 % CL.) for previous experiments in comparison. The first two columns show the experiment name and the model (decay channel) regarded. The third column visualizes the observed lower mass limits at 95 % CL, followed by the experiment's center-of-mass energy and the corresponding integrated luminosity.

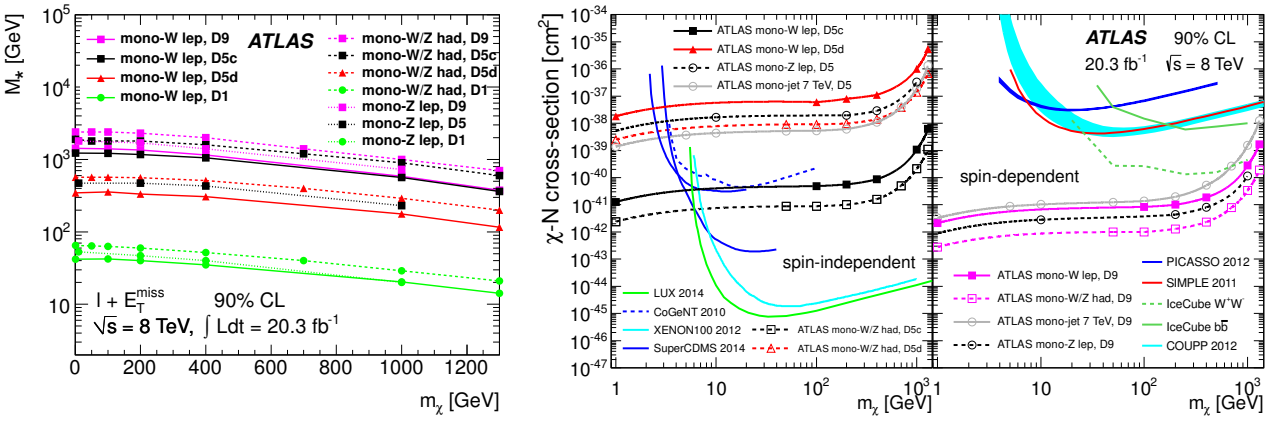


Figure 8.20: ATLAS exclusion contours to the mass scale $M_*$ of the unknown interaction (left) and to the corresponding WIMP-nucleon scattering cross-section (right), both in dependence of the WIMP mass and for a coincidence level of 90 %. They are competitive to those of other direct searches, shown here exemplarily for spin-dependent and -independent operators (D9, D5(c,d)) treating the WIMP as Dirac particle [ATL14d].

# 9 Summary and Outlook

Although the SM provides the opportunity to describe all known elementary particles and basic processes of three of the four fundamental interactions with few assumptions only in high precision, still not all observations and theoretical questions are covered. In fact, many models take the SM as a good approximation of natural phenomena in already discovered energy regions, but extend it in various ways. Nearly all of them are based on symmetry principles and predict in the sequel of involved symmetry breakings new (heavier) gauge bosons. Such new physics scenarios are commonly expected to arise for scales of at least 1 TeV and it is convenient to search for these in those high energy regions. The LHC provides the opportunity to look into these energy ranges using proton-proton collisions at significantly higher center-of-mass energies and corresponding integrated luminosities than previous experiments.

This dissertation analyzed the whole data set recorded in 2012 with the ATLAS detector at a center-of-mass energy of $\sqrt{s}$ =8 TeV and a corresponding integrated luminosity of about $L_{int}$ =20 fb$^{-1}$, focusing on leptonic final-states involving a high energy electron or positron and large missing transverse energy. To find any evidence to the existence of new physics beyond the SM, especially the spectrum of the combined transverse mass was searched for significant deviations between the data recorded and the expectations due to SM processes.

So, besides basic trigger studies that are crucial for understanding the underlying particle reconstruction and identification performances, the important SM processes arising were considered in detail and typical kinematic quantities were analyzed. The SM background contributions were, thereby, mainly based on official ATLAS Monte Carlo simulation sets, except that of mis-identified electrons. Such QCD events were derived by a data-based fake factor method. Summarizing, all spectra show the expected kinematic behavior and a good overall agreement between the data observed and the considered SM background contributions.

Unfortunately, no significant excess could be observed and exclusion limits to three different new physics scenarios were provided. Thereby, besides a so-called Sequential Standard Model (SSM) predicting additional spin-1 vector gauge bosons (namely W$'$ bosons for the charged current), the possible existence of (charged) chiral bosons called W$^*$ has been accounted for. While the first are assumed to carry the same couplings as SM W bosons with a strongly increased pole mass, the latter are expected to couple in an anomalous way, resulting in different kinematic distributions. In addition, also a dark matter interpretation involving WIMP (weakly interacting massive particles) pair production under initial-state radiation of a SM W boson decaying in turn leptonically has been considered.

A single-bin likelihood analysis was performed in terms of a Bayesian ansatz to determine limits to the cross-section times branching fraction of both, SSM W$'$ and chiral bosons. The final lower mass limits are derived at 95 % CL using the signal cross-section for W$'$ at next-to-next-to-leading order (NNLO) and for W$^*$ at leading order (LO). In case of a SSM W$'$ boson, they have been cross-checked via a profile likelihood based Frequentistic approach, too, demonstrating a good agreement within 10 % difference. Both approaches make use of the expected signal efficiencies, the amount of observed data and expected SM background events obtained within certain transverse mass regions depending on the regarded W$'$ mass point.
In addition, the observed data has been regarded in context of a search for DM particles with respect

to SM W boson radiation and exclusion limits were set similarly to the mass scale $M_*$ of the unknown interaction and the corresponding WIMP-nucleon scattering cross-section. Thereby, four operators were concerned in detail that treat WIMPs as Dirac fermions, namely D1, D5 (destructive mode), D5c (constructive mode) and D9.

Previously placed ATLAS exclusions could be strongly improved and the observed (expected) exclusion limits on the boson pole masses with respect to the full phase space raised to 3.13 TeV (3.13 TeV) for a SSM $W'$ boson and up to 3.08 TeV (3.08 TeV) for a charged chiral $W^*$ boson (with respect to final states with an electron involved) (at 95 % CL.). While the lower mass limit with respect to a fiducial volume does not change considering $W^*$ bosons, the exclusion limit slightly increases for SSM $W'$ bosons to 3.16 TeV (3.16 TeV). Because of the missing tail dependency comparing fiducial to full cross-section limits and its fundamental different kinematic properties, it is important to consider charged chiral bosons in addition to the commonly used SSM $W'$. These results are in a good agreement with the most recent published limits of ATLAS [ATL14d] and the CMS Collaboration [CMS08]. Also the dark matter exclusions derived with respect to initial-state radiation of a SM W boson (at 90 % CL.) are competitive with previous results of direct searches.

Nevertheless, the analysis procedure is still not fully optimized. The background description has a need, especially in higher transverse mass regions, for more statistics in Monte Carlo simulations (regarding in particular such side effects like W boson decays into a (anti-)neutrino and a tauon decaying in turn involving electrons). Also the possibility of using fitting functions to better describe the high energy regions (e.g. in the case of top background processes) may be followed up further. For up-coming analyses, it would be also reasonable to think about the usage of another event trigger. For this dissertation, a trigger was used with a high trigger threshold of 120 GeV introducing high cuts on the transverse electron momentum. In 2012, that unprescaled single photon trigger comprised the lowest energy threshold and was therefore reasonable to use to not refuse events which might be interesting for a search of new physics scenarios. Also the difficulty of describing the QCD background in a sufficient way played a role as the loose identification level required in coincidence with the trigger threshold provided the opportunity for a data-driven QCD background determination under usage of the signal trigger.
Considering also the treatment of arising pileup effects, caution should be required regarding the strongly increased center-of-mass energies and luminosities in present and up-coming data taking periods. Such effects will occur in an increased extent and will be, therefore, crucial in the determination (the resolution respectively) of the missing transverse energy.
Newer developments of the Monte Carlo generators (such as PYTHIA 8) would also provide the opportunity to include interference effects between SM W boson decays and those of additional heavy vector gauge bosons like the SSM $W'$ in a simple manner. These effects are well-known from the theory point of view and can cause significant differences in the transverse mass spectrum. Indeed, counting events above a certain transverse mass value to compare the observation to the SM expectations as it has been done within this dissertation and previous LHC analyses, may overestimate the amount of expected events and, thus, biases the limits obtained especially while interference effects are involved. So, the choice of that minimal transverse mass cut has to be optimized carefully or, respectively, the distribution shape has to be accounted for. A first estimation of the change in the lower mass limit on a left-handed $W'$ boson while considering also interference effects, has been performed by CMS resulting in an increase up to 3.41 TeV related to destructive interference (electron channel, 95 % CL.) and 3.54 TeV for constructive interference effects (electron channel, 95 %

CL.) (comparing to 3.22 TeV at 95 % CL. in the electron chain without interference effects taken into account) [CMS14].

In April 2015, the LHC started again with first beams at a center-of-mass energy of $\sqrt{s}$ =13 TeV, the bunch spacing has been changed later to 25 ns. With this, an integrated luminosity of about $L_{int}$ =3.3 fb$^{-1}$ has been recorded at the end of 2015. First up-dates of the ATLAS working groups have been published in spring 2016 presenting W′ mass limits increased to about 4 TeV at 95 % CL. [ATL15c]. A further increase of the center-of-mass energy to $\sqrt{s}$ =14 TeV is planned during Run 2 until mid of 2018 and a reach of significantly higher invariant masses and thus, a detection or, at least, significantly higher cross-section exclusions to the new physics scenarios will be possible.

# A Appendix

## A.1 Datasets

| |
|---|
| mc12_8TeV.158781.Pythia8_AU2MSTW2008LO_Wprime_emu_Flat.merge.NTUP_SMWZ.e1555_a159_a171_r3549_p1328/ |
| mc12_8TeV.158762.Pythia8_AU2MSTW2008LO_Wprime_emutau_3000.merge.NTUP_SMWZ.e1525_s1499_s1504_r3658_r3549_p1328/ |
| mc12_8TeV.158761.Pythia8_AU2MSTW2008LO_Wprime_emutau_1000.merge.NTUP_SMWZ.e1525_a159_a171_r3549_p1328/ |
| mc12_8TeV.158760.Pythia8_AU2MSTW2008LO_Wprime_emutau_500.merge.NTUP_SMWZ.e1525_a159_a171_r3549_p1328/ |
| mc12_8TeV.110931.MadGraphPythia8_CTEQ6L1_Wprime_tb_right_M3000.merge.NTUP_COMMON.e1555_s1499_s1504_r3658_r3549_p1562/ |
| mc12_8TeV.110964.MadGraphPythia8_CTEQ6L1_Wprime_tb_left_M3000.merge.NTUP_COMMON.e1555_s1499_s1504_r3658_r3549_p1562/ |
| mc12_8TeV.110762.MadGraphPythia8_AU2CTEQ6L1_Wprime_left_tb_hadronic_M3000.merge.NTUP_COMMON.e1817_s1499_s1504_r3658_r3549_p1562/ |
| mc12_8TeV.110729.MadGraphPythia8_AU2CTEQ6L1_Wprime_right_tb_hadronic_M3000.merge.NTUP_COMMON.e1817_s1499_s1504_r3658_r3549_p1562/ |
| mc12_8TeV.158763.CalcHepPythia8_AU2CTEQ6L1_WStar_template_enu.merge.NTUP_SMWZ.e1533_s1499_s1504_r3658_r3549_p1328/ |
| mc12_8TeV.158753.CalcHepPythia8_AU2CTEQ6L1_WStar_3000_enu.merge.NTUP_SMWZ.e1533_a159_a171_r3549_p1328/ |
| mc12_8TeV.158752.CalcHepPythia8_AU2CTEQ6L1_WStar_1000_enu.merge.NTUP_SMWZ.e1533_a159_a171_r3549_p1328/ |
| mc12_8TeV.158751.CalcHepPythia8_AU2CTEQ6L1_WStar_500_enu.merge.NTUP_SMWZ.e1533_a159_a171_r3549_p1328/ |
| mc12_8TeV.158820.MadgraphPythia8_AU2MSTW2008LO_WimpPair_D1_DM1_MS1000_lep.merge.NTUP_SMWZ.e1552_a159_a171_r3549_p1328/ |
| mc12_8TeV.158821.MadgraphPythia8_AU2MSTW2008LO_WimpPair_D1_DM100_MS1000_lep.merge.NTUP_SMWZ.e1552_a159_a171_r3549_p1328/ |
| mc12_8TeV.158822.MadgraphPythia8_AU2MSTW2008LO_WimpPair_D1_DM200_MS1000_lep.merge.NTUP_SMWZ.e1552_a159_a171_r3549_p1328/ |
| mc12_8TeV.158823.MadgraphPythia8_AU2MSTW2008LO_WimpPair_D1_DM400_MS1000_lep.merge.NTUP_SMWZ.e1552_a159_a171_r3549_p1328/ |
| mc12_8TeV.158824.MadgraphPythia8_AU2MSTW2008LO_WimpPair_D1_DM1000_MS1000_lep.merge.NTUP_SMWZ.e1552_a159_a171_r3549_p1328/ |
| mc12_8TeV.158825.MadgraphPythia8_AU2MSTW2008LO_WimpPair_D1_DM1300_MS1000_lep.merge.NTUP_SMWZ.e1552_a159_a171_r3549_p1328/ |
| mc12_8TeV.158826.MadgraphPythia8_AU2MSTW2008LO_WimpPair_D9_DM1_MS1000_lep.merge.NTUP_SMWZ.e1552_a159_a171_r3549_p1328/ |
| mc12_8TeV.158827.MadgraphPythia8_AU2MSTW2008LO_WimpPair_D9_DM100_MS1000_lep.merge.NTUP_SMWZ.e1552_a159_a171_r3549_p1328/ |
| mc12_8TeV.158828.MadgraphPythia8_AU2MSTW2008LO_WimpPair_D9_DM200_MS1000_lep.merge.NTUP_SMWZ.e1552_a159_a171_r3549_p1328/ |
| mc12_8TeV.158829.MadgraphPythia8_AU2MSTW2008LO_WimpPair_D9_DM400_MS1000_lep.merge.NTUP_SMWZ.e1552_a159_a171_r3549_p1328/ |
| mc12_8TeV.158830.MadgraphPythia8_AU2MSTW2008LO_WimpPair_D9_DM1000_MS1000_lep.merge.NTUP_SMWZ.e1552_a159_a171_r3549_p1328/ |
| mc12_8TeV.158831.MadgraphPythia8_AU2MSTW2008LO_WimpPair_D9_DM1300_MS1000_lep.merge.NTUP_SMWZ.e1552_a159_a171_r3549_p1328/ |
| mc12_8TeV.158832.MadgraphPythia8_AU2MSTW2008LO_WimpPair_D5_DM1_MS1000_lep.merge.NTUP_SMWZ.e1552_a159_a171_r3549_p1328/ |
| mc12_8TeV.158833.MadgraphPythia8_AU2MSTW2008LO_WimpPair_D5_DM100_MS1000_lep.merge.NTUP_SMWZ.e1552_a159_a171_r3549_p1328/ |
| mc12_8TeV.158834.MadgraphPythia8_AU2MSTW2008LO_WimpPair_D5_DM200_MS1000_lep.merge.NTUP_SMWZ.e1552_a159_a171_r3549_p1328/ |
| mc12_8TeV.158835.MadgraphPythia8_AU2MSTW2008LO_WimpPair_D5_DM400_MS1000_lep.merge.NTUP_SMWZ.e1552_a159_a171_r3549_p1328/ |
| mc12_8TeV.158836.MadgraphPythia8_AU2MSTW2008LO_WimpPair_D5_DM1000_MS1000_lep.merge.NTUP_SMWZ.e1552_a159_a171_r3549_p1328/ |
| mc12_8TeV.158837.MadgraphPythia8_AU2MSTW2008LO_WimpPair_D5_DM1300_MS1000_lep.merge.NTUP_SMWZ.e1552_a159_a171_r3549_p1328/ |
| mc12_8TeV.158838.MadgraphPythia8_AU2MSTW2008LO_WimpPair_D52_DM1_MS1000_lep.merge.NTUP_SMWZ.e1552_a159_a171_r3549_p1328/ |
| mc12_8TeV.158839.MadgraphPythia8_AU2MSTW2008LO_WimpPair_D52_DM100_MS1000_lep.merge.NTUP_SMWZ.e1552_a159_a171_r3549_p1328/ |
| mc12_8TeV.158840.MadgraphPythia8_AU2MSTW2008LO_WimpPair_D52_DM200_MS1000_lep.merge.NTUP_SMWZ.e1552_a159_a171_r3549_p1328/ |
| mc12_8TeV.158841.MadgraphPythia8_AU2MSTW2008LO_WimpPair_D52_DM400_MS1000_lep.merge.NTUP_SMWZ.e1552_a159_a171_r3549_p1328/ |
| mc12_8TeV.158842.MadgraphPythia8_AU2MSTW2008LO_WimpPair_D52_DM1000_MS1000_lep.merge.NTUP_SMWZ.e1552_a159_a171_r3549_p1328/ |
| mc12_8TeV.158843.MadgraphPythia8_AU2MSTW2008LO_WimpPair_D52_DM1300_MS1000_lep.merge.NTUP_SMWZ.e1552_a159_a171_r3549_p1328/ |
| mc12_8TeV.147800.PowhegPythia8_AU2CT10_Wplusenu.merge.NTUP_SMWZ.e1169_s1469_s1470_r3542_r3549_p1328/ |
| mc12_8TeV.147803.PowhegPythia8_AU2CT10_Wminenu.merge.NTUP_SMWZ.e1169_s1469_s1470_r3542_r3549_p1328/ |
| mc12_8TeV.147802.PowhegPythia8_AU2CT10_Wplustaunu.merge.NTUP_SMWZ.e1169_s1469_s1470_r3542_r3549_p1328/ |
| mc12_8TeV.147805.PowhegPythia8_AU2CT10_Wmintaunu.merge.NTUP_SMWZ.e1169_s1469_s1470_r3542_r3549_p1328/ |
| mc12_8TeV.129566.PowhegPythia8_AU2CT10_Wminenu_200M500.merge.NTUP_SMWZ.e1506_a159_a171_r3549_p1328/ |
| mc12_8TeV.129561.PowhegPythia8_AU2CT10_Wplusenu_200M500.merge.NTUP_SMWZ.e1506_a159_a171_r3549_p1328/ |
| mc12_8TeV.129567.PowhegPythia8_AU2CT10_Wminenu_500M1500.merge.NTUP_SMWZ.e1506_a159_a171_r3549_p1328/ |
| mc12_8TeV.129562.PowhegPythia8_AU2CT10_Wplusenu_500M1500.merge.NTUP_SMWZ.e1506_a159_a171_r3549_p1328/ |
| mc12_8TeV.129563.PowhegPythia8_AU2CT10_Wplusenu_1500M2500.merge.NTUP_SMWZ.e1506_a159_a171_r3549_p1328/ |
| mc12_8TeV.129568.PowhegPythia8_AU2CT10_Wminenu_1500M2500.merge.NTUP_SMWZ.e1506_a159_a171_r3549_p1328/ |
| mc12_8TeV.129564.PowhegPythia8_AU2CT10_Wplusenu_2500M3000.merge.NTUP_SMWZ.e1506_s1499_s1504_r3658_r3549_p1328/ |
| mc12_8TeV.129569.PowhegPythia8_AU2CT10_Wminenu_2500M3000.merge.NTUP_SMWZ.e1506_s1499_s1504_r3658_r3549_p1328/ |
| mc12_8TeV.129602.PowhegPythia8_AU2CT10_Wminenu_3000M3500.merge.NTUP_SMWZ.e1506_a159_a171_r3549_p1328/ |
| mc12_8TeV.129600.PowhegPythia8_AU2CT10_Wplusenu_3000M3500.merge.NTUP_SMWZ.e1506_a159_a171_r3549_p1328/ |
| mc12_8TeV.129603.PowhegPythia8_AU2CT10_Wminenu_3500M.merge.NTUP_SMWZ.e1506_a159_a171_r3549_p1328/ |
| mc12_8TeV.129601.PowhegPythia8_AU2CT10_Wplusenu_3500M.merge.NTUP_SMWZ.e1506_a159_a171_r3549_p1328/ |

mc12_8TeV.129590.PowhegPythia8_AU2CT10_Wplusenu_LeptonFilterPt100.merge.NTUP_SMWZ.e1552_a159_a171_r3549_p1328/
mc12_8TeV.129593.PowhegPythia8_AU2CT10_Wminenu_LeptonFilterPt100.merge.NTUP_SMWZ.e1552_a159_a171_r3549_p1328/
mc12_8TeV.129620.PowhegPythia8_AU2CT10_Wplusenu_LeptonFilterPt150.merge.NTUP_SMWZ.e1552_a159_a171_r3549_p1328/
mc12_8TeV.129623.PowhegPythia8_AU2CT10_Wminenu_LeptonFilterPt150.merge.NTUP_SMWZ.e1552_a159_a171_r3549_p1328/
mc12_8TeV.129633.PowhegPythia8_AU2CT10_Wminenu_LeptonFilterPt200.merge.NTUP_SMWZ.e1552_a159_a171_r3549_p1328/
mc12_8TeV.129630.PowhegPythia8_AU2CT10_Wplusenu_LeptonFilterPt200.merge.NTUP_SMWZ.e1552_a159_a171_r3549_p1328/
mc12_8TeV.129640.PowhegPythia8_AU2CT10_Wplusenu_LeptonFilterPt300.merge.NTUP_SMWZ.e1552_s1499_s1504_r3658_r3549_p1328/
mc12_8TeV.129643.PowhegPythia8_AU2CT10_Wminenu_LeptonFilterPt300.merge.NTUP_SMWZ.e1552_s1499_s1504_r3658_r3549_p1328/
mc12_8TeV.129581.PowhegPythia8_AU2CT10_Wplustaunu_200M500.merge.NTUP_SMWZ.e1951_a188_a171_r3549_p1328/
mc12_8TeV.129586.PowhegPythia8_AU2CT10_Wmintaunu_200M500.merge.NTUP_SMWZ.e1951_a188_a171_r3549_p1328/
mc12_8TeV.129582.PowhegPythia8_AU2CT10_Wplustaunu_500M1500.merge.NTUP_SMWZ.e1951_a188_a171_r3549_p1328/
mc12_8TeV.129587.PowhegPythia8_AU2CT10_Wmintaunu_500M1500.merge.NTUP_SMWZ.e1951_a188_a171_r3549_p1328/
mc12_8TeV.129583.PowhegPythia8_AU2CT10_Wplustaunu_1500M2500.merge.NTUP_SMWZ.e1951_a188_a171_r3549_p1328/
mc12_8TeV.129588.PowhegPythia8_AU2CT10_Wmintaunu_1500M2500.merge.NTUP_SMWZ.e1951_a188_a171_r3549_p1328/
mc12_8TeV.129584.PowhegPythia8_AU2CT10_Wplustaunu_2500M3000.merge.NTUP_SMWZ.e1951_a188_a171_r3549_p1328/
mc12_8TeV.129589.PowhegPythia8_AU2CT10_Wmintaunu_2500M3000.merge.NTUP_SMWZ.e1951_a188_a171_r3549_p1328/
mc12_8TeV.129608.PowhegPythia8_AU2CT10_Wplustaunu_3000M3500.merge.NTUP_SMWZ.e1951_a188_a171_r3549_p1328/
mc12_8TeV.129610.PowhegPythia8_AU2CT10_Wmintaunu_3000M3500.merge.NTUP_SMWZ.e1951_a188_a171_r3549_p1328/
mc12_8TeV.129609.PowhegPythia8_AU2CT10_Wplustaunu_3500M.merge.NTUP_SMWZ.e1951_a188_a171_r3549_p1328/
mc12_8TeV.129611.PowhegPythia8_AU2CT10_Wmintaunu_3500M.merge.NTUP_SMWZ.e1951_a188_a171_r3549_p1328/
mc12_8TeV.105200.McAtNloJimmy_CT10_ttbar_LeptonFilter.merge.NTUP_SMWZ.e1513_s1499_s1504_r3945_r3549_p1328/
mc12_8TeV.105861.PowhegPythia_AUET2BCT10_ttbar_LeptonFilter.merge.NTUP_SMWZ.e1317_a159_a165_r3549_p1328/
mc12_8TeV.108343.McAtNloJimmy_AUET2CT10_SingleTopSChanWenu.merge.NTUP_SMWZ.e1525_s1499_s1504_r3658_r3549_p1328/
mc12_8TeV.108345.McAtNloJimmy_AUET2CT10_SingleTopSChanWtaunu.merge.NTUP_SMWZ.e1525_s1499_s1504_r3658_r3549_p1328/
mc12_8TeV.117360.AcerMCPythia_AUET2BCTEQ6L1_singletop_tchan_e.merge.NTUP_SMWZ.e1346_s1499_s1504_r3658_r3549_p1328/
mc12_8TeV.117362.AcerMCPythia_AUET2BCTEQ6L1_singletop_tchan_tau.merge.NTUP_SMWZ.e1346_s1499_s1504_r3658_r3549_p1328/
mc12_8TeV.108346.McAtNloJimmy_AUET2CT10_SingleTopWtChanIncl.merge.NTUP_SMWZ.e1525_s1499_s1504_r3658_r3549_p1328/
mc12_8TeV.126892.Sherpa_CT10_llnunu_WW.merge.NTUP_SMWZ.e1434_s1499_s1504_r3658_r3549_p1328/
mc12_8TeV.126893.Sherpa_CT10_lllnu_WZ.merge.NTUP_SMWZ.e1434_s1499_s1504_r3658_r3549_p1328/
mc12_8TeV.126895.Sherpa_CT10_llnunu_ZZ.merge.NTUP_SMWZ.e1434_s1499_s1504_r3658_r3549_p1328/
mc12_8TeV.126894.Sherpa_CT10_llll_ZZ.merge.NTUP_SMWZ.e1434_s1499_s1504_r3658_r3549_p1328/
mc12_8TeV.157814.Sherpa_CT10_VVtoeeqq.merge.NTUP_SMWZ.e1515_s1499_s1504_r3658_r3549_p1328/
mc12_8TeV.157815.Sherpa_CT10_VVtomumuqq.merge.NTUP_SMWZ.e1515_s1499_s1504_r3658_r3549_p1328/
mc12_8TeV.157816.Sherpa_CT10_VVtotautauqq.merge.NTUP_SMWZ.e1515_s1499_s1504_r3658_r3549_p1328/
mc12_8TeV.157817.Sherpa_CT10_VVtoenuqq.merge.NTUP_SMWZ.e1515_s1499_s1504_r3658_r3549_p1328/
mc12_8TeV.157818.Sherpa_CT10_VVtomunuqq.merge.NTUP_SMWZ.e1515_s1499_s1504_r3658_r3549_p1328/
mc12_8TeV.157819.Sherpa_CT10_VVtotaunuqq.merge.NTUP_SMWZ.e1515_s1499_s1504_r3658_r3549_p1328/
mc12_8TeV.146436.AlpgenJimmy_AUET2CTEQ6L1_WgammaNp0_leptonPhotonFilter.merge.NTUP_SMWZ.e1260_s1469_s1470_r3542_r3549_p1328/
mc12_8TeV.146437.AlpgenJimmy_AUET2CTEQ6L1_WgammaNp1_leptonPhotonFilter.merge.NTUP_SMWZ.e1260_s1469_s1470_r3752_r3549_p1328/
mc12_8TeV.146438.AlpgenJimmy_AUET2CTEQ6L1_WgammaNp2_leptonPhotonFilter.merge.NTUP_SMWZ.e1260_s1469_s1470_r3542_r3549_p1328/
mc12_8TeV.146439.AlpgenJimmy_AUET2CTEQ6L1_WgammaNp3_leptonPhotonFilter.merge.NTUP_SMWZ.e1293_s1469_s1470_r3752_r3549_p1328/
mc12_8TeV.147806.PowhegPythia8_AU2CT10_Zee.merge.NTUP_SMWZ.e1169_s1469_s1470_r3542_r3549_p1328/
mc12_8TeV.147808.PowhegPythia8_AU2CT10_Ztautau.merge.NTUP_SMWZ.e1169_s1469_s1470_r3542_r3549_p1328/
mc12_8TeV.129506.PowhegPythia8_AU2CT10_DYee_250M400.merge.NTUP_SMWZ.e1248_s1469_s1470_r3542_r3549_p1328/
mc12_8TeV.129507.PowhegPythia8_AU2CT10_DYee_400M600.merge.NTUP_SMWZ.e1248_s1469_s1470_r3542_r3549_p1328/
mc12_8TeV.129508.PowhegPythia8_AU2CT10_DYee_600M800.merge.NTUP_SMWZ.e1248_s1469_s1470_r3542_r3549_p1328/
mc12_8TeV.129509.PowhegPythia8_AU2CT10_DYee_800M1000.merge.NTUP_SMWZ.e1248_s1469_s1470_r3542_r3549_p1328/
mc12_8TeV.129510.PowhegPythia8_AU2CT10_DYee_1000M1250.merge.NTUP_SMWZ.e1248_s1469_s1470_r3542_r3549_p1328/
mc12_8TeV.129511.PowhegPythia8_AU2CT10_DYee_1250M1500.merge.NTUP_SMWZ.e1248_s1469_s1470_r3542_r3549_p1328/
mc12_8TeV.129512.PowhegPythia8_AU2CT10_DYee_1500M1750.merge.NTUP_SMWZ.e1248_s1469_s1470_r3752_r3549_p1328/
mc12_8TeV.129513.PowhegPythia8_AU2CT10_DYee_1750M2000.merge.NTUP_SMWZ.e1248_s1469_s1470_r3542_r3549_p1328/
mc12_8TeV.129514.PowhegPythia8_AU2CT10_DYee_2000M2250.merge.NTUP_SMWZ.e1248_s1469_s1470_r3542_r3549_p1328/
mc12_8TeV.129515.PowhegPythia8_AU2CT10_DYee_2250M2500.merge.NTUP_SMWZ.e1248_s1469_s1470_r3542_r3549_p1328/
mc12_8TeV.129516.PowhegPythia8_AU2CT10_DYee_2500M2750.merge.NTUP_SMWZ.e1248_s1469_s1470_r3752_r3549_p1328/
mc12_8TeV.129517.PowhegPythia8_AU2CT10_DYee_2750M3000.merge.NTUP_SMWZ.e1248_s1469_s1470_r3752_r3549_p1328/
mc12_8TeV.129518.PowhegPythia8_AU2CT10_DYee_3000M.merge.NTUP_SMWZ.e1248_s1469_s1470_r3752_r3549_p1328/
mc12_8TeV.129546.PowhegPythia8_AU2CT10_DYtautau_250M400.merge.NTUP_SMWZ.e1248_s1469_s1470_r3542_r3549_p1328/
mc12_8TeV.129547.PowhegPythia8_AU2CT10_DYtautau_400M600.merge.NTUP_SMWZ.e1248_s1469_s1470_r3542_r3549_p1328/
mc12_8TeV.129548.PowhegPythia8_AU2CT10_DYtautau_600M800.merge.NTUP_SMWZ.e1248_s1469_s1470_r3542_r3549_p1328/
mc12_8TeV.129549.PowhegPythia8_AU2CT10_DYtautau_800M1000.merge.NTUP_SMWZ.e1248_s1469_s1470_r3542_r3549_p1328/
mc12_8TeV.129550.PowhegPythia8_AU2CT10_DYtautau_1000M1250.merge.NTUP_SMWZ.e1248_s1469_s1470_r3542_r3549_p1328/
mc12_8TeV.129551.PowhegPythia8_AU2CT10_DYtautau_1250M1500.merge.NTUP_SMWZ.e1248_s1469_s1470_r3542_r3549_p1328/
mc12_8TeV.129552.PowhegPythia8_AU2CT10_DYtautau_1500M1750.merge.NTUP_SMWZ.e1248_s1469_s1470_r3542_r3549_p1328/
mc12_8TeV.129553.PowhegPythia8_AU2CT10_DYtautau_1750M2000.merge.NTUP_SMWZ.e1248_s1469_s1470_r3542_r3549_p1328/
mc12_8TeV.129554.PowhegPythia8_AU2CT10_DYtautau_2000M2250.merge.NTUP_SMWZ.e1248_s1469_s1470_r3542_r3549_p1328/
mc12_8TeV.129555.PowhegPythia8_AU2CT10_DYtautau_2250M2500.merge.NTUP_SMWZ.e1248_s1469_s1470_r3542_r3549_p1328/
mc12_8TeV.129556.PowhegPythia8_AU2CT10_DYtautau_2500M2750.merge.NTUP_SMWZ.e1248_s1469_s1470_r3542_r3549_p1328/
mc12_8TeV.129557.PowhegPythia8_AU2CT10_DYtautau_2750M3000.merge.NTUP_SMWZ.e1248_s1469_s1470_r3542_r3549_p1328/
mc12_8TeV.129558.PowhegPythia8_AU2CT10_DYtautau_3000M.merge.NTUP_SMWZ.e1248_s1469_s1470_r3542_r3549_p1328/
mc12_8TeV.129646.PowhegPythia8_AU2CT10_Zee_LeptonFilterPt300.merge.NTUP_SMWZ.e1552_s1499_s1504_r3658_r3549_p1328/
mc12_8TeV.129646.PowhegPythia8_AU2CT10_Zee_LeptonFilterPt300.merge.NTUP_SMWZ.e1552_a159_a171_r3549_p1328/
mc12_8TeV.129636.PowhegPythia8_AU2CT10_Zee_LeptonFilterPt200.merge.NTUP_SMWZ.e1552_a159_a171_r3549_p1328/
mc12_8TeV.129626.PowhegPythia8_AU2CT10_Zee_LeptonFilterPt150.merge.NTUP_SMWZ.e1552_a159_a171_r3549_p1328/
mc12_8TeV.129596.PowhegPythia8_AU2CT10_Zee_LeptonFilterPt100.merge.NTUP_SMWZ.e1552_a159_a171_r3549_p1328/

| Run | Process | $N_{evt}$ [k] | Generator $\sigma B \varepsilon_{filt}$ [pb] | $K$-factor | $L_{\text{int}}$ [fb$^{-1}$] |
|---|---|---|---|---|---|
| Inclusive and mass binned $W \to e\nu$ | | | | | |
| 147800 | $W^+ \to e\nu$ | 22993 | 6.89E+03 | $K(m)$ | 3.3 |
| 147803 | $W^- \to e\nu$ | 16999 | 4.79E+03 | $K(m)$ | 3.5 |
| 129561 | $W^+(200,500) \to e\nu$ | 45 | 2.51E+00 | $K(m)$ | 18 |
| 129566 | $W^-(200,500) \to e\nu$ | 45 | 1.45E+00 | $K(m)$ | 31 |
| 129562 | $W^+(500,1500) \to e\nu$ | 45 | 7.67E-02 | $K(m)$ | 590 |
| 129567 | $W^-(500,1500) \to e\nu$ | 45 | 3.42E-02 | $K(m)$ | 1300 |
| 129563 | $W^+(1500,2500) \to e\nu$ | 45 | 3.20E-04 | $K(m)$ | 140000 |
| 129568 | $W^-(1500,2500) \to e\nu$ | 45 | 9.98E-05 | $K(m)$ | 450000 |
| 129564 | $W^+(2500,3000) \to e\nu$ | 45 | 4.37E-06 | $K(m)$ | 10000000 |
| 129569 | $W^-(2500,3000) \to e\nu$ | 45 | 1.47E-06 | $K(m)$ | 31000000 |
| 129600 | $W^+(3000,3500) \to e\nu$ | 45 | 5.54E-07 | $K(m)$ | 81000000 |
| 129602 | $W^-(3000,3500) \to e\nu$ | 45 | 2.13E-07 | $K(m)$ | 210000000 |
| 129601 | $W^+(> 3500) \to e\nu$ | 45 | 7.74E-08 | $K(m)$ | 580000000 |
| 129603 | $W^-(> 3500) \to e\nu$ | 45 | 3.46E-08 | $K(m)$ | 1300000000 |
| $p_T$ binned $W \to e\nu$ | | | | | |
| 129590 | $W^+(100,150) \to e\nu$ | 400 | 1.38E+01 | $K(m)$ | 28.9 |
| 129593 | $W^-(100,150) \to e\nu$ | 500 | 1.32E+01 | $K(m)$ | 37.8 |
| 129620 | $W^+(150,200) \to e\nu$ | 100 | 2.16E+00 | $K(m)$ | 46.2 |
| 129623 | $W^-(150,200) \to e\nu$ | 100 | 2.08E+00 | $K(m)$ | 48.2 |
| 129630 | $W^+(200,300) \to e\nu$ | 50 | 6.67E-01 | $K(m)$ | 75 |
| 129633 | $W^-(200,300) \to e\nu$ | 50 | 6.39E-01 | $K(m)$ | 78 |
| 129640 | $W^+(> 300) \to e\nu$ | 10 | 1.13E-01 | $K(m)$ | 88.6 |
| 129643 | $W^-(> 300) \to e\nu$ | 10 | 9.95E-02 | $K(m)$ | 100.5 |
| Inclusive and mass binned $W \to \tau\nu$ | | | | | |
| 147802 | $W^+ \to \tau\nu$ | 3999 | 6.89E+03 | $K(m)$ | 0.58 |
| 147805 | $W^- \to \tau\nu$ | 2995 | 4.79E+03 | $K(m)$ | 0.63 |
| 129581 | $W^+(200,500) \to \tau\nu$ | 45 | 2.51E+00 | $K(m)$ | 18 |
| 129586 | $W^-(200,500) \to \tau\nu$ | 45 | 1.45E+00 | $K(m)$ | 31 |
| 129582 | $W^+(500,1500) \to \tau\nu$ | 45 | 7.67E-02 | $K(m)$ | 590 |
| 129587 | $W^-(500,1500) \to \tau\nu$ | 45 | 3.42E-02 | $K(m)$ | 1300 |
| 129583 | $W^+(1500,2500) \to \tau\nu$ | 45 | 3.20E-04 | $K(m)$ | 140000 |
| 129588 | $W^-(1500,2500) \to \tau\nu$ | 45 | 9.98E-05 | $K(m)$ | 450000 |
| 129584 | $W^+(2500,3000) \to \tau\nu$ | 45 | 4.37E-06 | $K(m)$ | 10000000 |
| 129589 | $W^-(2500,3000) \to \tau\nu$ | 45 | 1.47E-06 | $K(m)$ | 31000000 |
| 129608 | $W^+(3000,3500) \to \tau\nu$ | 45 | 5.54E-07 | $K(m)$ | 81000000 |
| 129610 | $W^-(3000,3500) \to \tau\nu$ | 45 | 2.13E-07 | $K(m)$ | 210000000 |
| 129609 | $W^+(> 3500) \to \tau\nu$ | 45 | 7.74E-08 | $K(m)$ | 580000000 |
| 129611 | $W^-(> 3500) \to \tau\nu$ | 45 | 3.46E-08 | $K(m)$ | 1300000000 |

| Run | Process | $N_{evt}$ [k] | Generator $\sigma B \varepsilon_{filt}$ [pb] | $K$-factor | $L_{\text{int}}$ [fb$^{-1}$] |
|---|---|---|---|---|---|
| Inclusive and mass binned $Z \to ee$ | | | | | |
| 147806 | $Z \to ee$ | 9995 | 1.11E+03 | $K(m)$ | 9.0 |
| 129506 | $Z(250,400) \to ee$ | 100 | 5.49E-01 | $K(m)$ | 180 |
| 129507 | $Z(400,600) \to ee$ | 100 | 8.97E-02 | $K(m)$ | 1100 |
| 129508 | $Z(600,800) \to ee$ | 100 | 1.51E-02 | $K(m)$ | 6600 |
| 129509 | $Z(800,1000) \to ee$ | 100 | 3.75E-03 | $K(m)$ | 27000 |
| 129510 | $Z(1000,1250) \to ee$ | 100 | 1.29E-03 | $K(m)$ | 77000 |
| 129511 | $Z(1250,1500) \to ee$ | 100 | 3.58E-04 | $K(m)$ | 280000 |
| 129512 | $Z(1500,1750) \to ee$ | 100 | 1.12E-04 | $K(m)$ | 890000 |
| 129513 | $Z(1750,2000) \to ee$ | 100 | 3.84E-05 | $K(m)$ | 2600000 |
| 129514 | $Z(2000,2250) \to ee$ | 100 | 1.39E-05 | $K(m)$ | 7200000 |
| 129515 | $Z(2250,2500) \to ee$ | 100 | 5.23E-06 | $K(m)$ | 19000000 |
| 129516 | $Z(2500,2750) \to ee$ | 100 | 2.02E-06 | $K(m)$ | 50000000 |
| 129517 | $Z(2750,3000) \to ee$ | 100 | 7.89E-07 | $K(m)$ | 130000000 |
| 129518 | $Z(> 3000) \to ee$ | 100 | 5.04E-07 | $K(m)$ | 200000000 |
| $p_T$ binned $Z \to ee$ | | | | | |
| 129596 | $Z(100,150) \to ee$ | 1398 | 8.25E+00 | $K(m)$ | 170 |
| 129626 | $Z(150,200) \to ee$ | 299 | 1.31E+00 | $K(m)$ | 230 |
| 129636 | $Z(200,300) \to ee$ | 100 | 4.11E-01 | $K(m)$ | 240 |
| 129646 | $Z(> 300) \to ee$ | 20 | 6.75E-02 | $K(m)$ | 300 |
| Inclusive and mass binned $Z \to \tau\tau$ | | | | | |
| 147808 | $Z \to \tau\tau$ | 5000 | 1.11E+03 | $K(m)$ | 4.5 |
| 129546 | $Z(250,400) \to \tau\tau$ | 20 | 5.49E-01 | $K(m)$ | 36 |
| 129547 | $Z(400,600) \to \tau\tau$ | 20 | 8.97E-02 | $K(m)$ | 220 |
| 129548 | $Z(600,800) \to \tau\tau$ | 20 | 1.51E-02 | $K(m)$ | 1300 |
| 129549 | $Z(800,1000) \to \tau\tau$ | 20 | 3.75E-03 | $K(m)$ | 5300 |
| 129550 | $Z(1000,1250) \to \tau\tau$ | 20 | 1.29E-03 | $K(m)$ | 15000 |
| 129551 | $Z(1250,1500) \to \tau\tau$ | 20 | 3.58E-04 | $K(m)$ | 56000 |
| 129552 | $Z(1500,1750) \to \tau\tau$ | 20 | 1.12E-04 | $K(m)$ | 180000 |
| 129553 | $Z(1750,2000) \to \tau\tau$ | 20 | 3.84E-05 | $K(m)$ | 520000 |
| 129554 | $Z(2000,2250) \to \tau\tau$ | 20 | 1.39E-05 | $K(m)$ | 1400000 |
| 129555 | $Z(2250,2500) \to \tau\tau$ | 20 | 5.23E-06 | $K(m)$ | 3800000 |
| 129556 | $Z(2500,2750) \to \tau\tau$ | 20 | 2.02E-06 | $K(m)$ | 9900000 |
| 129557 | $Z(2750,3000) \to \tau\tau$ | 20 | 7.89E-07 | $K(m)$ | 25000000 |
| 129558 | $Z(> 3000) \to \tau\tau$ | 20 | 5.04E-07 | $K(m)$ | 40000000 |
| Diboson | | | | | |
| 126892 | $WW \to \ell\ell\nu\nu$ | 2700 | 5.50E+00 | 1.06 | 490 |
| 126893 | $WZ \to \ell\ell\ell\nu$ | 2700 | 9.75E+00 | 1.05 | 280 |
| 126894 | $ZZ \to \ell\ell\ell\ell$ | 1800 | 8.74E+00 | 1.00 | 210 |
| 126895 | $ZZ \to \ell\ell\nu\nu$ | 900 | 4.96E-01 | 1.05 | 1800 |
| 179975 | $WZ \to \ell\nu\nu\nu$ | 400 | 1.40E+00 | 1.05 | 280 |
| 157814 | $VV \to eeqq$ | 200 | 1.70E+00 | 1.00 | 120 |
| 157817 | $VV \to e\nu qq$ | 890 | 9.56E+00 | 1.00 | 93 |
| 157816 | $VV \to \tau\tau qq$ | 200 | 1.70E+00 | 1.00 | 120 |
| 157819 | $VV \to \tau\nu qq$ | 1000 | 9.56E+00 | 1.00 | 100 |
| Top | | | | | |
| 105861 | $t\bar{t} \to \ell X$ | 14968 | 1.14E+02 | 1.200 | 137 |
| 108343 | s-channel $t \to We\nu$ | 200 | 5.64E-01 | 1.075 | 350 |
| 108345 | s-channel $t \to W\tau\nu$ | 200 | 5.64E-01 | 1.074 | 350 |
| 108346 | s-channel $t \to W\tau\nu$ | 1000 | 2.07E+01 | 1.083 | 48 |
| 117360 | t-channel $\to eX$ | 300 | 8.59E+00 | 1.104 | 35 |
| 117362 | t-channel $t \to \tau X$ | 293 | 8.58E+00 | 1.105 | 34 |

Table A.1: Cross-sections times branching ratio times $\varepsilon_{filt}$ (the filter efficiency reported by the generator) and corresponding integrated luminosities for various simulated background processes. Each data set is defined by the ATLAS Monte Carlo run number and the simulated physics process (including the mass range in GeV when appropriate). The number of generated events is also given, as well as the applied k-factor (whereby $K(m)$ denotes a mass dependent correction).

| Mass | | | | Generator | | |
|---|---|---|---|---|---|---|
| m [GeV] | $\Gamma$ [GeV] | $B(W' \to \ell\nu)$ | Run | $N_{evt}$ [k] | $\sigma B$ [pb] | $L_{int}$ [fb$^{-1}$] |
| $W' \to \ell\nu$ | | | | | | |
| Flat | | | 182599 | 1989 | 0.0257 | 39000.0 |
| 500 | 16.70 | 0.0851 | 158760 | 180 | 50.2 | 1.2 |
| 1000 | 34.78 | 0.0824 | 158761 | 180 | 2.81 | 21 |
| 3000 | 106.46 | 0.0818 | 158762 | 180 | 0.00387 | 16000 |
| $W^* \to e\nu$ | | | | | | |
| Flat | | | 158763 | 700 | 8.455 | 28 |
| 500 | 16.8 | 0.0841 | 158751 | 20 | 16.22 | 0.41 |
| 1000 | 33.8 | 0.0834 | 158752 | 20 | 8.84E-01 | 7.5 |
| 3000 | 101.5 | 0.0833 | 158753 | 20 | 4.90E-04 | 14000 |
| D1 Operator ($M_* = 10\ GeV$) | | | | | | |
| 1 | | | 158820 | 40 | 439 | 0.030 |
| 100 | | | 158821 | 40 | 332 | 0.040 |
| 200 | | | 158822 | 40 | 201 | 0.066 |
| 400 | | | 158823 | 40 | 64.6 | 0.21 |
| 1000 | | | 158824 | 40 | 1.60 | 8.3 |
| 1300 | | | 158825 | 40 | 0.213 | 63 |
| D9 Operator ($M_* = 1\ TeV$) | | | | | | |
| 1 | | | 158826 | 40 | 0.0966 | 140 |
| 100 | | | 158827 | 40 | 0.0870 | 150 |
| 200 | | | 158828 | 40 | 0.0695 | 190 |
| 400 | | | 158829 | 40 | 0.0365 | 370 |
| 1000 | | | 158830 | 40 | 0.00227 | 5900 |
| 1300 | | | 158831 | 40 | 0.000412 | 32000 |
| D5d Operator ($M_* = 100\ GeV$) | | | | | | |
| 1 | | | 158832 | 40 | 72.2 | 0.18 |
| 100 | | | 158833 | 40 | 70.8 | 0.19 |
| 200 | | | 158834 | 40 | 58.8 | 0.23 |
| 400 | | | 158835 | 40 | 32.9 | 0.41 |
| 1000 | | | 158836 | 40 | 2.37 | 5.6 |
| 1300 | | | 158837 | 40 | 0.454 | 29 |
| D5c Operator ($M_* = 1\ TeV$) | | | | | | |
| 1 | | | 158838 | 40 | 0.0608 | 220 |
| 100 | | | 158839 | 40 | 0.0575 | 230 |
| 200 | | | 158840 | 40 | 0.0488 | 270 |
| 400 | | | 158841 | 40 | 0.0279 | 480 |
| 1000 | | | 158842 | 40 | 0.00192 | 7000 |
| 1300 | | | 158843 | 40 | 0.000351 | 38000 |

Table A.2: Monte Carlo signal samples. The first three columns are the mass, width and branching fraction of the W$'^{/*}$. The fourth column is the ATLAS run number used to identify the particular sample followed by the generated number of events and the corresponding cross-section (before $k$-factor corrections). The last column shows the effective integrated luminosity. For such samples generated with a fixed signal pole mass, the W$'$ decay modes included are $W' \to \ell\nu$ where $\ell = e$, $\mu$ and $\tau$ whereas the simulation flat in the invariant boson mass includes the decay mode $W' \to e\nu$ only. The DM samples are grouped by the operators that couple dark matter to SM particles whereby, the first column denotes the mass of the WIMP.

## A.2 Single Electron Trigger Studies

Figure A.1 shows the single fractions of pure W or Z events ($N_i$) compared to data events at L1 (upper left), L2 (upper right) and EF level (lower left) as a function of the transverse energy thresholds. The predicted MC contributions are derived separately for W and Z decays into electrons (plus missing transverse energy). Shown uncertainties are estimated using a simple Poissonian approach, $\Delta N = \sqrt{N}$. The fractions of offline medium and tight electrons in data after varying the energy thresholds are shown in red (med.) and green (tight) on the lower right side.

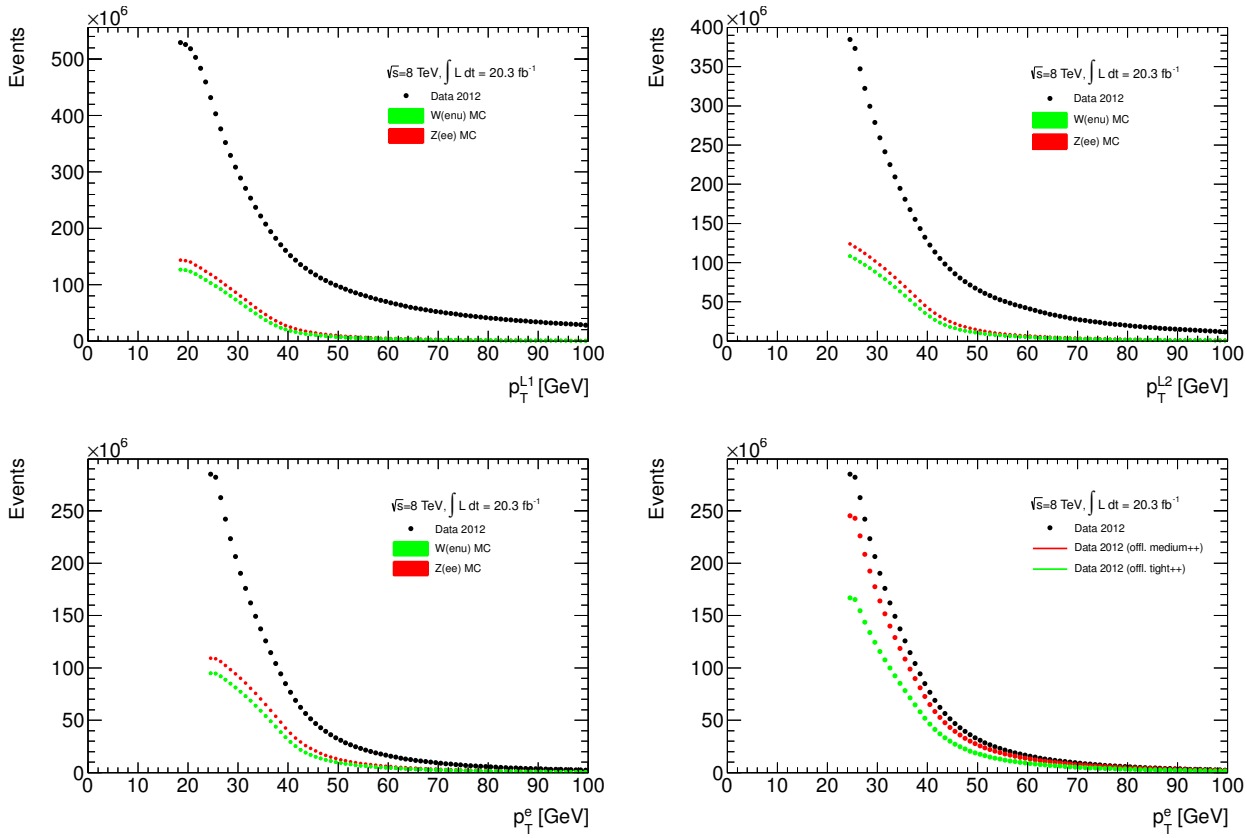


Figure A.1: Fractions of pure W or Z events ($N_i$) compared to data determined at L1 (upper left), at L2 (upper right) and EF level (lower left). The contributions of W and Z decays derived out of MC simulations are scaled with the predicted cross-sections to data luminosity and shown as stacked histograms. Shown uncertainties are Poissonian errors. The fractions of offline medium and tight electrons in data after varying the $p_T$ thresholds are shown in red (med.) and green (tight) on the lower right side.

## A.3 Event Selection

### Yield

The event selection cross-section for each run is defined by the fraction of selected events in the signal region ($m_T > 252\,\text{GeV}$) divided by the integrated delivered luminosity of each run: $\frac{N_{sel}}{L_{int}}$. Figure A.2 shows an overall flat behavior demonstrating a stable reconstruction and trigger efficiency.

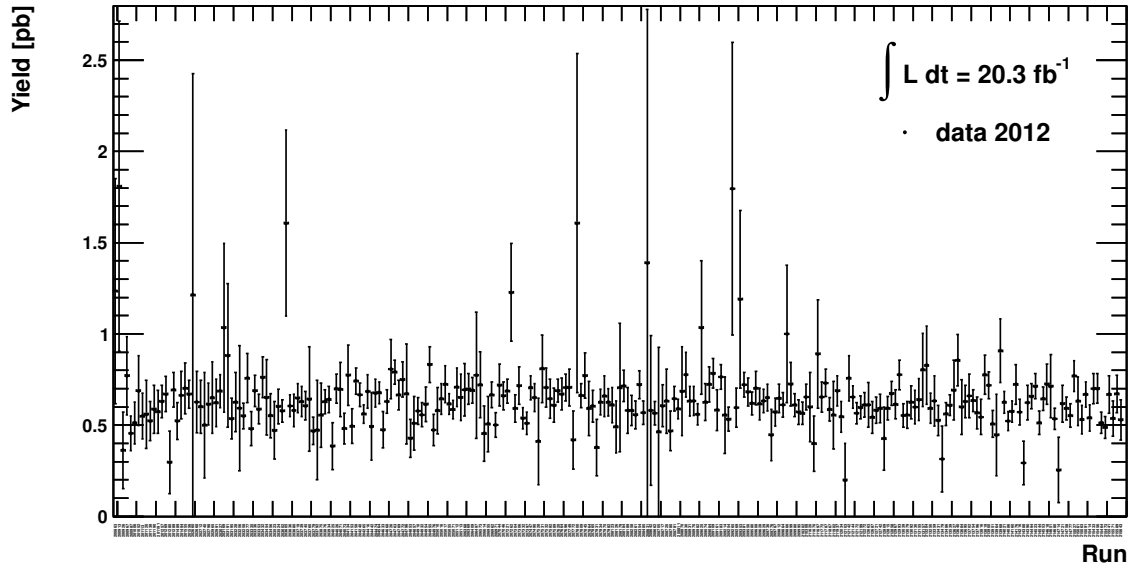


Figure A.2: Event selection cross section for each run after requiring the final event selection for events with $m_T > 252\,\text{GeV}$.

### Additional Signal Comparisons

Caused by different coupling behaviors to SM fermions, also the angular distributions resulting for the different bosons considered deviate significantly (Section 2.3.1). While electrons out of $W'$ decays can be mainly found within the innermost detector region (similar for SM W bosons), $W^*$ decays cause a lepton production with priority in the outer sections. Figures A.3 and A.4 visualize clearly the effect arising after applying the final selection criteria for events with $m_T > 252\,\text{GeV}$. Generally, high values of $\eta$ correspond to low values of the well-known polar angle.

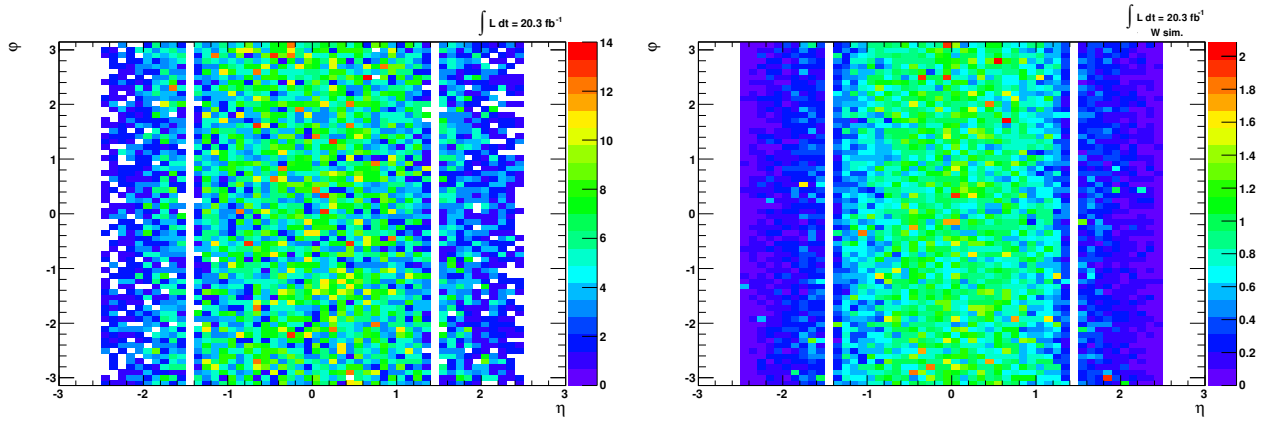


Figure A.3: Two-dimensional $\eta$,$\phi$ spectrum after final selection for events with $m_T > 252\,\text{GeV}$ derived in data (left) and in MC simulations for W decays to electrons and tauons (right). Entries of the simulated dataset are normalized to a data luminosity of about $20\,\text{fb}^{-1}$.

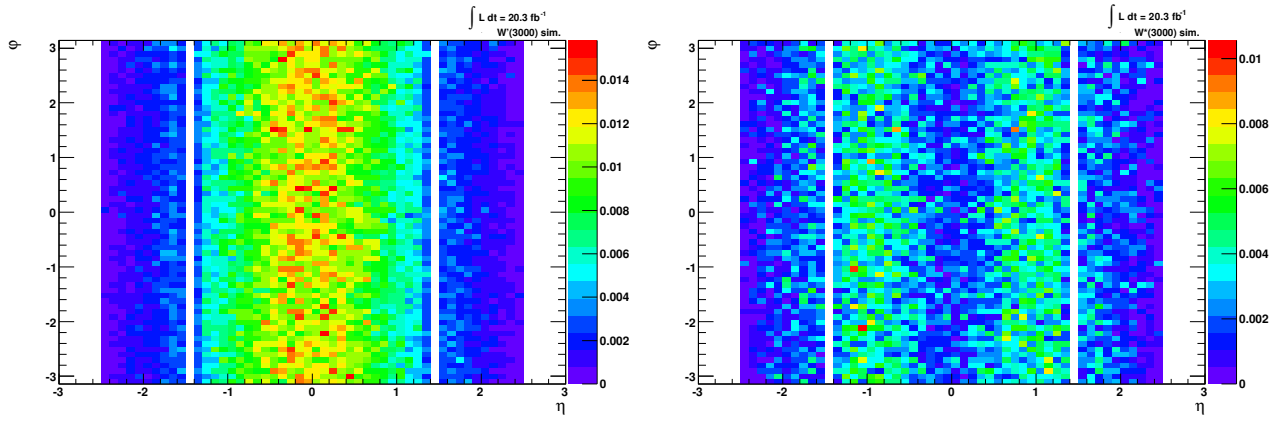


Figure A.4: Two-dimensional $\eta$,$\phi$ spectrum after final selection for events with $m_T > 252\,\text{GeV}$ derived by $W' \to e\nu$ (left) and $W^* \to e\nu$ decays (right) (each simulated for a pole mass of 3 TeV). The completely different behavior in $\eta$ for $W^*$ decays compared to a SM W or SSM $W'$ boson is visible. Entries are normalized to a data luminosity of about $20\,\text{fb}^{-1}$.

## Additional Control Histograms

Figure A.5 shows additionally the spectra of the transverse neutrino momentum and the transverse mass in case of SM W boson decays before any selection criteria are applied. As already seen before, a smooth transition between the single sample contributions is visible, demonstrating the correct treatment of the various simulation sets.

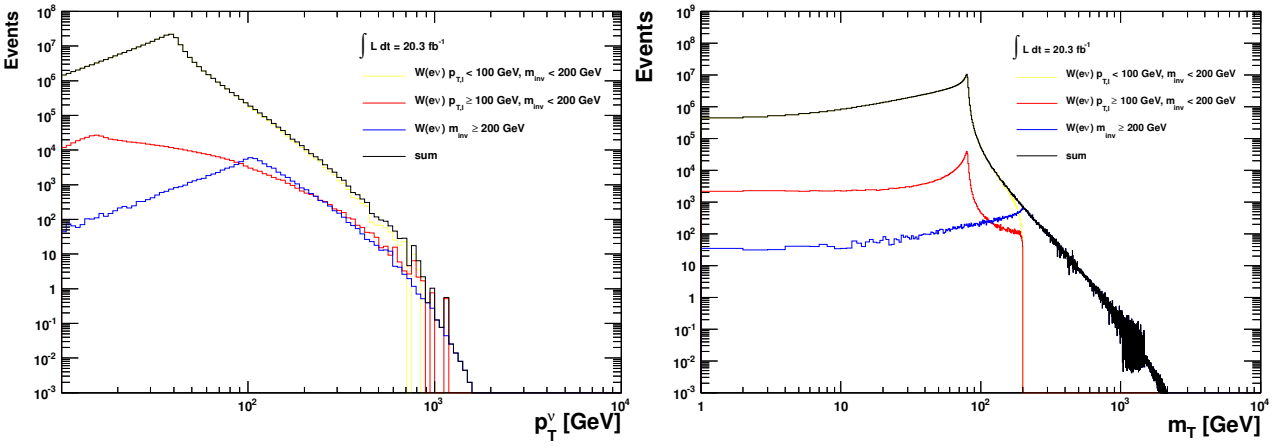


Figure A.5: Spectrum of the transverse neutrino momentum (left) and the transverse mass (right) before selection (truth level). The summed contributions due to mass filtered, $p_T$ filtered and unfiltered (used below 200 GeV only) samples are shown, as well as the resulting background contribution in total as black curve. For better visibility, only direct decays to electrons and neutrinos are taken into account.

## A.4 QCD - Inverse Id Method

Since QCD processes are hard to describe in Monte Carlo simulations, data-driven methods are used. To estimate their systematic uncertainties, comparisons among different approaches are meaningful. This section describes an alternative to the one mentioned before (Section 6.2), based on specific cut inversions. In fact, a highly QCD enriched template is obtained via an inversion on the electron identification using a medium electron identification with an inverted $\Delta\eta$ cut (that is, requiring "loose, but not medium"). Thereby, the isolation of the electron candidate is ignored whereas other selection criteria remain unchanged. Systematic uncertainties on the following template shape are estimated afterwards using an inverted isolation requirement instead, together with a standard medium electron identification. Each modified cut selection is required to both, data and MC simulations, to evaluate also the remaining contamination from non-QCD backgrounds. The shape of the final QCD template is received by subtracting those non-QCD processes from the enriched template while its normalization is done using a template fit of the $E_T^{miss}$ spectrum (Figure A.6 (left)). The fitting procedure requires distributions well distinguishable as provided by the $E_T^{miss}$ variable; so in order to use its whole spectrum, the $E_T^{miss}$ cut of 125 GeV is dropped for the template fit. Utilizing a ROOT based fitting method ("TFractionFit"), the QCD template shape (non-QCD contamination subtracted) and the other summarized SM backgrounds (out of MC) as second template are compared to data and optimized within their uncertainty in each bin. The optimization procedure aims to find the best possible agreement between the observation in data and *all* expected background processes (including QCD *and* EW backgrounds) using a so-called MIGRAD (or MINIMIZE) algorithm for calculations of the corresponding error matrix[120]. Determining the relative fraction of events that are in good agreement with the shape of the observed distribution, scaling factors are derived for each template that can be used for further normalization. Those factors are defined as

$$n = \frac{f \cdot N_{data}}{N_{template}}, \tag{A.1}$$

whereby $N_i$ denotes the amount of data or background events and $f$ the relative fraction derived by the template shape fit. The uncertainty to $f$ is calculated via Gaussian error propagation. The resulting scaling factors are $0.300695 \pm 0.002740$ for the QCD template and $0.897158 \pm 0.002771$ for the EW MC background (Figure A.6 (left)). Since the calculated MC normalization is not within the luminosity and cross section uncertainties, the fit is redone while forcing the MC scale to unity. The resulting difference of about 8.2 % in the QCD scaling factor is treated as additional systematic uncertainty. Shape differences in the $E_T^{miss}$ spectrum are taken into account by redoing the template fit using the QCD template with an inverted electron isolation requirement. Thereby, a scaling factor of $0.458795 \pm 0.001487$ for the isolation template (while forcing the MC scale to unity) leads to a relative uncertainty of about 65.1 % on the QCD scale. The final QCD normalization is determined as $0.277956 \pm 0.182386$, including all statistical and systematic uncertainties.

Accounting for limited statistics within the required signal regions, an extrapolation to higher transverse masses is performed. The final QCD estimate is achieved by fitting two functional forms to the QCD distribution and stitching the derived result to the original QCD spectrum above 700 GeV. Here, a dijet function

$$f_1 = a(1-x)^b x^{c+d\log(x)} \tag{A.2}$$

[120] MIGRAD uses a minimizing technique referring to the Davidon-Fletcher-Powell variable-metric algorithm that converges to the correct error matrix as it converges to the function minimum.

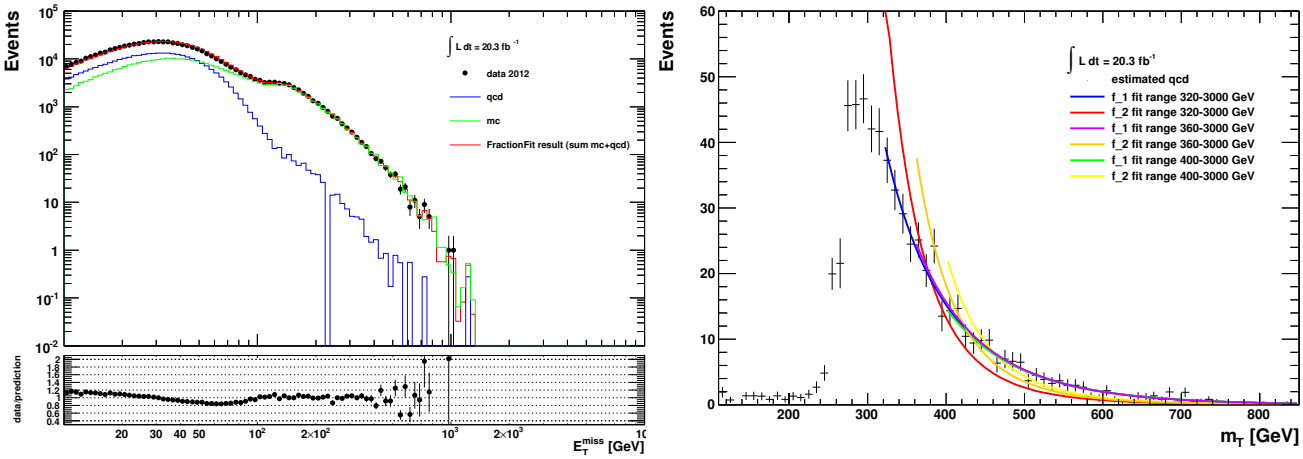


Figure A.6: $E_T^{miss}$ distribution with template shape fit (left) and final QCD extrapolation to higher transverse masses (right).

with $x = m_T/\sqrt{s}$ ($\sqrt{s} = 8\,\text{TeV}$) and fitted in the range of 360 to 3000 GeV is used as baseline, whereby a power law function

$$f_2 = ax^b \tag{A.3}$$

with $x = m_T/\sqrt{s}$ and $\sqrt{s} = 8\,\text{TeV}$ is used as alternative. The latter mainly underestimates the QCD background (Figure A.6 (right)). The variables $a$, $b$, $c$, $d$ denote constants varied in each fit anew while the fitting procedure is executed inductively using the derived parameters as starting point for further adjustments. Due to the low statistics, a log-likelihood method is used for the estimates since the default $\chi^2$ method excludes empty bins for fitting. In addition, the integral of the distribution in each bin is taken instead of the value at the particular bin center and errors estimation is performed using the MINOS technique[121]([Ead71], pp. 204-205). To estimate further systematic uncertainties on the fitting procedure itself, the fit range is varied up (400-3000 GeV) and down (320-3000 GeV). The final QCD estimates derived for several choices of minimum transverse mass thresholds and the corresponding uncertainties are listed in Table A.3 and Table A.4.

Compared to QCD background distributions derived via fake rates, a good overall agreement can be observed (Figures A.7). Slight deviations especially in the outermost $\eta$ regions arise, due to different calorimeter settings as changed cell granularity. Those properties are taken into account within the fake factor method via an additional optimization in four $\eta$ bins, but not for the Inverse Id method. Also an optimization in $p_T$ leads to slightly deviating values from the latter one, especially in the peak region. Still, the agreement within the spectra of the missing transverse energy and the transverse mass is good over all energy ranges.

[121] In contrast to the calculation after HESSE or MIGRAD (MINIMIZE), MINOS is able to provide different positive and negative errors due to another formulation of non-linearities.

| $m_{Tmin}$ [GeV] | 252 | | 317 | | 336 | | 377 | | 423 | | 448 | | 474 | | 564 | | 597 | | 710 | |
|---|---|---|---|---|---|---|---|---|---|---|---|---|---|---|---|---|---|---|---|---|
| $f_1$ (dijet fit func.) | 616.88 | ± 13.95 | 370.99 | ± 10.50 | 297.56 | ± 9.37 | 189.30 | ± 7.42 | 114.67 | ± 5.60 | 88.53 | ± 4.87 | 68.80 | ± 4.21 | 26.80 | ± 2.33 | 20.92 | ± 1.93 | 7.76 | ± 0.32 |
| $f_1$ (upper range) | 616.53 | ± 13.94 | 370.63 | ± 10.49 | 297.20 | ± 9.36 | 188.95 | ± 7.41 | 114.32 | ± 5.59 | 88.18 | ± 4.86 | 68.44 | ± 4.20 | 26.44 | ± 2.30 | 20.57 | ± 1.90 | 7.44 | ± 0.32 |
| $f_1$ (lower range) | 617.02 | ± 13.95 | 371.13 | ± 10.50 | 297.70 | ± 9.37 | 189.44 | ± 7.42 | 114.81 | ± 5.60 | 88.68 | ± 4.86 | 68.94 | ± 4.21 | 26.94 | ± 2.32 | 21.06 | ± 1.92 | 7.89 | ± 0.25 |
| $f_2$ (power law) | 613.95 | ± 13.95 | 368.05 | ± 10.50 | 294.62 | ± 9.37 | 186.36 | ± 7.42 | 111.73 | ± 5.60 | 85.60 | ± 4.86 | 65.86 | ± 4.21 | 23.86 | ± 2.32 | 17.98 | ± 1.92 | 5.16 | ± 0.26 |
| $f_2$ (upper range) | 614.58 | ± 13.95 | 368.68 | ± 10.50 | 295.25 | ± 9.37 | 187.00 | ± 7.42 | 112.37 | ± 5.61 | 86.23 | ± 4.87 | 66.49 | ± 4.22 | 24.50 | ± 2.34 | 18.62 | ± 1.94 | 5.75 | ± 0.38 |
| $f_2$ (lower range) | 613.08 | ± 13.94 | 367.18 | ± 10.49 | 293.75 | ± 9.36 | 185.50 | ± 7.41 | 110.87 | ± 5.59 | 84.73 | ± 4.86 | 64.99 | ± 4.20 | 23.00 | ± 2.31 | 17.12 | ± 1.91 | 4.36 | ± 0.17 |
| $f_1$ (inv. iso) | 409.49 | ± 15.65 | 286.74 | ± 13.02 | 242.82 | ± 12.01 | 170.70 | ± 9.69 | 122.09 | ± 8.04 | 102.80 | ± 7.33 | 82.53 | ± 6.50 | 39.39 | ± 4.14 | 32.20 | ± 3.68 | 12.66 | ± 1.96 |
| $f_2$ (inv. iso) | 400.61 | ± 15.51 | 277.87 | ± 12.85 | 233.95 | ± 11.83 | 161.82 | ± 9.46 | 113.22 | ± 7.77 | 93.93 | ± 7.02 | 73.65 | ± 6.16 | 30.51 | ± 3.58 | 23.33 | ± 3.03 | 4.50 | ± 0.25 |

| $m_{Tmin}$ [GeV] | 796 | | 843 | | 1002 | | 1062 | | 1191 | | 1337 | | 1416 | | 1500 | | 1683 | | 1888 | |
|---|---|---|---|---|---|---|---|---|---|---|---|---|---|---|---|---|---|---|---|---|
| $f_1$ (dijet fit func.) | 3.29 | ± 0.12 | 2.04 | ± 0.07 | 0.39 | ± 0.01 | 0.20 | ± 0.01 | 0.05 | ± 0.00 | 0.009 | ± 0.000 | 0.004 | ± 0.000 | 0.001 | ± 0.000 | 0.000 | ± 0.000 | 0.000 | ± 0.000 |
| $f_1$ (upper range) | 3.16 | ± 0.12 | 1.97 | ± 0.06 | 0.38 | ± 0.01 | 0.20 | ± 0.00 | 0.05 | ± 0.00 | 0.009 | ± 0.000 | 0.003 | ± 0.000 | 0.001 | ± 0.000 | 0.000 | ± 0.000 | 0.000 | ± 0.000 |
| $f_1$ (lower range) | 3.34 | ± 0.10 | 2.07 | ± 0.06 | 0.39 | ± 0.01 | 0.21 | ± 0.00 | 0.05 | ± 0.00 | 0.009 | ± 0.000 | 0.004 | ± 0.000 | 0.001 | ± 0.000 | 0.000 | ± 0.000 | 0.000 | ± 0.000 |
| $f_2$ (power law) | 2.73 | ± 0.13 | 1.98 | ± 0.09 | 0.76 | ± 0.03 | 0.55 | ± 0.02 | 0.29 | ± 0.01 | 0.152 | ± 0.006 | 0.111 | ± 0.004 | 0.080 | ± 0.003 | 0.042 | ± 0.001 | 0.022 | ± 0.001 |
| $f_2$ (upper range) | 3.03 | ± 0.19 | 2.19 | ± 0.13 | 0.83 | ± 0.05 | 0.60 | ± 0.03 | 0.31 | ± 0.02 | 0.164 | ± 0.008 | 0.119 | ± 0.005 | 0.086 | ± 0.004 | 0.045 | ± 0.002 | 0.024 | ± 0.001 |
| $f_2$ (lower range) | 2.33 | ± 0.09 | 1.70 | ± 0.06 | 0.66 | ± 0.02 | 0.48 | ± 0.02 | 0.25 | ± 0.01 | 0.135 | ± 0.004 | 0.098 | ± 0.003 | 0.072 | ± 0.002 | 0.038 | ± 0.001 | 0.020 | ± 0.000 |
| $f_1$ (inv. iso) | 5.84 | ± 1.00 | 3.77 | ± 0.67 | 0.80 | ± 0.16 | 0.43 | ± 0.09 | 0.11 | ± 0.02 | 0.021 | ± 0.005 | 0.008 | ± 0.002 | 0.003 | ± 0.001 | 0.000 | ± 0.000 | 0.000 | ± 0.000 |
| $f_2$ (inv. iso) | 2.40 | ± 0.13 | 1.75 | ± 0.09 | 0.67 | ± 0.03 | 0.49 | ± 0.02 | 0.26 | ± 0.01 | 0.138 | ± 0.006 | 0.100 | ± 0.004 | 0.073 | ± 0.003 | 0.039 | ± 0.001 | 0.021 | ± 0.001 |

Table A.3: QCD estimation for different values of $m_{Tmin}$ and different fits. Estimates are done for both template possibilities (inverse id and inverted isolation). Errors shown here are statistical errors only.

| $m_{Tmin}$ [GeV] | QCD estimate | total uncertainties | total syst.uncertainties | systematic uncertainties | | |
|---|---|---|---|---|---|---|
| | | | | scale | fit | shape |
| 252 | 616.9 | 213.9 | 213.5 | 50.5 | 3.8 | 207.4 |
| 317 | 371.0 | 90.2 | 89.6 | 30.3 | 3.8 | 84.2 |
| 336 | 297.6 | 60.7 | 60.0 | 24.3 | 3.8 | 54.7 |
| 377 | 189.3 | 25.6 | 24.5 | 15.5 | 3.8 | 18.6 |
| 423 | 114.7 | 13.7 | 12.6 | 9.4 | 3.8 | 7.4 |
| 448 | 88.5 | 17.2 | 16.4 | 7.2 | 3.8 | 14.3 |
| 474 | 68.8 | 15.9 | 15.3 | 5.6 | 3.8 | 13.7 |
| 564 | 26.8 | 13.5 | 13.3 | 2.2 | 3.8 | 12.6 |
| 597 | 20.9 | 12.2 | 12.0 | 1.7 | 3.8 | 11.3 |
| 710 | 7.8 | 6.0 | 6.0 | 0.6 | 3.4 | 4.9 |
| 796 | 3.3 | 2.7 | 2.7 | 0.3 | 1.0 | 2.6 |
| 843 | 2.0 | 1.8 | 1.8 | 0.2 | 0.3 | 1.7 |
| 1002 | 0.4 | 0.6 | 0.6 | 0.03 | 0.4 | 0.41 |
| 1062 | 0.2 | 0.5 | 0.5 | 0.02 | 0.4 | 0.23 |
| 1191 | 0.05 | 0.3 | 0.3 | 0.004 | 0.3 | 0.06 |
| 1337 | 0.01 | 0.2 | 0.2 | 0.001 | 0.2 | 0.01 |
| 1416 | 0.004 | 0.1 | 0.1 | 0.000 | 0.1 | 0.005 |
| 1500 | 0.001 | 0.1 | 0.1 | 0.000 | 0.1 | 0.002 |
| 1683 | 0.000 | 0.0 | 0.0 | 0.000 | 0.05 | 0.000 |
| 1888 | 0.000 | 0.0 | 0.0 | 0.000 | 0.02 | 0.000 |

Table A.4: Final estimate of QCD background in the electron channel and the corresponding systematical uncertainties for each $m_{Tmin}$ bin separately according a luminosity of about $20.3\,\mathrm{fb}^{-1}$ (using the inverse id method). The listed systematics according the fit are obtained as maximum deviation while varying the fit range and function.

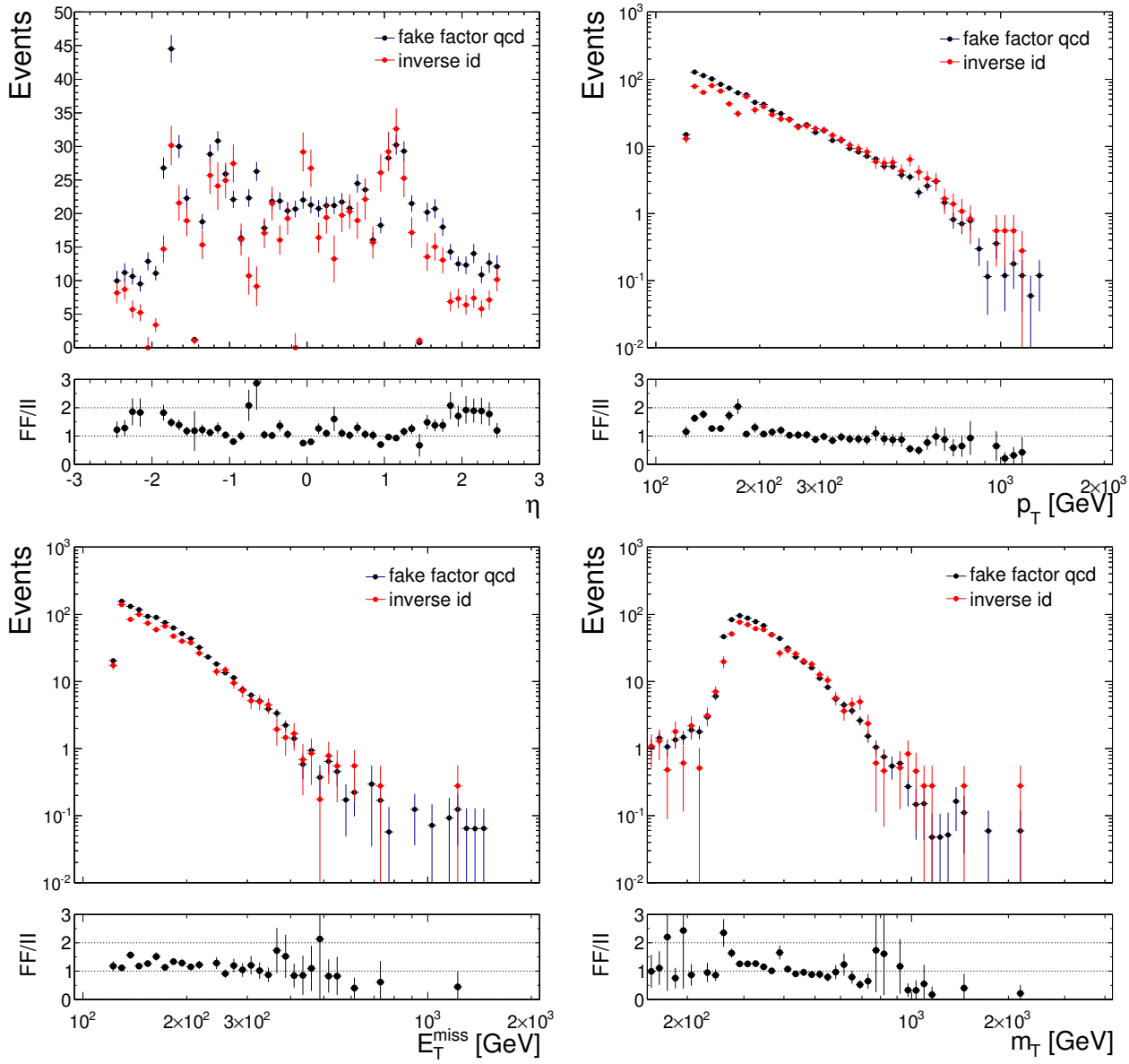


Figure A.7: QCD background distributions derived by the Inverse Id method in comparison with those estimated via fake rates. Shown uncertainties are statistical only.

## A.5 Corrections

### Pileup Reweighting

Characteristic distributions of the average activity of an event are shown for different data periods of 2012 data taking in Figure A.8.

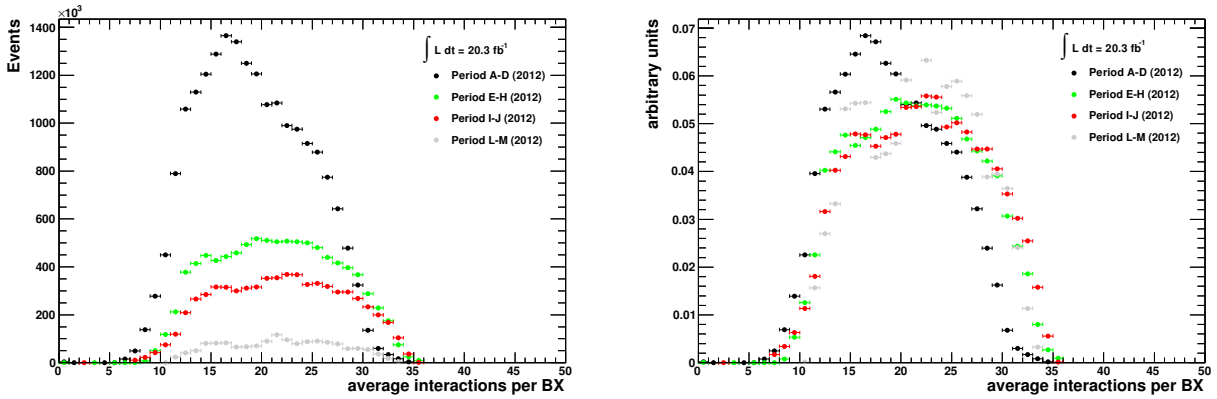


Figure A.8: Average interactions per bunch crossing for different data taking periods (right: normalized to unity). Apart from using the so-called egamma stream together with the appropriate GRL only, no further selection has been applied here.

### Vertex Reweighting

To account also for differences in the z vertex position distributions between reconstructed data and Monte Carlo simulation sets, a further reweighting is applied. The effect is shown in Figure A.9 for W decay processes involving electrons in the final state after all selection requirements have been applied. The bottom panel shows the appropriate data to MC ratios and visualizes the deviation due to applying the correction weights. In comparison to the selected data events, the weighted (red) distribution agrees better in both, width and maximum height.

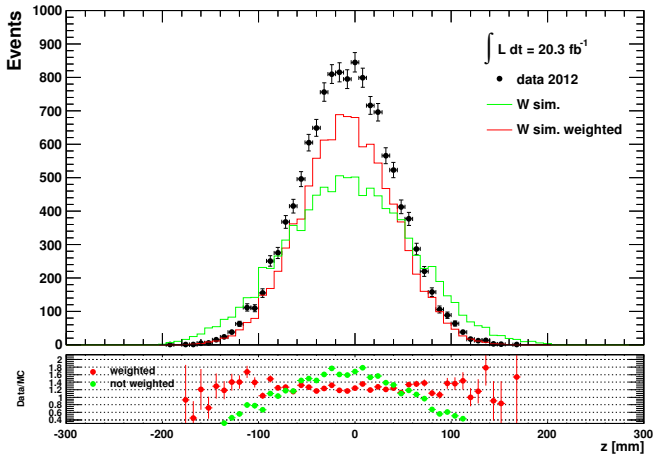


Figure A.9: The z position distribution of the primary vertex is shown after final event selection. The distributions are derived for both, reconstructed data events and predicted W decays to electrons and tauons. The latter are scaled to an integrated luminosity of about $20\,\mathrm{fb}^{-1}$ and are shown with and without correction weights applied.

### W $p_T$ Reweighting

Small deviations between data and SM expectations in the transverse electron momentum spectrum arise above 400 GeV probably due to a mis-modeling in the Monte Carlo simulations of boosted SM W bosons. Figure A.10 (left) shows the spectrum of the transverse electron momentum for transverse masses above (left) and below (right) 250 GeV after final event selection. The histogram involving events with $m_T > 250\,\mathrm{GeV}$ visualizes the energy region above which the decay products are expected to be produced nearly back-to-back (requiring them to have at least $p_T > 125\,\mathrm{GeV}$ and $E_T^{miss} > 125\,\mathrm{GeV}$) and an improved data-background agreement becomes obvious. In contrast to that, the deviations stay while looking to events of the inverse transverse mass region (that is $m_T < 250\,\mathrm{GeV}$). Here, the remaining SM W bosons have to be highly boosted (in the transverse plain) to still fulfill the transverse electron and missing transverse energy requirements.

Due to the difficulty of simulating such complex processes like boosted SM bosons, a reweighting procedure based on the transverse momentum of the decaying W is evaluated, as well as the usage of different MC generators for the SM W and diboson contributions. The transverse boson momentum, $p_T^W$, can be defined as in Equ. A.4 and is chosen as SM W decays constitute the main background and a reweighting should influence the appropriate decay products each in the same manner.

$$\begin{aligned} p_T^W &= \left| E_T^{miss} \begin{pmatrix} \cos\phi_\nu \\ \sin\phi_\nu \end{pmatrix} + p_T^e \begin{pmatrix} \cos\phi_e \\ \sin\phi_e \end{pmatrix} \right| \\ &= \sqrt{(E_T^{miss})^2 + (p_T^e)^2 + 2E_T^{miss} p_T^e \cos(\phi_\nu - \phi_e)} \\ &= \sqrt{(p_x + E_x^{miss})^2 + (p_y + E_y^{miss})^2} \end{aligned} \tag{A.4}$$

Figure A.11 shows a summary of the various approaches exemplified for the electron $p_T$ (left)

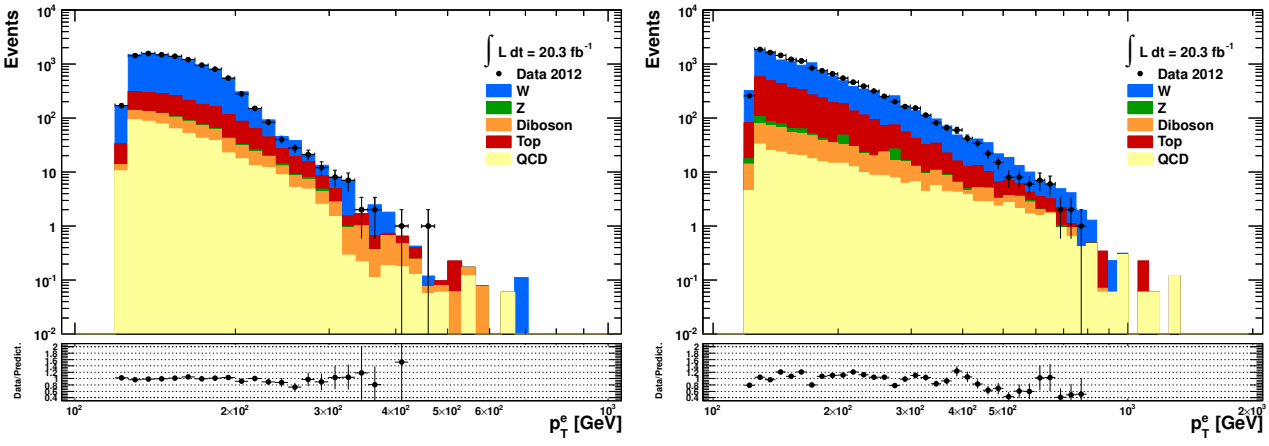


Figure A.10: Blinded spectrum of the transverse electron momentum for transverse masses above 252 GeV (left) and for events with $m_T < 252\,\text{GeV}$ involved (right), each derived for the final selection criteria. The MC samples used are normalized to a data luminosity of about $L_{int} = 20.3\,\text{fb}^{-1}$.

and the missing transverse energy spectra (right) for events with $m_T < 252\,\text{GeV}$ involved. The distributions visualized are derived relatively to the nominal (that is without any $p_T^W$ reweighting applied) to clarify the effective deviations. Beside the standard Sherpa MC simulations in the case of diboson contributions, also Herwig generated sets have been tested. The electron corrections shown have been calculated by using both separately. Removing all SM contributions expected, except that of SM W bosons, from data and comparing the remnant to the predicted simulation, a ratio is derived. This ratio is used event-wise as additional weight to the different kinematic distributions of the SM W background. The given term "muon correction" in Figure A.11 refers to a correction function derived in the same manner by the W′ working group especially for W decays involving muons in the final state which has been simply adapted for the electron decay channel. However, the reweighting procedures show a slightly improvement of the data to background agreement whereby the usage of Herwig diboson simulation sets makes a small influence only.

To verify that the reweighting of the transverse W boson momentum has no influence on the signal discriminant, meaning the transverse mass, the ratio of the reweighted (el. corr. Sherpa) and not reweighted transverse mass distribution is analysed in addition. Figure A.12 shows exemplarily the result referring to the "electron correction" with respect to a Sherpa diboson prediction.

Summarizing, as the reweighting function is close to unity over large ranges and the resulting effects nearly negligible, it has been decided within the W′ working group to not use any reweighting for subsequent analyses. To be consistent, the decision has been adapted for this dissertation, too.

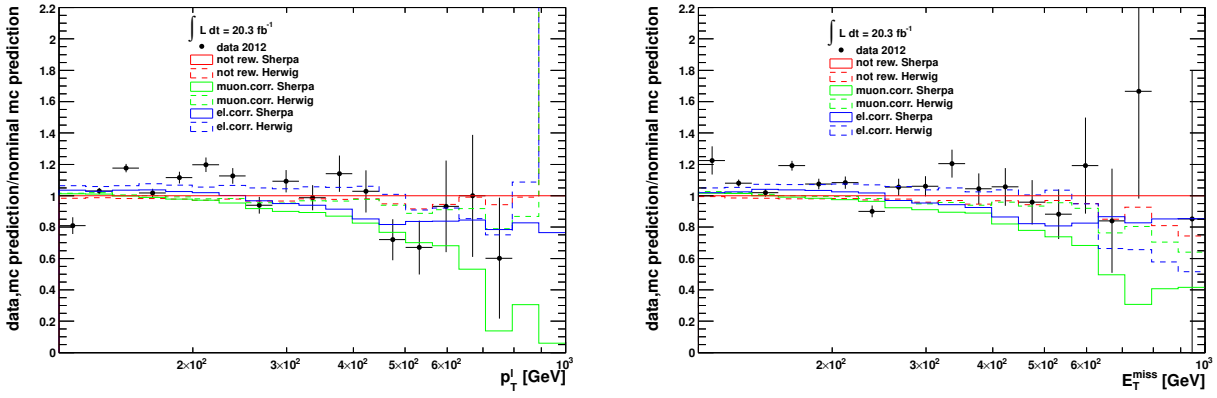


Figure A.11: Spectra of the transverse electron momentum (left) and the missing transverse energy (right) for events with $m_T < 252\,\text{GeV}$ involved only. The distributions are shown relatively to the nominal (that is without any $p_T^W$ reweighting applied) for different correction variations applied. The MC samples used were normalized to a data luminosity of about $L_{int} = 20.3\,\text{fb}^{-1}$; the final selection criteria had been applied. "Herwig" and "Sherpa" refer to the generator used for diboson process simulations.

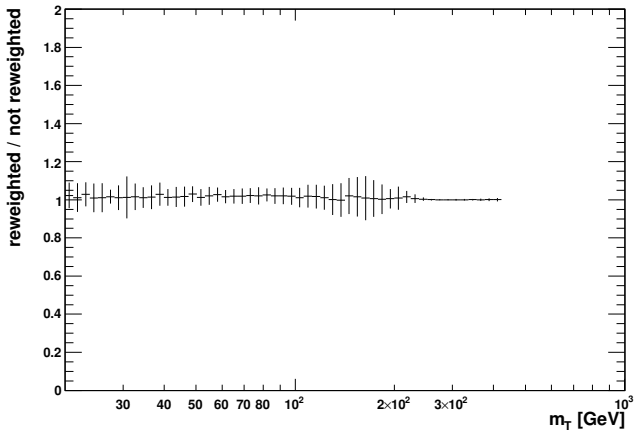


Figure A.12: Ratio of reweighted (el. corr. Sherpa) and not reweighted transverse mass distribution showing nearly no dependence on the W $p_T$ reweighting.

## A.6 SSM W′ reweighting procedure

In contrast to the discussed background processes, W′ signal samples are used which are generated flat in the invariant boson mass, meaning no resonance shape has been simulated. In order to receive signatures distinguishable for different W′ pole masses, a reweighting with the correct line shape can be applied event-wise.
Comparing to different samples simulated for certain W′ pole masses, the reweighting procedure has been validated. Figure A.13 shows various distributions for W′ pole masses of 1000 GeV and 3000 GeV derived by the signal sample generated flat in the invariant boson mass in comparison to those derived by direct simulation sets. A good overall agreement is visible.

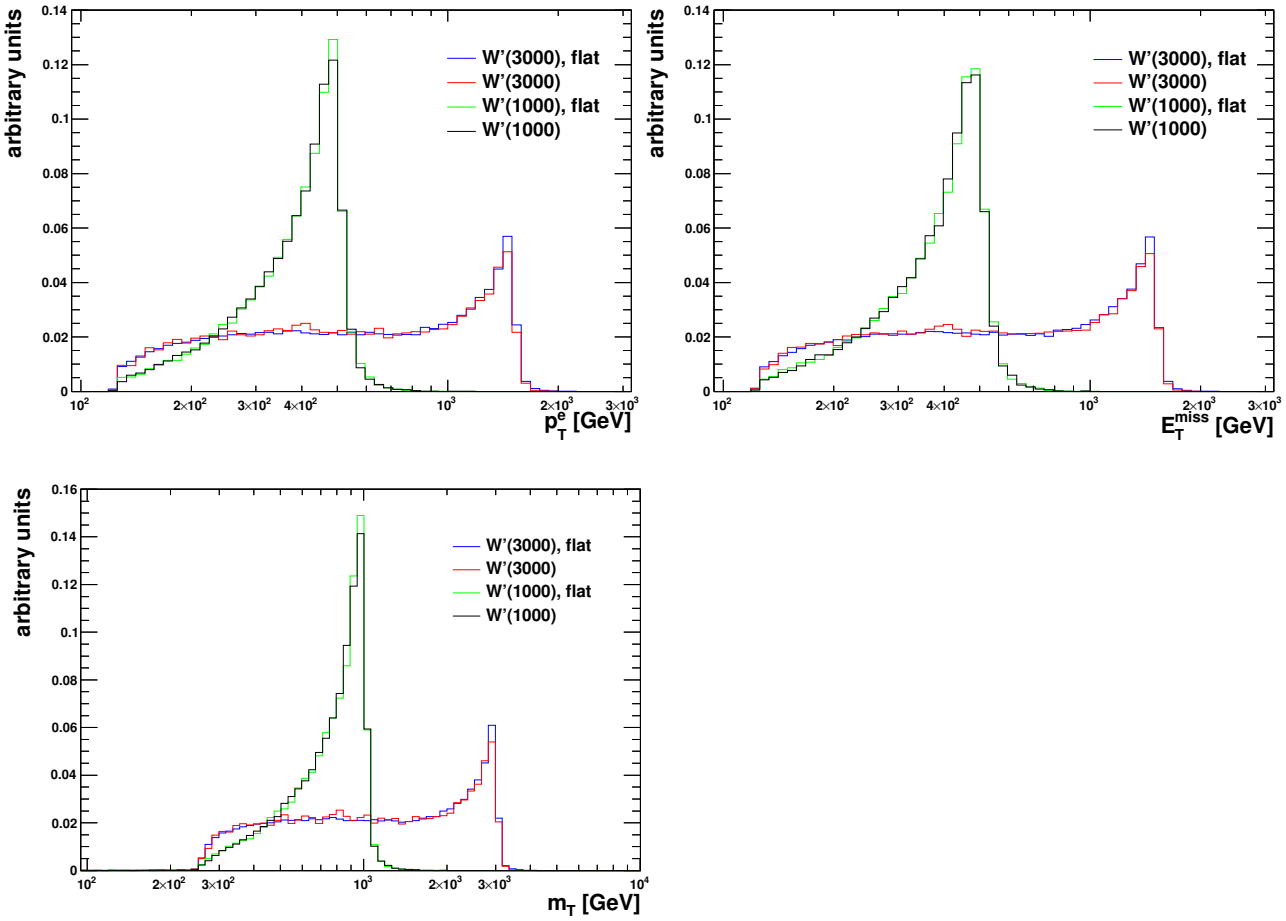


Figure A.13: Validation of W′ reweighting procedure exemplified for W′ pole masses of 1000 GeV and 3000 GeV. The comparisons are shown in the spectra of the transverse electron momentum (top left), the missing transverse energy (top right) and the transverse mass (bottom) after final event selection. The single distributions are normalized to unity to better compare the shapes.

## A.7 Prior Comparisons in different Limit Setting Approaches

In addition to the limit setting procedures described in Chapter 8, both formalisms considered were redone using another distribution for defining the nuisance parameters.
Figure A.14 demonstrates the difference between the two distributions exemplified for a W′ signal efficiency uncertainty of about 15.8 % corresponding to a W′ pole mass of 3 TeV. While the Gaussian has a nicely shaped bell curve, the log-normal distribution ascends steeply and falls flatter.

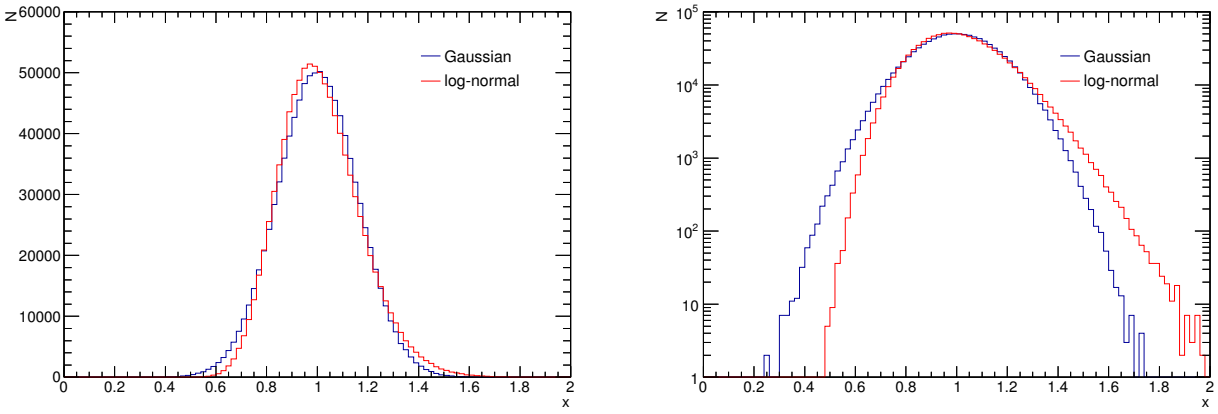


Figure A.14: Comparison between a Gaussian and a log-normal distribution around unity. The width compares to a W′ signal efficiency uncertainty of about 15.8 % (for a W′ pole mass of 3 TeV).

Regarding the Bayesian approach firstly using truncated Gaussian functions for describing the nuisance parameters, the impact of larger systematic uncertainties strongly increases for higher W′ pole masses. Figure A.15 shows a comparison of observed and expected Bayesian limits derived for both, a fiducial (left) and the full phase space (right) using the two different constraining distributions. As already described before, the PDF uncertainties become larger with increasing W′ pole masses due to steeply falling parton distribution functions at high values of Bjørken-x (Sect. 2.3.1 and 8.3) and the related distortion of the line shapes for higher W′ pole masses. The impact is most obvious regarding the total cross-section limits at high masses.

The deviation between Frequentist limits obtained using Gaussian-distributed constraint terms once (Equ. 8.12) and nuisance parameters constrained by truncated log-normal distributions as alternative, is shown in Figure A.16 with respect to a fiducial (left) and the full phase space (right). In contrast to the Bayesian derived exclusions, the dependence at high W′ pole masses is less obvious.

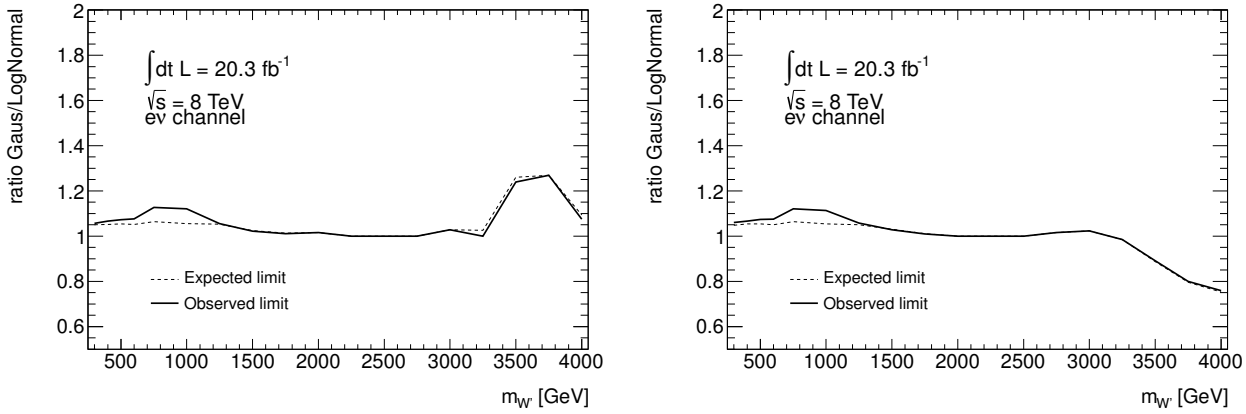


Figure A.15: Comparison of observed and expected Bayesian limits using Gaussian-distributed nuisance parameters once and a truncated log-normal distribution as alternative. The comparison was performed for both, fiducial (left) and total cross-section limits (right).

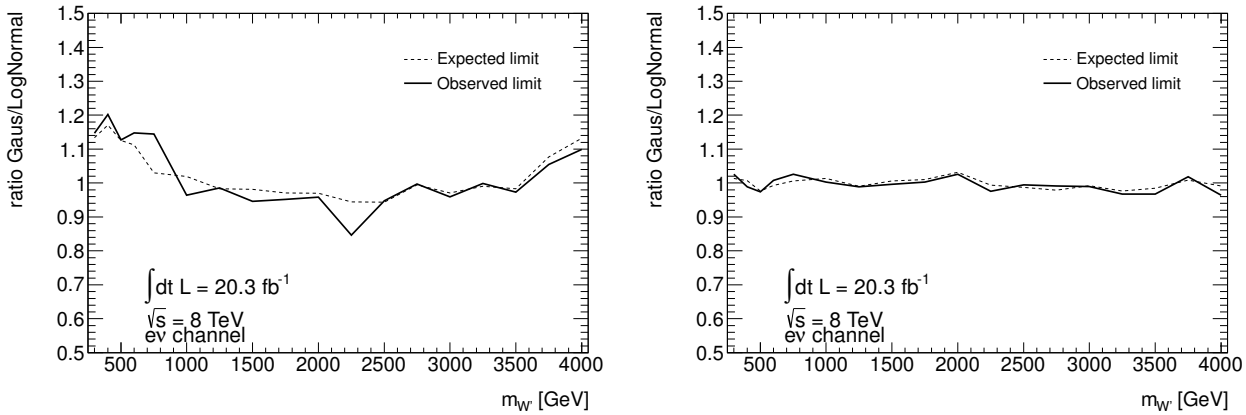


Figure A.16: Comparison of observed and expected Frequentist limits obtained with the profile likelihood ratio based analysis using Gaussian-distributed nuisance parameters once and a truncated log-normal distribution as alternative. The comparison was performed for both, fiducial (left) and total cross-section limits (right).

## A.8 Dark Matter Interpretation ("mono-W")

Regarding WIMP pair production via initial-state radiation of a SM W boson, various operators might be used to describe the interactions occurring. However, as already described before, only a few characteristic kinematic distributions exist (Section 2.3.2).

To consider both, operators accounting for the spin-dependent and spin-independent parts of the elastic WIMP-nucleon scattering cross-section, not only the operator D9 but also D1 and D5 are regarded whereby each treat the WIMP as Dirac fermions. To better estimate also the influence of simulating different dark matter masses for a given operator, Figures A.17 to A.19 show the resulting distributions for D1, D5 (considering both, constructive and destructive modes) and D9 with respect to an effective scale, $M^*$, of 1000 GeV. The spectra of the electron position in $\eta$ as well as the transverse momentum of the W boson and the appropriate electron candidate are shown before any selection criteria have been applied. For comparison reasons, the distributions have been scaled to unity. As expected, they agree well regarding a single operator.

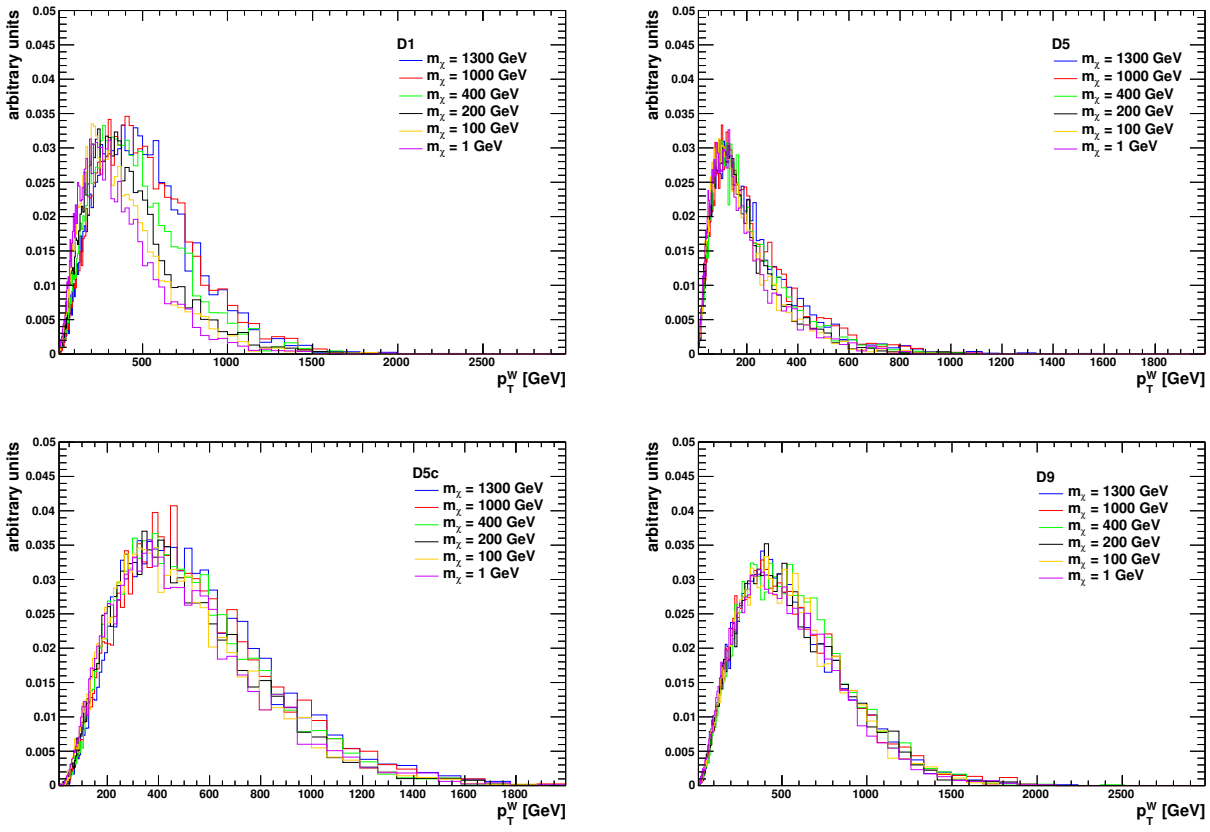


Figure A.17: Comparing different dark matter mass points for the operators D1 (upper left), D5 (destructive mode, upper right), D5c (constructive mode, lower left) and D9 (lower right). The spectrum of the W transverse momentum is shown before any selection criteria are applied. The distributions are normalized to unity.

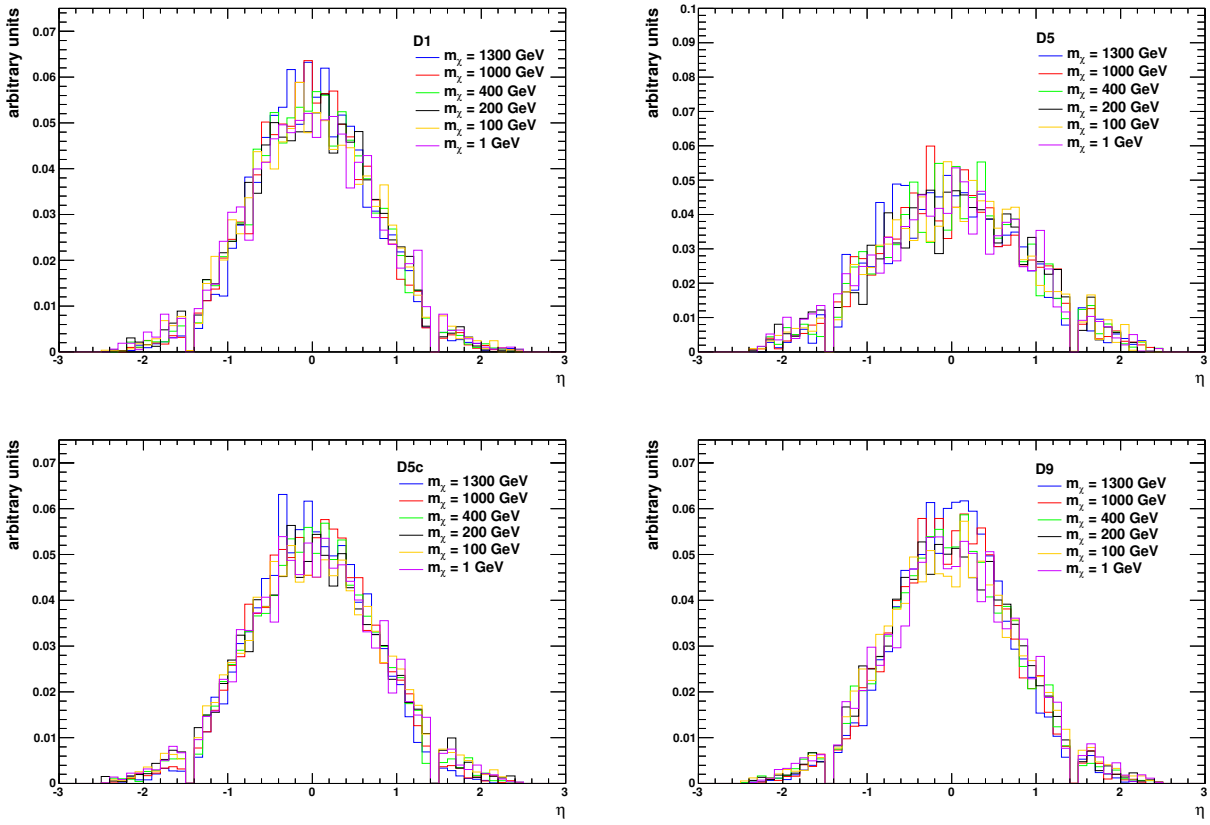


Figure A.18: Comparing different dark matter mass points for the operators D1 (upper left), D5 (destructive mode, upper right), D5c (constructive mode, lower left) and D9 (lower right). The electron $\eta$ spectrum is shown before any selection criteria are applied. The distributions are normalized to unity.

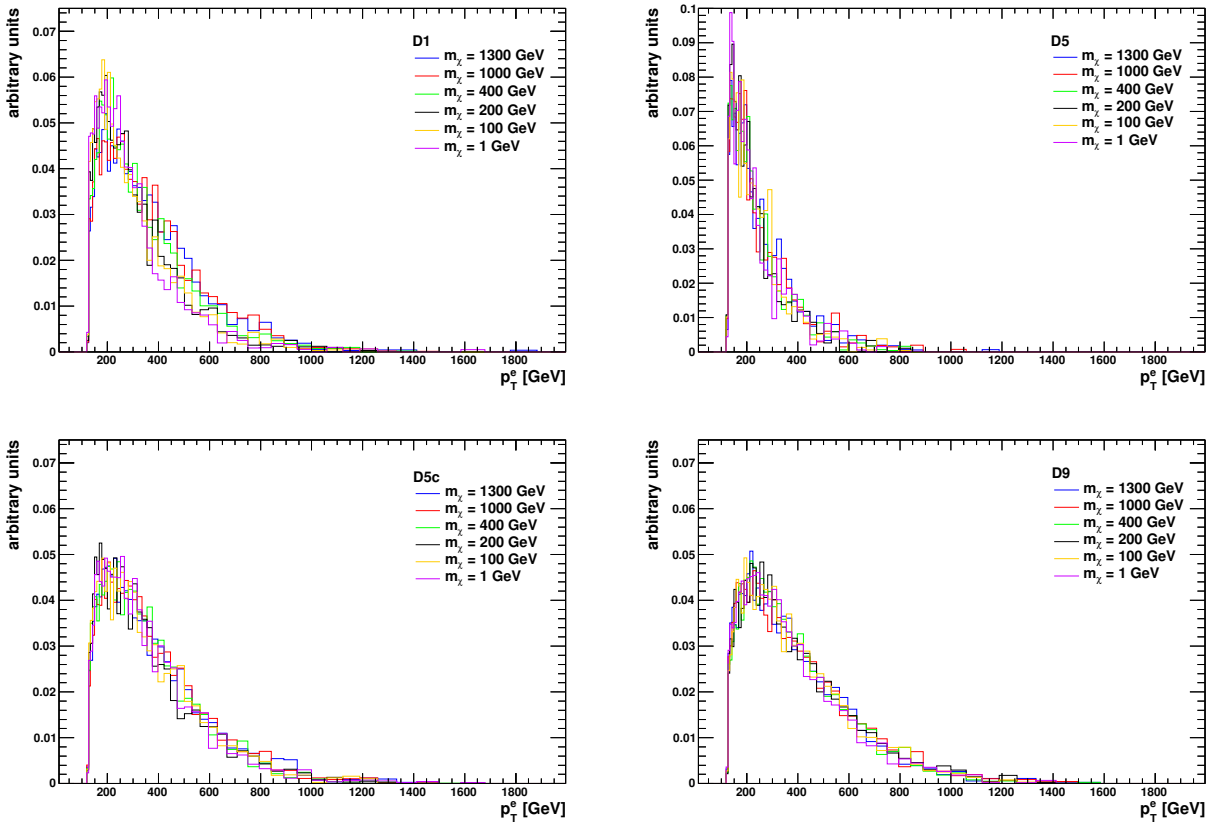


Figure A.19: Comparing different dark matter mass points for the operators D1 (upper left), D5 (destructive mode, upper right), D5c (constructive mode, lower left) and D9 (lower right). The spectrum of the electron transverse momentum is shown before any selection criteria are applied. The distributions are normalized to unity.

# List of Figures

# List of Tables

# References


[Acc12] E. ACCOMANDO, D. BECCIOLINI, S. DE CURTIS, D. DOMINICI, L. FEDELI, C. SHEPHERD-THEMISTOCLEOUS: *Interference effects in heavy W′-boson searches at the LHC.* Phys. Rev. D 85 (2012) 115017.

[Ago03] S. AGOSTINELLI ET AL.: *Geant4: A Simulation toolkit.* Nucl. Instrum. Meth. A506 (2003) 250-303.

[ALI08] ALICE COLLABORATION, K. AAMODT ET AL.: *The ALICE Experiment at the CERN LHC.* JINST 3 (2008) S08002.

[Alt77] G. ALTARELLI, G. PARISI: *Asymptotic Freedom in Parton Language.* Nucl. Phys. B 126 (1977) 298.

[Alt89] G. ALTARELLI, B. MELE, M. RUIZ-ALTABA: *Searching for new heavy vector bosons in p anti-p colliders.* Z. Phys. C45 (1989) 109.

[Alw14] J. ALWALL, R. FREDERIX, S. FRIXIONE, V. HIRSCHI, F. MALTONI, O. MATTELAER, H.-S. SHAO, T. STELZER, P. TORRIELLI, M. ZARO: *The automated computation of tree-level and next-to-leading order differential cross sections, and their matching to parton shower simulations.* JHEP 07 (2014) 079, arXiv:1405.0301 [hep-ph].

[App87] T. APPELQUIST.: *Modern Kaluza-Klein theories.* Addison-Wesley, Redwood City 1987.

[ATL08a] ATLAS COLLABORATION, G. AAD ET AL.: *The ATLAS Experiment at the CERN Large Hadron Collider.* JINST 3 (2008) S08003.

[ATL08b] ATLAS COLLABORATION: *Exotic Processes.* Dec 2008, pp. 1726-1749. [http://cdsweb.cern.ch/record/1159637?ln=en].

[ATL08c] ATLAS COLLABORATION: *Standard Model.* Dec 2008, pp. 747-776. [http://cdsweb.cern.ch/record/1159596?ln=en].

[ATL10a] ATLAS COLLABORATION: *Electron and photon reconstruction and identification in ATLAS: expected performance at high energy and results at* $\sqrt{s}$*=900 GeV.* ATLAS-CONF-2010-005 (2010).

[ATL10b] ATLAS COLLABORATION, G. AAD ET AL.: *Search for New Particles in Two-Jet Final States in 7 TeV Proton-Proton Collisions with the ATLAS Detector at the LHC.* Phys. Rev. Lett. 105 (2010) 16, 161801.

[ATL10c] ATLAS COLLABORATION, D. L. ADAMS ET AL.: *Search for high-mass states with lepton plus missing transverse energy using the ATLAS Detector with* $36\,pb^{-1}$ *of pp collisions at* $\sqrt{s}$*=7 TeV.* ATL-COM-PHYS-2010-1073 (2010). Internal.

[ATL11a] ATLAS COLLABORATION: *Luminosity Determination in pp Collisions at* $\sqrt{s}$*=7 TeV using the ATLAS Detector at the LHC.* Eur. Phys. J. C. 71 (2011) 1630.

[ATL11b] ATLAS COLLABORATION, P. STEINBERG: *Recent Heavy Ion Results with the ATLAS Detector at the LHC.* arXiv: 1107.2182 [nucl-ex].

[ATL11c] ATLAS Collaboration, D. L. Adams et al.: *Search for high-mass states with one lepton plus missing transverse momentum in proton-proton collisions at $\sqrt{s}$=7 TeV with the ATLAS detector.* Phys. Lett. B 701 (2011) 50-69, arXiv:1103.1391 [hep-ex].

[ATL11d] ATLAS Collaboration, D. L. Adams et al.: *Search for a heavy gauge boson decaying to a charged lepton and a neutrino in 1 $fb^{-1}$ of pp collisions at $\sqrt{s}$=7 TeV using the ATLAS detector.* Phys. Lett. B 705 (2011) 28-46, arXiv:1108.1316 [hep-ex].

[ATL12a] ATLAS Collaboration: *Summary of ATLAS Pythia 8 tunes.* ATL-PHYS-PUB-2012-003, ATL-COM-PHYS-2012-738.

[ATL12b] ATLAS Collaboration: *Performance of the ATLAS Trigger System in 2010.* Eur. Phys. J. C. 72 (2012) 1849.

[ATL12c] ATLAS Collaboration: *Measurement of the centrality dependence of open heavy flavor production in lead-lead collisions at $\sqrt{s_{NN}}$ = 2.76 TeV with the ATLAS detector.* ATLAS-CONF-2012-050.

[ATL12d] ATLAS Collaboration: *Performance of the ATLAS Minimum Bias and Forward Detector Triggers in 2011 Heavy Ion Run.* ATLAS-CONF-2012-122.

[ATL12e] ATLAS Collaboration, G. Aad et al.: *Search for new physics in the dijet mass distribution using 1 $fb^{-1}$ of pp collision data at $\sqrt{s}$=7 TeV collected by the ATLAS detector.* Phys. Lett. B 708 (2012).

[ATL12f] ATLAS Collaboration: *Observation of a New Particle in the Search for the Standard Model Higgs Boson with the ATLAS Detector at the LHC.* Phys. Lett. B 716 (2012) 1-29, arXiv:1207.7214.

[ATL12g] ATLAS Collaboration.: *ATLAS search for a heavy gauge boson decaying to a charged lepton and a neutrino in pp collisions at $\sqrt{s}$ =7 TeV.* Eur. Phys. J. C 72 (2012) 2241, arXiv:1209.4446 [hep-ex].

[ATL12h] ATLAS Collaboration.: *Performance of the ATLAS Electron and Photon Trigger in pp Collisions at $\sqrt{s}$=7 TeV in 2011.* ATLAS-CONF-2012-048, https://cds.cern.ch/record/1450089.

[ATL13a] ATLAS Collaboration, G. Aad et al.: *Measurements of $W\gamma$ and $Z\gamma$ production in pp collisions at $\sqrt{s}$=7 TeV with the ATLAS detector at the LHC.* Phys. Rev. D 87 (2013) 112003.

[ATL13b] A. Coccaro, M. Dunford, O. Igonkina, W. Lampl, S. Xella: *Report on the usefulness of L4 trigger.* https://cds.cern.ch/record/1566607/files/ATL-COM-DAQ-2013-058.pdf.

[ATL14a] ATLAS Collaboration.: *Search for high-mass dilepton resonances in pp collisions at $\sqrt{s}$ = 8 TeV with the ATLAS detector.* PRD 90, 052005 (2014).

[ATL14b] ATLAS Collaboration, G. Aad et al.: *Search for dark matter in events with a hadronically decaying W or Z boson and missing transverse momentum in pp collisions at $\sqrt{s}$=8 TeV with the ATLAS detector.* Phys. Rev. Lett 112 (2014) 041802, arXiv:1309.4017.

[ATL14c] ATLAS COLLABORATION: *Search for high-mass states with one lepton plus missing transerve momentum in pp collisions at $\sqrt{s}$=8 TeV with the ATLAS detector.* ATLAS-CONF-2014-017.

[ATL14d] ATLAS COLLABORATION: *Search for new particles in events with one lepton and missing transverse momentum in pp collisions at $\sqrt{s}$=8 TeV with the ATLAS detector.* JHEP 09 (2014) 037.

[ATL14e] ATLAS COLLABORATION: *Electron reconstruction and identification efficiency measurements with the ATLAS detector using the 2011 LHC proton-proton collision data.* Eur. Phys. J. C 74 (2014) 2941, arXiv:1404.2240 [hep-ex].

[ATL14f] ATLAS COLLABORATION: *Electron and photon energy calibration with the ATLAS detector using LHC Run 1 data.* Eur. Phys. J. C 74 (2014) 3071, arXiv:1407.5063 [hep-ex].

[ATL14g] ATLAS COLLABORATION.: *Search for dark matter in events with a Z boson and missing transverse momentum in pp collisions at $\sqrt{s}$ =8 TeV with the ATLAS detector.* PRD 90 (2014) 012004, arXiv:1404.0051.

[ATL14h] ATLAS COLLABORATION.: *Electron and photon trigger performance plots using 2012 data.* ATL-COM-DAQ-2014-058, https://cds.cern.ch/record/1706278.

[ATL14i] ATLAS COLLABORATION.: *Electron efficiency measurements with the ATLAS detector using the 2012 LHC proton-proton collision data.* ATLAS-CONF-2014-032, https://cds.cern.ch/record/1706245.

[ATL15a] ATLAS COLLABORATION.: *Search for $W' \to tb$ in the lepton plus jets final state in proton-proton collisions at a center-of-mass energy of $\sqrt{s}$ =8 TeV with the ATLAS detector.* Phys. Lett. B 743 (2015) 235, arXiv:1410.4103.

[ATL15b] ATLAS COLLABORATION.: *Search for new phenomena in final states with an energetic jet and large missing transverse momentum in pp collisions at $\sqrt{s}$ =8 TeV with the ATLAS detector.* arxiv:1502.01518.

[ATL15c] ATLAS COLLABORATION.: *Search for new resonances in events with one lepton and missing transverse momentum in pp collisions at $\sqrt{s}$ =13 TeV with the ATLAS detector.* ATLAS-CONF-2015-063, http://cds.cern.ch/record/2114829.

[Bai13] Y. BAI, T.M.P. TAIT: *Searches with Mono-Leptons.* Phys. Lett. B 723 (2013) 384-387.

[Bas11] A. BASHIR, R. BERMUDEZ, L. CHANG, C. D. ROBERTS: *Dynamical chiral symmetry breaking and the fermion-gauge-boson vertex.* arXiv:1112.4847 [nucl-th].

[Bel12] A. BELYAEV, N. D. CHRISTENSEN, A. PUKHOV: *CalcHEP 3.4 for collider physics within and beyond the Standard Model.* arXiv:1207.6082v2 [hep-ph].

[Bjø69] J. BJØRKEN: *Asymptotic Sum Rules at Infinite Momentum.* Phys.Rev. 179 (1969) 1547-1553.

[Bon13] S. G. BONDARENKO, A. A. SAPRONOV: *NLO EW and QCD proton-proton cross section calculations with mcsanc-v1.01.* Comput. Phys. Commun. 184 (2013) 2343-2350, arXiv:1301.3687v3 [hep-ph].

[Boo04] E. BOOS ET AL. (COMPHEP COLLABORATION): *CompHEP 4.4: Automatic computations from Lagrangians to events.* Nucl. Instrum. Meth. A 534 (2004) 250, arXiv:hep-ph/0403113.

[Bor13] G. R. BOROUN, B. REZAEI: *Decoupling of the DGLAP evolution equations at next-to-next-to-leading order (NNLO) at low-x.* Eur. Phys. J. C 73 (2013) 2412, arXiv:1402.0164[hep-ph].

[Bru09] R. BRUN, F. RADEMAKERS: *ROOT - An Object-Oriented Data Analysis (Users guide).* [https://root.cern.ch/download/doc/Users_Guide_5_26.pdf].

[Cac08] M. CACCIARI, G. P. SALAM, G. SOYEZ: *The anti-$k_t$ jet clustering algorithm.* JHEP 04 (2008) 063.

[Cal09] A. CALDWELL, D. KOLLÃ¡R, K. KRÖNINGER: *BAT - The Bayesian Analysis Toolkit.* Comp. Phys. Commun. 180 (2009) 2197.

[Cam07] J. M. CAMPBELL, J. W. HUSTON, AND W. J. STIRLING: *Hard interactions of quarks and gluons: a primer for LHC physics.* Rept. Prog. Phys. 70 (2007) 89, hep-ph/0611148.

[Cor01] G. CORCELLA ET AL.: *Herwig 6: an event generator for hadron emission reactions with interfering gluons (including supersymmetric processes).* JHEP, 0101 (2001) 010.

[CDF07a] CDF COLLABORATION, A. ABULENCIA ET AL.: *Search for W-prime boson decaying to electron-neutrino pairs in p anti-p collisions at $\sqrt{s}$=1.96 TeV.* Phys. Rev. D 75 (2007) 091101.

[CDF07b] CDF COLLABORATION, T. AALTONEN ET AL.: *Search for New Physics in High-Mass Electron-Positron Events in $p\bar{p}$ Collisions at $\sqrt{s}$=1.96 TeV.* Phys. Rev. Lett. PRL 99 (2007) 171802.

[CDF11] CDF COLLABORATION, T. AALTONEN ET AL.: *Search for a New Heavy Gauge Boson $W'$ with Electron + missing ET Event Signature in $p\bar{p}$ collisions at $\sqrt{s}$=1.96 TeV.* Phys. Rev. D 83 (2011) 031102.

[Chi00] M. CHIZHOV: *On the two kinds of vector particles.* arXiv:hep-ph/0008187.

[Chi06] M. CHIZHOV: *Production of new chiral bosons at Tevatron and LHC.* arXiv:hep-ph/0609141.

[Chi08] M. CHIZHOV, V. A. BEDNYAKOV, J. A. BUDAGOV: *Proposal for chiral bosons search at LHC via their unique new signature.* Phys. Atom. Nucl. 71 (2008) 2096-2100, arXiv:0801.4235 [hep-ph].

[Chi11] M. CHIZHOV, G. DVALI: *Origin and Phenomenology of Weak-Doublet Spin-1 Bosons.* Phys. Lett. B 703 (2011) 593-598, arXiv:0908.0924 [hep-ph].

[CMS08] CMS COLLABORATION, S. CHATRCHYAN ET AL.: *The CMS Experiment at the CERN LHC.* JINST 3 (2008) S08004.

[CMS11a] CMS COLLABORATION, V. KHACHATRYAN ET AL.: *Search for a heavy gauge boson $W'$ in the final state with an electron and large missing transverse energy in pp collisions at $\sqrt{s}$=7 TeV.* Phys. Lett. B 698 (2011) 21-39.

[CMS11b] CMS COLLABORATION, S. CHATRCHYAN ET AL.: *Search for a W′ boson decaying to a muon and a neutrino in pp collisions at $\sqrt{s}$=7 TeV.* Phys. Lett. B 701 (2011) 160-179.

[CMS12] CMS COLLABORATION: *Observation of a new boson at a mass of 125 GeV with the CMS experiment at the LHC.* Phys. Lett. B 716 (2012) 30, arXiv:1207.7235v2 [hep-ex].

[CMS14] CMS COLLABORATION.: *Search for physics beyond the standard model in final states with a lepton and missing transverse energy in proton-proton collisions at $\sqrt{s}$ =8 TeV.* arXiv:1408.2745v1 [hep-ex].

[D099] D0 COLLABORATION, B. ABBOTT ET AL.: *Measurement of W and Z boson production cross sections in $p\bar{p}$ collisions at $\sqrt{s}$=1.8 TeV.* Phys. Rev. D 60, 052003 (1999).

[D008] D0 COLLABORATION, V. ABAZOV ET AL.: *Search for W-prime bosons decaying to an electron and a neutrino with the D0 detector.* Phys. Rev. Lett. 100 (2008) 031804.

[Dem02] L. DEMORTIER: *Bayesian treatments of systematic uncertainties.* http://citeseerx.ist.psu.edu/viewdoc/summary?doi=10.1.1.205.7146.

[Dob01] M. DOBBS, J. B. HANSEN: *The HepMC C++ Monte Carlo event record for High Energy Physics.* Comput. Phys. Commun. 134 (2001) 41.

[Dok77] Y. L. DOKSHITZER: *Calculation of the Structure Functions for Deep Inelastic Scattering and $e^+e^-$ Annihilation by Perturbation Theory in Quantum Chromodynamics.* Sov. Phys. JETP 46 (1977) 641.

[Dre70] S. D. DRELL, T.-M. YAN: *Massive Lepton Pair Production in Hadron-Hadron Collisions at High-Energies.* Phys. Rev. Lett. 25 (1970) 316.

[Ead71] W.T.EADIE, D.DRIJARD, F.JAMES, M.ROOS, AND B.SADOULET: *Statistical Methods in Experimental Physics.* North-Holland, 1971.

[Eva08] L. EVANS, P. BRYANT: *The CERN Large Hadron Collider: Accelerator and Experiments - LHC Machine.* JINST 3 (2008) S08001.

[Fri07] S. FRIXIONE, P. NASON, C. OLEARI: *Matching NLO QCD computations with Parton Shower simulations: the POWHEG method.* JHEP 11 (2007) 070, arXiv:0709.2092.

[Gai99] M. K. GAILLARD, P. D. GRANNIS, F. J. SCIULLI: *The Standard Model of Particle Physics.* Rev. Mod. Phys.71 (1999) 96-111, arXiv:hep-ph/9812285.

[Gar04] L. GARREN, I.G. KNOWLES, S. NAVAS, T. SJÖSTRAND, T. TRIPPE: *34. Monte Carlo Particlenumbering Scheme.* revised March 2004, [http://pdg.lbl.gov/2005/reviews/montecarlo rpp.pdf].

[Gav13] R. GAVIN, Y. LI, F. PETRIELLO, S. QUACKENBUSH: *FEWZ 2.1: W Physics at the LHC with FEWZ 2.1.* Comput. Phys. Commun. 184 (2013) 208, arXiv:1201.5896.

[Gei09] H. GEIGER, E. MARSDEN: *On a Diffuse Reflection of the α-Particles.* Proc. Roy. Soc. 1909 A vol. 82, pp. 495-500.

[Gia04] F. GIANOTTI: *Physics at the LHC.* Phys. Rep. Vol. 403-404 (Dec 2004).

[Gla61] S. GLASHOW: *Partial Symmetries of Weak Interactions.* Nucl. Phys. 22 (1961), pp. 579-588.

[Gle09] T. GLEISBERG, S. HOCHE, F. KRAUSS, M. SCHONHERR, S. SCHUMANN, F SIEGERT, J. WINTER: *Event generation with Sherpa 1.1.* JHEP 02 (2009) 007, arXiv:0811.4622.

[Gol06] P. GOLONKA, Z. WAS: *PHOTOS Monte Carlo: A Precision tool for QED corrections in Z and W decays.* Eur. Phys. J. C 45 (2006) 97, arXiv:hep-ph/0506026 [hep-ph].

[Goo10] J. GOODMAN, M. IBE, A. RAJARAMAN, W. SHEPHERD, T.M.P. TAIT, H.-B. YU: *Constraints on Dark Matter from Colliders.* Phys. Rev. D 82 (2010) 116010, arXiv:1008.1783v2 [hep-ph]. A recent bug was found in the formula giving $\sigma^{D8D9}$. A factor of $4.7 \times 10^{39}\,\mathrm{cm}^2$ should be applied instead of $9.18 \times 10^{40}\,\mathrm{cm}^2$.

[Gra15] P. GRAFSTRÖM, W. KOZANECKI: *Luminosity determination at proton colliders.* Progress in Particle and Nuclear Physics (2015), [http://dx.doi.org/10.1016/j.ppnp.2014.11.002].

[Gri72] V. N. GRIBOV, L. N. LIPATOV: *Deep Inelastic Electron Proton Scattering in Perturbation Theory.* Sov. J. Nucl. Phys. 15 (1972) 438.

[H1Z10] H1 AND ZEUS COLLABORATION, F. AARON ET AL.: *Combined Measurement and QCD Analysis of the Inclusive $e^{\pm}p$ Scattering Cross Sections at HERA.* JHEP 1001 (2010) 109.

[H1Z12] H1 AND ZEUS COLLABORATION, K. LIPKA AND Z. EXPERIMENTS: *Recent results from HERA and their impact for LHC.* EPJ Web Conf. 28 (2012) 02008, arXiv:1201.4486.

[Hal84] F. HALZEN, A. D. MARTIN: *Quarks And Leptons: An Introductory Course In Modern Particle Physics.* Wiley, 1984.

[Ham91] R. HAMBERG, W. L. VAN NEERVEN, T. MATSUURA: *A Complete calculation of the order $\alpha_s^2$ correction to the Drell-Yan K factor.* Nucl. Phys. B 359 (1991) 343-405; Erratum-ibid. 644 (2002) 403.

[Han05] T. HAN: *Collider phenomenology: Basic knowledge and techniques.* MADPH-05-1434, arXiv: hep-ph/0508097v1.

[Hig64] P. W. HIGGS: *Broken symmetries, massless particles and gauge fields.* Phys. Lett. 12 (1964) 132.

[Kam08] KAMLAND COLLABORATION: *KamLAND's precision measurement of neutrino oscillation parameters.* J. Phys. Conf. Ser. 136 (2008) 022005.

[Ker12] B. P. KERSEVAN, E. RICHTER-WAS: *The Monte Carlo Event Generator AcerMC 2.0 with Interfaces to PYTHIA 6.2 and HERWIG 6.5.* arXiv:hep-ph/0405247.

[Lai10] H.-L. LAI, M. GUZZI, J. HUSTON, Z. LI, P. M. NADOLSKY, ET AL.: *New parton distributions for collider physics.* Phys.Rev. D82 (2010) 074024, arXiv:1007.2241 [hep-ph].

[Lai97] H.-L. LAI, J. HUSTON, S. KUHLMANN, F. OLNESS, J. OWENS, D. SOPER, W. K. TUNG, H. WEERTS: *Improved parton distributions from global analysis of recent deep inelastic scattering and inclusive jet data.* Phys. Rev. D 55 (1997) 1280-1296.

[Lev11] J. LEVÊQUE, B. TROCMÉ: *LAr Data Quality - What CP groups need to know about the data.*LAr DQ Summary, [https://twiki.cern.ch/twiki/bin/viewauth/AtlasProtected/ LArCleaningAndObjectQuality].

[LHC] http://www.lhc-facts.ch/index.php?page=atlas.

[LHC08a] LHCB COLLABORATION, A. AUGUSTO ALVES JR. ET AL.: *The LHCb Detector at the LHC.* JINST 3 (2008) S08005.

[LHC08b] LHCF COLLABORATION, O. ADRIANI ET AL.: *The LHCf Detector at the CERN Large Hadron Collider.* JINST 3 (2008) S08006.

[Luk12] W. LUKAS (FOR ATLAS COLLABORATION): *Fast Simulation for ATLAS: Atlfast-II and ISF.* J. Phys.: Conf. Ser. 396 (2012) 022031.

[Man58] S. MANDELSTAM: *Determination of the Pion-Nucleon Scattering Amplitude from Dispersion Relations and Unitarity. General Theory.* Phys. Rev. 112 (1958) 1344-1360.

[Man03] M. L. MANGANO, M. MORETTI, F. PICCININI, R. PITTAU, A. POLOSA: *ALPGEN, a generator for hard multi-parton processes in hadronic collisions.* JHEP 0307 (2003) 001, arXiv:hep-ph/0206293.

[Mar09] A. D. MARTIN, W. J. STIRLING, R. S. THORNE, G. WATT: *Parton distributions for the LHC.* Eur. Phys. J. C. 63 (2009) 189-285.

[MIN11] MINOS COLLABORATION: *First direct observation of muon anti-neutrino disappearance.* Phys. Rev. Lett. 107 (2011) 021801.

[Mir94] E. MIRKES, J. OHNEMUS: *W and Z Polarization Effects in Hadronic Collisions.* University of Wisconsin - Madison, MAD/PH/834, UCD-94-23 (1994).

[Nas12] P. NASON, B. WEBBER: *Next-to-Leading-Order Event Generators.* arXiv:1202.1251 [hep-ph].

[Per00] D. H. PERKINS: *Introduction to High Energy Physics.* Cambridge University Press, 4th edition, 2000.

[Pov08] B. POVH, K. RITH, C. SCHOLZ, F. ZETSCHE: *Teilchen und Kerne. Eine EinfÃ¼hrung in die physikalischen Konzepte.* Springer Verlag, 6th edition, 2008.

[Ran12] G. RANUCCI.: *The profile likelihood ratio and the look elsewhere effect in high energy physics.* arXiv:1201.4604 [physics.data-an].

[Ros84] G. G. ROSS.: *Grand Unified Theories.* Benjamin, 1984.

[Rut11] E. RUTHERFORD.: *The scattering of $\alpha$ and $\beta$ particles by matter and the structure of the atom.* Philosophical Magazine Series 6, vol. 21, pp. 669-688 (1911).

[Sal68] A. SALAM: *Weak and Electromagnetic Interactions.* Conf. Proc. C 680519 (1968), pp. 367-377.

[Sch11] S. SCHMITT: *Tutorial/Lecture on limits*: Tutorial for the Terascale Statistics School (April 5, 2011).

[Sjö08] T. SJÖSTRAND, S. MRENNA, P. SKANDS: *A Brief Introduction to PYTHIA 8.1.* Comp. Phys. Comm. 178 (2008) 852, arXiv:0710.3820.

[Sti13] W.J. STIRLING, PRIVATE COMMUNICATION: http://www.hep.ph.ic.ac.uk/ wstirlin/plots/plots.html (2013).

[TOT08] TOTEM COLLABORATION, G. ANELLI ET AL.: *The TOTEM Experiment at the CERN Large Hadron Collider.* JINST 3 (2008) S08007.

[UA183] UA1 COLLABORATION: *Experimental Observation of Isolated Large Transverse Energy Electrons with Associated Missing Energy at* $\sqrt{s}$ *=540 GeV.* Phys. Lett. B 122 (1983) 103-116.

[UA283] UA2 COLLABORATION: *Evidence for* $Z^0 \to e^+e^-$ *at the CERN anti-p p Collider.* Phys. Lett. B 129 (1983) 130-140.

[Wei67] S. WEINBERG: *A Model of Leptons.* Phys. Rev. Lett. 19 (1967) 1264-1266.

[Wen13] J. WENNINGER: *Energy Calibration of the LHC Beams at 4 TeV.* Tech. Rep. CERN-ATS-2013-040, CERN, Geneva, May, 2013.

[Whi08] C. WHITE: *Single Top Production in the Wt Mode with MC@NLO.* HERA-LHC 2008, arXiv:0805.3067, hep-ph.

[Yam11] T. YAMANAKA (FOR ATLAS COLLABORATION): *The ATLAS calorimeter simulation FastCaloSim.* J. Phys.: Conf. Ser. 331 (2011) 032053.

[Yos88] G. P. YOST ET AL.: *Particle Data Group.* Phys. Lett. B 204, 1 (1988).

# Acknowledgment

Entfernt aus datenschutzrechtlichen Gründen.

# Curriculum vitæ

Entfernt aus datenschutzrechtlichen Gründen.